Direct Dark Matter Search with XENON1T and Developments for Multi-Ton Liquid Xenon Detectors

Dissertation
zur
Erlangung der naturwissenschaftlichen Doktorwürde
(Dr. sc. nat.)

vorgelegt der
Mathematisch-naturwissenschaftlichen Fakultät
der
Universität Zürich

von
Julien Wulf
aus
Deutschland

Promotionskommission
Prof. Dr. Laura Baudis (Vorsitz)
Prof. Dr. Marc Schumann
Prof. Dr. Ben Kilminster

Zürich, 2018

Abstract

The presence of non-luminous, non-baryonic, non-relativistic dark matter in our universe has been pointed out by numerous astrophysical observations, and its nature is an unanswered question of modern physics. A favourite dark matter candidate is the weakly interacting massive particle (WIMP), and many experiments in the world are specialised in its direct detection.

The world's most sensitive direct dark matter experiment is the XENON1T detector, which was constructed in the underground laboratory of LNGS in Italy. XENON1T searches for galactic WIMP interactions with nuclei in a target of 2 t liquid xenon by using the technology of a dual-phase time projection chamber (TPC). The XENON1T detector acquired 278.2 days of science data, leading to the most stringent exclusion limit on spin-independent WIMP-nucleon cross sections above masses of $6\,\mathrm{GeV}/c^2$, with a minimum of $4.1 \times 10^{-47}\,\mathrm{cm}^2$ at a mass of $30\,\mathrm{GeV}/c^2$. Its successor, XENONnT is currently under design, and its construction is expected to begin by the end of 2018. It will use ~ 6 t of liquid xenon as an active target and aims on improving the sensitivity by one order of magnitude. Meanwhile, the DARWIN collaboration is working on the development of the ultimate dark matter detector with ~ 40 t of liquid xenon as an active target, which will be able to probe the WIMP-nucleon cross sections down to $\sim 10^{-49}\,\mathrm{cm}^2$, at a mass of $\sim 50\,\mathrm{GeV}/c^2$.

This thesis presents several achievements related to the work on the XENON1T, XENONnT and DARWIN experiments. One of the primary topics of my PhD work was the design, validation, characterisation, installation and commissioning of the XENON1T TPC, including its PMTs. In addition, measurement procedures were developed to characterise the PMTs during the TPC operation and to monitor and simulate their response during the data taking.

Contributions to the analysis of the XENON1T science data are also part of this thesis. The predictions of the detector specific electric drift and extraction field, as well as the electron drift velocity and trajectories, were performed with an electrostatic simulation framework, developed for this purpose. Furthermore, to ensure a proper event selection, two data quality cuts were developed to reject non-physical events. These cuts were included in the dark matter search analyses, which resulted in the best spin-independent WIMP-nucleon cross sections at the time of writing.

In the case of XENONnT, a dual channel amplifier was developed to address the challenge of obtaining a linear response of the TPC from a few keV to the MeV energy range, in order to study different physics channels at various energies. In addition, a single phase liquid xenon detector was designed and commissioned, in order to characterise a significant fraction of the XENONnT PMTs prior to their installation in cryogenic conditions, including liquid xenon.

Another topic of this work was to investigate the potential use of novel vacuum ultraviolet radiation sensitive silicon photomultipliers (SiPMs) for the planned DARWIN experiment. A series of measurement procedures and an evaluation setup were established to characterise SiPMs reliably down to cryogenic temperatures. In addition, a SiPM array for the light detection of a small-scale xenon-based TPC was developed, including the precise modelling of the scintillation light collection with Monte Carlo simulations. This development allows an event reconstruction in the x-y plane with sub-millimetre precision by using a neural network pattern recognition algorithm.

This work overall contributed to the advancement of the direct detection experiments, which will reach an unexpected sensitivity to dark matter particles in the near future.

Acknowledgements

The moment had come... After months of writing, I start to write the last page of my thesis. With a smile in one eye and a tear in the other, I look over my four years of study and see so many individual people and institutions, without whose support and help this thesis would not have been possible. Although all your names are not mentioned here, your help has not gone unnoticed.

First of all, I would like to thank my PhD advisor, Prof. Laura Baudis, who gave me the opportunity to work on the foremost front in the field of direct dark matter detection and for supervising me with great expertise at any time of my study. She gave me her trust and the freedom to develop my own research goals while advising me wisely over the past four years.
A special thank to Prof. Marc Schumann and Prof. Ben Kliminster for being part of my doctoral committee and continuously evaluating my work.
I thank all the members of the XENON collaboration for the friendly and motivating working atmosphere, and of course, all the fun during the collaboration meetings. Thanks in particular to Dr. Junji Naganoma for the fruitful discussions and for always making me enjoy my periods at LNGS a lot, even in times of earthquakes. I will miss the nice moments at Poco Loco.
Thanks to all of the present and past group members at the UZH, with whom I had a lot of inspiring discussions and a great time, even outside work. Especially with Dr. Yuehuan Wei, Dr. Shingo Kazama, Dr. Giovanni Benato, Dr. Gaudenz Kessler, Dr. Peter Barrow, Dr. Roman Hiller, Dr. Patricia Sanchez (whom I would also like to thank for proofreading my thesis) and Adam Brown.
A special thank to Dr. Alexander Kish. He gave me always valuable comments to my work and to the manuscript. He is an example of a good scientist.
None of the experimental work in this thesis would have been possible without the technical expertise of Andreas James. Thanks for helping me times and times again and being a good friend.
Furthermore, I would like to thank the people in the physics institute and the people in the mechanical and electronic workshop for all the help during my time as a PhD student. It was a kind atmosphere and I enjoyed every year to be part of the SOLA relay team.
A special thank goes to Daniel Florin with whom I spent so many hours in the electronic workshop. His professional view on the problems helped always to design the different necessary electronics.

I thank my family for constantly believing, supporting and encouraging me, no matter what. A special word of thanks goes to my mother, who has always an open ear and mind. She was always there for me whenever needed. I am also grateful to my sister, which encouraged and motivated me to study physics. Thanks for advising me.
I thank all my friends scattered around the world. In particular Sandro D'Amato and Peter Fehlner. Thank you for your time, whenever I needed a friend and to counterbalance myself.
Finally, I am grateful to my beloved girlfriend, Irena, for always supporting and helping me in difficult moments. Thanks for the patience while I was working on this thesis and for proofreading. I am immensely happy that the long months of writing stuck together made our bond even stronger. Ајде, фала за се!
My last words go to my father, who always believed in my ability to be successful in anything and he taught me to enjoy life while pursuing my curiosity. You may not know of my over-ten-years-long journey in physics, but you made this journey possible.

Contents

“Know how to solve every problem that has ever been solved.”
Richard Feynman

CHAPTER 1

Introduction - The Dark Universe

Observations at cosmological and astronomical scales indicate that the majority of matter in our Universe is in the form of non-relativistic and long-lived dark matter particles, which is one of the unanswered questions of modern physics. A favourite candidate for dark matter is the Weakly Interacting Massive Particle (WIMP), and it is an ingredient for many alternative theories and extensions of the Standard Model [1]. The Standard Model of cosmology ΛCDM (Λ Cold Dark Matter) is a well-tested model, which has been developed based on measurements of astrophysical systems. It accounts baryonic matter with 4 %, dark matter with 27 % and dark energy with 69 % of the total energy content in the Universe [2]. Λ refers to the dark energy, which explains the continuous accelerated expansion of the Universe [3].

In section 1.1 of this introduction, we will outline some of the observational evidence for dark matter. It is followed by section 1.2, which will introduce the most popular dark matter models. Section 1.3 will briefly describe the various dark matter detection techniques, whereas section 1.4 will focus on the direct dark matter detection with a xenon-based dual-phase time projection chamber. The chapter will be closed with an outline of the thesis. A more detailed review of the nature of dark matter and its detection mechanism can be found in [4, 5].

1.1 Observation Evidence for Dark Matter

The Swiss physicist Fritz Zwicky was the first who claimed the existence of non-luminous dark matter in 1933 by observing the velocities of extragalactic nebulae in the Coma cluster [6, 7]. He found that the gravitational mass reconstructed with the virial theorem contradicts the amount of mass estimate from the luminosities of the galaxies. He explained this discrepancy by the presence of dark matter[1]. Since then, different cosmological and astrophysical observations resulted in the same conclusions [8].

An additional strong evidence for dark matter was found by Vera Rubin in 1970, by precise rotation velocity measurements of stars and gas in disk galaxies [9]. She measured the rotation velocity as a function of the distance to the galactic centre. According to Newtonian mechanics [10] the rotational velocity is given by the following expression:

$$v(r) = \sqrt{\frac{GM(r)}{r}}, \tag{1.1}$$

where G is the Newton’s constant, and $M(r)$ is the total mass of the galaxy inside the radius r from the centre of the galaxy. One would expect according to equation 1.1 that the rotation velocity decreases after reaching the outer region of the galaxies with $v(r) \propto \frac{1}{r}$. Vera Rubin found that the

---

[1] *“...würde sich also das überraschende Resultat ergeben, dass dunkle Materie in sehr viel grösserer Dichte vorhanden ist als leuchtende Materie.“* [6]

rotational velocity stayed flat far beyond the outer region of the galaxies (>10 kpc), as shown in Figure 1.1 (left). The suggested explanation was the presence of a dark matter halo with $M(r) \propto r$, which accounts for the observed behaviour. Measurements of different spiral galaxies, including the Milky Way, show the same behaviour [11, 12].

One of the strongest evidence for the existence of dark matter comes from the observation of the collision of galaxy clusters. The most famous example of a collision of two galaxy clusters is the bullet cluster (1E 0657-558), which is shown in Figure 1.1 (right). The stars and galaxies are shown in white and orange respectively, and passed each other without influencing expect via the gravitational force. The X-ray measurement with the Chandra X-ray Observatory [14] is shown in pink and represents the two hot intergalactic gas clouds, which heat up and slow down during the collision. The blue region is obtained from gravitational lensing of the background luminous objects and is due to the presence of dark matter, which is unaffected by the collision. According to Einstein, mass has the ability to deflect light, and therefore a large amount of mass can act like a lens, which is called gravitational lensing. The bullet cluster is a remarkable evidence for the existence of dark matter and was confirmed by further observations of different galaxy cluster collisions [15].

The absolute abundance of dark matter in the Universe can be measured from the cosmic microwave background (CMB). The CMB was discovered in 1965 by Penzias and Wilson, and it is a leftover radiation from the Big Bang. Around 380 000 years after the Big Bang, the Universe was cold enough to form neutral atoms and the photons decoupled from the baryon-photon plasma. The CMB is, therefore, the relict of the last scattering before the recombination and has cooled down until today, due to the continuous expansion of the Universe. The CMB was measured by the COBE [16], WMAP [17] and Planck [18] satellites. The CMB exhibits a perfect blackbody spectrum with a temperature of 2.725 K. The CMB shows a maximum angular anisotropy in the order of

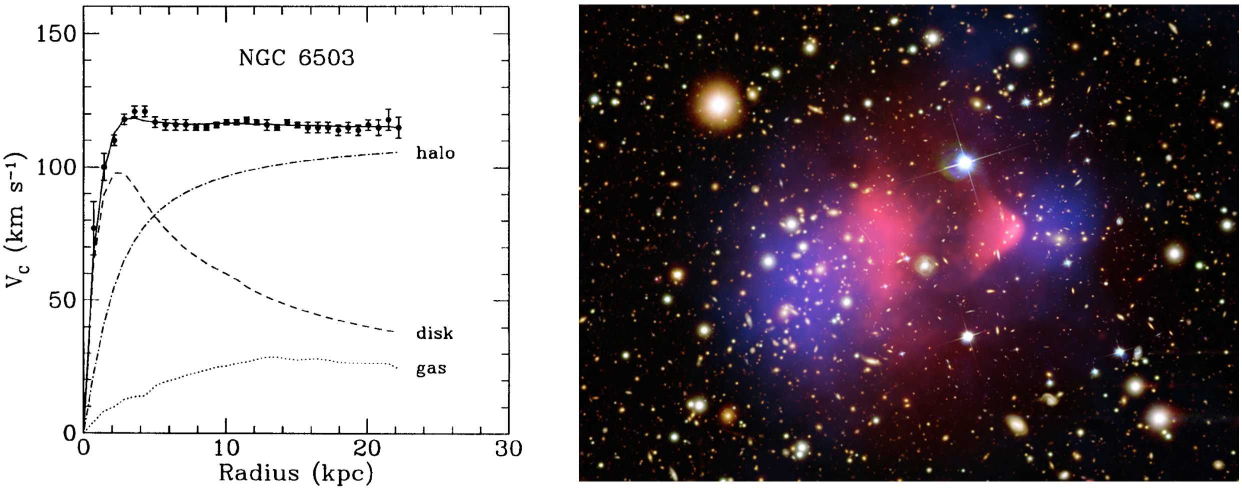

Figure 1.1: Left: Rotation velocity curve of the spiral galaxy NGC 6503 as a function of distance from the galactic centre. The visible component (dashed line), the gas component (dotted line) and the dark matter halo sum up to the predicted model (solid line), which is in agreement with the data. Figure taken from [13]. Right: Overlaid images of the bullet cluster 1E 0657-558. The optical image shows the galaxies in orange and white. The X-ray emission of the baryonic matter is shown in red, and the mass distribution by gravitational lensing is shown in blue. The baryonic matter is separated from the dark matter, responsible for the lensing effects after the collision. Image credit: Optical: (NASA/STScI; Magellan/U.Arizona/D.Clowe et al.); X-ray (NASA/CXC/CfA/M.Markevitch et al.); Lensing Map: (NASA/STScI; ESO WFI; Magellan/U. Arizona/D. Clowe et al.)

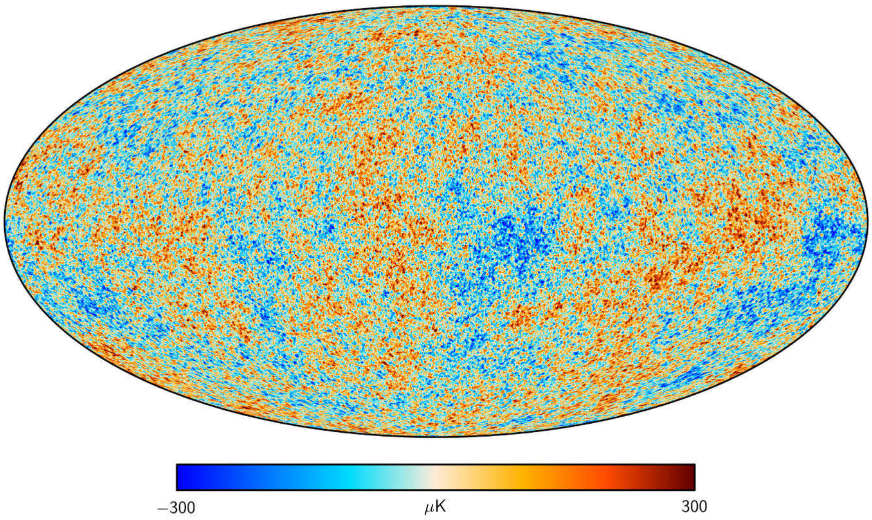

Figure 1.2: Sky map of temperature fluctuations in the measured cosmic microwave background derived from the joint analysis of Planck, WMAP and 408 MHz observations. Figure taken from [18].

300 μK, as shown in Figure 1.2, due to acoustic oscillations in the baryon-photon plasma in the early Universe. The temperature fluctuations in the early Universe are responsible for the formation of the observed large-scale structures. The power spectrum of the temperature fluctuations, which is the correlation strength between every possible combination of two points in the sky-map as a function of the angular distance, depends on the baryonic matter ($\Omega_b h^2$), cold dark matter ($\Omega_c h^2$) and dark energy (Ω_Λ) densities. The most precise measurements of the cosmological parameters have been recently performed by the Planck satellite, which resulted in the following energy densities [19]:

$$\Omega_\Lambda = 0.692 \pm 0.012, \qquad \Omega_c h^2 = 0.1186 \pm 0.0020, \qquad \Omega_b h^2 = 0.02226 \pm 0.00023, \tag{1.2}$$

where the density parameters Ω_b, Ω_c and Ω_Λ are the ratios between the average densities of matter/energy and the critical density ρ_c, and h is the Hubble parameter. The cosmological parameters are in a remarkable agreement with the Standard Model of cosmology.

There is strong evidence for the presence of cold dark matter, but its nature is still not known. The weakly interacting massive particle is one of the most popular candidates for dark matter and will be discussed in the next section. It has to be mentioned that there are many other dark matter candidates, which are beyond the scope of this thesis, some of which will be briefly outlined in the coming section.

1.2 Weakly Interacting Massive Particle

There have been several attempts to explain the astronomical observations discussed in the previous section without introducing a new particle. A possible solution to solve some of the mentioned astronomical measurements is the modification of the gravitational laws, such as the MOND [20] model or the relativistic extension TeVeS [21]. However, MOND is not able to explain the large-scale structures, the details of the CMB [22] and it is excluded at the level of galaxies [23]. Furthermore, TeVeS cannot simultaneously explain observations from gravitational lensing and the rotation velocity curves [24]. Other dark matter candidates are large massive objects in our Universe like black holes, neutron stars and other massive objects, which emit almost no radiation. However, a survey for such massive compact halo objects (MACHOs) showed that only 20 % of the dark matter in the

Milky Way galaxy consists of MACHOs [25]. Therefore, a common assumption is that the dark matter is a particle. Among the known particles in the Standard Model, the neutrino can be a candidate for dark matter, which meets the constraints of astronomical observations. The list of constraints on dark matter includes: not being of baryonic nature, having a weak self-interaction, having no electromagnetic interaction and having a very weak interaction with baryonic matter. Similar to the CMB, there is a relic neutrino background in the Universe. However, constraints on the neutrino mass show that the total relic density of neutrinos is $\Omega_\nu h^2 < 0.07$, which is not sufficient to be the dominant component of dark matter. In addition, neutrinos decoupled around 1 s after the Big Bang and since then they travel at relativistic speeds, which gives them the name hot dark matter. N-body simulations of our Universe show that neutrinos as a main dark matter component would not result in the observed large structure [26]. Therefore, it is necessary to go beyond the Standard Model to find a suitable dark matter particle.

A potential dark matter candidate is the axion introduced by Peccei and Quinn (PQ), which resolves the strong CP problem in quantum chromodynamics (QCD) and could have been non-thermally generated in the early Universe [27, 28, 29]. Other non-thermally generated dark matter candidates are WIMPzillas, super heavy particles ($10^{12} - 10^{16}$ GeV[2]) [30], which could be responsible for the observed ultra-high-energy cosmic rays above the Greisen-Zatsepin-Kuzmin cutoff [31, 32]. Furthermore, sterile neutrinos are also possible dark matter candidates, which can interact with ordinary matter by oscillations into the active sector [33, 34, 35]. However, the focus of this thesis lies on the weakly interacting massive particle (WIMP).

WIMPs were in thermal equilibrium with the plasma after the Big Bang, and therefore, produced and annihilated into Standard Model particles at equal rates. As the Universe expands and the temperature falls below the WIMP mass, the WIMP production reactions stop, and the WIMP density starts to decrease, due to the continuous WIMP annihilation. The WIMP annihilation stops as soon as the expansion rate H of the Universe becomes larger than the annihilation rate Γ_{ann}, and a relic WIMP density remains. This process is known as thermal freeze-out and is shown in Figure 1.3. The relic WIMP density is then given by the following expressions [36]:

$$\Omega_c h^2 = \frac{m_\chi n_\chi}{\rho_c} \approx \frac{3 \times 10^{-27}\,\text{cm}^3\text{s}^{-1}}{\sigma_{\text{ann}} v}, \tag{1.3}$$

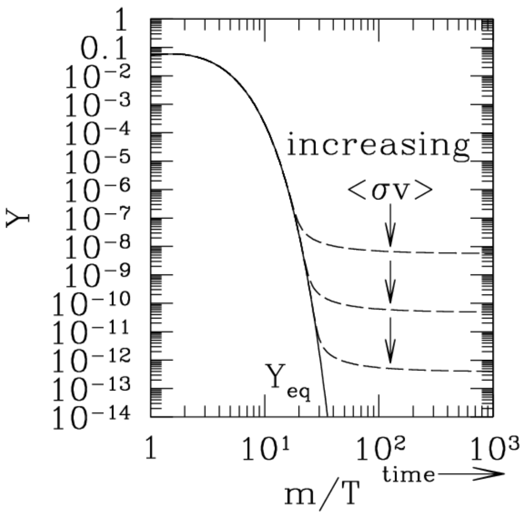

Figure 1.3: Evolution of the WIMP density n normalised by the entropy density s from the epoch of thermal equilibrium until the time of the WIMP decoupling from the thermal plasma. The x-axis (m/T) is the ratio between the WIMP mass m and the temperature T, which is proportional to the time after the Big Bang. After the temperature drops below the WIMP mass, the WIMP production reactions stop, and the WIMP density starts to decrease, due to the continuous WIMP annihilation. The WIMP annihilation stops as soon as the expansion rate H of the Universe becomes larger than the annihilation rate Γ_{ann}, and a relic WIMP density remains. The WIMP density depends on σ_{ann} (dashed line). Figure taken from [36].

---

[2] Throughout the thesis (except the figures) we will use 'natural units', where $\hbar = 1$ and $c = 1$.

where m_χ is the WIMP mass, n_χ is the number density, ρ_c is the critical density, σ_{ann} is the thermally-averaged WIMP annihilation cross section, and v is the relative velocity of the annihilating particles. The equation 1.3 results in the correct dark matter abundance, if σ_{ann} is on the order of the weak interaction scale. The mass of the WIMP ranges between 1 GeV and several TeVs in order to account for the observed gravitational effects.

There are several different WIMP models which provide the required properties, like the extra-dimensional Kaluza-Klein model [37, 38]. One of the best-motivated WIMP models results from the supersymmetry theories, which are an extension of the Standard Model and solve the hierarchy problem, as well as unify the four fundamental forces. In the minimal supersymmetric extension to the Standard Model (MSSM), the lightest supersymmetric particle (LSP) - the neutralino, is a favoured dark matter candidate [39]. The neutralino is stable and has a mass in the range from a few GeVs to several TeVs with an interaction to ordinary matter on the order of the weak interaction scale [40]. The neutralino is not yet ruled out, and it is a subject of study in many dark matter detection experiments, which will be discussed in the next section.

1.3 Dark Matter Detection Experiments

There are several approaches to detect the WIMPs introduced in the last section, as shown in Figure 1.4. WIMPs can be detected by production at particle colliders, indirectly by self-annihilation products and directly from scattering off Standard Model particles.

The Large Hadron Collider (LHC) [41] at CERN aims to produce WIMPs by the collision of two Standard Model particles (proton-proton collision). The production process of the WIMP involves different Standard Model particles, and the WIMP would escape the detector without any signature. A WIMP signature can be detected by a discrepancy in the energy before the collision and the total energy of the produced Standard Model particles [42, 43]. With the experiments CMS and ATLAS, no evidence for WIMPs at a centre of mass energy of 13 TeV has been found so far [44, 45]. Even if a WIMP signature is detected with a collider experiment, the existence of the dark matter in our galaxy still needs to be proven.

WIMPs can be indirectly detected through the self-annihilation products. Therefore, indirect

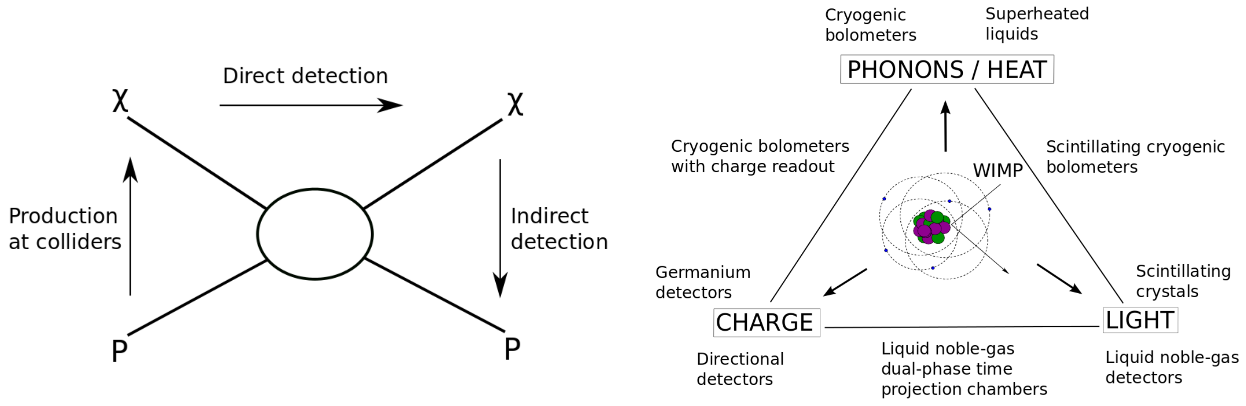

Figure 1.4: Left: Schematic of possible WIMP (χ) detection channels with Standard Model particles (P). WIMPs can be detected by production at particle colliders, indirectly by self-annihilation products and directly from scattering off Standard Model particles. Right: Schematic of possible WIMP signatures in direct detection experiments. The recoil energy can be transformed into a measurable signal, such as scintillation light, charge, or phonons (heat). Figures taken from [5].

detection experiments observe the self-annihilation products from astrophysical objects, such as dwarf galaxies, our sun and the galactic centre. In such a massive object, a high WIMP density is expected due to the enhanced gravitational force, and therefore, the WIMP self-annihilation rate is increased [46]. The indirect WIMP search focuses mainly on the following self-annihilation products [5]:

$$\begin{aligned} &\chi\bar{\chi} \rightarrow \gamma\gamma, \gamma Z, \gamma H; \\ &\chi\bar{\chi} \rightarrow q\bar{q}, W^{-}W^{+}, Z\bar{Z}, \end{aligned} \tag{1.4}$$

where the unstable particles decay further into $e^{+}e^{-}$, $p\bar{p}$, γ-rays and neutrinos. Earth-bound Cherenkov telescopes and satellites search for WIMP self-annihilation products. Fermi [47], MAGIC [48], HESS [49] and CTA [50] look for the photons, IceCube [51] and ANTARES [52] search for neutrinos and AMS [53] could detect anti-fermions. So far, in all indirect experiments, no evidence for WIMPs has been observed [54].

The direct detection focuses on the WIMP-nucleus scattering inside the target of an Earth-bound detector [55, 56]. The WIMPs produce nuclear recoils between a few of tens of keV, and therefore a very low energy detector threshold is necessary. The recoil energy can be transformed into a measurable signal, such as scintillation light, charge, or phonons (heat). There are several experiments, which try to detect the recoil energy with one or with a combination of the mentioned signal channels in order to achieve a better background discrimination.

The DAMA/LIBRA [57] and SABRE [58] experiments use solid scintillation detectors to search for an annual modulation of the WIMP rate. The Earth orbits around the sun and the sun around the galactic centre through the WIMP halo. Therefore, the Earth's relative speed to the galactic centre is largest in summer and lowest in winter, which would result in an annual modulation of the WIMP interactions [59].

The CRESST [60] experiment is based on the bolometric technique and utilises Ca_2WO_4 crystals operated at a temperature of $\sim 15\,\mathrm{mK}$. The detectors measure the deposited recoil energy via generated phonon and scintillation light during the scattering process. SuperCDMS [61] and EDELWEISS [62] are also based on the bolometric technique and measure phonons and ionisation electrons mainly in germanium crystals.

The DAMIC [63] experiment uses charge-coupled devices (CCDs) to detect the charge generated by the WIMP-nucleus elastic scattering in silicon. The PICO [64] experiment uses a bubble chamber filled with superheated C_3F_8, which captures bubble images and the acoustic signals from bubble nucleation. The XMASS [65] and DEAP-3600 [66] experiment operated a single-phase detector filled with xenon and argon, respectively, observing the scintillation light. The DarkSide [67] and ArDM [68] experiments use argon-based dual-phase time projection chamber to detect the charge and light generated by the WIMP-nucleus elastic scattering.

The focus of this thesis is the direct dark matter detection with a xenon-based dual-phase time projection chamber, which will be introduced in details in the next section.

1.4 Direct Dark Matter Detection

The focus in this section is the direct dark matter detection. In the first part, we will discuss the expected nuclear recoil scattering rates of WIMPs with ordinary matter. This is followed by a description of xenon as a direct dark matter detection target material. The section will be closed with the direct dark matter detection technique using a xenon-based dual-phase time projection chamber.

1.4.1 Nuclear Recoil Scattering Rates

The expected WIMP-nucleus scattering rate R in direct dark matter experiments can be expressed with the following equation:

$$R = N_T \frac{\rho_0}{m_\chi} \bar{v} \sigma(E_R, v), \tag{1.5}$$

where N_T is the number of target nuclei, ρ_0 is the local WIMP density, m_χ is the WIMP mass, $\bar{v}$ is the average WIMP velocity relative to the target, and $\sigma(E_R, v)$ is the total elastic scattering cross section of WIMPs on ordinary matter, which depends on the recoil energy and velocity of the incoming particle. In addition, one has to take into account the WIMP velocity distribution, which is commonly assumed to be isotropic Maxwell-Boltzmann distribution:

$$f(\boldsymbol{v}) = \frac{1}{\sqrt{2\pi\sigma_0}} \times \exp\left(-\frac{|\boldsymbol{v}|^2}{2\sigma_0^2}\right), \tag{1.6}$$

where $\sigma_0 = \sqrt{3/2} \times v_0$ is the circular velocity dispersion, and v_0 is the circular velocity of our sun. However, a direct dark matter experiment measures the interactions per unit recoil energy E_R and detector mass M_T. Therefore, equation 1.5 can be written as a differential rate normalised by the target mass ($M_T = N_T \times m_N$) with an integral over v:

$$\frac{\mathrm{d}R}{\mathrm{d}E_R} = \frac{\rho_0}{m_\chi m_N} \int_{v_{\mathrm{min}}}^{v_{\mathrm{esc}}} v f(\boldsymbol{v}) \frac{\mathrm{d}\sigma(E_R, \boldsymbol{v})}{\mathrm{d}E_R} \mathrm{d}^3 v, \tag{1.7}$$

where m_N is the mass of a single target nucleus, v_{min} is the minimal WIMP velocity necessary to cause a recoil energy, and v_{esc} is the escape velocity, which indicates the velocity where the gravitational force of the galaxy can be overcome. The minimal WIMP velocity can be calculated with the classical Newtonian kinematics (WIMPs are assumed to be non relativistic) of a 180 ° elastic back-scatter, which is given by the following expression:

$$v_{min}(E_{\mathrm{max}}) = \sqrt{\frac{m_N E_{\mathrm{max}}}{2\mu^2}} \qquad \text{with} \qquad \mu = \frac{m_N m_\chi}{m_N + m_\chi}, \tag{1.8}$$

where μ is the reduced WIMP-nucleon mass. The result interpretation of a direct detection experiment depends on astrophysical and nuclear physics assumptions, as shown in equation 1.7. Therefore, direct dark matter detection experiments assume a standard halo model with $v_0 = 220\,\mathrm{km/s}$ [69], $\rho_0 = 0.3\,\mathrm{GeV}/(\mathrm{cm}^3)$ [70] and $v_{\mathrm{esc}} = 544\,\mathrm{km/s}$ [71] to ensure a comparison with each other.

The term $\mathrm{d}\sigma(E_R, \boldsymbol{v})$ in equation 1.7 depends on how the WIMP couples to the target nucleus. The interaction can be spin-independent (SI) or spin-dependent (SD). In the SI interaction, the neutrons and protons contribute equally, whereas in the SD interaction, the unpaired nucleon spins contribute to the scattering. The cross section of the interaction is given by the sum of both:

$$\frac{\mathrm{d}\sigma(E_R, v)}{\mathrm{d}E_R} = \frac{m_N}{2\mu^2 v^2} \left[\sigma_0^{\mathrm{SI}} F_{\mathrm{SI}}^2(E_R) + \sigma_0^{\mathrm{SD}} F_{\mathrm{SD}}^2(E_R)\right], \tag{1.9}$$

where σ_0^{SI} and σ_0^{SD} are the cross sections in the limit at zero momentum transfer for SI and SD interactions respectively, and F_{SI} and F_{SD} are the nuclear form factors for SI and SD interactions, respectively.

For the spin-independent interactions, the analytic Helm form factor is commonly used [72], and the cross section at zero momentum transfer is given by the following expression [73]:

$$\sigma_0^{\mathrm{SI}} = \frac{4\mu}{\pi} \left[Z f_p + (A - Z) f_n\right]^2, \tag{1.10}$$

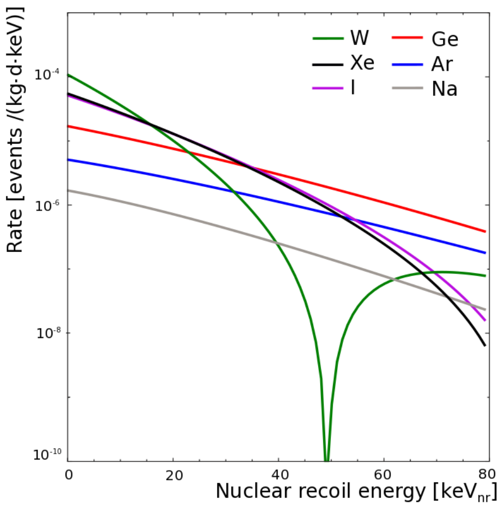

Figure 1.5: The differential recoil spectra from WIMP-nucleon scattering using tungsten (green), xenon (black), iodine (magenta), germanium (red), argon (blue) and sodium (grey) as target materials. A WIMP mass of $m_\chi = 100\mathrm{GeV}$ and a WIMP-nucleon spin-independent cross section of $\sigma_0^{\mathrm{SI}} = 1 \times 10^{-45}\,\mathrm{cm}^2$ are assumed. The interaction rate scales with A^2, which makes heavier target materials preferable for direct dark matter search experiments. The nuclear form factor is responsible for the decrease of the interaction rate with increasing recoil energy, due to the loss of coherence. Figure taken from [5].

where Z is the atomic number, A is the atomic mass number, and f_p and f_n are the SI coupling strengths of WIMPs to protons and neutrons, respectively. A commonly used assumption is $f_p \approx f_n$ [74], which simplifies equation 1.10 to:

$$\sigma_0^{\mathrm{SI}} \approx \frac{4\mu^2}{\pi}(f_p A)^2. \tag{1.11}$$

Direct dark matter search experiments report their result on the SI cross section normalised to the cross section of a WIMP with a single proton $\left(\sigma_p^{\mathrm{SI}} = \frac{4\mu_p^2}{\pi} f_p^2\right)$, due to the model dependence on f_p:

$$\sigma_0^{\mathrm{SI}} = \left(A\frac{\mu}{\mu_p}\right)^2 \sigma_p^{\mathrm{SI}}, \tag{1.12}$$

where μ_p is the WIMP-proton reduced mass. Figure 1.5 shows the differential recoil spectra (equation 1.7) considering a SI WIMP-nucleon scattering off different target materials. The interaction rate scales with A^2, which makes heavier target materials preferable for direct dark matter search experiments. The nuclear form factor is responsible for the decrease of the interaction rate with increasing recoil energy, due to the loss of coherence[3].

In the case of the spin-dependent interaction, the form factor is calculated from the nuclear shell model [75], and the cross section at zero momentum transfer is given by the following equation:

$$\sigma_0^{\mathrm{SD}} = \frac{32}{\pi}\mu G_F \left(a_p\langle S_p\rangle + a_n\langle S_n\rangle\right)^2 \frac{J+1}{J}, \tag{1.13}$$

where G_F is the Fermi-constant, a_p and a_n are the SD couplings strengths of WIMPs to protons and neutrons, respectively, J is the spin of the nucleus, and $\langle S_p\rangle$ and $\langle S_n\rangle$ are the expectation values of the spin state of the protons and neutrons, respectively. Therefore, direct dark matter experiments using a target with an odd mass number are sensitive to the SD WIMP-nucleon scattering.

However, the potential interaction between dark matter and baryons can be described in more details in the context of a non-relativistic effective field theory (EFT) [76, 77, 78]. The possible interactions can be described by 14 operators $\mathcal{O}_i$, which do not treat the nucleus as a point-like particle. These additional interactions are from a great interest in order to extract more information from

---

[3] The wavelength associated with the momentum transfer becomes smaller than the nuclear radius [35].

direct detection experiments, due to the explicit dependence of some operators on the momentum transfers [4, 79]. However, the SI and SD interactions (described by the operators $\mathcal{O}_1$ and $\mathcal{O}_4$) are the two main types of interactions, and the SI interaction is the focus of this thesis.

A preferred used target material in direct detection experiments is the noble gas xenon (Xe), which offers an excellent sensitivity to the SI WIMP-nucleon cross sections, due to its high mass number. Furthermore, there are two isotopes in xenon (^{129}Xe and ^{131}Xe), with a spin of $1/2$ and $3/2$, respectively, which offer an excellent sensitivity to the SD WIMP-nucleon cross sections. Particle detection with liquid xenon will be discussed in the next section.

1.4.2 Particle Detection with Liquid Xenon

As discussed in the previous section, the noble gas xenon offers an excellent sensitivity to SI and SD WIMP-nucleon interactions. Xenon has a concentration of 0.1 ppm in the Earth's atmosphere, and it is the heaviest non-radioactive noble gas element. Xenon is also a favourite target material in rare event searches, due to the absence of any long-lived radioisotopes, besides double-beta emitter ^{136}Xe with a half-life of 2.165×10^{21} years [80]. The abundance of ^{136}Xe in natural xenon is a possible source to detect the neutrinoless double beta decay at a Q-value at 2.458 MeV. Xenon exists in nature in nine stable isotopes. The xenon isotopes ^{129}Xe and ^{131}Xe can be used to probe spin-dependent WIMP-nucleon interactions, due to the presence of a non-zero nuclear spin ($1/2$ and $3/2$). Furthermore, liquid xenon has a high stopping power for penetrating background radiations, due to its high density of $2.86\,\mathrm{g/cm^3}$ [81]. WIMPs or neutrons scatter off the xenon nuclei (nuclear recoil - NR), whereas γ-rays and electrons interact with the atomic electrons (electronic recoil - ER) when passing through liquid xenon. Figure 1.6 shows the attenuation length for γ-rays and neutrons in liquid xenon.

The energy transfer of the particle interaction with the xenon atom is split between ionisation (electron-ion pairs - $\mathrm{Xe}^+ + e^-$), excitation (excitons - Xe^*) and heat without any ionisation or scintillation process [84, 85, 72]. By collisions with the neighbouring xenon atoms, the excitons create excited molecular states (excimers - Xe_2^*). The electron-ion pairs can recombine, or some of the electrons may escape from the interaction site. The number of escaped electrons is higher when a drift field is applied. Even in the absence of any applied drift field, some of the electrons can thermalise far from the ion and hence not recombine [86]. In case of a successful electron pair

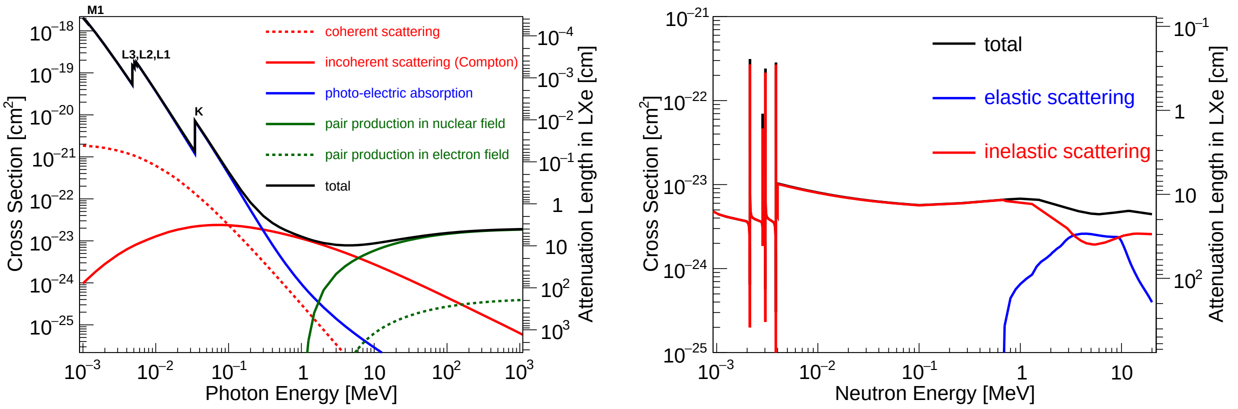

Figure 1.6: Left: Cross section and attenuation length of photons in liquid xenon ($2.86\,\mathrm{g/cm^3}$) as a function of energy. Data points taken from [82]. Right: Cross section and attenuation length of neutrons in liquid xenon (^{132}Xe, $2.86\,\mathrm{g/cm^3}$) as a function of energy. Data points taken from [83].

recombination, an excimer will be produced by the following processes:

$$\begin{aligned} \mathrm{Xe}^+ + \mathrm{Xe} &\rightarrow \mathrm{Xe}_2^+ \\ \mathrm{Xe}_2^+ + e^- &\rightarrow \mathrm{Xe}^{**} + \mathrm{Xe} \\ \mathrm{Xe}^{**} &\rightarrow \mathrm{Xe}^* + \mathrm{heat} \\ \mathrm{Xe}^* + \mathrm{Xe} &\rightarrow \mathrm{Xe}_2^* \end{aligned} \tag{1.14}$$

The excimers decay within a few to tens nanoseconds from the single or triplet spin state further to the ground state under the emission of a vacuum ultraviolet (VUV) photon centred at a wavelength of 178 nm (7 eV) with a width of 13 nm [87, 88, 89]:

$$\mathrm{Xe}_2^* \rightarrow 2\mathrm{Xe} + h\nu \tag{1.15}$$

Therefore, the xenon atoms do not absorb the emitted VUV photons produced by the de-excitation of the excimers, and xenon is a fast scintillator. Furthermore, liquid xenon has a large band gap (9.28 eV) between the valence and the conduction band, which makes it a strong insulator [90].

In addition, nuclear recoils create a denser ionisation track than electronic recoils, due to their higher stopping (dE/dx). Therefore, the electron-ion recombination in the dense nuclear recoil track is higher than the recombination in the non-dense electron recoil track, even in the presence of a strong drift field, due to charge shielding effects [91]. This is the basis of the discrimination between WIMPs (nuclear recoils) and background γ-rays and β-particles (electronic recoils). The next section will explain the xenon-based dual-phase time projection chamber, which takes advantage of the discrimination between nuclear and electronic recoils.

1.4.3 Xenon-Based Dual-Phase Time Projection Chamber

The xenon-based dual-phase time projection chamber (TPC) measures the prompt scintillation signal (S1 signal) and the ionisation signal (S2 signal) of an energy deposition in liquid xenon. In Figure 1.7 the working principle is shown. The TPC consists of an active xenon target and a gaseous xenon layer on top. A particle interaction inside the active liquid xenon creates both

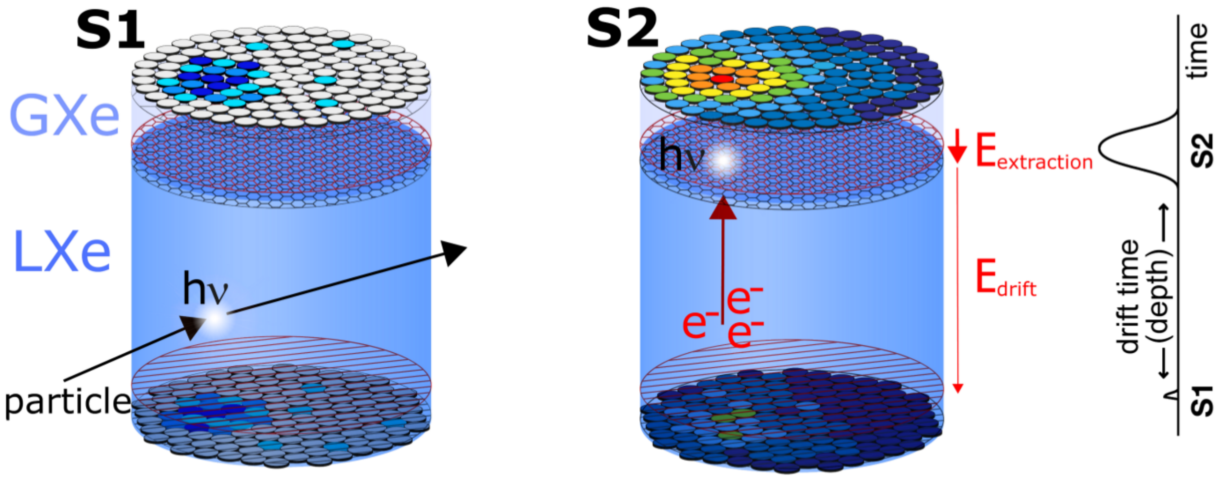

Figure 1.7: Working principle of a xenon-based dual-phase time projection chamber. A particle interaction inside the active liquid xenon creates both scintillation photons and ionisation electrons. The scintillation photons are detected by two PMT arrays below and above the target. A detailed explanation is given in the main text. Figure adapted from [92].

scintillation photons and ionisation electrons. The prompt scintillation photons (S1) are detected by two arrays of photomultiplier tubes (PMTs) below and above the target. A homogenous drift field applied across the target (E_{drift}), drifts some of the electrons from the interaction site to the liquid/gaseous xenon boundary. The electrons are extracted into the gas phase by a strong extraction field ($E_{\mathrm{extraction}} > 10\,\mathrm{kV/cm}$), which ensures a 100 % extraction efficiency [93]. The electrons are accelerated in the high electric field region, and they produce an electro-luminescence signal (S2) [94, 93], which is proportional to the number of extracted ionisation electrons.

The time delay between the S1 and S2 signals can be used to determine the z coordinate of the interaction site. The S2 signal is strongly localized in the x-y plane, and therefore, the hit pattern on the top PMT array can be used to reconstruct the x and y coordinates of the interaction. Such 3D position reconstruction allows for an excellent external background rejection capability by fiducialization of the active target volume.

Furthermore, the ratio between the prompt scintillation signal (S1) and secondary ionisation signal (S2) differs for nuclear recoils (signal - WIMPs) and electronic recoils (electromagnetic background - γ-rays, β-decays), and can be used to reduce the background further.

$$\left(\frac{S2}{S1}\right)_{ER} > \left(\frac{S2}{S1}\right)_{NR} \tag{1.16}$$

With this technique, discrimination of electronic recoils at the level of $\sim$99.5 % can be achieved [95]. In Figure 1.8, ER and NR events are shown in the discrimination parameter space (log10(S2/S1), S1).

In addition, WIMPs are expected to scatter once in the fiducial volume, due to its very low scattering cross section. Neutrons are likely to scatter multiple times in a large detector and produce therefore two distinct signals, which can be used to further reduce the neutron background in the analysis.

The most sensitive direct dark matter detectors use the technology of a xenon-based dual-phase TPC [96, 97, 98]. This PhD work was performed in the context of direct dark matter search with a xenon-based dual-phase TPC within the XENON and DARWIN collaborations. The outline of my PhD work is given in the next section.

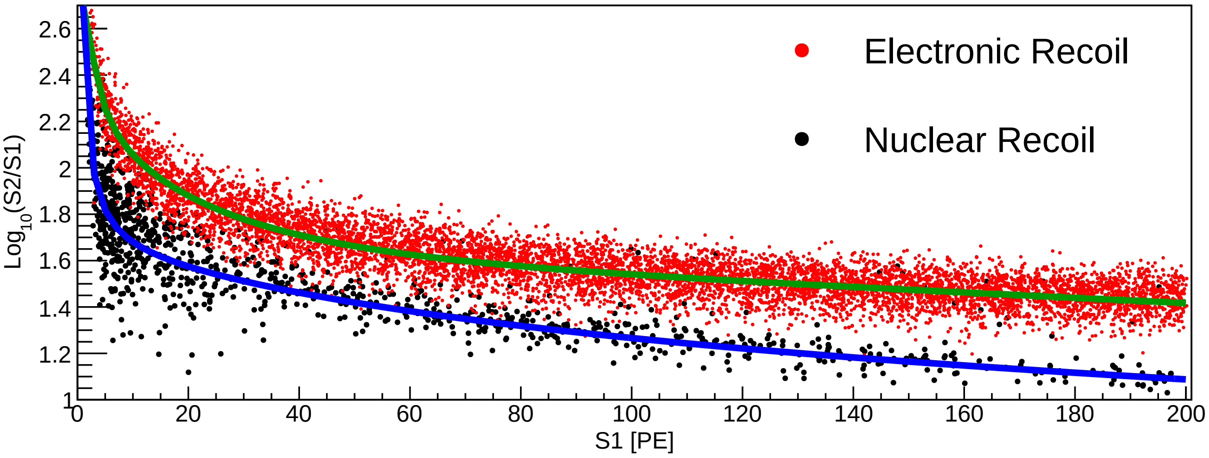

Figure 1.8: Distribution of ER (red points) and NR (black point) events from XENON1T calibration data (^{220}Rn, ^{241}AmBe) in the discrimination parameter space ($\log_{10}$(S2/S1), S1). The ER and NR events populate two overlapping bands, due to a different recombination probability. The green and blue curve represent the band median of ER and NR, respectively.

1.5 Outline of the Thesis

This PhD thesis will present the work performed on the XENON1T, XENONnT and DARWIN experiments. These experiments use the technology of a xenon-based dual-phase TPC, and at the time of writing XENON1T has set the best limit on the spin-independent WIMP-nucleon scattering cross-section above 6 GeV, which excludes a large fraction of previously unexplored WIMP parameter space. It needs to be mentioned that the XENON1T detector is the first successfully operative multi-ton xenon-based dual-phase TPC. In Figure 1.9 an overview of the current limits on the spin-independent WIMP-nucleon cross section of leading experiments is given.

The primary goal of the first part of my PhD work was the design validation, characterisation, installation, commissioning and operation of the XENON1T TPC, including the PMTs, as well as the dark matter data analysis. The goal of the second part of my PhD work was the development of a dual channel amplifier to address the challenge of obtaining a linear response of the XENONnT TPC from a few keV to the MeV energy range. In addition, an evaluation setup was developed (hardware and software) in order to characterise a significant fraction of the XENONnT PMTs prior to their installation in the TPC in cryogenic conditions, including liquid xenon. The final goal of my PhD work was to investigate the possible usage of novel vacuum ultraviolet radiation sensitive silicon photomultipliers (SiPMs) for the DARWIN experiment. In this context, dedicated SiPM research and development (R&D) was performed, and a xenon-based dual-phase TPC was designed, which employs SiPMs for the light detection and enables sub-millimetre position reconstruction precision by using a neural network pattern recognition algorithm. The presented thesis is organised as follows:

Chapter 2 will introduce and show the performance of a developed electrostatic field simulations framework specifically designed to perform 3D electric field simulations and electron particle tracking of noble gas dual-phase TPCs. The simulation framework is based on the highly efficient simulation techniques developed for the KATRIN experiment since detailed electrostatic simulations of large

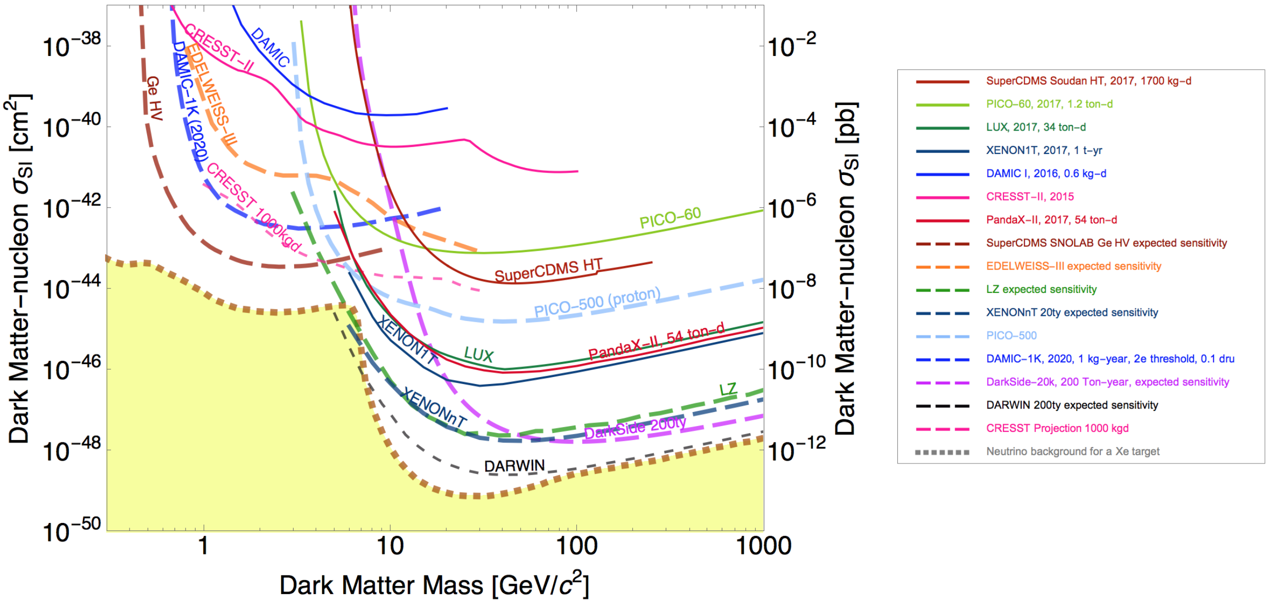

Figure 1.9: Overview of the current spin-independent limits on the WIMP-nucleon cross section (solid lines) from current experiments and the expected sensitivities for planned direct detection experiments (dashed lines). The irreducible neutrino background (yellow area) restricts the possibility to probe the WIMP-nucleon cross section at small values. Figure produced with [99].

detectors with commercially available simulation software tools are not capable of performing this task without any assumption on the geometry.

The XENON1T detector employs 248 3-inch PMTs, and it is the world largest xenon-based dual-phase TPC. Chapter 3 first introduces the XENON1T experiment briefly and in details the heart and eyes of the XENON1T detector, the TPC and PMTs. It is followed by the PMT readout validation and the cryogenic validation of the TPC. The chapter is closed with a detailed description of the construction and assembly phase, which led to a successfully operating XENON1T detector.

Chapter 4 will introduce the XENON1T TPC condition during the data taking, and their implications on the liquid target mass and TPC drift length. It is followed by the analysis of the regularly performed PMT calibrations during detector operation and stability over time of their response. The results from the analysis framework were stored in a dedicated database. Furthermore, detailed electrostatic simulations of the TPC were performed and compared to the data. The chapter is closed with the contributions to the dark matter search analysis, which led to the world best limit on the spin-independent WIMP-nucleon cross section at the time of writing this thesis.

The planned successor of the XENON1T is the XENONnT detector with a $\sim 8.2\,\mathrm{t}$ liquid xenon total mass. Chapter 5 will introduce the XENONnT experiment. It is followed by the hardware and software developments for a PMT evaluation setup, in order to characterise the XENONnT PMTs in cryogenic conditions (including liquid xenon), prior to their installation in the TPC. The measurement results of 10 PMTs during the commissioning run will be reported, which led to a better understanding of various PMT characteristics. The chapter will be closed with the development and validation of a dual channel amplifier, which addresses the challenge of obtaining a linear response of the TPC from a few keV to the MeV energy range. This development will allow to search for the neutrinoless double beta decay in XENONnT with high efficiency.

One of the ultimate direct dark matter detectors using xenon will be DARWIN. Chapter 6 will introduce the DARWIN experiment and will investigate the potential use of VUV-sensitive SiPMs in a xenon-based dual-phase TPC. A series of measurement procedures and an evaluation setup were established to characterise SiPMs reliably down to cryogenic temperatures. Furthermore, a SiPM array for the light detection of a small-scale xenon-based TPC was developed, including the precise modelling of the scintillation light collection with Monte Carlo simulations. This development allows an event reconstruction with sub-millimetre precision by using a neural network pattern recognition algorithm.

Finally, chapter 7 will present a summary and conclusion of my PhD work.

"The significant problems we have cannot be solved at the same level of thinking with which we created them."

Albert Einstein

CHAPTER 2

Electrostatic Simulation Framework

Xenon-based dual-phase TPCs continue to increase in size, due to the ease of scaling up of the technology and the simultaneous reduction of backgrounds. Electrostatic field simulations of the TPC are indispensable for the optimisation of the electrostatic design and the understanding of the data in the later analysis. Commercially available simulation frameworks such as COMSOL [100] are commonly based on the Finite Element Method (FEM) [101] and show strong deficits in the simulation of large-scale detectors in terms of computational power. Therefore, we adapted the simulation technique of KEMField [102], developed for the KATRIN [103] experiment, into a new framework for the simulation of xenon-based dual-phase TPCs. The framework is based on the Boundary Element Method (BEM) and performs the simulations on novel Graphics Processing Units (GPUs), which results in a fast computational time. In addition, the BEM has the advantage over the FEM in finding an accurate solution within a shorter time scale [104].

In section 2.1 of this chapter, we introduce the BEM and the solving technique with KEMField. Section 2.2 outlines the technical implementation of the developed simulation framework. It is followed by section 2.3, which reports the validation of the framework with various electrostatic problems. The framework will also be used in chapter 4 for the simulation of the XENON1T detector.

2.1 The Boundary Element Method

The usage of the Finite Element Method (FEM) for electrostatic field simulations requires discretisation of the entire computational domain in trapezoids, even the empty space between the electrodes. That implies a very high allocation of memory and consumption of computation time. In addition, the computational domain is restricted to a user-defined boundary.

On the other hand, electrostatic field simulations with the Boundary Element Method (BEM) require only the surface of the electrodes and dielectrics to be meshed in a finite number of so-called *sub-elements*. Each sub-element has a constant charge density distributed homogeneously over the surface. The form of the sub-elements is commonly restricted to triangles, rectangles and wires so that the resulting Coulomb-matrix element can be easily derived from it. The computational domain is not restricted, and this allows for open electrode systems. Complex electrodes can be modelled with a variable level of accuracy by using a different number of sub-elements, which are proportional to the computational time. Therefore, a geometry S can be expressed with the following equation:

$$S = \sum_{j}^{N} S_j, \tag{2.1}$$

where S_j is the j^{th} sub-element, and N is the total number of sub-elements. The charge density of each sub-element S_j is assumed to be constant and not known a priori. The voltages applied to the electrodes are known, and therefore the unknown charge density of sub-element S_j can be set in relation to the applied electrode voltage with the following expression:

$$U_i = \sum_{j=1}^{N} C_{ij}\sigma_j, \tag{2.2}$$

where U_i is the electric potential of sub-element S_i, σ_j is the charge density of sub-element S_j, and C_{ij} is the Coulomb-matrix element, which represents the electric potential of sub-element S_j at the centre point of sub-element S_i. Equation 2.2 describes a N×N matrix and the Coulomb-matrix elements can be obtained by the integration over the geometrical shape of sub-element S_j:

$$C_j\left(\vec{r}_i\right) = \frac{1}{4\pi\epsilon_0}\int_{S_j}\frac{1}{\vec{r}_i - \vec{r}_{S_j}}\mathrm{d}^2\vec{r}_{S_j}, \tag{2.3}$$

where ϵ_0 is the electric permittivity, $\vec{r}_i$ is the centre point of sub-element S_i, and $\vec{r}_{S_j}$ is a point on sub-element S_j. The calculation of the Coulomb-matrix elements for triangles, rectangles and wires, as well as a more detailed mathematical description of the BEM can be found in [105].

It needs to be mentioned that a dielectric sub-element can be treated with the following condition in the corresponding matrix element of equation 2.2 [106]:

$$\epsilon_i^+\vec{E}_i^+\vec{n}_i + \epsilon_i^-\vec{E}_i^-\vec{n}_i = 0, \tag{2.4}$$

where $\epsilon^{+/-}$ is the permittivity above and below the surface of the sub-element S_i, respectively, $\vec{E}_i^{+/-}$ is the electric field at the centre point above and below the surface of the sub-element S_i, respectively, and $\vec{n}_i$ is the surface normal vector of the sub-element S_i.

Once the Coulomb-matrix elements have been calculated, the matrix equation 2.2 can be numerically solved for the charge densities σ_j of the individual sub-elements. This can be done by using, for example, a Gauss-Jordan-algorithm. However, this algorithm needs a massive amount of computational time, and the memory allocation scales in this case with $\mathcal{O}(N^2)$. Therefore, the novel iterative Robin Hood method [107, 108, 109] is used for solving equation 2.2, in order to decrease the computational time and memory allocation, which scales with $\mathcal{O}(N)$. In addition, the Robin Hood method can be highly parallelized on modern platforms, which allows for the further decrease of the computation time [110].

The Robin Hood method is an iterative solving technique. In every iteration, it searches for the sub-elements S_i in equation 2.2 which differ the most from the equipotential surface. The potential on the surface of a sub-element S_i is given by the following expression:

$$U_i = \sigma_i C_{ii} + \sum_{j\neq i}^{N} C_{ij}\sigma_j. \tag{2.5}$$

The charge density of the sub-element S_i is then recalculated, in order to maintain the equipotential surface given by the applied voltage U_0:

$$\sigma_i = (U_0 - \sum_{j\neq i}^{N} C_{ij}\sigma_j)/C_{ii}. \tag{2.6}$$

Having calculated the new charge of the sub-element S_i, the potential for every other sub-element S_j is subsequently updated. The algorithm continues with the next iteration until the relative error θ on every sub-element S_i has reached a user-defined accuracy limit, which is defined by the following expression:

$$\theta = \frac{U_0 - U_i}{U_0}. \tag{2.7}$$

Using the Robin Hood algorithm does not require storage of the individual matrix elements of equation 2.2, but the individual potentials, which leads the memory requirements to grow linearly with N. The calculation of the sub-element potentials can be parallelized without any limitation except of the charge calculation itself, which makes the algorithm capable for usage on super computers, CPU or GPU farms. With the results of the charge densities of every individual sub-element S_i, the electric potential and field can be calculated at a given point $\vec{r}$ by the following expressions:

$$\begin{aligned} U\left(\vec{r}\right) &= \frac{1}{4\pi\epsilon_0}\sum_{j}^{N}\sigma_j\int_{S_j}\frac{1}{\vec{r}-\vec{r}_{S_j}}\mathrm{d}^2\vec{r}_{S_j}; \\ E\left(\vec{r}\right) &= \frac{1}{4\pi\epsilon_0}\sum_{j}^{N}\sigma_j\int_{S_j}\frac{\vec{r}-\vec{r}_{S_j}}{\left(\vec{r}-\vec{r}_{S_j}\right)^3}\mathrm{d}^2\vec{r}_{S_j}, \end{aligned} \tag{2.8}$$

which represent the superposition of the electric potential $U\left(\vec{r}\right)$ and field $E\left(\vec{r}\right)$ of all individual sub-elements S_j at a given point $\vec{r}$.

The Robin Hood solver and the Coulomb-matrix elements for triangles, rectangles and wires of the KEMField [102, 105] framework were adapted into a new simulation framework, which is described in the next section.

2.2 Implementation

This section is not a line-per-line program documentation of the framework but a basic description of the framework structure. The Application Programming Interface (API) of the developed simulation framework and the source code can be found in [111].

In Figure 2.1 a sketch of the framework is shown. The GPU BEM Robin Hood solver was taken from KEMField. Several managers organise the communication to KEMField, the geometry and the field calculation routines. The geometry, which is passed to the BEM solver, needs to be programmed in C++ [112] by the user with wires, rectangles or triangles. This allows the user to control the geometry discretisation and to balance between a faithful representation of the system,

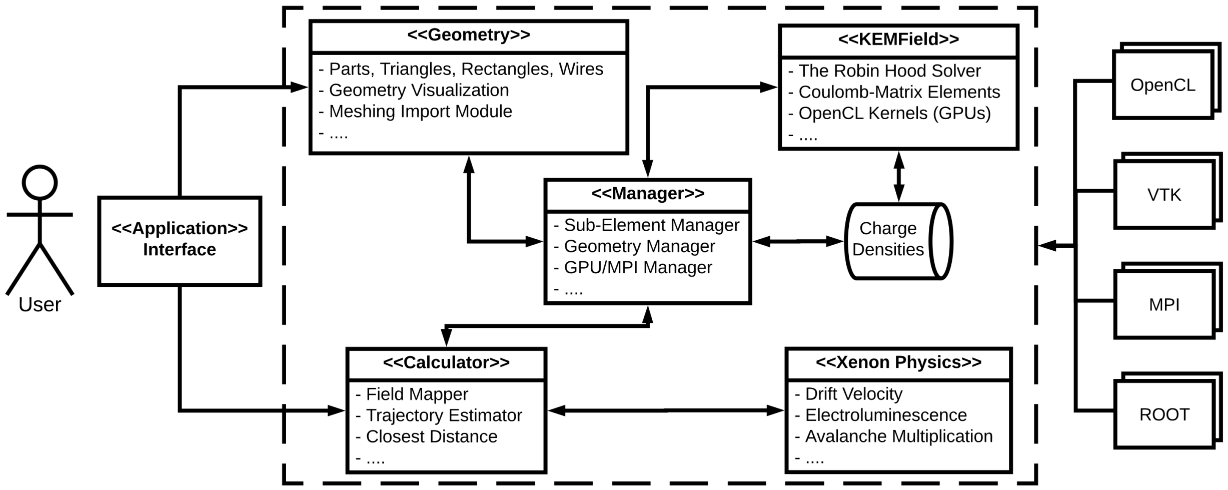

Figure 2.1: Simplified Unified Modelling Language (UML) diagram of the developed simulation framework. The user needs to provide the geometry to the framework, which will be solved for the charge densities. Furthermore, the calculated charge densities can be used for the electric potential and field calculation.

the computation time and the accuracy of the solution. Finding the correct discretisation of the geometry is crucial, as we will see in the next subsections, and needs to follow a set of rules, which can be found in [110, 113]. The discretisation can be also done by pre-existing software packages like GMSH [114], SALOME [115] or Computer-aided design (CAD), and imported to the framework. The framework uses the Visualisation Toolkit (VTK) [116] to create 3-dimensional visual models, which can be visualised with ParaView [117]. After the geometry is created and discretised, the charge densities are estimated by KEMField using the iterative Robin Hood solver on multiple GPUs by using Message Passing Interface (MPI) [118].

The iterative solving for the charge densities is finished after reaching the user-defined accuracy. An accurate simulation result is achieved of an individual sub-element accuracy below 10^{-8} [105, 113] and is therefore set as a default value. With the simulated charge densities, the electric fields and potentials can be calculated at a given point $\vec{r}$. For this purpose, an electric potential and field map can be calculated in a 3D region by using multiple GPUs with MPI. In addition, the electric field lines can be calculated with a user-defined accuracy with the following expression:

$$\vec{r}\,' = \vec{r} + \vec{n} \times \mathrm{d}L, \tag{2.9}$$

where $\vec{r}\,'$ is the next point on the field line, $\vec{r}$ is the current point on the field line, $\vec{n}$ is the direction of the electric force, and $\mathrm{d}L$ is the user defined step distance between two points on the field line. The field line calculation is terminated as soon the detector surface comes closer than $0.1\,\mu$m to the field line. Therefore, during the process of the field line calculation, the closest distance from the geometry to the field line is continuously calculated. The closest distance is analytically calculated for every individual sub-element and is implemented on GPUs, in order to increase the computational power. The generated data is stored on the disk with the help of the ROOT framework [119] for further analysis.

In the next section, the performance of the simulation framework will be verified on different electrostatic examples. Furthermore, the framework will be used to calculate the drift field, extraction field, as well as the electron trajectories and the implied produced electroluminescence photons (S2 signal, described in section 1.4.3) of a xenon-based dual-phase TPC.

2.3 Case Studies

In this section, we will discuss the performance of the simulation framework using different electrostatic examples. First, we will discuss the simulation of the unit cube. It is followed by simulations of two simple electrostatic problems: the spherical capacitor and the dual-phase plate capacitor. The section will be concluded with the electric field simulation of a realistic xenon-based dual-phase TPC, which validates the framework for large-scale TPCs simulations.

2.3.1 Unit Cube

The unit cube is a cube which sides are all 1 m long with a total surface area of $6\,\mathrm{m}^2$ and volume of $1\,\mathrm{m}^3$. There is no analytical expression for the electrical capacitance of the unit cube and solving this problem is of great interest in computational physics [120]. The capacitance of the unit cube has been numerically estimated to high accuracy by various Monte Carlo methods, and one of the current best value in units of $4\pi\epsilon_0$ is [121] :

$$C_{\mathrm{MC}} = 0.6606782 \pm 1 \times 10^{-7}. \tag{2.10}$$

The unit cube was implemented into the framework by using rectangular sub-elements with the same surface areas. In addition, the number of sub-elements was successively changed, in order to study how the accuracy improves with an increased resolution and to benchmark the computational

Sub-Element Area $\times 10^{-4}$ [m^2]	16	4	1	0.25	0.00625
C_{BEM} [$4\pi\epsilon_0$]	0.6597006	0.660285	0.6605205	0.6606154	0.6606530
$(C_{\text{MC}} - C_{\text{BEM}}) \times 10^{-4}$ [$4\pi\epsilon_0$]	9.77	3.931	1.577	0.628	0.251

Table 2.1: The simulated unit cube capacitance for different sub-element areas.

time. A voltage of 1 V was applied to the unit cube, and therefore, the simulated capacitance is given by the following expression:

$$C_{\text{BEM}} = \sum_{j}^{N} \sigma_j A_j, \tag{2.11}$$

where A_j is the surface area of the sub-element S_j, and σ_j is the charge density of the sub-element S_j . The simulations for the charge distributions were performed until the relative error of the individual sub-elements was below 10^{-8}. Figure 2.2 (left) presents the simulated charge densities of the unit cube with a sub-element surface area of 2.5×10^{-5} m^2. The charge densities near the edge of the cube are much higher than those further away from the edges, and the simulated total capacitance is in a remarkable agreement with the predicted value. In Table 2.1, the simulated capacitance for different sub-element surface area is summarized, and the differences from the predicted value are shown. By increasing the number of the sub-elements and therefore applying smaller elements, the simulated unit cube capacitance becomes closer to the value reported in equation 2.10, due to the finer discretisation of the edges. Overall, the simulation results are in excellent agreement with the predicted value of $\mathcal{O}(10^{-4})$.

Dividing the unit cube into more sub-elements, the area of the individual sub-elements decreases and the accuracy of the unit cube capacitance increases, which results in an increase of the computational time. In Figure 2.2 (right) the computational time for the charge distribution as a function

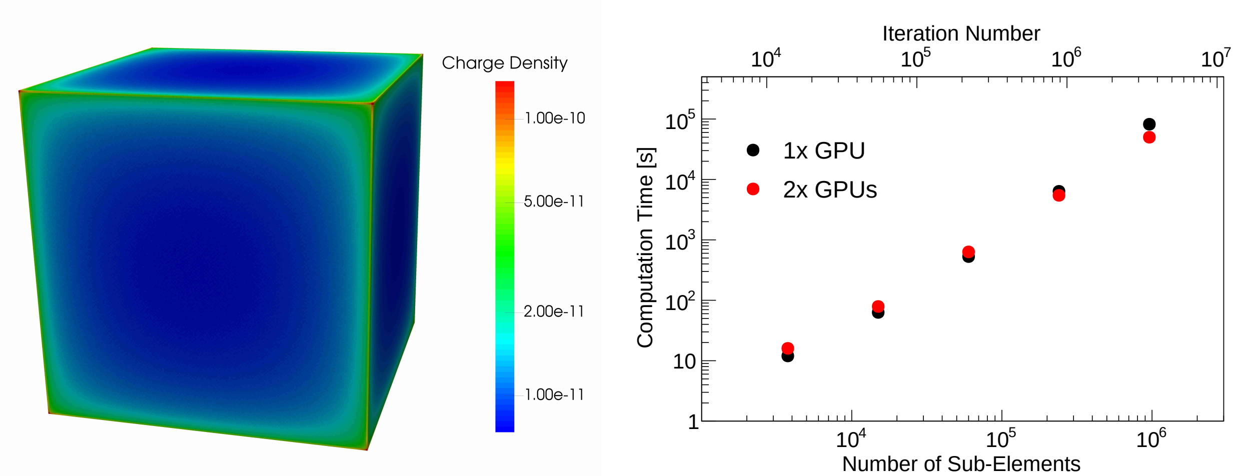

Figure 2.2: Left: The simulated charge densities (colour coded) of the unit cube with an individual sub-element area of 2.5×10^{-5} m^2 in units of [C$\times$m^{-2}]. The simulation for the charge distribution, in this example, results in a capacitance of $C_{\text{BEM}} = 0.6606154$ in units of $4\pi\epsilon_0$, which is in remarkable agreement with the predicted value. Right: The computational time for the charge distribution of the unit cube as a function of the number of sub-elements and number of iterations. The computation was performed on a single GPU (black points) and on two GPUs (red points). With an increased number of sub-elements, the number of iterations increases and the usage of more GPUs becomes advantageous.

of the number of sub-elements is shown. The simulations were performed until the relative error (equation 2.7) of the individual sub-elements was below 10^{-8}. The computations were performed on a single GPU (black points) and on two GPUs (red points). One can see that for the unit cube with more than 240 000 sub-elements, it is useful to parallelise multiple GPUs. For a small number of sub-elements, the gain in computational time from using multiple GPUs is smaller than the time spent on the data transfer between the GPUs, which makes the parallelisation inefficient. It needs to be mentioned that the computational time also depends on the choice of GPUs.

As shown with the example of the unit cube, the discretisation of a geometry needs to be carefully chosen in order to achieve an accurate result in a reasonable time. In the next subsection, we will discuss the spherical and dual-phase plate capacitor, in order to verify that the electric fields and potentials from the simulations are in agreement with the analytical solutions.

2.3.2 Spherical Capacitor

The spherical capacitor consists of two concentric conducting spherical shells. The inner shell has a radius $R_1 = 1\,\text{m}$, and the outer shell has a radius $R_2 = 2\,\text{m}$. The inner shell is on a potential of 1 V, and the outer shell is grounded. Therefore, the conductive shells have equal and opposite charges $+Q$ and $-Q$. In Figure 2.3 (left) a sketch of the spherical capacitor is shown.

The spherical capacitor was implemented into the framework by using triangular sub-elements. The discretisation was done by GMSH with a total number of 60 000 triangles. The simulation for the charge distribution was performed with a single GPU until the relative error of the individual sub-elements was below 10^{-8}. In Figure 2.3 (right) the spherical capacitor implemented into the simulation framework is shown. The spherical capacitor problem can be analytically solved for the capacitance, potential and electric field, which makes this geometry suitable for the validation of the simulation framework.

The electric field between the shells goes radially outward, due to the symmetry of the geometry. The total electric field can be derived with the help of Gauss law [122], which is given by:

$$\oint_S \vec{E}\,\mathrm{d}\vec{A} = \frac{Q}{\epsilon_0}, \tag{2.12}$$

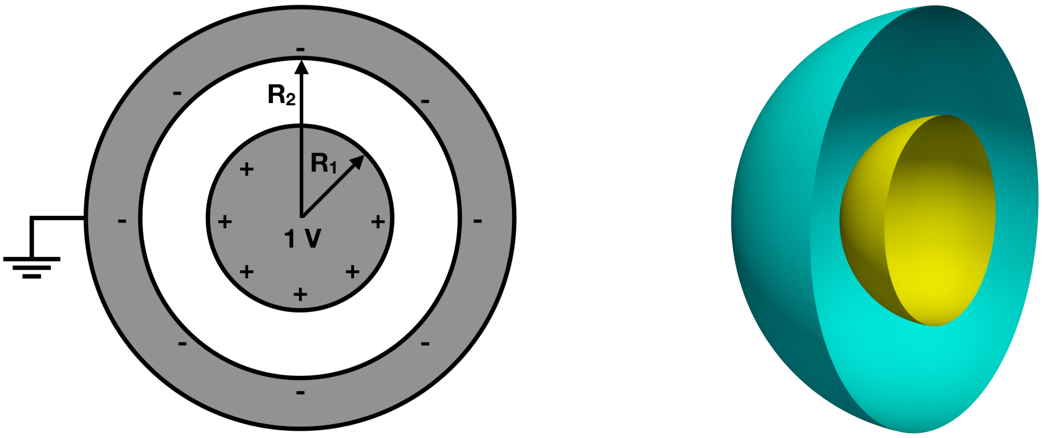

Figure 2.3: Left: The sketch of the spherical capacitor. The spherical capacitor consists of two concentric conducting spherical shells. Right: The implementation of the spherical capacitor into the framework. The geometry consists of 60 000 triangles. The inner sphere (yellow) is on a potential of 1 V, and the outer sphere (cyan) is grounded. The resulting electric potential and field were calculated inside the spherical capacitor.

where $\vec{E}$ is the electric field, and Q is the charge enclosed in the Gaussian surface. As a Gaussian surface, we chose a sphere of radius r. Thus, the electrical field inside the spherical capacitor is given by the following expression:

$$E(r) = \begin{cases} 0 & \text{for } r < R_1 \\ \frac{Q}{4\pi\epsilon_0 r^2} & \text{for } R_1 < r < R_2 \end{cases}. \tag{2.13}$$

The electric potential is given by the line integral along a radial path between the two shells:

$$\phi(r) = -\int_C \vec{E} \mathrm{d}\vec{l}, \tag{2.14}$$

where C is the radial path which connects two points. Thus, the electrical potential is given by:

$$\phi(r) = \begin{cases} \phi_0 & \text{for } r < R_1 \\ \frac{Q}{4\pi\epsilon_0 r} & \text{for } R_1 < r < R_2 \end{cases}, \tag{2.15}$$

where ϕ_0 is the applied voltage of 1 V. The capacitance C can be derived from equation 2.14 by evaluating the line integral from R_1 to R_2:

$$C = \frac{Q}{\Delta V} = \frac{4\pi\epsilon_0 R_1 R_2}{R_2 - R_1}. \tag{2.16}$$

In Figure 2.4 the electric potential (left) and field (right) calculated with the BEM are compared with the analytical solution. The obtained results are in outstanding agreement with the analytical solution.

In the next section, a plate capacitor half-filled with liquid xenon will be solved with the BEM and compared to the analytical solution. This will be the last validation experiment before solving a realistic xenon-based dual-phase TPC with the developed framework.

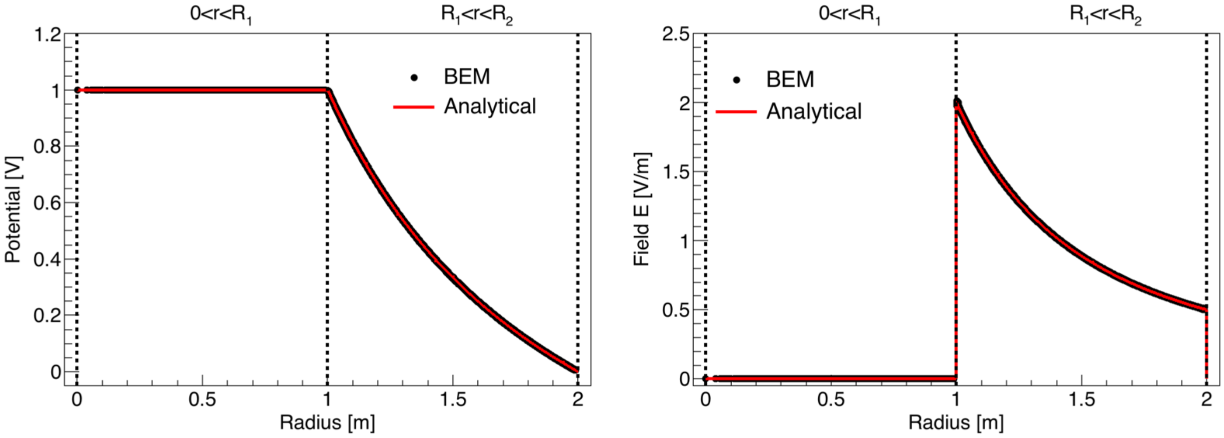

Figure 2.4: Left: The simulated averaged electric potential (black points) and the analytical solution (red line) as a function of radius. The potential is constant until it reaches the radius $R_1 = 1\,\mathrm{m}$, after which it decreases with $\propto 1/r$. The analytical solution is in an impressive agreement with the simulation. Right: The averaged simulated absolute electric field strength (black points) and the analytical solution (red line) as a function of radius. The simulated data is well described by the analytical solution.

2.3.3 Dual-Phase Plate Capacitor

The dual-phase plate capacitor consists of two parallel conducting plates, separated by a distance d of 2 cm from each other. Both plates are 1 m in length and width. The bottom plate is grounded, and the top plate is on a potential of 1 V. In addition, the plate capacitor is half-filled with liquid xenon ($\epsilon_1 = 2$) from the bottom and with gaseous xenon ($\epsilon_2 = 1$) from the top. In Figure 2.5 (left) a sketch of the dual-phase plate capacitor is shown.

The dual-phase plate capacitor was implemented into the framework by using rectangular sub-elements. The dielectrics were considered with a dielectric boundary in the centre of the capacitor, which follows equation 2.4. The discretised geometry consists of 480 000 rectangles. The simulation for the charge distribution was performed on a single GPU until the relative error of the individual dual-phase capacitor implemented into the simulation framework is shown. This problem can be analytically solved for the capacitance, potential and electric field. Therefore, the electric potential and field were calculated inside the capacitor and compared to the analytical solution.

The analytical solution can be derived with the multiple usages of the Gauss law. Assuming infinitely large plates, the electric field inside the capacitor is given by:

$$\begin{aligned} E_{\mathrm{LXe}} &= \frac{Q_1}{\epsilon_0 A}; \\ E_{\mathrm{GXe}} &= \frac{Q_2}{\epsilon_0 A}, \end{aligned} \tag{2.17}$$

where A is the surface area of the conducting plate, Q_1 is the charge on the bottom plate, and Q_2 is the charge on the top plate. Gauss law across the dielectric boundary yields:

$$\begin{aligned} E^{||}_{\mathrm{LXe}} &= E^{||}_{\mathrm{GXe}}; \\ \epsilon_1 E^{\perp}_{\mathrm{LXe}} &= \epsilon_2 E^{\perp}_{\mathrm{GXe}}, \end{aligned} \tag{2.18}$$

where $E^{||}_{\mathrm{LXe}}$ and $E^{||}_{\mathrm{GXe}}$ are the parallel electric field components to the dielectric boundary in the liquid and gaseous xenon, respectively, $E^{\perp}_{\mathrm{LXe}}$ and $E^{\perp}_{\mathrm{GXe}}$ are the vertical electric field components

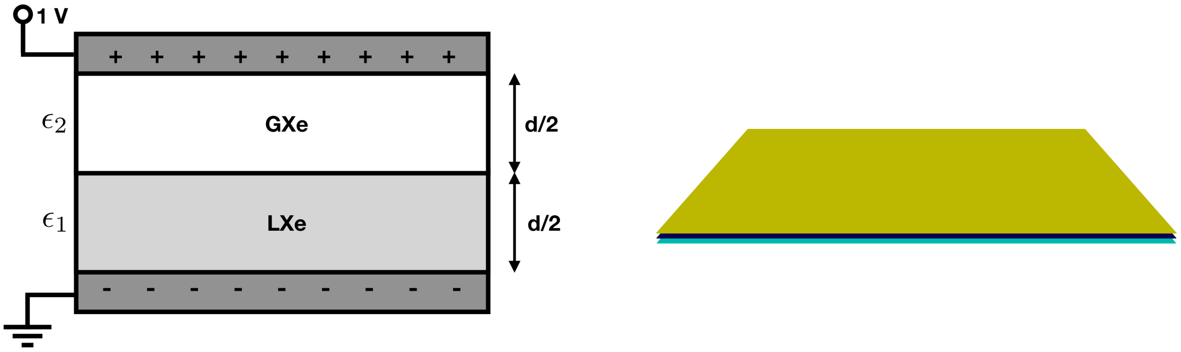

Figure 2.5: Left: Sketch of the dual-phase plate capacitor. The capacitor is half filled with liquid and gaseous xenon. The bottom plate is grounded, and the top plate is on a potential of 1 V. Right: The implementation of the dual-phase plate capacitor into the framework. The geometry consists of 480 000 rectangles. The bottom plate (cyan) grounded and the top plate (yellow) is on a potential of 1 V. The plate in between (blue) represents the charged dielectric boundary. The resulting electric potential and field were calculated inside the capacitor.

to the dielectric boundary in the liquid and gaseous xenon, respectively, and ϵ_1 and ϵ_2 are the corresponding dielectric constants of liquid and gaseous xenon. The vertical component of the electric field is not continuous through the interface, whereas the parallel component of the electric field is continuous through the interface. The electric potential is given by the linear integral from the plates to the dielectric boundary, which yields:

$$\begin{aligned}\Delta V_{\mathrm{LXe}} &= \frac{Q_1 d}{2\epsilon_0 A};\\ \Delta V_{\mathrm{GXe}} &= \frac{Q_2 d}{2\epsilon_0 A}.\end{aligned} \tag{2.19}$$

The total electric potential across the capacitor is given by:

$$V = \Delta V_{\mathrm{LXe}} + \Delta V_{\mathrm{GXe}}. \tag{2.20}$$

In the plate capacitor, the electric field exists only in the z-direction, which by using equations 2.17, 2.18, 2.19 and 2.20 results in:

$$E = \begin{cases} \frac{2V}{(\epsilon_2/\epsilon_1+1)d} & \text{LXe} \\ \frac{2V}{(\epsilon_2/\epsilon_1+1)d} \times \frac{\epsilon_1}{\epsilon_2} & \text{GXe} \end{cases}. \tag{2.21}$$

In Figure 2.6 the electric potential (left) and field (right) calculated with the BEM are compared to the analytical solution. The simulation results are identical to the analytical solution. It has to be mentioned that the measured dielectric constant for xenon (ϵ_1) in the literature [123] differs up to ∼9 % from the value used in the simulation. This would result in a differently charged simulated dielectric boundary. According to equation 2.4, the strength of this effect is directly related to the electric field flux through the dielectric boundary and the used dielectric constants. Therefore, the absolute electric field inside the dual-phase plate capacitor has a maximal uncertainty of ∼9 %, due to the absence of any electric field component parallel to the dielectric boundary.

In the next subsection, a xenon-based dual-phase TPC will be solved with the developed framework method, which validates that the framework can be used for large-scale TPCs.

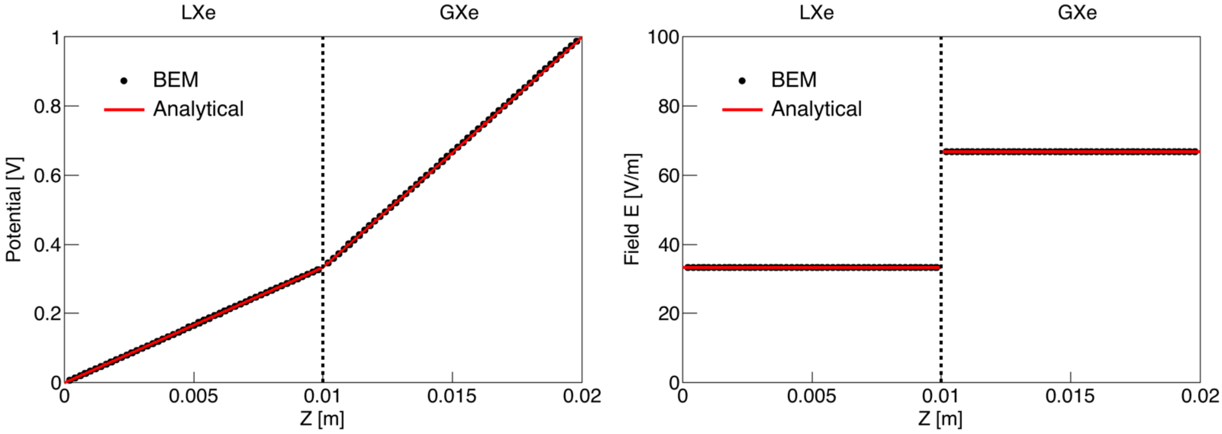

Figure 2.6: Left: The simulated electric potential (black points) and the analytical solution (red curve) inside the dual-phase plate capacitor. The analytical and simulated potentials are in a remarkable agreement. Right: The simulated absolute electric field strength (black points) and the analytical solution (red curve) inside the dual-phase plate capacitor. The analytical and simulated electric fields show the same behaviour. The electric field increases by a factor of two after crossing the liquid/gaseous xenon boundary, due to the change in the dielectric constant.

2.3.4 Xenon-Based Dual-Phase TPC

In this subsection, we will discuss the electrostatic simulation of the Xurich [124] xenon-based dual-phase TPC. The detector is designed to study ionisation and scintillation yields of low-energy electronic and nuclear recoils and will be further discussed in section 6.4.

The Xurich TPC consists of a cylindrical chamber enclosed by a PTFE reflector with a diameter of 31 mm and a drift length of 30.5 mm. Seven field shaping rings are placed around the target volume to ensure a homogeneous drift field. The cathode, gate and anode consist of hexagonal meshes with an optical transparency of 93 % and thickness of 100 μm. The gate and the anode are separated by a distance of 4 mm and the liquid/gaseous xenon boundary is set in between both electrodes. Two cylindrical 2-inch Hamamatsu-R9869 PMTs are placed in a PTFE holder above and below the target for the detection of photons produced by an incident particle. A detailed description of the design can be found in [125].

The detector is nominally operated at a cathode voltage of -3 kV and an anode voltage of 4 kV, and the simulation results reported in this section consider these voltage values. In Appendix A, the simulated drift and extraction field for different applied cathode voltages can be found. The detector was implemented into the framework in great details, as shown in Figure 2.7 (left). The geometry consists of 472 412 sub-elements (triangles and rectangles) and the individually implemented components with their corresponding electric potentials can be found in Appendix A. The simulation for the charge distributions took $\sim$8.8 hours and 670 000 iterations with the Robin Hood solver until an accuracy below 10^{-8} for the equipotential surfaces was reached. The accuracy for some of the equipotential surfaces as a function of iteration number is shown in Figure 2.7 (right). The convergence of the individual equipotential surfaces scales exponentially with the number of iterations.

The electric potential and field were calculated inside the TPC, in order to extract the drift and extraction field. The absolute electric field inside the TPC defines the drift field and the absolute electric field inside the gas gap defines the extraction field. The averaged drift field inside the TPC was calculated to be (0.96 ± 0.03) kV/cm, which is consistent with the assumption of a simple plate

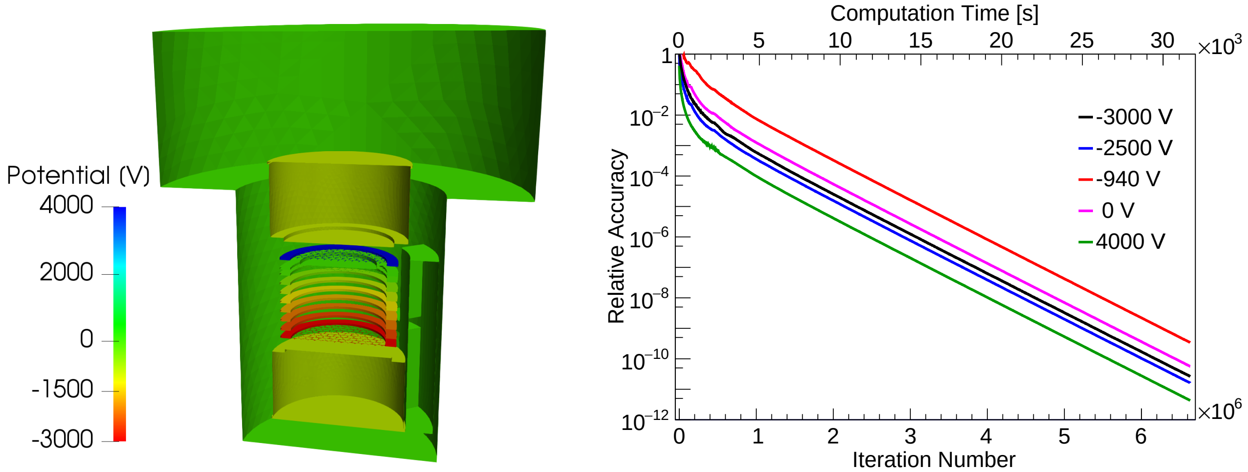

Figure 2.7: Left: The Xurich geometry implemented into the simulation framework. The applied potential configuration is indicated in different colours The implemented parts and potentials on every electrode can be found in Appendix A. Right: Some of the equipotential surfaces as a function of iteration number and computational time during the simulation of the charge distribution. The convergence of the individual equipotential surfaces scales exponentially with the number of iterations, which makes the Robin Hood method highly efficient for solving the matrix equation 2.2.

capacitor. In Figure 2.8 (left) the phi-averaged deviation map from the mean drift field is shown. The averaged total deviation in the target volume is 2.8 %, due to the high-field regions close to the cathode (-3.05 cm) and the gate (0 cm). Regions with small deviations from the mean can be identified, which depend on the geometrical arrangement of the field shaping rings and the applied electric potentials. Fiducialising the target by removing 3 mm from the top and the bottom reduces the non-uniformity to an average value of 0.9 %.

In Figure 2.8 (right) the absolute electric field as a function of the z coordinate between the gate and the anode is shown. The electric field increases by a factor of two after passing the liquid/gaseous xenon boundary, due to the change in the dielectric constant. The mean extraction field was calculated to be (10.32 ± 0.14) kV/cm, which results in 100 % extraction efficiency [93] of electrons from the liquid to gaseous xenon phase.

In addition, the electric field lines were calculated from the cathode to the anode, and the number of produced electroluminescence photons along the field lines were estimated. The number of electroluminescence photons along the field lines in gaseous xenon was calculated with the following empirical expression [93]:

$$N_\gamma^{e^-} = \int \alpha N_e (E/p - \beta) p \mathrm{d}l, \tag{2.22}$$

where $N_\gamma^{e^-}$ is the number of produced photons from a single electron, α is the amplification factor, N_e is the number of extracted electrons, E is the absolute electric field strength, p is the gas pressure, β is the threshold of the reduced field for proportional light, and $\mathrm{d}l$ is an infinitesimal distance along the field line in gaseous xenon. A measurement of the secondary scintillation gain as a function of electric field yields $\alpha = (151 \pm 19)$ photons/e$^-$/kV and $\beta = (0.97 \pm 0.13)$ kV/cm/bar [126].

Furthermore, one has to take into account the electron multiplication process in the gas gap. The free electrons in the gas gap collide with gas molecules and may consequently set additional electrons free, which produce electroluminescence photons as well. The number of additional free electrons can be expressed by the following equation:

$$N_{e^-} = \int \alpha(E, T, P) \mathrm{d}l, \qquad \text{with} \qquad E \geq E_T, \tag{2.23}$$

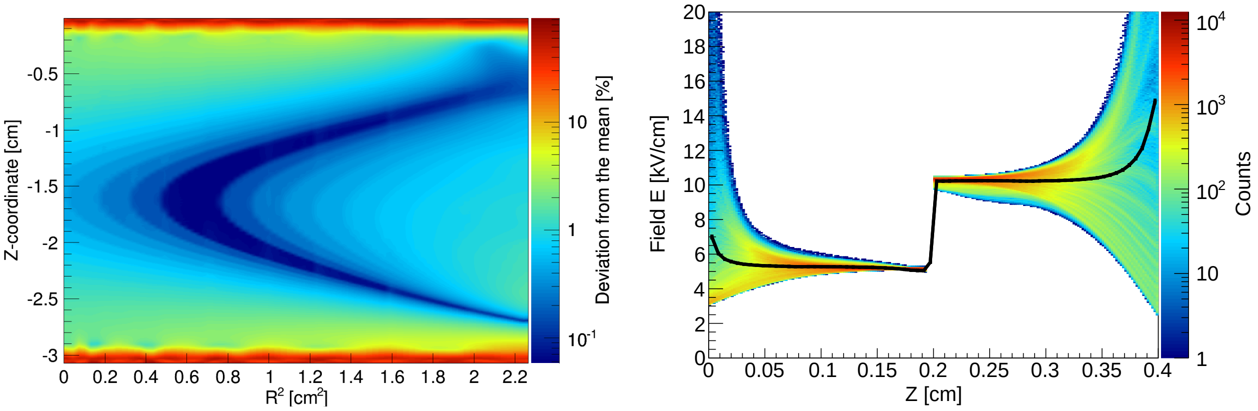

Figure 2.8: Left: The simulated phi-averaged electric field uniformity map inside the liquid xenon target of the Xurich TPC. The top and bottom of the map correspond to the gate and cathode electrodes, respectively. The mean deviation from the mean drift field (0.96 ± 0.03) kV/cm in the target volume is 2.8 %. Figure published in [124]. Right: The simulated absolute electric field as a function of the z coordinate between the gate and anode electrodes. The black line indicates the mean value, which increases by a factor of two after passing the liquid/gaseous xenon boundary, due to the change in the dielectric constant. The mean extraction field is (10.32 ± 0.14) kV/cm.

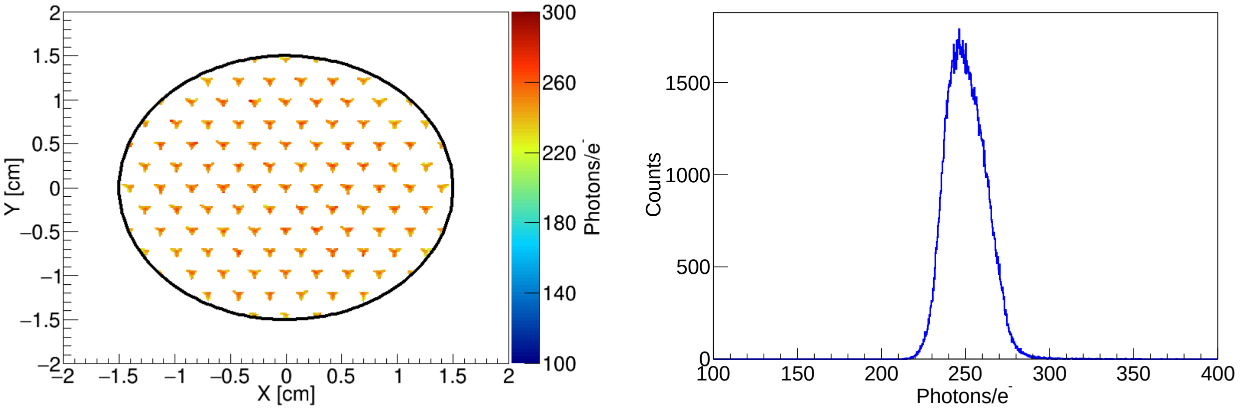

Figure 2.9: Left: The simulated final position of the field lines in the x-y plane coming from the cathode. The colour indicates the number of produced photons in the gas gap. The field lines end onto the anode electrode and therefore show a regular pattern. Right: Simulated distribution of the produced photons/charge. A single electron will produce a mean number of 250.4 photons with an rms of 11.8 photons.

where $\alpha(E,T,P)$ is the first Townsend coefficient which depends on the local electric field E, the pressure P and the temperature T, and E_T is the threshold for electron multiplication. The first Townsend coefficient curve $\alpha(E,T,P)$ was taken from [127], and E_T was assumed to be $\sim 14\,\mathrm{kV/cm}$ [128].

In Figure 2.9 (left) the final positions of the calculated field lines from the cathode are shown in the x-y plane. The field lines are focused through the gate mesh onto the anode electrode and therefore show a regular pattern. In addition, the number of produced photons/charge in the gas gap is calculated from equations 2.22 and 2.23, and are indicated with colours in Figure 2.9 (left). In Figure 2.9 (right) the distribution of the produced photons/charge is shown. A single electron will produce a mean number of 250.4 photons with a root mean square (rms) of 11.8 photons. This value can be converted to photoelectrons detected by the bottom PMT with the following expression:

$$N_{\mathrm{PE}} = N_{\gamma}^{\mathrm{e}^-} \times \mathrm{LCE} \times \mathrm{QE} \times \mathrm{CE} = (24.5 \pm 1.1)\,\mathrm{PE/charge}, \tag{2.24}$$

where $N_{\gamma}^{\mathrm{e}^-}$ is the mean number of produced S2 photons in the gas gap by a single extracted electron. The S2 light collection efficiency (LCE) for the bottom PMT is $\sim 32\,\%$, the bottom PMT quantum efficiency (QE) is $\sim 35\,\%$ and the bottom PMT photoelectron collection efficiency (CE) is $\sim 90\,\%$. The charge amplification gain of the Xurich TPC was measured with a monoenergetic calibration source to be $(24.4 \pm 0.4)\,\mathrm{PE/charge}$ [124], which is in excellent agreement with the simulated value of (24.5 ± 1.1), PE/charge, assuming a $100\,\%$ extraction efficiency of the single electrons into the gaseous xenon.

As shown in this chapter, the developed simulation framework based on the BEM is able to perform detailed 3D electrostatic field simulations in a reasonable time frame. The solutions of the electrostatic field simulations are in agreement with the analytical solutions. Furthermore, we showed that the electrostatic simulation of a realistic xenon-based dual-phase TPC is identical with the measured data. Therefore, the simulation framework can be reliably used for a detailed electrostatic simulation of the XENON1T detector, which will be described in the following two chapters.

"An expert is someone who knows some of the worst mistakes that can be made in his subject, and how to avoid them."

Werner Heisenberg

CHAPTER 3

The XENON1T Time Projection Chamber

The XENON1T experiment follows the success of the XENON100 experiment [95] and also addresses the direct detection of dark matter in the form of WIMPs using a xenon-based dual-phase TPC. As shown in chapter 1, this technology allows for an excellent position reconstruction in 3D and simultaneous background discrimination. The XENON1T detector is designed for a target mass of approximately 2 t and a low γ and neutron-background level.

In section 3.1, we will give an introduction to the XENON1T experiment. It is followed by sections 3.2 and 3.3, which give a detailed description of the XENON1T TPC and electrode structure. Section 3.4 describes the XENON1T light sensors, cold electronics and readout validation of their signal linearity. The field cage design and mechanical low-temperature validation will be reported in section 3.5. Finally, in section 3.6, we will describe the complete TPC construction and the assembly phase in winter 2015 at LNGS.

3.1 The XENON1T Experiment

The XENON1T experiment is located in Hall B of the underground research laboratory at Laboratori Nazionali del Gran Sasso (LNGS) in Italy. The underground laboratory is covered by ~ 1400 m of rock (~ 3800 m water equivalent), which results in a cosmic muon flux reduction down to $(3.41 \pm 0.01) \times 10^{-4}\,\mathrm{m}^{-2}\mathrm{s}^{-1}$ [129].

The XENON1T TPC is designed for a target mass of ~ 2 t of liquid xenon and it will be extensively discussed in section 3.2. The TPC within the vacuum insulated cryostat is located in the centre of a water tank ~ 10 m high and ~ 9.6 m diameter, which acts as a water Cherenkov detector and as a muon veto. The inner surface of the water tank is covered with a reflective foil (DF2000MA, 99 % reflectivity for wavelengths between 400 and 1000 nm), which reflects and shifts the wavelength of the produced Cherenkov photons to the blue region. The photons are detected by 84 8-inch Hamamatsu R5912ASSY PMTs, which a have high quantum efficiency (~ 30 %). Their geometric arrangement has been optimised by Monte Carlo simulations. In this configuration, the muon veto has a high detection efficiency for muons (>99.5 %) and showers of secondary particles from muon interactions in the surrounding rock (>70%) [130].

An infrastructure building is located next to the water tank, which houses on three floors the cryogenic and xenon purification system (second floor), the data acquisition system (DAQ) (first floor), and the krypton distillation column and the xenon storage system (ground floor). A stainless steel cryogenic pipe of 7.5 m length and 350 mm inner diameter connects the TPC through the cryostat and water tank with the second floor of the infrastructure building. The pipe houses the high voltage and signal cables for the PMTs, the optical fibres, which are used to transmit blue LED light (~ 450 nm) to the TPC for different calibrations of the PMTs, and several smaller pipes. The smaller pipes transport the xenon to the TPC and back.

All signal and high voltage cables exit the cryogenic pipe through installed potted feedthroughs at a breakout box into the second floor of the infrastructure building. The optical fibres are connected to a vacuum feedthrough at the same breakout box. The second floor of the infrastructure building holds the cryogenic and xenon purification system as well. For purification, the gaseous xenon is recirculated through two heated getters to remove water and electronegative impurities, such as oxygen. The cooling system, which serves to keep the xenon in the liquid phase, consists of two pulse tube refrigerators (PTRs) and one liquid nitrogen cooling tower. In operation, one PTR provides the necessary cooling power, while the other two systems provide redundancy in case of emergency or power failure.

The signal and high voltage cables, as well as the optical fibres, are routed towards the first floor of the infrastructure building, which is dedicated to the DAQ system. The first floor consists of a climate controlled room, which houses NIM and VME crates for the readout of the muon veto and TPC. The optical fibres are connected to four blue LEDs, which are powered by a pulse generator (BNC 505-4c [131]) during the PMT calibrations. The high voltage cables are connected to a CAEN [132] 1345 power supply and the PMT signal cables are routed into several ten-fold Phillips [133] 776 linear amplifier NIM modules, which provide two amplified output signals for each channel. The first amplified signals are digitised by 32 CAEN v1724 flash analogue-to-digital converters (ADCs) with a sampling frequency of 100 MHz and a bandwidth of 40 MHz. The ADCs are read out by six computers, simultaneously, independently and asynchronously. Therefore, every signal pulse above a ~0.3 photoelectron (PE) digitisation threshold is read out and stored with a time stamp for further event reconstruction, which is described in [134]. For this purpose, a new firmware was developed in cooperation with CAEN, which allows for a maximum data rate of ~300 MB/s. The PMT signals of the second amplified channel are summed up, attenuated and routed to a high-energy veto module (SkuTek DDC10 [135]). It tags and rejects high energy events by sending a veto signal to the ADCs, if the summed signals exceed an user-defined threshold. The events acquired by the ADCs are processed by the data processor PAX [136].

On the ground floor, the krypton distillation column [137] and the xenon storage and recovery system (ReStoX) [138] are located. ReStoX is a vacuum-insulated stainless-steel sphere with a diameter of 1 m, which is used for storing the pure liquid xenon and for a fast recovery of the liquid xenon from the TPC, in case of an emergency. It can store up to ~7.6 t of xenon in liquid or gaseous

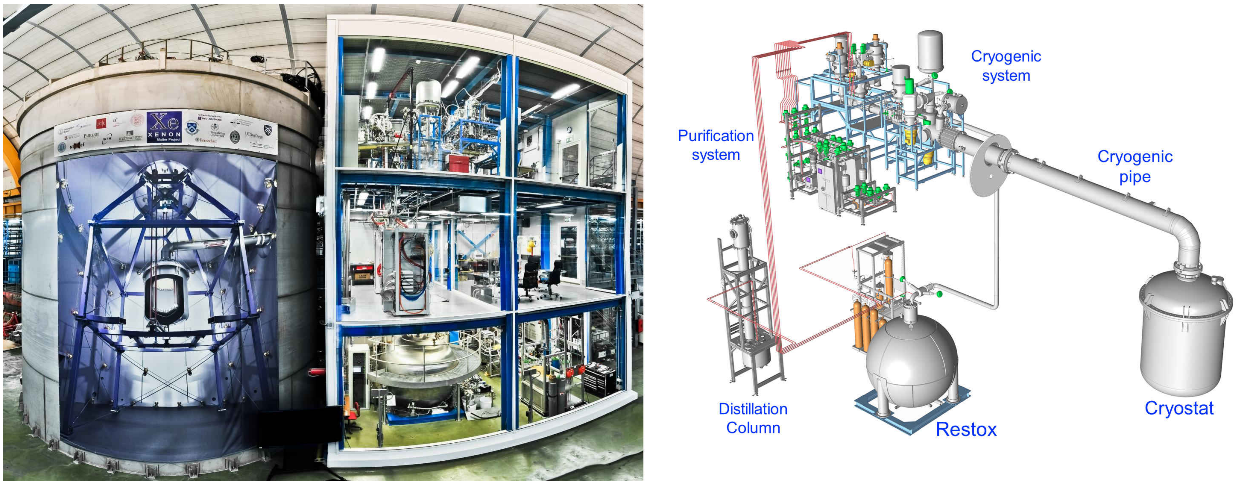

Figure 3.1: Left: A picture of the XENON1T experiment located in the underground lab at LNGS. It shows the water tank and the infrastructure building next to it. A sketch of the internal structure of the water tank is attached to the outside. Right: A sketch of the XENON1T gas systems. The TPC, located inside the cryostat, is connected over a cryogenic pipe to the service building.

phase. The sphere is cooled down by 16 liquid nitrogen lines welded to the outer surface of the inner vessel. The vacuum insulation reduces the total heat load of the system to ∼ 50 W. ReStoX is connected to the TPC and to the purification system, in particular to the krypton distillation column. Xenon gas has a concentration of natural krypton at the ppb[1] level. Natural krypton consists at the level of $\sim 10^{-11}$ of the β-decaying isotope ^{85}Kr [139]. It has a half-life of 10.76 years and an endpoint energy of 687 keV, which produces an intrinsic background. The krypton distillation column with a height of ∼ 5 m is used to reduce the $^{\mathrm{nat}}$Kr concentration by cryogenic distillation, in order to reach the designed XENON1T sensitivity [140]. With this technique, the $^{\mathrm{nat}}\mathrm{Kr/Xe}$ concentration was reduced to a concentration of (0.66 ± 0.11) ppt[2]. The low gas concentrations are measured with a rare-gas-mass-spectrometer (RGMS) [137, 141].

3.2 TPC Design

The TPC working principle was introduced in section 1.4. In this section, the technical XENON1T TPC design will be discussed. The XENON1T TPC consists of several main components. The bottom electrode stack with the bottom PMT array, the field cage, the top electrode stack and a diving bell with the top PMT array. In Figure 3.3 the CAD drawings of the XENON1T TPC are shown.

The field cage is enclosed by 24 sliding polytetrafluoroethylene (PTFE, Teflon®) reflectors that are held in place between 24 fixed PTFE reflectors to form an irregular 48-sided polygon. Each fixed PTFE reflector has a 2 mm polyamide-imide (Torlon®) pin at its bottom, which extends from the bottom of the fixed reflectors into a groove at the bottom of the sliding reflectors, in order to keep the sliding reflectors in place. The surface of the PTFE reflector panels were treated with a diamond tool in order to obtain a 99 % reflectivity to VUV photons [142, 143]. 24 support pillars hold the fixed reflector panels and 74 field shaping rings to ensure the uniformity of the drift field. The field shaping rings are made from low-radioactivity oxygen-free high-thermal-conductivity copper (OFHC). The weight of the field shaping rings is equally distributed over all support pillars, which ensures a good stability of the TPC. The PTFE support pillars are held in place on the top by a stainless steel ring and on the bottom by a copper ring. Between the top ring and the support pillars, Torlon® inserts are placed. A 1 mm thick PTFE sheet is wrapped around the field cage and attached to the support pillars, in order to prevent discharges between the field shaping rings and the stainless steel cryostat vessel. Six 1-inch PMTs (Hamamatsu R8520) are installed on the top stainless steel ring in the outer part of the TPC for possible diagnostics of the detector. The specification from the manufacturer (Amsler & Frey) for the used PTFE gives a thermal expansion

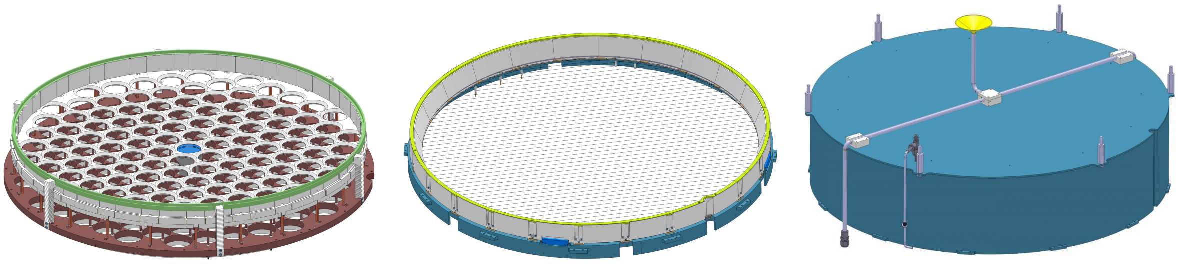

Figure 3.2: Left: CAD drawing of the bottom stack mounted to the bottom PMT array. Centre: CAD drawing of the top TPC stack mounted to the TPC ring. Right: CAD drawing of the pressurised diving bell with the piping for the liquid xenon input.

---

[1] Parts per billion, $1\,\mathrm{ppb} = 1 \times 10^{-9}$ mol/mol.

[2] Parts per trillion, $1\,\mathrm{ppt} = 1 \times 10^{-12}$ mol/mol.

coefficient of $16.5 \times 10^{-5}\,\mathrm{K}^{-1}$, which results in a ~1.5 % contraction at the operation temperature of −96 °C. The interlocking PTFE panels design optically separates the target volume from the outside xenon volume and ensures that the vertical length is only reduced during operation. The radial length stays constant during the cooling process because it is dominated by the contraction of the copper field shaping rings, which is negligibly small for our purposes. The radius to the centre of the fixed PTFE reflectors is 47.85 cm, and the radius to the centre of the sliding PTFE reflector is 47.87 cm. The drift length is defined by the distance from the cathode to the gate, which was measured to be ~ 981.8 mm at 22 °C.

A CAD drawing of the bottom electrode stack is shown in Figure 3.2 (left). The bottom electrode stack, mainly made out of copper and PTFE, has the function to hold the cathode, screening mesh and the bottom PMT array. 121 3-inch PMTs (Hamamatsu R11410-21) are placed inside a copper plate, which is covered by a PTFE reflector. The PMTs are arranged in a hexagonal structure in order to cover the entire diameter of the TPC and therefore to maximise the light collection efficiency (LCE). The cables from the bottom PMT array are guided to the cryogenic pipe along cable trays, screwed to the field cage support pillars. A screening mesh is placed above the PMTs in order to minimise the electric field produced by the voltage difference between the cathode and the PMTs. The cathode rests on six PTFE pillars, which are connected to the copper plate. The distance between the cathode and the screening mesh is ~ 7 cm. In this configuration, the PMTs are protected from discharges generated by the cathode. The gap is enclosed by 48 small PTFE reflectors, which have a regular pattern of horizontal grooves on their inner surface, in order to reduce the probability of a discharge along the PTFE surface and increase the LCE of the bottom PMTs. Two PTFE reflectors have an inlet, which enables the liquid xenon to be filled into the TPC. Every second PTFE reflector is mounted to the copper plate with copper pillars. Sliding PTFE reflectors fill the gaps between two fixed reflectors. The copper plate is mounted with stainless steel screws to the bottom copper ring of the field cage, and thus closes the TPC from the bottom.

A CAD drawing of the top stack is shown in Figure 3.2 (centre). The top electrode stack, mainly made out of PTFE, has the function to hold the gate, the anode and top PMT screening mesh. It is mounted on top of the TPC top stainless steel ring. 24 Torlon® pieces are inserted into the groove of the top TPC ring, which isolates the gate from the ring and prevent the sliding reflectors

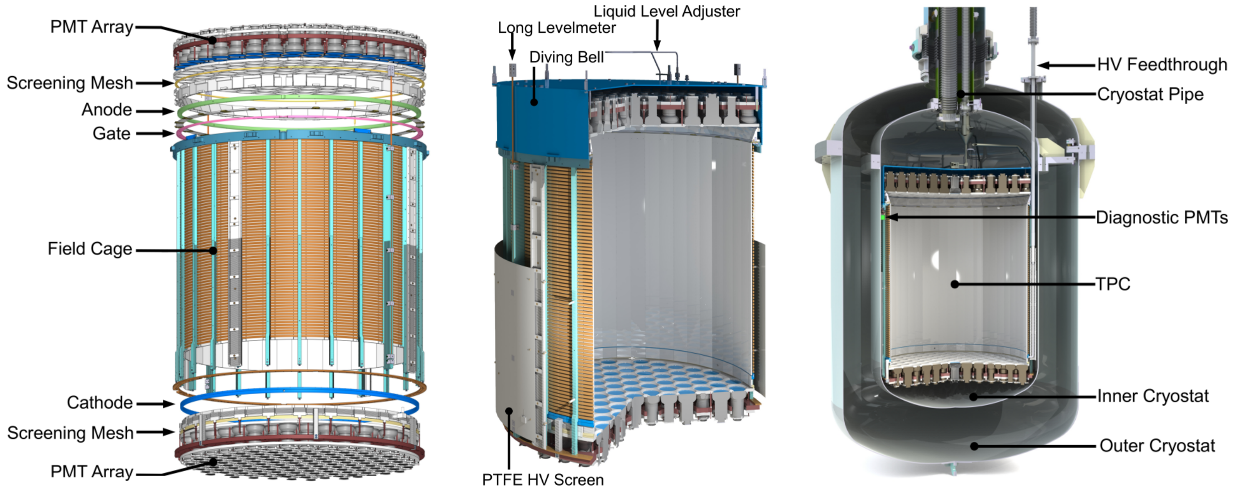

Figure 3.3: Left: CAD exploded drawing of the XENON1T TPC. The TPC can be subdivided in 4 subparts (Bottom Stack, Field Cage, Top Stack and Bell) Centre: The CAD drawing of the assembled TPC. The TPC is inserted into a stainless steel diving bell, which holds the TPC and sets the liquid-gaseous xenon level. Right: The CAD drawing of the assembled TPC inside the cryostat.

of the field cage from moving upwards. The gate is placed on top of the Torlon® insulating pieces. 23 Torlon® pieces without being fully tightened to the top TPC ring hold-down the gate ring, and set the distance between the gate and the anode to 5 mm. The space between two neighbouring Torlon® pieces is filled with PTFE pieces in order to increase the LCE at the edge. The anode is placed on top of the Torlon® and the PTFE pieces, and is tightened to the Torlon® pieces. 24 cone-shaped PTFE reflectors are placed on top of the anode and screwed to the top TPC ring. The reflectors set the distance to the top PMT array and increase the LCE. The PMT screening mesh is screwed on top of it.

The top PMT array consists of 127 PMTs (Hamamatsu R11410-21), which are arranged in concentric circles. In this configuration, the radial resolution in the position reconstruction is superior at the edge, in comparison to the most compact arrangement. The PMTs are placed inside a copper plate, and the gap between individual PMTs is covered by a PTFE reflector. The entire PMT array is inserted into a stainless steel diving bell, which can be pressurised in order to control the liquid xenon level. The CAD drawing of the diving bell is shown in Figure 3.2 (right). The liquid xenon level is adjusted through the gaseous xenon flow into the bell and with a vertically controlled gas-exhaust tube. Four capacitive levelmeters are placed on the top TPC ring in order to measure the liquid xenon level inside the bell. The levelmeters cover the range between the gate and the anode with a precision of $\sim 30\,\mu$m and are used to place the liquid xenon level in the centre of both electrodes and adjust possible tilts of the TPC. Two capacitive levelmeters attached to the support pillars of the field cage cover a range from below the cathode to above the bell and are used to monitor the liquid xenon level during filling and recovery. The cables from the top PMT array are routed along special cable trays out of the bell. The diving bell is screwed with 12 stainless steel wings to the top TPC ring and thus closes the TPC from the top. Two pipes are installed on the top of the bell to guide the purified xenon to the bottom inlet of the TPC. The purified xenon drops into the pipes through a funnel. The bell is connected with six silver plated stainless steel screws to the top cryostat dome, which is shown in Figure 3.3 (right). All of the screws used for mounting the TPC were made out of stainless steel, copper or PolyEther-Ether-Ketone (PEEK®).

3.3 Electrodes Design

In the previous section, we described the XENON1T TPC design. In this section, we will describe the XENON1T electrodes which generate the drift and extraction field for the ionisation charge.

The electric drift field and the proportional amplification field is generated by highly optical transparent electrodes (top screening mesh, anode, gate, cathode and bottom screening mesh). The

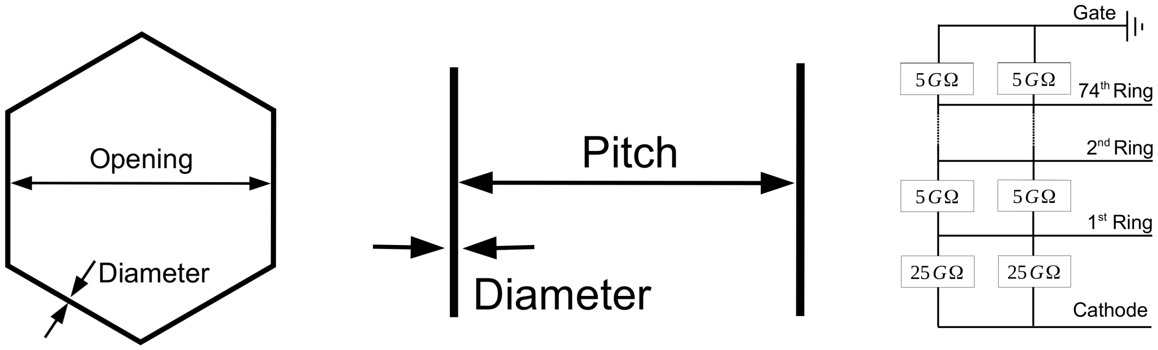

Figure 3.4: Left: The geometrical definition of a single cell of the hex-mesh electrodes. Centre: The geometrical definition of two parallel wires of the wire electrodes. Right: The resistor chain between the field shaping electrodes. The total resistance of the voltage dividing network is 197.5 GΩ.

electrodes allow for simultaneous measurements of S1 and S2 signals with the PMT arrays above and below the liquid xenon target. The optical transparency is defined as the ratio of the optically opaque area to the total area. The anode, gate and top screening electrodes are meshes with a hexagonal wire pattern. The cathode and bottom screening electrodes consist of parallel wires in order to achieve an optimal S1 light collection, which is dominated by the PMT array below the target. The geometrical definition of a parallel wire and a hex mesh electrode can be found in Figure 3.4.

The cathode and bottom screen wires have a diameter of 216 μm and a pitch to each other of 7.75 mm, which results in an optical transparency of 97.2 % in both cases. The bottom screening wires have in addition a single wire installed perpendicularly to all others. This was done in order to reduce the mechanical deformation of the frame. All the wires were gold plated to reduce the work function of the metal. The screening mesh is placed $\sim$7 cm below the cathode and $\sim$1 cm above the windows of the bottom PMT array. The thickness of the gate and anode is 127 μm and 178 μm, respectively. The single cell opening is 3.5 mm in both cases, which results in an optical transparency of 92.7 % for the gate and 89.8 % for the anode. The anode is placed 5 mm above the gate, and the hex mesh cells are shifted by half a cell to each other in order to increase the S2 resolution. The top screening mesh has a thickness of 178 μm and a cell opening of 10.2 mm for an increased optical transparency of 96.5 %. The mesh is placed $\sim$7 cm above the anode and $\sim$2 mm below the windows of the top PMT array. A summary of the electrode structures is listed in Table 3.1.

The meshes were produced by chemical etching of a stainless steel foil and spot welded to a stainless steel ring. The cathode and bottom screening wires were stretched on an external structure and clamped between the upper and lower part of the frames [145]. In addition, the same low-radioactivity stainless steel is used for the frames like the one used for the cryostat. All the electrodes were electropolished. The cathode and the bottom screen frames have an inner diameter of $\sim$972 mm. The anode and gate have an inner diameter of $\sim$975 mm. The top screening mesh has an inner diameter of $\sim$1010 mm.

The TPC is surrounded between the cathode and the gate by 74 field shaping electrodes to ensure a drift field homogeneity. The cross-section of one ring is $\sim 10 \times 5\,\mathrm{mm}^2$, and the rings are placed at a distance of $\sim$2.5 cm to each other. As a material, oxygen-free, high-thermal-conductivity copper (OFHC) is used. The field shaping electrodes are connected to each other by two chains of resistors, one of which is used for redundancy. The first ring is connected with two 25 GΩ resistors to the cathode, and the last ring is connected with two 5 GΩ resistors to the gate. In this configuration, the field uniformity at the edge of the TPC is optimised, as shown in section 4.3. In Figure 3.4 (right) the sketch of the two resistor chains is shown.

Electrode	Structure	Wire Diameter	Pitch/Cell Opening	Transparency
Bottom Screen	parallel wires	216 μm	7.75 mm	97.2 %
Cathode	parallel wires	216 μm	7.75 mm	97.2 %
Gate	hex mesh	127 μm	3.5 mm	92.7 %
Anode	hex mesh	178 μm	3.5 mm	89.8 %
Top Screen	hex mesh	178 μm	10.2 mm	96.5 %

Table 3.1: The specification of the XENON1T electrodes. The wires of the bottom screen and cathode electrode are aligned parallel to each other, in order to minimise the electric field in front of the PMTs. The anode and gate are shifted by half cell to each other, in order to achieve a good S2 resolution. Values published in [144].

The TPC was designed for an applied cathode voltage of −100 kV and an anode voltage of 5 kV. The gate is designed to be held on ground but can be biased in order to ground the anode. The screening meshes are designed for an applied voltage of about −1500 V in order to reduce the electric field in front of the PMTs, which are also nominally operated at −1500 V, and to protect the PMTs from electric discharges.

3.4 Light Detector Sensors

In this section, we will discuss the XENON1T photosensors. First, we will introduce the TPC PMTs, their readout electronics and intrinsic properties. This is followed by the verification of the PMT's base dynamic range in a specially developed measurement setup. The section will be concluded by a measurement of the under-amplified electron contribution to the total PMT response.

3.4.1 The XENON1T Photomultiplier Tubes (PMTs)

PMTs are commonly used as light sensors due to their single photon counting capability, high gain, high quantum efficiency (QE), fast timing, low dark current, and stable operation at cryogenic temperature. An incident photon enters the evacuated PMT through a transparent window and creates a photoelectron (PE) through the photoelectric effect [146], which is emitted into the vacuum of the PMT. The photoelectron is then accelerated by an applied electric field towards the first dynode, where it is amplified by a secondary emission of electrons. The produced secondary electrons are accelerated and then consecutively amplified in several dynode stages. Therefore, every dynode stage is held at a different electric potential. The resulting amplified signal is read out at the anode, and it is proportional to the number of the initial photons.

The XENON1T TPC is equipped with 248 Hamamatsu PMTs (R11410-21) with a 7.6 cm diameter circular window. This PMT model was specifically designed to be operated in liquid xenon and to withstand an absolute pressure up to 6 atm. It consists of 12 dynode stages, and its window is produced out of synthetic silica (quartz), which transmits ultraviolet radiation down to 160 nm. The photocathode is made out of a specifically developed alloy (bialkali) with a work function of W ≈1.5–2 eV, which results in a spectral response in the region of 160–650 nm. The PMT uses a

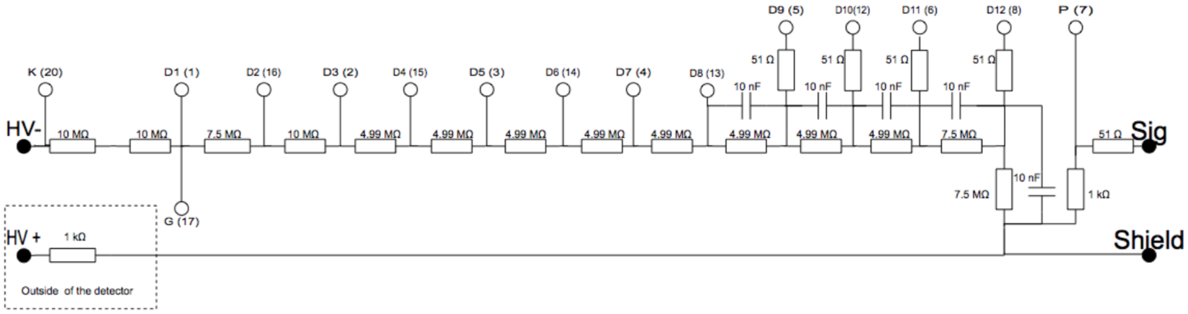

Photocathode - D1	D1 - D2	D2 - D3	D3 - D11	D11 - D12	D12 -Readout Anode
4	1.5	2	1	1.5	1.5

Figure 3.5: Top: The electronic schematic of the voltage divider network for the XENON1T PMTs. Schematic taken from [147] Bottom: Resistor ratios between the dynode stages (D1-D12), the photocathode and the anode of the XENON1T voltage divider network.

focusing grid in order to focus the produced photoelectron onto the first dynode, which results in a ∼90 % collection efficiency. The PMTs selected for XENON1T show, therefore, a mean quantum efficiency of ∼35 % at the xenon scintillation wavelength of 178 nm. The PMT schematic is shown in Figure 3.6 (left), and a front view is shown in Figure 3.6 (centre). The material selection was optimised with the manufacturer in order to reduce the radioactivity of the materials. The ^{238}U activity from the measured activity for ^{235}U is about (8 ± 1) mBq/PMT [148]. The PMT body consists of a low-radioactivity Co-free Kovar alloy and an aluminium seal at the window. The dynodes are insulated with quartz from each other. The readout pin and the voltage supply pins for the different dynodes are sealed with a ceramic stem at the back of the PMT. A further advanced version of this PMT has a thin chromium oxide (Cr_2O_3) layer on top of the ceramic stem, in order to reduce a charge up of the stem. All the PMTs for the XENON1T TPC were investigated for traces of radioactive isotopes. For this purpose, the technique of γ-spectrometry was employed, by the University of Zurich high purity germanium detector facility, Gator [149].

A voltage divider network (base) is used to provide the voltage gradient between the different dynode stages needed to accelerate the secondary electrons between the stages and to read out the signal electrons at the anode. A negative potential is applied to the photocathode, and the anode is held at ground potential. In this configuration, the signal is entirely decoupled from the high voltage source, which results in no signal artefacts coming from the high voltage line. The resistor ratios between the dynode stages were suggested by Hamamatsu in order to achieve an optimal gain. The electronic schematic and the resistor ratios are shown in Figure 3.5. The absolute resistor values where optimised regarding the heat dissipation and the dynamic range of the signal, which will be discussed in the subsection 3.4.3. The base design and its development can be found in [147]. The total resistivity of the base is 92.5 MΩ, which results in a base current of 16.2 μA at the nominal operating voltage of −1500 V. The heat dissipation is, therefore, 0.024 W per base and ∼6 W for all 248 TPC bases. The circuit board substrate is made out of Cirlex® (all-polyimide sheet material), which offers a stable operation in a temperature range from −269 °C to 351 °C and a low intrinsic radioactivity in comparison to standard material substrate [145, 151]. The voltage divider network is biased with high voltage Kapton® (4,4'-oxydiphenylene-pyromellitimide) insulated wires, which are soldered through a stress relief onto the PMT base. The signal is read out with a coaxial PTFE cable (RG196), which is also soldered through a stress relief onto the PMT base [152]. The Cirlex® base is connected through 15 lead-free spring-loaded sockets (Be-Cu, gold plated) to the PMT pins, which offers a convenient way to mount and remove the Cirlex® base. Figure 3.6 (right) shows the voltage divider network on a Cirlex® substrate.

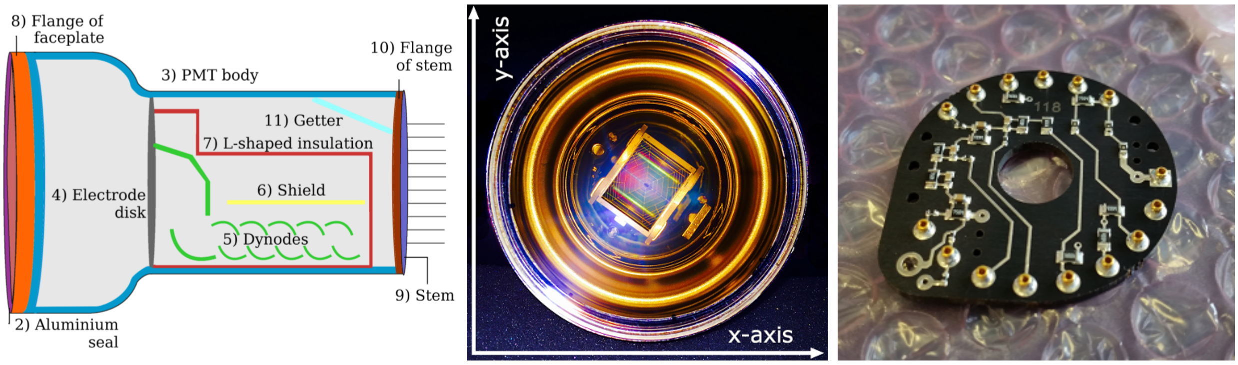

Figure 3.6: Left: Schematic of the R11410-21 Hamamatsu PMT. Published in [150]. Centre: Front view of the R11410-21 Hamamatsu PMT. Right: The voltage divider network on a Cirlex® base.

3.4.2 Photomultiplier Tube Characteristics

The mean number of signal electrons produced by the PMT in response to one photoelectron is called amplification *gain*, which is determined by the secondary emission of electrons through all dynode stages. The secondary emission ratio is the mean number of produced secondary electrons per primary electron, which can be expressed for every dynode i with:

$$\delta_i = a\Delta V_i^k, \tag{3.1}$$

where ΔV_i is the voltage difference between the i^{th} and $i^{\text{th}-1}$ dynode, and k and a are constants depending on the dynode structure and material. The gain is given by the product of the secondary emission ratios of all dynodes. The voltage difference ΔV_i between the i^{th} and $i^{\text{th}-1}$ dynode is constant for the given resistor ratios in Figure 3.5. The overall gain can be expressed with:

$$G = \prod_i^n \delta_i = \left(a\Delta V_i^k\right)^n = a^n \left(\frac{V_{\text{bias}}}{n+1}\right)^{kn} \tag{3.2}$$

where n is the number of dynodes and V_{bias} is the bias voltage of the PMT. From equation 3.2, it can be seen that the gain of the PMT can be adjusted by changing the bias voltage of the PMT.

In the absence of any light source, the photocathode can emit electrons into the vacuum, which will undergo the amplification process and will generate a signal that is indistinguishable from a single photoelectron. These signals are called *dark count events*, and their origin comes from the fact that some electrons in the photocathode gain sufficient thermal energy to exceed the work function of the material (thermionic emission). The number of dark count events per second (dark count rate - DCR) at room temperature is dominated by thermionic emission and is independent of the bias voltage. The thermionic emission decreases rapidly with temperature, by following the Richardson's law [153]:

$$\text{DCR}(T) \propto T^2 e^{\frac{-W}{kT}}, \tag{3.3}$$

where T is the temperature, W is the work function of the material, and k is the Boltzmann constant. At cryogenic temperatures, the dark count rate produced by thermionic emission becomes negligible, and the dark count rate produced by field emission becomes dominant. High local electric fields inside the PMT can produce small discharges, and the corresponding emission of photons can reach the photocathode and generate a dark count event. This effect is highly bias voltage dependent and known as *micro-light* emission, which will be further discussed in section 4.2 and 5.2 along with PMT *flashes*, which are large discharges inside the PMT.

PMTs are evacuated, in order to increase the free mean path of the electrons, and thus to limit the interactions of the electrons with the residual gas. The quantum efficiency is therefore maximised in a perfectly evacuated PMT in general. A perfect PMT vacuum cannot be achieved, and in most of the PMTs there are small traces of He_2, CH_4, Ne_2, N_2 and Ar. Photoelectrons and secondary electrons produced by an incident photon can hit a single gas molecule along their trajectory and ionise it. Due to its positive charge, the produced ion travels back to the photocathode and with its kinetic energy releases free electrons into the vacuum. The free electrons undergo the amplification process and generate a signal, which is delayed with respect to the original signal coming from the incident photon. This delayed signal is called an *afterpulse* and the delay time to the original signal depends on the ion mass, the charge and the bias voltage of the PMT. The following dependency of the delay time can be found in [154]:

$$t_{\text{Delay}} = \left(1.134 \left[\frac{V\mu\text{s}}{\text{cm}}\right]\right) \sqrt{\frac{L^2}{V_0^2}\frac{M}{Q}}, \tag{3.4}$$

where M is the number of nucleons of the ion, Q is the ionisation number of the ion, L is the distance from the photocathode to the focusing grid, and V_0 is the potential difference between the photocathode and the first dynode. Another type of afterpulse is generated by secondary electrons, which are back-scattered from the dynodes. These electrons return to the dynode and participate in the amplification process as well. This results in a smaller signal, delayed by a few nanoseconds with respect to the original signal. The afterpulse study of the XENON1T PMTs will be discussed in section 4.2 and a detailed analysis of the XENONnT PMTs in section 5.2.

3.4.3 Dynamic Range

In the last subsection, we discussed that the number of signal electrons read out at the anode of the PMT is proportional to the number of photoelectrons produced by the incident photons. The proportionality is given by the amplification gain, and as long as the signal electrons increase linearly with the number of incident photons, the PMT response is linear. PMTs offer a linear response from single photon up to several thousands of photons.

One non-linear behaviour effect can be observed when the PMT output signal starts saturating the ADC. The ADCs used in XENON1T (see section 3.1) have an input voltage range of 0–2.25 V. That implies that if an input signal is larger than 2.25 V, saturation effects are observable. Considering a 1 μs long signal, which is approximately equal to the length of the S2 signal, and a combined gain (PMT gain + amplifier gain) of 2×10^7, the maximum number of recorded photoelectrons are:

$$\mathrm{PE_{max}} = \frac{C_{\mathrm{max}}}{eG} = \frac{I_{\mathrm{max}} t}{eG} = \frac{U_{\mathrm{max}} t}{eGR} = 14\,050\,\mathrm{PE}, \tag{3.5}$$

where e is the electron elementary charge, G is the combined gain (2×10^7), C_{max} is the maximum capacitance, I_{max} is the maximum observable current pulse, R is the ADC impedance of $50\,\Omega$, U_{max} is the maximum ADC voltage range (2.25 V - v1724 CAEN flash ADC), and t is the length of the expected signal (S2 $\sim$ 1 μs).

Other non-linear behaviour effects are related to the voltage divider network design. The last dynodes of the PMT need to provide most of the charge for the amplified signal, due to the increased number of secondary electrons. In case the number of secondary electrons becomes large, the amount of available charge on the last dynodes is not sufficiently high and the output signal starts to degenerate. In the final XENON1T base design this issue was solved by adding a 10 nF capacitor ($\sim$5 nF at liquid xenon temperature) to each of the last five dynode stages.

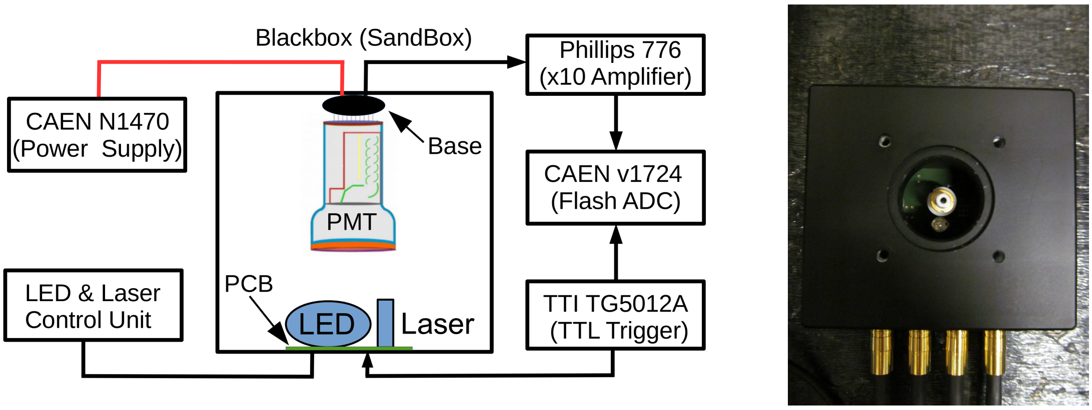

Figure 3.7: Left: The experimental setup for the dynamic range measurements. The PMT is placed above a laser, and an LED inside a light-tight box and the electronic scheme is following the XENON1T chain. Right: The PCB board housing the LED and the laser inside an enclosure box.

In addition, for a large number of produced photoelectrons, the secondary electron density between the last dynodes is drastically increased, which causes space charge effects. Therefore, the resulting current flow from the last dynode towards the anode (I_a) counterflows the direction of the base current (I_b) and reduces the voltage between the last dynode and the anode. However, the total applied voltage across all dynode stages is fixed by the power supply and is therefore redistributed over the previous dynode stages. The voltage between the last dynode and the anode does not contribute to the total gain, and it only serves for the collection efficiency of the secondary electrons onto the anode. The increase of the voltage on the previous dynode stages leads to an increase of the gain, which is known as over-linearity. The reduction of the collection efficiency onto the anode lead to saturation effects. This effect can be minimised by increasing the base current so that the anode current is negligible. A linearity of $\pm 1\,\%$ can be expected, as long as the anode current makes up for less than $1\,\%$ of the base current [155].

The dynamic range of the PMT and its readout base was verified in an experimental setup, which is shown in Figure 3.7 (Left). A R11410 PMT with its connected readout base is placed in the centre of a light-tight box $\sim 7\,\mathrm{cm}$ above a custom made PCB board, which houses a blue LED and a blue laser ($\lambda = 405\,\mathrm{nm}$). The PMT is powered by a CAEN N1470 high voltage module. The signal from the PMT is amplified by a ten-fold Philips 776 amplifier and digitised by a CAEN v1724 flash ADC with a sampling frequency of 100 MHz. The laser can provide up to several thousands of photons, and the light intensity can be changed by adjusting the pumping current of the laser with a potentiometer. The LED can generate light pulses with a small number of photons, and it is set to a fixed voltage. The ADC is triggered by a TTL signal produced by a pulse generator (TTi TG5012A), which also triggers the LED or laser, depending on the configuration of the custom-made control unit.

In this configuration, the response of the PMT to a small LED intensity for different large laser intensities can be investigated. The linearity is given with the following expression:

$$L(S_\mathrm{Laser}) = \frac{S_\mathrm{Laser+LED} - S_\mathrm{Laser}}{S_\mathrm{LED}}, \tag{3.6}$$

where S_Laser is the number of photoelectrons produced by the laser, S_LED is the number of photoelectrons produced by the LED, and $S_\mathrm{Laser+LED}$ is the number of photoelectrons produced by the laser and the LED triggered simultaneously. As long as the PMT response is linear, the simultaneous signal from the laser and the LED should be the same size as the sum of the laser and the

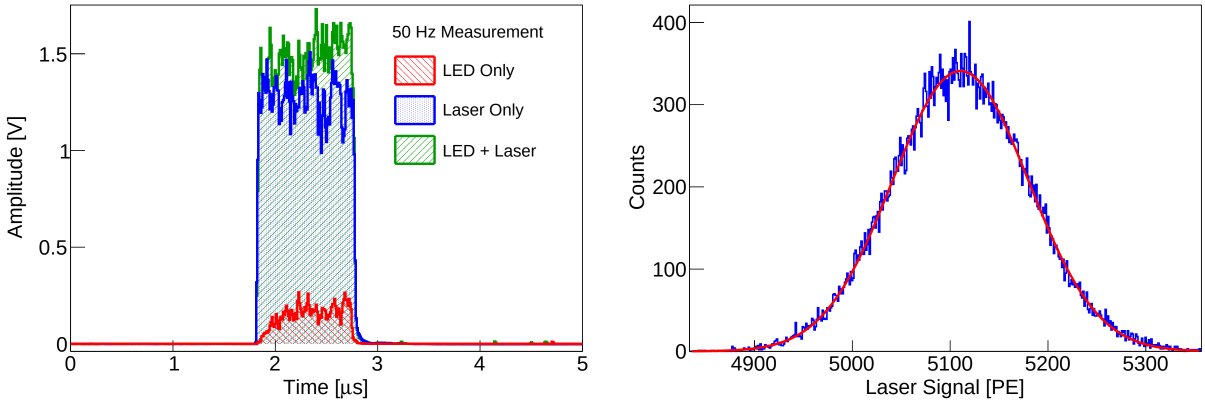

Figure 3.8: Left: Example waveforms of a dynamic range measurement at a pulse frequency of 50 Hz. The red histogram shows the LED-only, the blue one the laser-only and the green one the combined response of the PMT. Right: An example of the charge spectrum of the laser-only measurement. The distribution is fitted with a Gaussian function (red curve).

LED signals measured separately. Therefore, equation 3.6 indicates signal saturation (L<1) and over-linearity (L>1).

In order to evaluate the PMT response conservatively, the combined gain of the PMT was set to the lowest gain of 2×10^7. Therefore, the PMT voltage was set to -1320 V, which resulted in a base current of $\sim 14.2\,\mu$A. The pulse width of the laser and LED was set to $1\,\mu$s and pulsed with different frequencies (50 Hz up to 2 000 Hz). It has to be mentioned that the PMT response is independent of the pulse width for the same number of detected photoelectrons. However, it is strongly dependent on the pulse frequency due to the space charge effect. The LED was fixed to a constant light intensity, and the laser intensity was varied. The produced charge of the PMT signal was calculated by the data processor (described in section 5.2.2), which analyses the digitised traces. Sample signal traces of one measurement are shown in Figure 3.8 (left). For every laser intensity setting, the LED- only, the laser-only and the combined spectrum were measured. The spectra were fitted with independent Gaussian functions, and the means were used for the linearity calculation of equation 3.6. An example of the laser-only spectrum is shown in Figure 3.8 (right).

The results of the performed measurements are shown in Figure 3.9 (left). The PMT response is linear for small and large signals in a frequency range of 0–100 Hz until the saturation point of the ADC at around 14 050 PE, as predicted using equation 3.5. For an increased signal frequency (above $\sim$250 Hz) the signal of the PMT starts to deviate from the linear response. At around 1 % increase of the base current, over-linearity can be observed for signal frequencies above $\sim$250 Hz. Saturation effects due to the reduction of the collection efficiency onto the anode are visible for a frequency of 2 000 Hz, which results in a decrease of the linearity before the saturation point of the ADC.

In a second measurement, the combined gain was reduced from 2×10^7 to 2×10^6, bypassing the ten-fold Phillips 776 amplifier. The measurement procedure stayed the same. The results of the performed measurements with a gain of 2×10^6 are shown in Figure 3.9 (right). For a frequency range between 0 and 50 Hz, the PMT response is linear within 1 % over the whole ADC range. Saturation of the ADC can be observed at around 140 000 PE, which is in agreement with the predicted value. For signal frequencies above 50 Hz, an over-linearity can be observed, and saturation effects become dominate, due to the reduction of the collection efficiency onto the anode.

The XENON1T R11410 PMT response is linear over the whole XENNON1T ADC range with and without an external amplifier for frequencies up to 50 Hz. For higher frequencies, an over-linearity can be observed for signals which are larger than $\sim$1 % of the base current. The XENON1T expected signal rate during data taking does not exceed 50 Hz, and the calibration sources produce low energies ER and NR recoils so that over-linearity and the base saturation become irrelevant. For physics

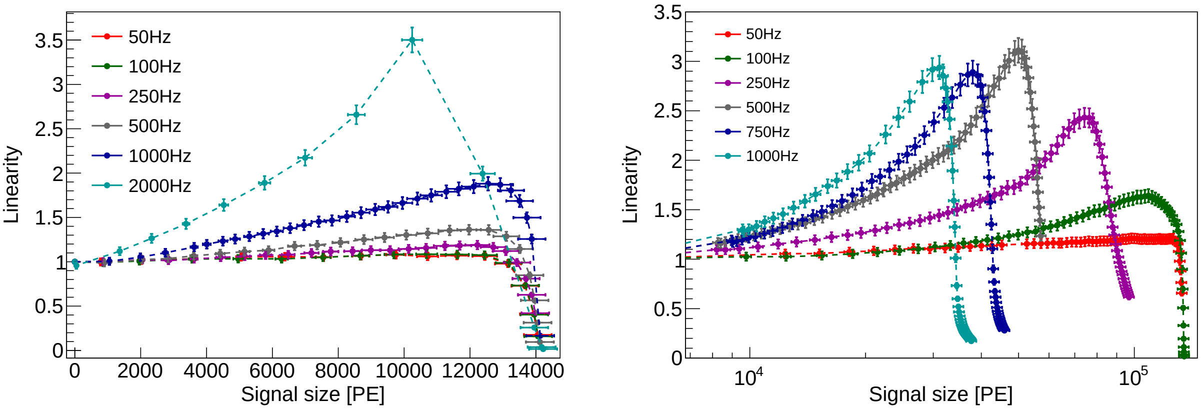

Figure 3.9: Left: Dynamic range measurement of a R11410 PMT with a combined gain of 2×10^7. Right: Dynamic range measurement of a R11410 PMT with a combined gain of 2×10^6.

channel at higher energies, the PMT response is still linear for frequencies below 50 Hz.[3] However, the limiting factor is the saturation of the used digitisers. Therefore, a dual channel amplifier was developed for future dark matter experiments to avoid amplifier and digitiser saturations. The developed amplifier will be discussed in chapter 5.

The dynamic range study was also performed for the 'diagnostic' 1-inch PMTs (Hamamatsu R8520) of the TPC (described in section 3.2). The detailed description and study of this PMT can be found in [147]. The result of the dynamic range measurement in the setup for a gain of 2×10^7 can be found in Appendix B.

3.4.4 Under-Amplified Electrons

The gain of a R11410 PMT can be obtained from the acquired single photoelectron (SPE) spectrum. Therefore, the PMT is illuminated with a light source of single photon intensity, and the response of the PMT is digitised. The number of produced signal electrons of the PMT is calculated by a data processor (described in section 5.2.2) by integrating the pulse areas. The number of produced photoelectrons follows a binomial distribution, which can be well approximated with a Poisson distribution. The gain of the PMT can be extracted by fitting the spectrum with Gaussian functions with amplitudes modulated by the Poissonian statistics. The electronic noise peak of the spectrum can be fitted with an additional Gaussian function, and the entire fit function is given by the following formula:

$$f(x) = A_0 \exp\left(-\frac{(x-\mu_0)^2}{2\sigma_0^2}\right) + A\sum_{k=1}^{n}\frac{\lambda^k e^{-\lambda}}{k!}\exp\left(-\frac{(x-k\mu)^2}{2k\sigma^2}\right), \tag{3.7}$$

where A_0 is the amplitude, μ_0 is the mean and σ_0 is the standard deviation of the noise peak, k is the number of observed photoelectrons, λ is the mean number of photoelectrons at the first dynode, and A is the amplitude, μ is the mean and σ is the standard deviation of the SPE peak.

An example of the resulting single photoelectron spectrum at a PMT voltage of −1500 V is shown in Figure 3.10 (left). The overall fit is indicated in red, and the gain can be extracted from the mean position of the first photoelectron peak. A valley can be identified between the noise and the SPE peak. These additional events can be clearly correlated with signals coming from the light source

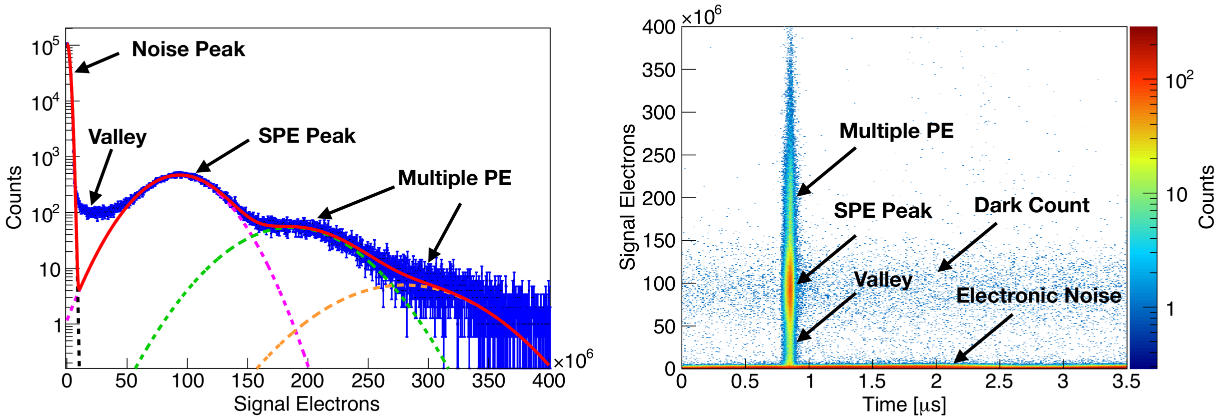

Figure 3.10: Left: The SPE spectrum of a R11410 PMT at −1500 V. It consists of an electronic noise peak (black curve), a valley, the SPE peak (pink curve) and multiple photoelectrons (green and orange curves) produced by the LED. The overall fit to extract the gain is indicated in red. Right: The produced signal electrons of the R11410 PMT at −1500 V in a waveform in presence of an LED signal. The valley events are mainly produced when the LED is on.

---

[3] The conversion from energy to detected S1-S2 photons per PMT is detector specific.

as shown in Figure 3.10 (right). The LED emits photons at a timestamp of $\sim 0.9\,\mu$s and produces, in addition to the multiple photoelectrons, the 'valley' events between the SPE and the noise peak. The valley events are so-called *under-amplified secondary electrons* and have less charge than those at the SPE peak since they do not participate fully in the PMT amplification process [156, 157]. A photon from the light source may not be absorbed in the photocathode and thus may directly strikes the first dynode [158, 159]. In this case, the number of produced secondary electrons will be reduced, because the amplification of the first stage was skipped.

The photoelectrons produced at the first dynode can be directly measured with a modified voltage divider network. A Hamamatsu R11410 PMT is nominally operated at -1500 V, and therefore has an electric potential of -1175 V at the first dynode. Applying this voltage directly to the first dynode and skipping the photocathode results in a measurement of the photoelectrons produced on the first dynode. A dedicated study was performed with a voltage divider network, where the first dynode can be biased separately, and the photoelectrons produced at the photocathode are held back. The study was performed at 22 C°, and the experimental setup is described in details in [160, 161]. The setup consists of a light-tight black box, which houses a collimated blue LED ($\lambda = 405$ nm) attached on a two-axis scanner (x-y). A R11410 PMT was placed 1 mm above the collimator, which resulted in an illuminated spot on the photocathode with a diameter of 0.7 m. The two-axis scanner moved in the plane parallel to the photocathode, the LED was biased by a pulse generator ($\sim$3 000 PE), and the PMT response was digitised by a v1724 CAEN ADC. In this configuration, the position-dependent response of the PMT could be investigated. The pulse areas were calculated with a data processor described in section 5.2.2.

An initial photocathode scan was performed with the nominally used voltage divider network. The mean number of produced secondary electrons was extracted for every pixel, which is proportional to the number of detected photoelectrons. The pixel with the highest number of mean secondary electrons defines the 100 % sensitivity. All other pixels are scaled according to this value. Figure 3.12 (left) shows the result of the initial PMT scan. The inner structure of the PMT becomes visible because some of the incident photons are not absorbed in the photocathode and are reflected at the inner surface of the PMT. A higher reflectivity can be observed on the blank metal surfaces and the reflectivity is reduced at the screws. The first dynode increases the sensitivity in the centre of the PMT, due to the absorption of the transmitted photons through the photocathode. See Figure

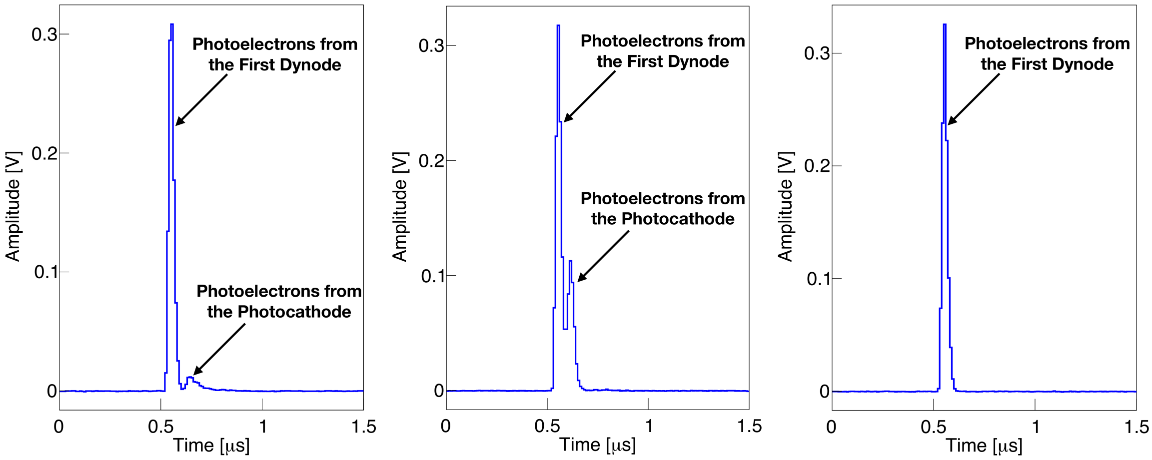

Figure 3.11: Left: The R11410 PMT response to an LED. The first dynode and the photocathode are held on the same potential. Centre: The R11410 PMT response to an LED. The first dynode is held at -1175 V and the photocathode is held at -1184 V. Right: The R11410 PMT response to an LED. The first dynode is held at -1175 V and the photocathode is held at -1166 V.

3.6 (centre) for the comparison with the inner structure of the PMT.

In a second configuration, the first dynode and the photocathode were set to the same potential (−1175 V) by bypassing the first resistors of the voltage divider network. The voltage was chosen in order to have the same amplification configuration throughout the later dynode stages. The PMT was illuminated with the collimated LED. An example PMT response is shown in Figure 3.11 (left). Two pulses are observable in response to the LED pulse. The first pulse corresponds to the amplified photoelectrons from the first dynode and the second pulse corresponds to the amplified photoelectrons from the photocathode. The electric field between the first dynode and the photocathode is strongly reduced, due to the same applied electric potential. Some of the generated photoelectrons in the photocathode can reach the first dynode with a short time delay after the LED pulse, and generate secondary electrons. This pulse is much smaller than the pulse from the first dynode, due to the decreased collection efficiency and kinetic energy of the photoelectrons. By increasing the electric potential on the photocathode with a 9 V battery from −1175 V to −1184 V, the second pulse can be increased, due to the increased electric field as shown in Figure 3.11 (centre). In the performed measurements, the electric potential of the photocathode was reduced with a 9 V battery to −1166 V and the first dynode was held on −1175 V. In this configuration, photoelectrons produced in the photocathode did not undergo the amplification process, and therefore, only the photoelectrons from the first dynode were measured. The pure signal from the first dynode is shown in Figure 3.11 (right).

A photocathode scan was performed with the modified voltage divider configuration. The analysis procedure was kept the same as in the initial photocathode scan. Figure 3.12 (right) shows the result of the PMT scan. The first dynode becomes visible in the sensitivity map because the applied electric potential was lower on the photocathode than on the first dynode. A comparison with Figure 3.6 shows that the first dynode does not have a uniform response. The area in its centre has the highest sensitivity and the outer regions do not have sensitivity to the incident photons. The ratio between the initial PMT scan and the scan with the modified voltage divider configuration gives the relative amplification of photoelectrons coming from the first dynode. The photoelectrons on the first dynode show an amplification between 0 and 0.1 relative to the photoelectrons produced in the photocathode. Therefore, photoelectrons produced at the first dynode can explain part of the valley

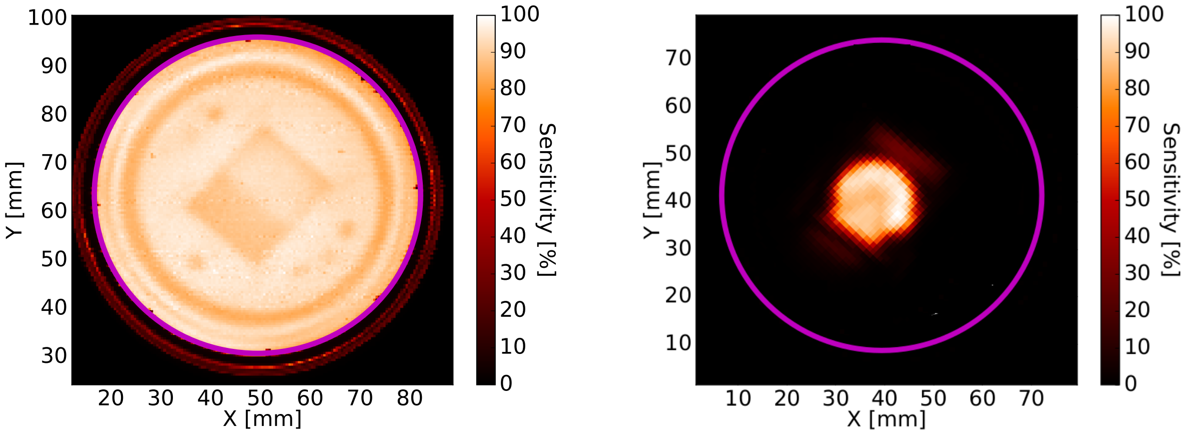

Figure 3.12: Left: The result of the performed photocathode uniformity scan of a R11410 PMT with the nominal voltage divider network. The magenta circle indicates the PMT radius. The explanation is given in the text. Right: The result of the performed first dynode scan of a R11410 PMT with the photocathode on a lower potential (−1166 V) than the first dynode (−1175 V). The magenta circle indicates the PMT radius. The explanation is given in the text.

events in Figure 3.10 (left). The events from the first dynode are at the lower end of the spectrum close to the electronic noise peak but can not explain the appearance of the valley completely.

The appearance of the under-amplified secondary electrons over-estimates the PMT gain by 10-20 % when using equation 3.7. This is important to be taken into account in order not to underestimate the number of detected photoelectrons. Therefore, a method has been developed for the XENON1T PMT gain calibration, which does not need any assumption of the shape of the SPE spectrum and extracts the gain values statistically [162]. The gain calibration procedure with the model-independent method will be discussed in section 4.2.

3.5 Cryogenic Validation of the Field Cage

The XENON1T electric field cage, described in section 3.2, was assembled at the University of Zurich and tested for structural integrity in a cryogenic environment. Next, we describe the experimental setup for the low-temperature validation of the field cage, followed by a description of the trial field cage assembly at the University of Zurich and the results of the cryogenic temperature validation.

3.5.1 Experimental Setup and Measurement Procedure

The TPC field cage was cooled down to a temperature of around $-100\,^\circ$C to verify the structural stability due to the PTFE contraction of the support pillars and panels. This temperature was chosen according to the expected liquid xenon temperature in XENON1T. In order to cool down the field cage with an approximate height of 1100 mm, a dewar produced by CryoFab (CF-4858) with a $\sim$1320 mm inner diameter and a $\sim$1432 mm height was used.

The dewar can be filled from the bottom with liquid nitrogen that enters through a side port, which is connected to an external liquid nitrogen tank. The dewar is insulated by a vacuum jacket and pumped out down to a pressure of $\sim 10^{-3}$ mbar. During the preparation stage, we found out that four fans were needed inside the dewar to circulate the cold nitrogen gas. A specially designed

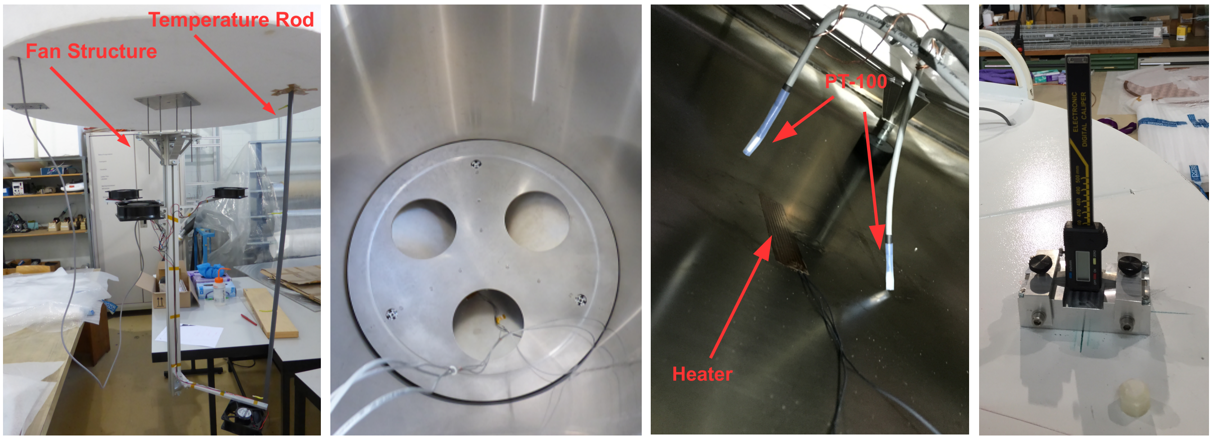

Figure 3.13: Left: The fan structure attached to the dewar lid, which holds four fans at different heights in the centre of the dewar. Pt-100 temperature sensors are placed along a plastic rod at different heights. Centre left: An aluminium plate with three cutouts is placed at the bottom of the dewar to allow gaseous nitrogen circulation and to support the field cage. Centre right: Three heaters are placed on the bottom of the dewar in order to avoid liquid nitrogen collection. Two Pt-100 sensors are placed next to the heaters to monitor the liquid nitrogen height. Right: The digital depth caliper fixed to the outside of the dewar lid. It stays in place with the help of two aluminium clamps. The digital depth caliper extends until the top ring of the TPC.

fan structure was attached to the top lid of the dewar, as shown in Figure 3.13 (left). The fan structure holds three fans at different angles and at the same height as the top stainless steel field cage ring. One fan was held by the fan structure at the bottom of the field cage. The flow current of the fans was set to the maximum, and the current between the top fans and the bottom fan was to an opposite direction. In this configuration, the temperature was uniform throughout the entire dewar. An aluminium plate with adjustable feet was placed at the bottom of the dewar to support the field cage and flatten the floor as shown in Figure 3.13 (centre). The aluminium plate had three large cutouts for nitrogen gas circulation. Three heaters and two temperature sensors were placed below the support plate to heat and monitor the temperature in this region. The heaters, in addition to a very low flow from the external liquid nitrogen tank, prevented liquid nitrogen formation at the bottom, thus allowing for a slow and consistent cooldown rate and stability at $(-100 \pm 2)\,^{\circ}\mathrm{C}$. A rod that holds a string of four Pt-100 temperature sensors at different heights was connected to the lid of the dewar in a slightly smaller radius than the radius of the field cage. These temperature sensors were used to monitor the absolute temperature at different heights in the gaseous nitrogen. In addition, four Pt-100 temperature sensors were directly attached to the support pillars at different heights, in order to monitor the temperature gradient across the field cage.

The relative difference in length was measured using a digital depth caliper, which extends from the top of the dewar lid to the top TPC stainless steel ring. Therefore, a hole was drilled through the dewar lid and positioned at a radius that is directly above the stainless steel ring on the top of the TPC field cage. The digital depth caliper was fixed to the outside of the lid with a holding structure, which is shown in Figure 3.13 (right). The vertical dimension of the field cage can be measured by extending the digital depth callipers from this fixed position outside the dewar, through the hole, and onto the stainless steel ring on the top of the TPC. Changes in the vertical dimension of the structure can be ascertained by comparing these results to baseline measurements of the TPC using the same method at room temperature. In addition, the lid was rotated to obtain measurements at different azimuthal positions of the field cage at cryogenic temperature and a room temperature.

The specification of the used PTFE from the manufacturer gives a linear thermal expansion coefficient of $16.5 \times 10^{-5}\,\mathrm{K}^{-1}$. The support pillar length as specified in the drawings was $(1087.55 \pm 0.20)\,\mathrm{mm}$, 967.4 mm of which supports the TPC from the cathode wires to the top of the pillar. A subsample of the pillars after production showed an average measured length of $(1086 \pm 0.2)\,\mathrm{mm}$ at $22\,^{\circ}\mathrm{C}$. Using the value specified by the manufacturer yields to an expected contracted length

Figure 3.14: Left: The Kapton® foils with the soldered resistors on top, screwed to the inside of the field shaping rings. Centre: The inside of the field cage enclosed by the PTFE reflector panels. The bottom PMT array copper plate and PTFE reflector were attached to the field cage. Right: The assembled field cage with the support structure.

of $\sim 1064\,\mathrm{mm}$ ($\sim 2.0\,\%$) at $-100\,^{\circ}\mathrm{C}$. The radial dimension of the field cage is given by the copper field shaping rings with a thermal expansion coefficient of $\sim 1.7 \times 10^{-5}\,\mathrm{K}$ [163]. This led in a radial reduction of $\sim 0.2\,\%$, which is negligibly small.

3.5.2 Field Cage Trial Assembly

At the time of the cryogenic temperature validation of the electric field cage, the final top stainless steel TPC ring was still in production. In order to be able to assemble the field cage, a less complex aluminium top TPC ring was designed, produced and used as a mock-up to support the field cage. During the assembly, a support structure made of aluminium Bosch frames was attached to the bottom field copper ring and the top TPC ring. In this configuration, the support frame keeps the field cage stable, particularly against rotation and torsional stress. An overhead crane was attached to rotatable eye hooks on the support frame, which are connected to the top TPC ring in order to support the field cage during assembly.

The top TPC ring was then vertically positioned above the bottom copper ring to allow for the connection of the support pillars, as well as the Torlon® inserts between the top TPC ring and the support pillar. The pillars were screwed with stainless steel screws to the bottom and top TPC ring. For the insertion of the copper field shaping rings, half of the pillars were removed again, so that 15 support pillars were left to hold the entire structure. We found that 15 support pillars constitute the most stable configuration to hold the structure, while still being able to accommodate the diameter of the field shaping rings. The field shaping rings were loaded from the top to the bottom and once all of the rings were installed, the remaining pillars were attached. The holes of the rings for the resistor chains were aligned by rotating the rings into the correct position. A subsection of the resistor chain was screwed to the field shaping rings as shown in Figure 3.14 (left). The resistors are soldered onto thin Kapton® foils, and the Kapton® foils with the soldered resistors on top were screwed to the field shaping ring. We found that this configuration is fragile and the subsection of the resistor chain had to be handled with great care. The total weight at this stage of the assembly was $\sim 128\,\mathrm{kg}$ (including the Bosch frame support structure). A picture of the assembled field cage is shown in Figure 3.14 (right). The Bosch frame support structure underneath the bottom copper ring was used to support the field cage while allowing for the installation of the remaining cable trays to the support pillars. The support structure was removed after the assembly was completed.

In the next step, the PTFE reflector panels were inserted. First, the fixed reflector panels were

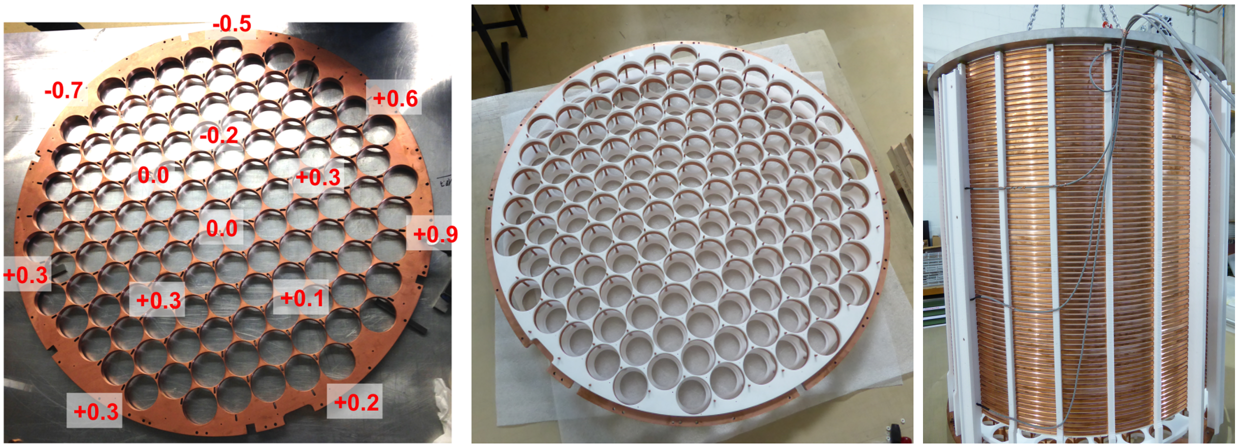

Figure 3.15: Left: The measured deviations of the bottom PMT array copper plate with respect to the centre in units of mm. Centre: The assembled bottom PMT array structure. Right: The assembled field cage with inserted temperature sensors at different support pillar heights.

installed by sliding them into the grove of the support pillars. Afterwards, the sliding reflectors were inserted. During the installation of the sliding reflectors, we found that they did not stop above the cathode and due to the risk of damaging the cathode during operation at low temperature, small modifications were made. On each fixed reflector, 2 mm diameter Torlon® pins were inserted at the bottom to keep the sliding reflector in place, as described in section 3.2. The installed PTFE reflector panels are shown in Figure 3.14 (centre).

Once the installation of the PTFE reflectors was completed, the bottom PMT array structure was assembled and attached to the bottom copper plate of the field cage. As a first step, the flatness of the PMT array copper plate was measured. The copper plate was moved to a heavy, flat table and placed onto three stainless steel blocks. The flatness was measured with callipers from the table to the top of the copper plate. The results of the measurements are shown in Figure 3.15 (left). The values represent the difference in mm with respect to the centre of the copper plate. The deviation was between 0.9 mm and −0.7 mm and the plate thickness varied between 18.70 mm and 18.77 mm. After validation of the flatness of the copper plate, the array was assembled and 127 copper rods were screwed into the PTFE bottom array reflector. Afterwards, the copper plate was placed on top of the PTFE spacers attached to the rods and fixed with a second PTFE reflector and PTFE nuts. The assembled bottom PMT array structure is shown in Figure 3.15 (centre). The bottom PMT array structure was then finally screwed to the field cage copper ring, and the entire field cage was placed on aluminium support blocks, such that it did not rest on the PTFE plate and the weight of the field cage did not deform the PTFE.

3.5.3 Thermal Contraction Measurements

Five Pt-100 temperature sensors were attached to the support pillars of the field cage at different heights, in order to measure the temperature of the PTFE. A picture of the temperature sensors attached to the field cage is shown in Figure 3.16 (left). The field cage with the attached bottom PMT array was lowered into the setup (described in 3.5.1). An initial baseline measurement with the digital depth caliper was performed at room temperature (22 °C), in order to correct for any tilts of the field cage. Therefore, the distance between the top of the dewar to the top of the TPC ring was measured for different angles and normalised to the measured distance at an angle of 0 °

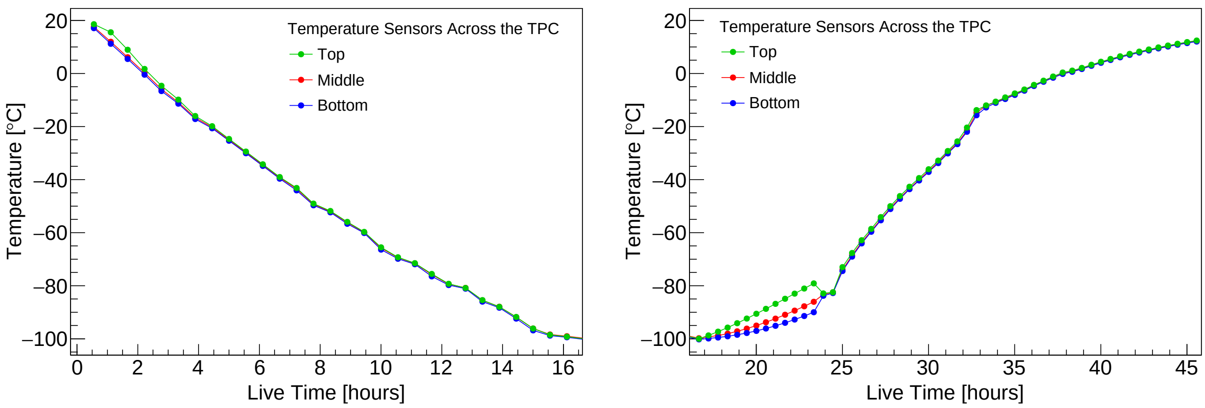

Figure 3.16: Left: Temperature evolution of the PTFE pillars during the cooldown. The temperature points at different field cage heights are overlapping. Right: Temperature evolution inside the gaseous nitrogen vapour during the warm-up process of the field cage. Overnight the fans were turned off, which is visible in a temperature gradient across the dewar. In the morning the fans were turned on again, and the temperature points at different dewar heights are overlapping again.

(reference point). It was measured that the distances for different angles have a maximum deviation of ∼ 5 mm with respect to the measured distance at 0 °.

The setup with the field cage was cooled down by adjusting the liquid nitrogen flow from the external liquid nitrogen tank through a needle valve into the dewar. The fans and heaters were set to their maximum value in order to minimise the temperature gradient inside the dewar. The field cage was cooled down for 10 hours to a final temperature of $(-100 \pm 2)\,°\mathrm{C}$. The cooling rate was set to ∼ 2 °/h to ensure a uniform temperature through the field cage components and thus to avoid internal stress in the material. The temperatures across the field cage during cooldown are shown in Figure 3.16 (left). The temperature from the top to the bottom of the field cage is uniform, due to the usage of the additional fans to circulate the cold nitrogen gas.

During the cooldown, the distance between the top of the dewar to the top of the TPC ring was continuously measured at the reference point. These measured values were used to calculate the contraction of the PTFE support pillars. The measured PTFE support pillars length as a function of temperature is shown Figure 3.17 (left). The PTFE shows a non-linear contraction between 20 °C and 17 °C. This was noted in previous measurements [164, 165]. In this temperature regime, the crystal structure of the PTFE undergoes a transition from a hexagonal to triclinic structure [166], which results in a non-linear shrinkage. Between −10 °C and −100 °C the PTFE follows a linear shrinkage. However, the linear expansion coefficient can vary based on the method of forming the PTFE [165]. The thermal expansion coefficient was measured to be $(9.48 \pm 0.39) \times 10^{-5}\,\mathrm{K}^{-1}$ by fitting the measured points with a linear function from 0 °C to −100 °C. The obtained thermal expansion coefficient will be used in section 4.1 to calculate the target mass of the XENON1T TPC.

At a temperature of −100 °C the distance between the top of the dewar to the top of the TPC ring was again measured for different azimuthal angles and normalised to the reference point. The measurements at room temperature 22 °C and at −100 °C are shown in Figure 3.17 (right). The field cage contracted uniformly for different azimuthal angles and is within the baseline measurements at room temperature. The dominant systematic error is the machining tolerance of the pillars, as well as the flatness of both the mockup top ring and the bottom plate of the dewar. Furthermore, the rotation of the dewar lid to the exact position was an additional systematic error of ±5 °.

Once the measurements were completed, the field cage was slowly warmed up to room temperature. The temperature across the field cage during the warm-up is shown in Figure 3.16 (right). A temperature gradient occurred during the warm-up process because the fans were shut down

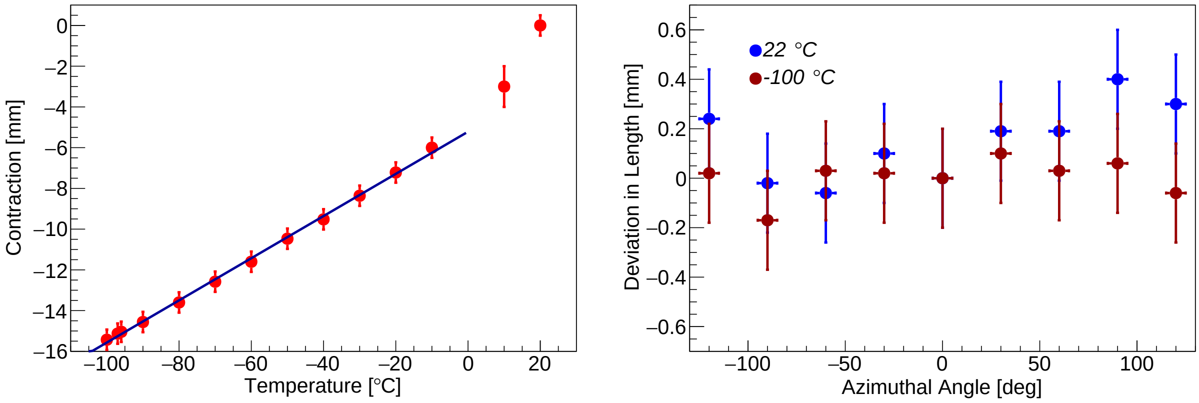

Figure 3.17: Left: The measured PTFE support pillars contraction as a function of temperature. The PTFE shows a non-linear contraction between −10 °C and 22 °C. Right: Distance between the top of the dewar to the top of the TPC ring normalised to the reference point at 0 ° for different angles and temperatures. The field cage shrinks uniformly for different angles.

overnight and turned on again in the morning, due to safety regulations. After the warm up, the field cage was inspected visually. The resistor chain was still intact, and no irregularities were found. The field cage was then disassembled and packed for further cleaning and the final assembly at LNGS, which will be described in the following section.

3.6 TPC Cleaning and Construction

In this section, we will first describe the performed cleaning procedure of the PTFE, PEEK® and Torlon® components of the TPC. This is followed by a detailed description of the assembly of the TPC in the aboveground XENON dedicated laboratory at LNGS. The section will be closed with the description of the installation of the TPC inside the XENON1T water tank located in Hall B of the LNGS underground laboratory.

3.6.1 Cleaning of TPC Components

The materials used for the TPC were selected based on their radiopurity. Prior to their final installation, they underwent a special cleaning procedure, in order to further reduce their surface radioactivity, in particular the contamination from ^{222}Rn plated onto the inner surface. In addition, residual water, grease and other contaminants needed to be removed from the material surfaces in order to avoid contamination of the highly purified xenon and thus to increase the overall light yield.

The PTFE, PEEK® and Torlon® parts used in the TPC with the exception of the parts from the PMT arrays, were brought to the University of Münster and cleaned. The University of Münster offers a large scale ultrasonic bath which was built for the KATRIN experiment. A special container was designed and constructed for the transportation of the corresponding parts consisting of a vessel which houses several trays for the components. The vessel and the trays were wiped down beforehand with pure acetone and ethanol. The vessel can be evacuated with vacuum turbopumps to a pressure of $\sim 10^{-6}$ mBar. The transport vessel loaded with the parts is shown in Figure 3.18 (left). The PTFE support pillars and reflectors are mounted onto the stainless steel trays of the transportation vessel, and the Torlon® and PEEK® components are placed between the flange and the trays.

Figure 3.18: Left: The interior part of the vacuum transportation vessel for the PTFE, Torlon® and PEEK® parts. Centre: The PTFE reflector panels inside the ultrasonic bath at the University of Münster. Right: The transportation vessel connected to the gas system in order to evacuate it and to fill with pure nitrogen gas (6.0).

The cleaning process at the University of Münster consisted of several steps. In the first step the parts were placed for 15 mins inside an ultrasonic bath, filled with a soap solution (Almeco P3) in order to remove dust particles and grease from the production process. Afterwards, the components were rinsed with deionised water and placed inside the ultrasonic bath for an additional 10 mins. In the second step, the components were placed in a 5 % HNO_3 solution for 15 mins in order to remove radioactive isotopes from the surface. After this step, the components were rinsed with deionised water again, placed in the ultrasonic bath for another 10 mins and finally rinsed with pure ethanol. Figure 3.18 (centre) shows the trays with the PTFE reflector placed inside the ultrasonic bath.

After all components underwent the cleaning procedure, the parts were sprayed with nitrogen gas, in order to remove remaining ethanol, and put back into the transportation vessel. The transportation vessel was connected to three turbomolecular pumps (Figure 3.18, right) and pumped out for $\sim$17 hours. The pressure inside the vessel before disconnecting the pumps was $\sim 10^{-3}$ mBar. The vessel was then filled with gaseous nitrogen to an absolute pressure of $\sim$3 bar to avoid further surface contamination. The vessel containing the cleaned parts was brought afterwards to LNGS, and the TPC was assembled, which will be described in the next section.

3.6.2 Aboveground TPC Assembly

The TPC assembly started in an ISO class 5 cleanroom in Lab 2 at LNGS. In a first step, the diving bell was fixed to a support structure, which had the task to hold the assembled TPC and to transport the TPC into the underground laboratory. The support structure had, in addition, four winches, in order to lift and lower a moveable table, as well as to connect the top PMT array to the bell and the bottom PMT array to the TPC, as shown in Figure 3.21 (right).

In the first step, the field cage was assembled. The top TPC steel ring was connected to the winches and the support pillars were connected to the top TPC ring. During this step we found that the Torlon® inserts between the top TPC ring and the support pillars did not fit, because the edge of the grove of the top TPC ring was after the production process not as in the CAD drawing. Therefore, the Torlon® inserts were modified by cutting them at an angle of 45 °. After this modification and the installation of the support pillars, the field shaping rings were inserted as described in subsection 3.5.2. Afterwards, the field cage was placed onto the movable table, and the two resistor chains were installed. Figure 3.19 (left) shows the assembled field cage. We noticed

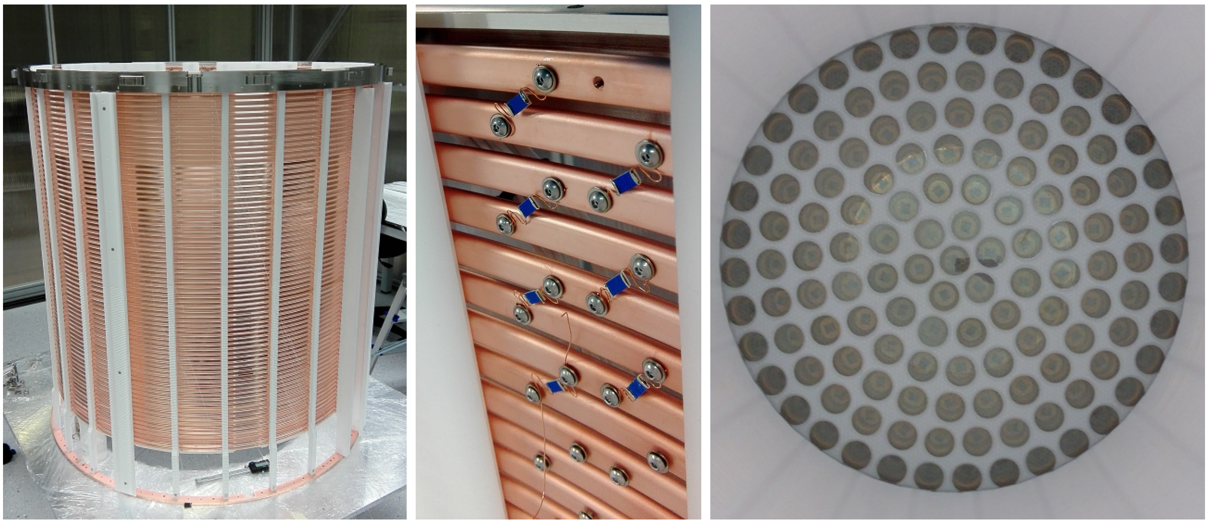

Figure 3.19: Left: The assembled field cage in the cleanroom. Centre: The modified resistor chain connected to the field shaping rings. Right: The top PMT array inserted into the diving bell.

that the resistors soldered onto the Kapton® foil led to the dysfunctionality of the resistor chain. Due to this, each resistor was soldered onto two copper wires, and each end of the copper wires was connected to a neighbouring field ring. This configuration was more stable against any vibrations of the TPC. A picture of the installed resistor chains is shown in Figure 3.19 (centre). In the next step, the PTFE reflector was installed and the optical fibres for the PMT calibration were routed inside the TPC. The description of the installation of the optical fibres can be found in [167], and the PTFE reflector installation was described in subsection 3.5.1. In addition, at this point of the assembly, the pre-assembled top PMT array was installed into the diving bell. In Figure 3.19 (right) the top PMT array installed inside the diving bell is shown.

In the next step, the top stack of the TPC was assembled on top of the field cage. First, Torlon® insulation pieces were inserted into the grove of the top TPC ring in order to prevent the sliding reflectors from floating upwards during operation. On top of the Torlon® pieces, the gate was placed. The gate was separated from the anode by Torlon® spacers and PTFE pieces. The Torlon® spacers were loosely screwed to the top TPC ring, and the anode and gate were fixed with PEEK® screws to the Torlon® spacers, which set the distance between the anode and the gate precisely to 5 mm. During this installation, we found that the gate mesh had a broken mesh cell. The mesh cell was visually inspected with a lens, and we found that the cell was still intact. Next, the cone-shaped reflectors were installed on top of the anode, which enclosed the volume between the anode and the screening mesh. The reflectors were fixed with copper screws to the top TPC ring. On top of the cone-shaped reflectors, the screening mesh was screwed on. The electrical connections to the anode, the gate and the screening mesh were realised with individual copper rods, which were screwed into the electrodes and insulated with PTFE tubes. In the last step of the assembly of the top stack, the four capacitive levelmeters were installed at the top TPC ring in order to measure the liquid xenon level between the gate and the anode. The assembled top stack is shown in 3.2 (left). Afterwards, the field cage was attached via the top ring to the diving bell with stainless steel screws. The cables from the top PMT array were routed out of the diving bell through four cutouts to the top of the diving bell. At this stage of the assembly we found out that the diving bell was not perfectly round, and therefore, not all of the stainless screws could be inserted from the top TPC ring into the diving bell. Furthermore, four of the stainless steel screws were not able to screw completely inside the bell, due to galling of the screws. The reason for the galling of the screws was due to the clean environment and the resulting high friction between the same materials.

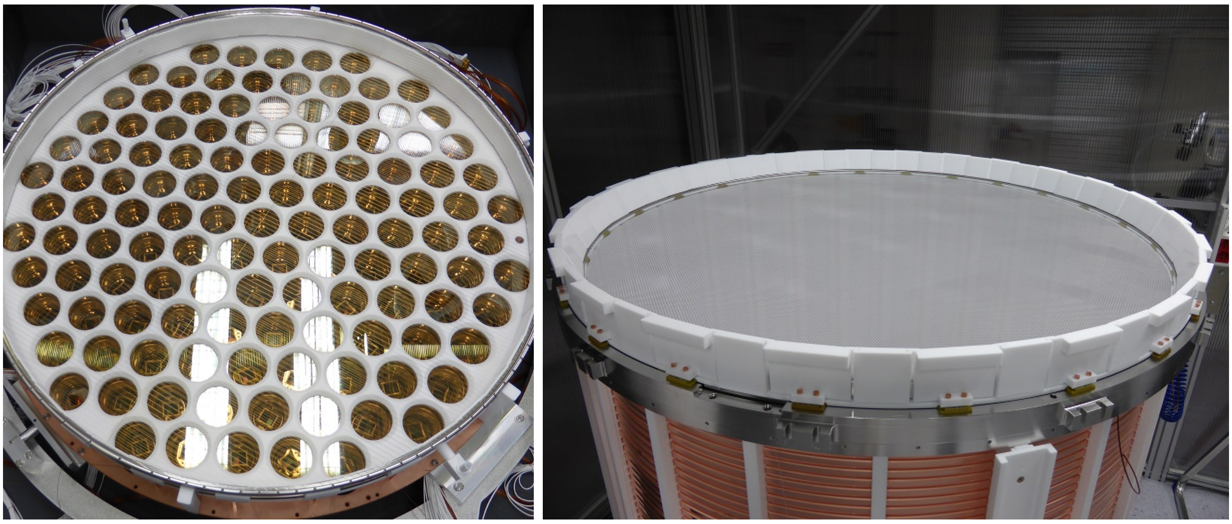

Figure 3.20: Left: The assembled bottom PMT array and its stack. Right: The assembled top TPC stack onto the top TPC ring.

The last step of the TPC assembly in the aboveground laboratory was the construction of the bottom stack. First, the screening mesh was placed on the pre-assembled bottom PMT array, and the six PTFE support pillars for the cathode were mounted to the bottom PMT array copper plate. Afterwards, the fixed PTFE reflectors were placed onto the screening mesh and fixed with a copper rod to the bottom PMT array copper plate. Two of the fixed reflectors had a hole with an inlet for the liquid xenon. The sliding reflectors were placed between the fixed reflector on top of the screening mesh, and the cathode was placed on top of the support pillars. A picture of the assembled bottom PMT array is shown in Figure 3.20 (right). The entire structure was connected to the bottom copper ring of the field cage. The electric connection of the cathode with the resistor chain was realised with a pressure contact. The electric connection to the screening mesh was realised with a stainless steel metal part soldered to a Kapton® cable, which was squeezed between the PTFE reflector and the screening mesh frame. The cables from the bottom PMT array were routed to the top of the diving bell through four cable trays attached to the outside of the support pillars of the field cage.

3.6.3 Underground TPC Installation

The assembled TPC was brought to the underground laboratory of LNGS in order to make the final connection of the TPC to the XENON1T cryostat. The TPC was lifted from the bottom of the XENON1T water tank with three winches attached to the TPC support structure to the cryostat dome. In the first step, the TPC diving bell was connected with six stainless steel rods to the cryostat dome, and the TPC support structure was removed. This position was lower than the final position in order to enable the final piping, cable connections and installation of the 'diagnostic' PMTs.

In the first step of the underground installation, the two long capacitive levelmeters were attached to the support pillars, and the piping on top of the bell with the funnel was installed. The two endings of the pipes were connected with flexible PTFE tubes to the two inlets below the cathode, in order to fill the TPC with liquid xenon. In addition, another three PTFE tubes were routed below the bottom PMT array in order to purify and to recover the liquid xenon from the cryostat into ReStoX at the end of the detector operation. In the second step, all of the cables and optical fibres were connected on the top of the bell. In order to protect the optical fibres from the cables, a quarter

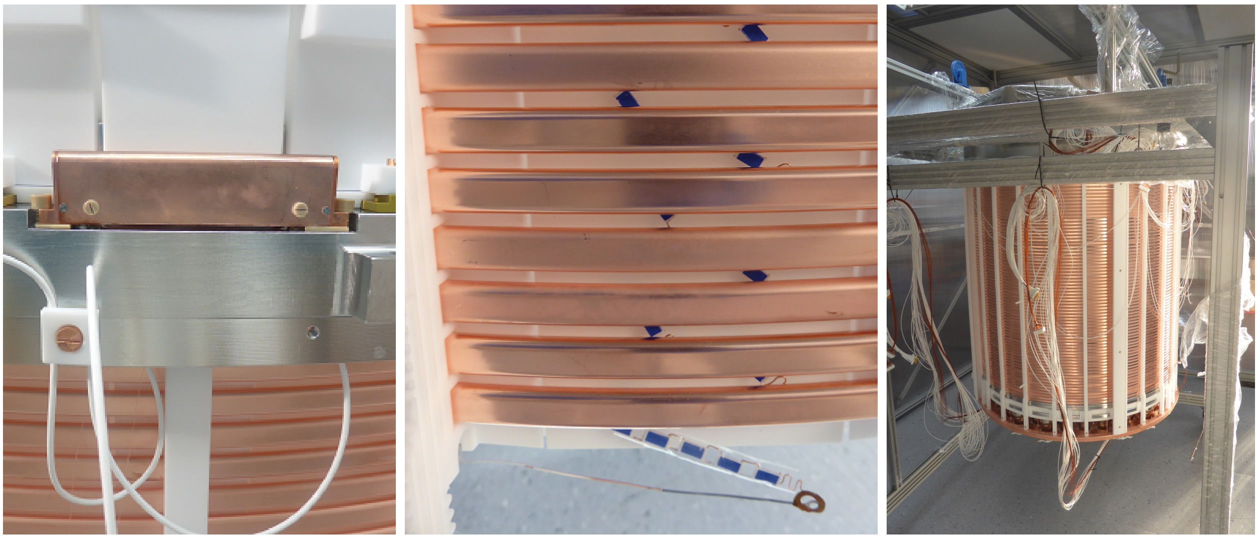

Figure 3.21: Left: The short levelmeter assembled to the top TPC ring. Centre: The resistor chain contact to the cathode. Right: The assembled TPC in the aboveground clean room attached to the support structure.

of the bell was left cable-free, and the optical fibres were fixed there. The inlet of the diving bell was connected to the gas system in order to pressurise it during operation, and the outlet was connected with a levelling mechanism to an exhaust pipe on the side of the diving bell, which can be positioned with a motion feedthrough. This configuration makes it possible to set the liquid xenon level precisely to 2.5 mm above the gate and below the anode. In Figure 3.22 (left) the connections and piping on top of the diving bell are shown.

In the next steps, six 1-inch PMTs were installed to the top TPC ring for diagnostic purpose of the TPC during calibration and normal operation. The positions of the PMTs were chosen to be at the same side as the external calibration belts for the radioactive sources. Therefore, three 1-inch PMTs were grouped together in order to cover both sides of the belt system. In Figure 3.22 (centre) one side of the three 1-inch PMTs is shown. The PMTs were attached with a copper structure to the top TPC ring and insulated with a PTFE sheet to the field shaping rings. Optical fibres were routed to each sector of 1-inch PMTs for calibration purposes. After the installation of the 'diagnostic' PMTs the contact of the cathode was established. A stainless steel rod was screwed into the cathode with a set screw and inserted into the spring contact of the high voltage feedthrough. The cathode contact was insulated from the surrounding with several PTFE tubes.

In the last step before closing the cryostat, the lower part of the TPC was covered with a 1 mm thick PTFE sheet. The purpose of the sheet was to serve as a physical barrier between the grounded cryostat and the field shaping rings so that electrons can not reach the cryostat in case of a discharge. After this operation, the TPC was attached to the cryostat dome by replacing the stainless steel rods with shorter silver plated stainless steel spacers. The diving bell was screwed to the spacers with its wings. In Figure 3.22 (right), the TPC is shown in its final position before closing the cryostat.

With the successful construction of the TPC, the commissioning phase of the detector started. We found during the commissioning phase that the 1-inch 'diagnostic' PMTs were introducing electronic noise inside the TPC PMTs. Therefore, the 1-inch 'diagnostic' PMTs were not used during data acquisition and were turned off. In addition, the maximum achieved cathode voltage was −12 kV but lower than the TPC design of −100 kV. Furthermore, the gate was short-circuited to the ground, which did not affect the data acquisition. Once the commissioning phase was finished, the science data acquisition process started, which will be described in the next chapter.

Figure 3.22: Left: The TPC in an intermediate position in order to perform all of the connections on top of the diving bell. Centre: Three out of the six installed 'diagnostic' PMTs. Right: The TPC in the final position before the cryostat closing with the attached PTFE high voltage sheet.

"An experiment is a question which science poses to Nature and a measurement is the recording of Nature's answer."

Max Planck

CHAPTER 4

Dark Matter Search with XENON1T

The XENON1T detector was filled with ∼3.2 liquid xenon at the beginning 2016, and all of the subsystems were commissioned in the next several months. The first science run (SR0) with 32.1 live days of data was performed between November 22nd 2016 and January 18th 2017, until a 5.7 magnitude earthquake temporarily interrupted the detector operations. After two weeks of maintenance, the second science run (SR1) with 246.7 live days of data was performed from February 2nd 2017 until February 8th, 2018. After SR1, until today, the detector has been in operation and collecting data. The conditions of the detector during SR1 were the same as in SR0, except the cathode voltage, which was lowered from $-12\,\mathrm{kV}$ in SR0 to $-8\,\mathrm{kV}$ in SR1. The fiducial mass was $(1.30 \pm 0.01)\,\mathrm{t}$, which corresponds to a total exposure of a one tonne×year of science data.

In section 4.1 we report the TPC detector conditions during the science runs and we show a detailed calculation of the TPC target mass while taking into account the cryogenic measurement results from the previous chapter. It is followed by section 4.2, which summarises the light detector sensors calibration and performance during SR0 and SR1. Section 4.3 describes the performed electrostatic field simulations and corrections in order to extract important detector parameters, such as the drift velocity of the electrons in liquid xenon. The chapter will be concluded with the results on the spin-independent WIMP-nucleon interaction cross section of the combined science runs, which includes two developed data quality cuts for the dark matter search.

4.1 Detector Conditions and Target Mass Calculation

Throughout the entire SR0 and SR1 runs the detector conditions maintained stably. The pressure in the gaseous xenon was at 1.94 bar, and the temperature of the liquid xenon was at $-96\,^{\circ}\mathrm{C}$. The pressure and temperature fluctuations were less than 0.02 % from the average. The liquid xenon level was placed between the gate and anode electrodes, 2.5 mm above the gate. The liquid xenon level varied within 2 % due to the readout systematics of the short levelmeters. 35 out of the 248 PMTs were excluded in the analysis of the SR0 data, and 36 PMTs were excluded in the SR1 data, due to low single photoelectron (SPE) acceptance, instabilities, vacuum leaks or light emission, which will be further discussed in section 4.2. The electrode voltages in SR0 and SR1 remained stable

Bottom Screening Mesh [kV]	Cathode [kV]	Gate [kV]	Anode [kV]	Top Screening Mesh [kV]
−1.55	−12	0	4	−1.55
−2.5	−8	0	4	−1.55

Table 4.1: Electrode voltages in SR0 (first row) and SR1 (second row).

and are given in Table 4.1. A cathode voltage of -12 kV was achieved in SR0, which is significantly lower than the design value of -100 kV, due to single electron and light emission from the cathode at higher voltages. On January 18th 2017, a 5.7 magnitude earthquake temporarily interrupted the detector operations. At a cathode voltage of -12 kV, light emission was observed around the centre of the bottom PMT array, which is shown in Figure 4.1 (left). The light emission did not correspond to a single electron emission from the cathode, due to the unchanged measured single electron rate. The light emission decreased with decreasing cathode voltage and increasing bottom screening mesh voltage. Therefore, this light emission from the cathode was correlated to the produced electric field between the cathode and the bottom screening mesh. The detector was recovered at a cathode voltage of -8 kV and a bottom screening mesh voltage of -2.5 kV without showing any light emission from the cathode.

Several internal and external radioactive sources were deployed to calibrate the detector during the two science runs. The gaseous xenon from the detector can be flushed through a ^{83}Rb source to introduce $^{83\mathrm{m}}$Kr into the TPC. It provides a homogeneous event distribution inside the TPC with 9.4 keV and 32.1 keV conversion electrons, which are used for the free electron lifetime measurement and various spatial corrections. The gaseous xenon can be also flushed through a ^{228}Th source, which emanates the noble gas isotope ^{220}Rn. The ^{220}Rn decays through several α and β decays to the ground state, which are used for the detector calibration. In particular, the β decay of ^{212}Pb is used for the calibration of the ER detector response. A ^{241}AmBe source can be deployed with a calibration system from the top of the water tank next to the cryostat and is used for the calibration of the NR response. A Deuterium-Deuterium (DD) fusion neutron generator (NG) can be placed next to the cryostat in the water tank, which creates neutrons with energies of around 2.2 MeV and 2.7 MeV and is also used for the calibration of the NR response [168].

The total mass of liquid xenon inside the TPC was calculated using the results obtained in section 3.5. It was measured that the PTFE of the support pillars contract $(1.40 \pm 0.02)\,\%$ at $-96\,°$C. The measured support pillar length after production showed an average measured length of (1086 ± 0.2) mm at $22\,°$C, of which (966 ± 0.2) mm supports the TPC from the cathode wires to the top of the pillar. This yields a contracted length of (953.5 ± 2.1) mm. The total TPC drift length is the distance between the cathode and the gate, which is given by the length of all parts

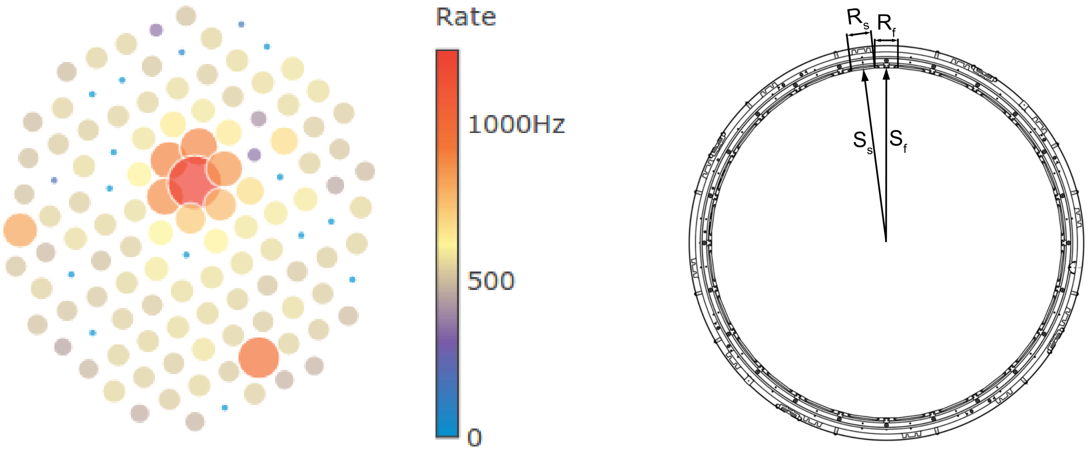

Figure 4.1: Left: PMT rates in the bottom PMT array after the earthquake on January 18th 2017. Light emission is observable around the centre of the bottom PMT array, which is correlated with the electric field between the cathode and the bottom screening mesh. Right: Sketch of the radial distance of the fixed (S_f) and sliding (S_s) PTFE reflector to the centre of the XENON1T TPC.

after the contraction from the technical drawings of the TPC. The XENON1T TPC drift length was calculated to be:

$$L_{\text{drift}} = (969.5 \pm 2.1)\,\text{mm}. \tag{4.1}$$

The radius to the centre of the fixed PTFE reflectors (R_{f}) is (47.86 ± 0.1) cm and the radius to the centre of the sliding PTFE reflectors (R_{s}) is (47.87 ± 0.1) cm, where the error originates from the tolerances of the top stainless steel ring. The width of the sliding (S_{s}) and fixed (S_{f}) reflector exposed to the field cage is (63.5 ± 0.2) mm and (62 ± 0.2) mm, respectively. A sketch of the TPC radial distances is shown in Figure 4.1 (right). The total target mass can be calculated with the volume enclosed by the PTFE panels. The ground surface of the TPC is therefore calculated by two types of triangles, which is given by the following expression:

$$A_{\text{TPC}} = 0.5 \times 24 \times (S_f \times R_f + S_s \times R_s) = (7208.5 \pm 19.43)\,\text{cm}^2. \tag{4.2}$$

The XENON1T target mass is calculated between the cathode wires and the liquid xenon level enclosed by the PTFE reflector panels. The XENON1T target mass was calculated to be:

$$M_{\text{target}} = \rho_{\text{LXe}} \times A_{\text{TPC}} \times (L_{\text{drift}} + d_{\text{gate-anode}}) = (2005.31 \pm 7.53)\,\text{kg}, \tag{4.3}$$

where ρ_{LXe} is the liquid xenon density $(2.862 \pm 0.004)\,\text{g/cm}^3$, taken from NIST Chemistry WebBook [81] at 1.94 bar and a temperature of $-96\,^\circ$C, and $d_{\text{gate-anode}}$ is the distance from the gate to the liquid xenon level ($d_{\text{gate-anode}} = (2.5 \pm 0.05)$ mm).

In the next section, the calibration and performance of the light detector sensors for both science runs will be discussed.

4.2 Light Detector Sensor Calibration and Performance

The PMT response of the XENON1T TPC was closely monitored in order to guarantee a stable detector response. The mixture of the residual gas inside the PMT can be monitored by its afterpulse rates, as described in section 3.4. PMTs can open microscopic vacuum leaks during the operation

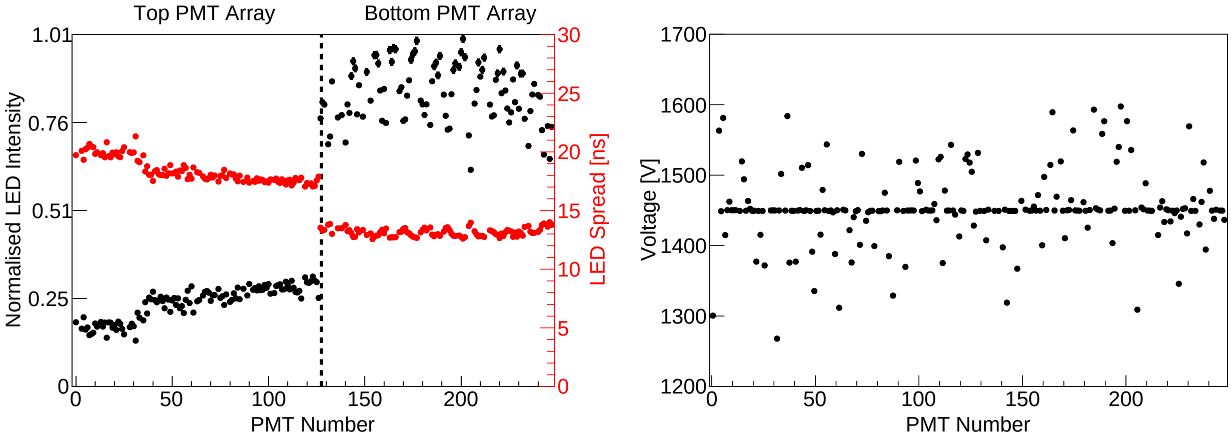

Figure 4.2: Left: Normalised LED intensities for the XENON1T TPC PMTs (black points). The 1σ spread of the LED light is indicated with red points for each PMT. The light intensities between the top and bottom array vary due to multiple reflections at the liquid/gas xenon boundary. Therefore, the spread of the LED light differs as well. Right: Applied voltages for each XENON1T TPC PMT at the end of SR1. The mean operational voltage was 1454 V with an rms of 51 V.

in liquid xenon, due to the thermal stress and pressure, which can be identified with afterpulses produced by xenon molecules. A vacuum leak will degenerate the PMT vacuum up to the point where the PMT begins to emit light and fails, due to an increased field emission probability. In order to understand the detector response, the afterpulses of the PMTs needed to be monitored. Furthermore, instabilities in the gain affect many parameters, such as the light/charge yield and the position reconstruction. Therefore, dedicated gain and afterpulse calibrations were performed at least once a week during SR0 and SR1. For both calibrations, the PMTs were illuminated with blue light produced by an LED ($\lambda \sim 470\,\mathrm{nm}$). The light was guided through optical fibres inside the liquid xenon phase of the TPC. The exact positions of the optical fibres inside the TPC can be found in [167].

In order to illuminate the top PMT (PMT numbers: 0–127) and the bottom PMT array (PMT numbers: 128–248) with a comparable number of photons, three different LED settings were necessary. The normalised detected LED intensities in the top and bottom PMT array can be found in Figure 4.2 (left). Different light intensities in the top and bottom PMT array are observable for one LED setting. This is because the optical fibres are pointing into the liquid xenon phase, and the photons are reflected at the liquid/gas xenon boundary before reaching the top PMT array. The outer ring of the top PMT array (PMT 0–25) is slightly covered by the PTFE reflector as shown in Figure 3.19 (right). Therefore, the LED light intensity is further reduced for those PMTs. The multiple reflections of the LED light before reaching the top array is also observable in the standard deviation (σ) of the LED pulse in the PMTs. The standard deviation of the LED pulse is increased for the top PMT array in comparison to the bottom PMT array.

In total, 35 PMTs (15 top and 20 bottom) were excluded from the analysis in SR0 and 36 in SR1 (15 top and 20 bottom). These PMTs were mainly not operable at a sufficient voltage, due to vacuum leaks and the single photoelectron efficiency was too low to be considered in the analysis. The voltages of the operable PMTs with a photoelectron efficiency above 80 % at the end of SR1 are shown in Figure 4.2 (right). The mean operating voltage was 1454 V with an rms of 51 V. The voltage fluctuations of the PMTs were less than 1 V during both science runs. This value is negligibly small to have any significant effect on the gain (described by equation 3.2).

In the next section, the gain and afterpulse calibration will be discussed.

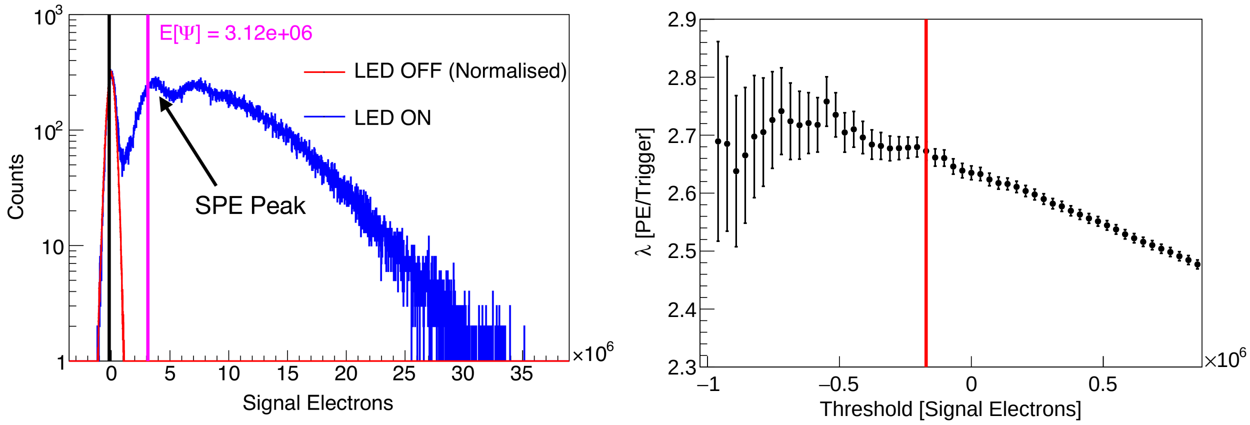

Figure 4.3: Left: Charge spectrum produced by the LED (blue) and in the absence of the LED (red) of PMT 141. The events below the calculated threshold (black line) are used to calculate A_s and A_b. The magenta line indicates the obtained gain, which is slightly lower than the SPE peak. Right: The occupancy λ for different thresholds of PMT 141. The threshold was chosen, where the occupancy increases less than 2 % with a statistical error smaller than 1 % (red line).

4.2.1 Gain and Afterpulse Analysis

As shown in section 3.4, the appearance of the under amplified secondary electrons decreases the SPE response of the PMT by 10–20 %. This is important to be taken into an account in order not to underestimate the number of detected photoelectrons. Therefore, for the XENON1T PMT gain calibration, a new method has been developed which does not need any assumption of the shape of the SPE spectrum and extracts the gain values statistically [162]. For each PMT two datasets are acquired: a dataset where the LED is on, at the level of single photon emission and a second dataset where the LED is off. The gain ($E\left[\Psi\right]$) of each PMT can be then calculated by the following formula:

$$E\left[\Psi\right] = \frac{E\left[T\right] - E\left[B\right]}{\lambda}, \tag{4.4}$$

where λ is the occupancy, which is the number of produced photoelectrons in each trigger, $E\left[T\right]$ is the mean value of the charge distribution when the LED is on, and $E\left[B\right]$ is the mean value of the charge distribution when the LED is off. The LED was set for every PMT to an occupancy of ~ 3 PE per trigger. The charge distributions are obtained by integrating the waveforms in a fixed time window. The integration window was chosen to be sufficiently large to include all the LED signals, but sufficiently small to reduce the noise effects. Therefore, the integration window was optimised for every PMT and fixed to a constant value, where the term $E\left[T\right] - E\left[B\right]$ was constant with increasing integration window. As discussed in section 3.4, the number of produced photoelectrons by the LED follows a Poisson distribution (L(k)). Therefore, the occupancy λ is directly related to the probability of producing zero-PE events by the LED:

$$L(0) = \frac{\lambda^0 e^{-\lambda}}{0!}, \tag{4.5}$$

which leads to:

$$\lambda = -\ln\left(\frac{N_0}{N}\right), \tag{4.6}$$

where N_0 is the number of zero-PE events produced by the LED, and N is the total number of acquired events.

N_0 can be determined with the help of the acquired charge distribution in the absence of the LED light. In a first step, the number of zero-PE events which fall below a fixed threshold produced by

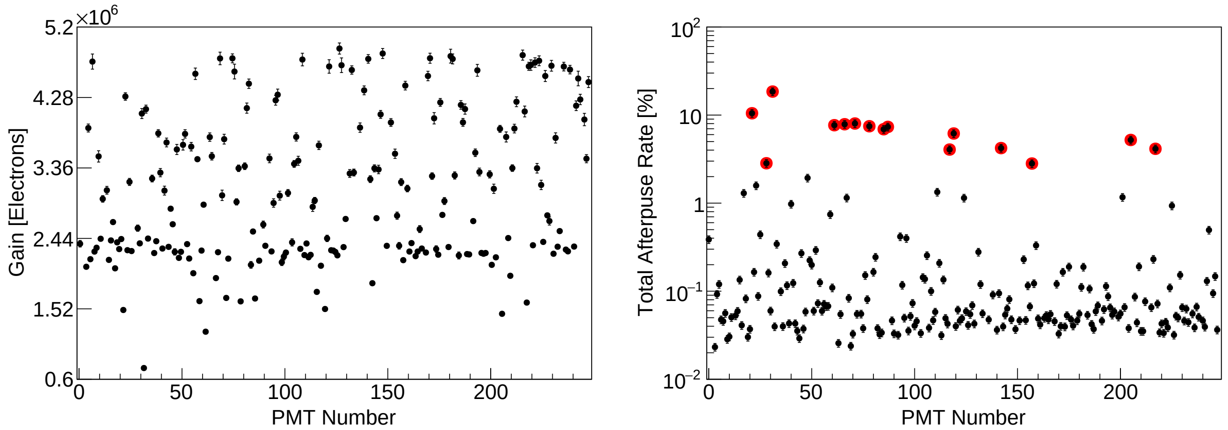

Figure 4.4: Left: The estimated gain of the XENON1T PMTs at the end of SR1. Right: The total afterpulse rate of the XENON1T PMTs at the end of SR1 (black points). PMTs, which showed a flashing behaviour during the science runs are marked with red.

the LED (A_s) is calculated. The threshold is required to be at a low value so that the contribution from under-amplified photoelectrons with a small charge is removed. In a second step, the number of zero-PE events below the same threshold in the absence of the LED (A_b) are calculated. The value A_s can be then corrected for the number of zero-PE triggers that fall above the threshold with the following formula:

$$N_0 = A_s \frac{A_b}{N}. \tag{4.7}$$

The threshold needs to be chosen in a way that only zero-PE triggers fall below the threshold. Therefore, λ as a function of threshold for every PMT was investigated, and the threshold was set where λ increases less than 2 % with decreasing threshold with a statistical error smaller than 1 %. Figure 4.3 (left) shows the charge distribution of PMT 141 induced by the LED (blue) and in the absence of the LED light (red). The threshold, in order to calculate A_s and A_b, is indicated as a black line and was optimised as shown in Figure 4.3 (right). The gain was calculated with equation 4.4. In XENON1T the mean gain of every PMT at one LED calibration was estimated by varying the fixed integration window between (0–100) ns. The mean statistical error was calculated as described in [162] and the rms of the gain was used for the systematic error uncertainty. In Figure 4.4 (left) the estimated gain at the end of SR1 for each PMT is shown. The mean gain of all PMTs at the end of SR1 is 3.06×10^6 with an rms of 0.96×10^6. Furthermore, the gain as a function of high voltage was measured for all of the PMTs and fitted with equation 3.2. The mean parameter k, which depends on the dynode structure and material, was measured to be (0.67 ± 0.01).

In order to monitor the residual gas mixture of the XENON1T TPC PMTs, the bottom PMT array was regularly illuminated with a mean LED intensity of 61.0 PE and rms of 5.9 PE. Due to the multiple reflections at the gaseous/liquid xenon boundary, the top PMT array was illuminated with a mean LED intensity of 17.4 PE and an rms of 3.4 PE. The generated photoelectrons by the LED inside the PMT ionise the residual gas and a delay time spectrum for each PMT can be measured as shown in Figure 4.5 (left). A (1–2) PE background is present after the LED illumination, which originates from dark count events and elastic back-scatters of the electrons from the dynodes. In

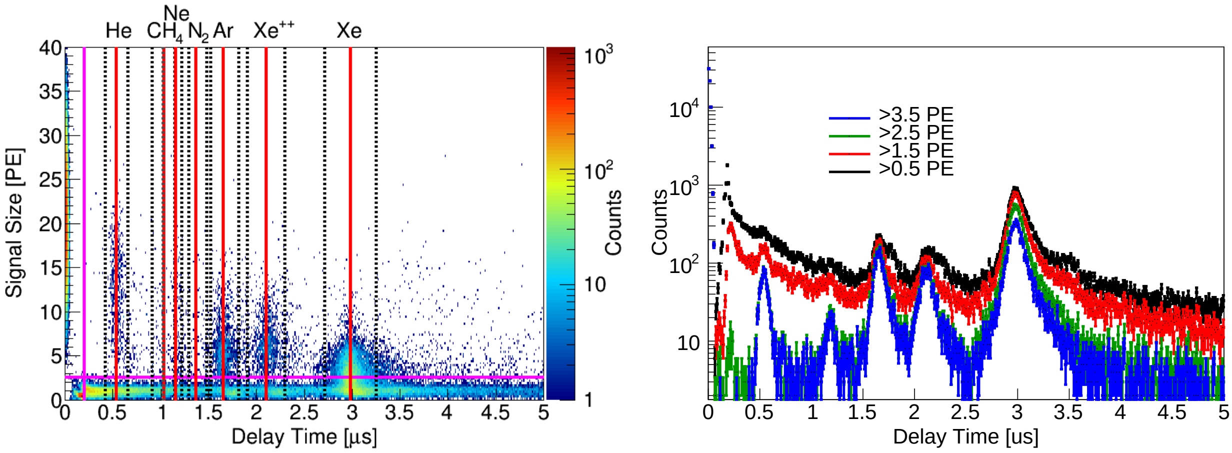

Figure 4.5: Left: Signal size as a function of the delay time of PMT 93. The magenta lines indicate the threshold of the signal size and delay time. The solid red lines indicate the theoretical value for the appearance of an afterpulse and the dashed black lines show the 3σ spread of the afterpulse delay time. The PMT has a vacuum leak due to the appearance of afterpulse events at the ion delay time of xenon. Right: The delay time spectrum of PMT 93 for different signal size thresholds. For higher thresholds, the (1–2) PE background noise can be reduced, and therefore, the sensitivity to the ion afterpulses increased.

Ion	He^+	CH_4^+/N^+	Ne^+/Ar^{++}	N_2	Ar^+	Xe^{++}	Xe^+
Mean [PE]	12.97	7.43	7.18	6.71	6.56	6.54	8.15
rms [PE]	1.25	1.35	1.45	0.86	0.61	0.63	0.90

Table 4.2: The mean afterpulse signal size of all XENON1T PMTs.

addition, several populations above 2 PE can be identified at different delay times, which can be correlated to the residual molecules inside the PMT. The determination of the delay times for the different ions will be discussed in section 5.2. The abundance of xenon in the atmosphere during the PMT production process is negligibly small. Therefore, a PMT is considered to have a vacuum leak due to the appearance of afterpulse events at the ion delay time of xenon. In order to achieve a better sensitivity to the ion afterpulse events, afterpulses above a signal size of 2.5 PE are considered in the analysis, as shown in Figure 4.5 (right), in order to suppress the (1–2) PE background. Afterpulses produced by ions are several photoelectrons large, due to the large kinetic energy of the ions when striking the photocathode. In Table 4.2 the observed gas residual and the mean afterpulse signal size of all XENON1T PMTs at liquid xenon temperature ($-96\,C^\circ$) are shown.

In order to quantify the vacuum quality, the total afterpulse rate of the PMT is defined with the following formula:

$$AP_{\text{total}} = \frac{N_{\text{AP}}}{\mu_{\text{LED}} \times N_{\text{Trigger}}} \times 100, \tag{4.8}$$

where N_{AP} is the number of events between $0.2\,\mu$s and $5\,\mu$s after the LED pulse above 2.5 PE (magenta lines in Figure 4.5, left), μ_{LED} is the mean number of photoelectrons produced by the LED, and N_{Trigger} is the number of LED pulses above 3 PE. The total afterpulse rate defined in equation 4.8 was measured to be independent of the initial mean LED pulse between $\sim$(1–300) PE. For larger pulses a non-linearity in the total afterpulse rate can be observed, and therefore, the initial LED pulse for XENON1T was chosen to be 61.0 PE in the bottom and 17.4 PE in the top PMT array. A dataset of $\sim 10^5$ events was taken at least once a week in order to calculate the afterpulse rate. In Figure 4.4 (right) the total afterpulse rate at the end of SR1 for each PMT is shown. The

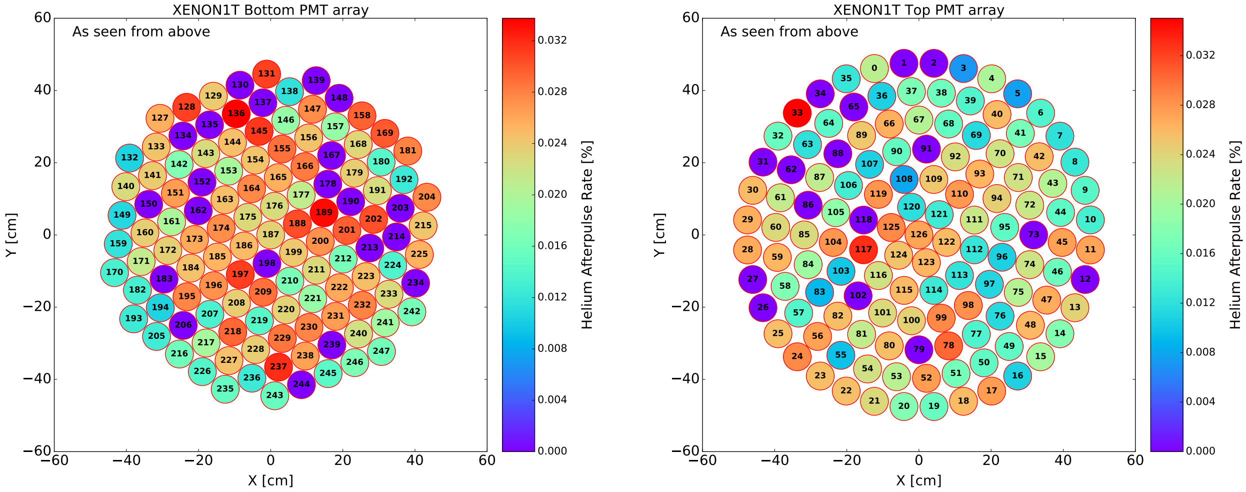

Figure 4.6: The mean helium afterpulse rate in the bottom (left) and in the top (right) PMT array. The helium afterpulse rate of each PMT is stable through both science runs, which confirms the precise calculation of the ion afterpulse rate. PMTs with a zero value are turned off.

mean total afterpulse rate is 0.63 % with an rms of 2.02 %. Some of the PMTs show a high total afterpulse rate due to a large vacuum leak.

Furthermore, the precise residual gas mixture in a PMT can be determined with the per ion afterpulse rate, which is defined with the following formula:

$$AP_{\text{ion}} = \frac{N_{\text{ion}}}{\mu_{\text{LED}} \times N_{\text{Trigger}}} \times 100, \tag{4.9}$$

where N_{ion} is the number of events in a 3σ time window at the ion afterpulse delay time above 2.5 PE, μ_{LED} is the mean number of photoelectrons produced by the LED, and N_{Trigger} is the number of valid LED pulses above 3 PE. Helium is present in all of the XENON1T PMTs, and the afterpulse rate stays stable within 1 % across both science runs, which validates this analysis procedure. In Figure 4.6 the mean helium afterpulse rate in the top and bottom PMT array is shown. Nitrogen, argon and xenon molecules are present in some of the PMTs. The mean ion afterpulse rate of each PMT at the end of the SR1 can be found in Appendix C.

In the next section, the PMT performance during the science runs and the vacuum leak related implications will be discussed.

4.2.2 PMT Performance

The PMT gain and afterpulse rate was monitored at least once a week in order to correctly model the gain as a function of time and to measure the vacuum quality of the PMTs. 187 out of the 212 active PMTs showed a stable gain with an uncertainty on their stability of 1–2 % throughout SR0 and SR1. 25 PMTs showed a gain decrease, which was precisely modelled with the regularly performed gain calibrations. The gain decrease was correlated to PMTs which showed a total afterpulse rate larger than ∼1 %. A large amount of residual gas inside the PMT damages the dynodes and therefore decreases the secondary emission coefficient, and hence the gain. In Figure 4.7 (left) the gain evolution of some of the XENON1T PMTs are shown. In this subset of PMTs, PMT 11 shows a gain decrease with time, whereas the other PMTs stay stable throughout SR0 and SR1.

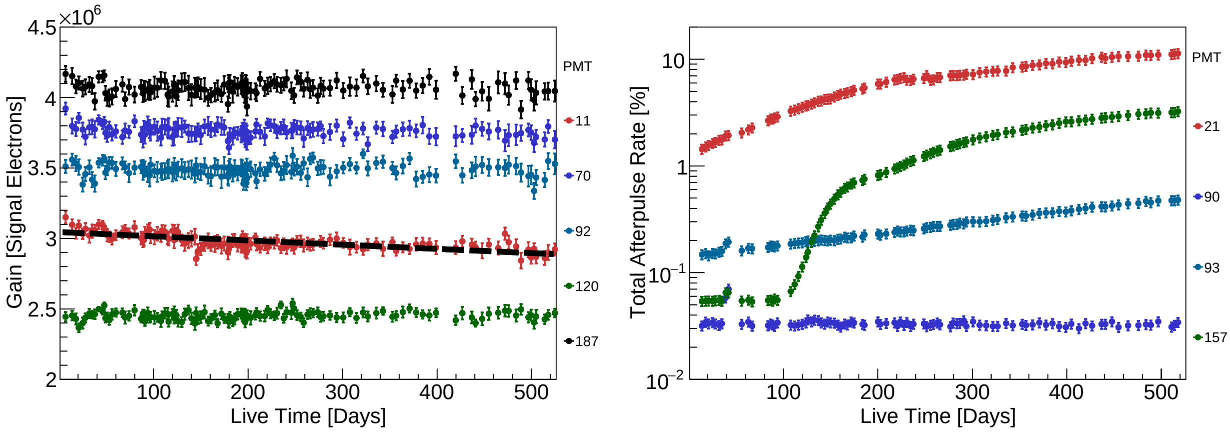

Figure 4.7: Left: The gain evolution of some of the XENON1T PMTs. The PMT gain is stable within 1–2 %. PMT 11 shows a gain decrease over time as indicated with the black dashed line. Right: The total afterpulse rate evolution of some of the XENON1T PMTs. PMTs with a vacuum leak (PMT 21 and PMT 93) show an increase in the total afterpulse rate as a function of time with different slopes. PMT 157 opened a vacuum leak after 100 days of operation. PMT 90 did not develop a leak, and the total afterpulse rate stays constant with time.

A PMT was considered to have a vacuum leak after the xenon afterpulse rate was above the sensitivity of ~0.01 %. In total 67 out of 248 PMTs showed a vacuum leak during the detector runtime. 33 leaky PMTs are located in the top and 34 in the bottom PMT array, indicating that the leak opening appears with the same frequency in the gaseous and in the liquid xenon phase. Most of the PMTs with vacuum leak showed an increase in the total afterpulse rate after initial filling the TPC with xenon. A small fraction of PMTs opened a vacuum leak during the detector operation, which was identified by a sudden increase of the total afterpulse rate over time. The leak rate of the different leaky PMTs varied between ~(0.01–0.5) % per week. In Appendix C the averaged leak rates of all PMTs can be found. In Figure 4.7 (right) the total afterpulse evolution of some of the XENON1T PMTs is shown.

The ions inside a PMT damage the dynodes and this effect is visible as a gain decrease over time. The total afterpulse rate is proportional to the number of ions inside the PMT. That implies that PMTs with a vacuum leak have a constant increase of ions and therefore show a substantial gain decrease over time. Figure 4.8 (left) shows the gain and total afterpulse rate of PMT 87 over time. Due to the vacuum leak of this PMT, its total afterpulse rate increases. At the same time, the gain decreases continuously over time. Once the total afterpulse rate reaches a value of ~4 %, the gain starts to drop significantly due to the decreased mean free path of the secondary electrons. Furthermore, PMTs with a total afterpulse rate above ~4 % become unstable, which is observable by frequent strong light emission. This effect can be explained by the spontaneous discharge of accumulated ions at the ceramic stem inside the PMT and is called *flash*. A flash is identified by an increase of the observed pulses per second (pulse rate) of a flashing PMT over several orders of magnitude. Figure 4.8 (right) shows a flash of a PMT with a total afterpulse rate of ~4 %. The pulse rate of the PMT suddenly increases over several orders of magnitude in less than 1 s. The pulse rate decreases afterwards over several minutes back to the same rate as before the flash. The flash is observable in all the other PMT channels, which can be explained by the emission of a large amount of light of the flashing PMT. Figure 4.4 (right) shows the correlation between the total afterpulse rate and flashes. PMTs with a total afterpulse rate above ~4 % show frequent flashes.

Besides the appearance of flashes, leaky PMTs have a decrease of their vacuum. That implies that the breakdown voltage to produce small field emission discharges increases (Paschen's law [169]).

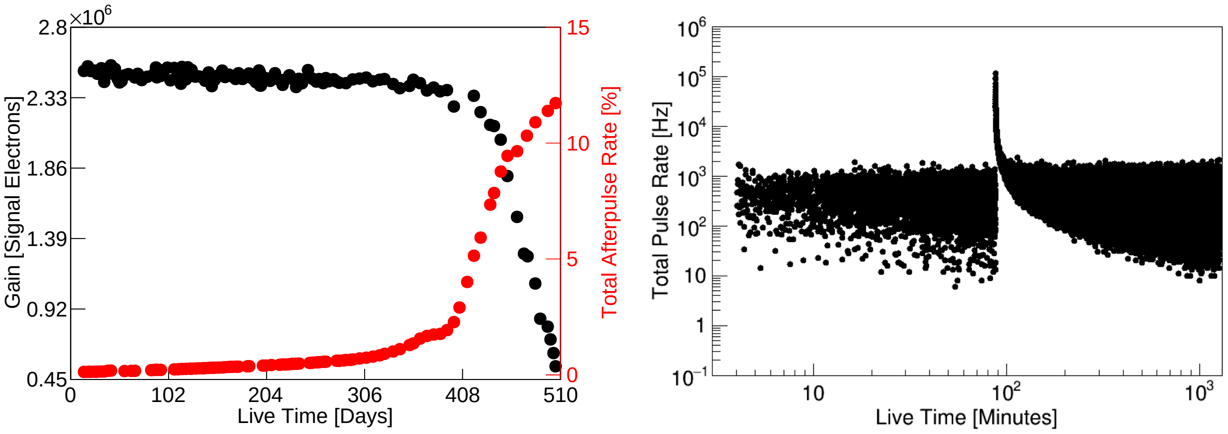

Figure 4.8: Left: The gain (black points) and total afterpulse rate (red points) of PMT 87 as a function of time. The PMT has a vacuum leak, which is visible in the increase of the total afterpulse rate. The ions damage the dynodes and hence decrease the gain of the PMT over time. Right: The pulse rate of PMT 87 as a function of time. The pulse rate increases suddenly over several order of magnitudes, due to strong light emission (flash).

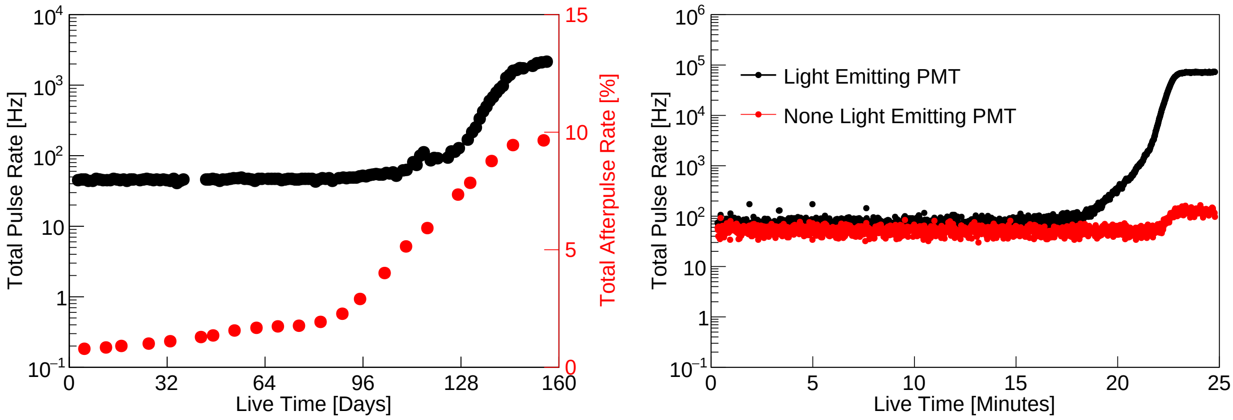

Figure 4.9: Left: The pulse rate (black points) and the total afterpulse rate (red points) of PMT 87 as a function of time. The zero point of the x-axis represents 300 days of the PMT in operation. The pulse rate increases with increasing total afterpulse rate, due to the increased probability of field emission discharges. Right: The pulse rate of PMT 150 (black points) and PMT 42 (red points) during one run. The pulse rate of PMT 150 increases towards the end of the run due to micro-light emission. The photons produced by PMT 150 are observed in PMT 42 as well, and therefore, the pulse rate of PMT 42 increases.

The high local electric fields inside the PMT can produce field emission discharges, and their corresponding emission of photons can reach the photocathode, which is called *micro-light emission*. Micro-light emission is strongly bias voltage dependent and can be also present in PMTs without leaks, due to the use of non-smooth surfaces during the PMT production. PMTs with a total afterpulse rate above $\sim 4\,\%$ also start to show an increased probability for micro-light emission. Figure 4.9 (left) shows the pulse rate and the total afterpulse rate of PMT 87. The total afterpulse rate increases over time due to a vacuum leak. The pulse rate of the PMT is stable at the beginning at around 300 Hz and increases with increasing total afterpulse rate due to the increased probability of micro-light emission. A fraction of the light produced by the PMT leaves the PMT and can be recorded in different PMTs of the TPC. Figure 4.9 (right) shows the pulses rate of PMT 150 and PMT 42. The pulse rate of PMT 150 increases due to micro-light emission and is detected by PMT 42, which also shows an increase in the pulse rate. The effect of micro-light emission can be reduced by sequentially lowering the operating voltage. This affects the gain and thus the SPE acceptance.

In addition, micro-light emission can produce an accidental coincidence event, which is not distinguishable from a real event. To avoid this, 36 PMTs were switched off due to strong micro-light emission or a too low SPE acceptance ($< 50\,\%$). PMTs, which showed flashes were kept on and the flashing periods were rejected in the later analysis.

Science Run	Turned off PMTs	Turned on PMTs	PMTs with a vacuum leak (on and off)
SR0	35	213	56
SR1	36	212	66

Table 4.3: PMT condition during data acquisition in SR0 (first row) and SR1 (second row).

4.2.3 PMT Database

A database was developed to store the results of the regularly performed gain and afterpulse calibrations, as well as to store all PMT related information, such as: data sheets, results of performed measurements before the installation, current pulse rate, current status, event history during operation, cabling, γ-spectrometry results and the timestamps of the science runs. The database is a MySQL [170] database located on a server at LNGS. It consists of several tables, which store the above-mentioned parameters.

In order to access the parameters of the database in a convenient way, a web interface was developed. The webpage is served by Apache and Hypertext Preprocessor (PHP) is used to access the database, create plots and upload data. JavaScript is used for client-side functionality, plots/graphs and AJAX (asynchronous JavaScript and Extensible Markup Language (XML)) is used to send and retrieve data to and from the server asynchronously. The calibration files can be inserted into the database through the web interface. The afterpulse spectra, gain spectra and the raw-data (text files) are uploaded to the disk of the server and the contents from the text files are inserted into the database. The database offers various possibilities for data visualisation. The data of all PMTs can be visualised for a specific timestamp with the corresponding spectra using JPgraph, and the time evolution with an additional animated picture can be displayed using highcharts. PMT events like trip, flash and others can be inserted by the client into the database. This is done via filling an online form, after which an email notification is sent automatically to the addresses specified in the mailing list.

In Figure 4.10, two screenshots of the database are shown. The web page has eight tabs. The *home* tab welcomes the client and contains a collection of dedicated PMT publications. Under the *monitoring and calibration* tab, the information of the regular PMT calibrations can be found. The client can visualise the calibration data stored in the database, as well as upload new data. Under the *PMT status* tab, the client can add events (e.g. flash, trips or others) to the PMT database. Here, the client can also find information about the status (on/off) of the PMTs inside the TPC and can change it. This action will send a notification to the addresses defined in the mailing list. The PMT status can be visualised with the PMT map. The remaining tabs contain the PMT results of performed measurements before the installation, γ-spectrometry results, data sheets and the cabling of the PMTs.

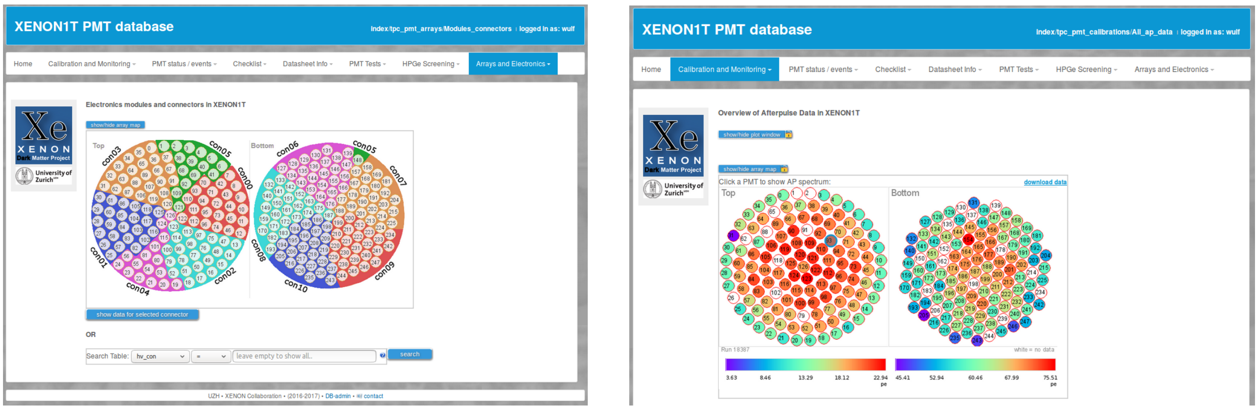

Figure 4.10: Left: Example screenshot of the web page of the XENON1T PMT database. This example shows the cabling of the top and bottom PMT array under the tab *array and electronics*. Right: Example screenshot of the web page of the XENON1T PMT database. This example shows the results of the afterpulse calibration of a specific time stamp under the tab *calibration and monitoring*. One can click on the PMTs in the map to extract further information.

4.3 Electrostatic Field Simulation

The electric field inside the XENON1T TPC is of great importance for the S1 and S2 signal model and various other analyse. Therefore, the XENON1T TPC was implemented in great details into the electric field simulation framework, described in chapter 2, based on the CAD drawings and final measurements during the TPC installation. The implemented components with their corresponding voltage and the number of discretised sub-elements are listed in Appendix D.

In Figure 4.11 (left) the implemented geometry is shown. The hexagonal meshes were considered as 2D surfaces in order to reduce the number of sub-elements by a factor of 10, and therefore to decrease the computation time. In Figure 4.11 (right) the implemented hexagonal anode mesh is shown. The liquid and gaseous xenon interphase was simulated as a charged dielectric boundary at the half distance between the anode and gate electrode. The (0,0,0) reference point is on the midpoint of the gate electrode. The field simulations were performed on the GPU cluster VESTA at the University of Zurich, which houses more than 16 Nvidia GPU cards. The total number of discretised sub-elements was 3 299 251, which resulted in a computation time of $\sim$4 weeks until the relative error of each sub-element was below 10^{-8}. For each science run a separate simulation was performed due to the fact that the cathode voltage was lowered from -12 kV in SR0 to -8 kV in SR1. The simulation steps and analysis procedure was the same for both science runs. In this section, the simulations results for SR1 will be discussed and the results for SR0 are presented in Appendix D.

4.3.1 Drift and Extraction Field

The drift and extraction field for both science runs were calculated with the developed electrostatic field simulation framework described in chapter 2. The absolute electric field was calculated with a spacing of 0.1 cm inside the XENON1T TPC. The resulting azimuthal averaged absolute electric field map in SR1 is shown in Figure 4.12 (left). The drift field is defined as the averaged absolute electric field inside the fiducial volume, which is indicated with the magenta lines in the Figure. In SR0 and SR1 the same 1.3 t fiducial volume was used in the final analysis. The drift field is homogeneous inside the fiducial volume. Close to the cathode holder (bottom right) and gate holder

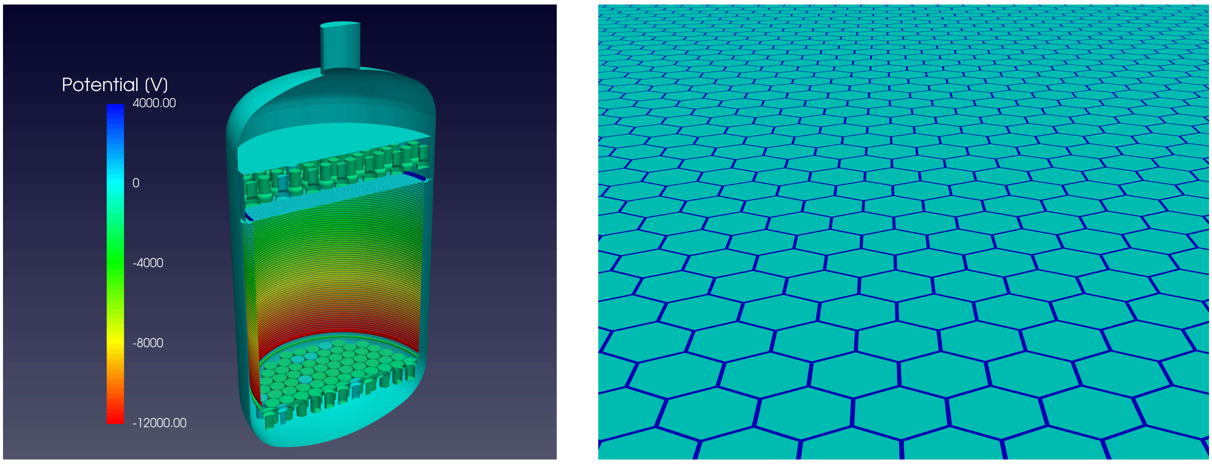

Figure 4.11: Left: The implemented XENON1T geometry into the developed simulation framework. The applied potential configuration is indicated in different colours. The potentials on every electrode can be found in Appendix D. Right: A zoom-in into the gate electrode, which is a hexagonal mesh. The hexagonal electrodes were implemented without any thickness in order to save sub-elements and to decrease the computation time.

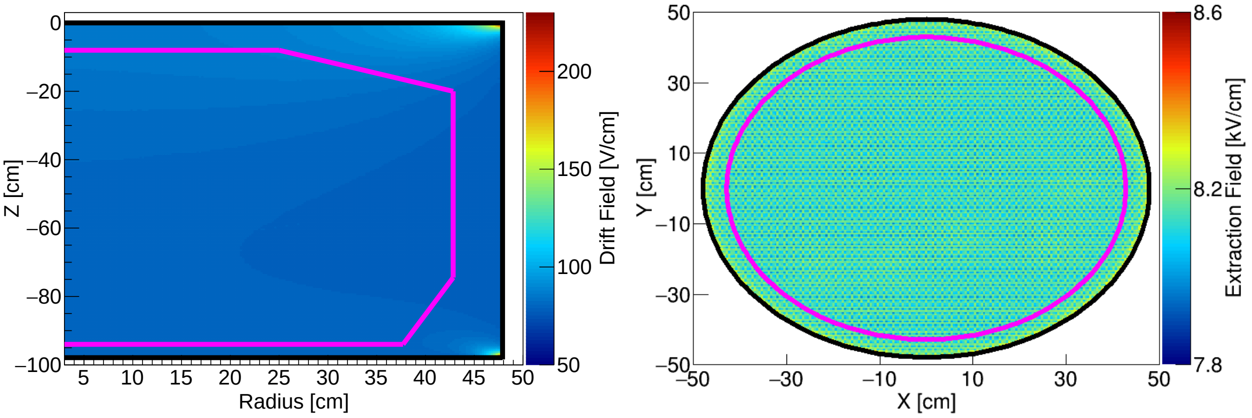

Figure 4.12: Left: The absolute electric field inside the TPC in SR1. The black lines indicate the TPC radius, cathode and anode. The purple lines indicate the 1.3 t fiducial volume. Right: The extraction field across the liquid/gaseous xenon boundary in SR1. The black circle indicates the TPC radius and the purple circle the radius of the 1.3 t fiducial volume.

(top right) high electric field regions can be identified. The mean drift field is listed in Table 4.4. The extraction field is defined as the absolute electric field 0.5 mm above the liquid/gaseous xenon boundary. This high electric field pulls the electrons from the liquid xenon to the gaseous phase. The extraction field across the gaseous/liquid xenon boundary in SR1 is shown in Figure 4.12 (right), it is uniform across the TPC radius. Negligible deviations are visible, due to the hexagonal structure of the electrodes. The extraction field values are listed in Table 4.4. A dielectric constant of $\epsilon_1 = 2$ was assumed for the liquid xenon in the performed simulations, whereas in the literature a value of $\epsilon_1 = 1.85$ is reported [171]. Therefore, the simulated extraction field is over-estimated by $\sim 9\,\%$, as it was discussed in section 2.3. A 100 % extraction efficiency is expected for fields above 10 kV/cm. However, in this configuration, the detector did not achieve this value neither for SR0 nor for SR1.

The position resolution, due to the cell opening of the gate and the number of proportional scintillation photons per electron were calculated by tracking single electrons through the gas gap. Single electrons were homogeneously distributed 1 cm below the gate in the simulation and tracked with a step resolution of 10 μm until they reached the anode surface. The position difference between the start and end of the track defines the position resolution. The number of produced electroluminescence photons in the gas phase were calculated at every tracking step, as described in section 2.3.4. The maximum difference between the initial position and the final position of the tracked electrons were simulated to be ~ 3.5 mm in both science runs, which is consistent with the cell opening of the gate. The number of produced proportional scintillation photons is the same in both science runs (Table 4.4), because the electric field between the gate and the anode is unaffected by the changed cathode voltage.

Configuration	Drift Field [V/cm]	Extraction Field [kV/cm]	S2 Photons/charge
SR0	119.08 ± 2.03	8.14 ± 0.07	235.53 ± 17.53
SR1	80.52 ± 2.10	8.15 ± 0.07	235.87 ± 17.87

Table 4.4: Drift field, extraction field and expected S2 signal size per electron in both science runs.

4.3.2 Field Correction

The XENON1T horizontal (x and y, given radius r) event reconstruction is performed with a neural network algorithm (Fast Artificial Neural Network Library [172]) which uses the light pattern in the top PMT array as an input. The neural algorithm was trained beforehand on the S2 light pattern in the top PMT array from Monte Carlo simulations. The Monte Carlo simulations include the realistic detector geometry, optical photon propagation, PMT QEs and gains. The vertical interaction position (z-coordinate) is calculated from the time difference between the S1 and S2 signal. The z-r reconstructed positions of acquired $^{83\mathrm{m}}$Kr data during SR1 is shown in Figure 4.13 (left). The $^{83\mathrm{m}}$Kr events are homogeneously distributed inside the detector. At high radii, a lack of $^{83\mathrm{m}}$Kr events can be recognised, which increases with the interaction depth of the events. The detector 'event edge' was calculated by fitting the event distribution as a function of r for different z-slices with a Fermi Dirac function of the form:

$$f(r) = \frac{A}{1 + e^{(r - r_{\mathrm{observed}})/b}}, \tag{4.10}$$

where r_{observed} is the observed detector event edge, A is the amplitude of the distribution and b is a free parameter. The calculated detector event edge is indicated with blue points in Figure 4.13 (left) and differs significantly from the real TPC radius, which is indicated with the black lines.

The origin of the inwards bias of the event edge was further investigated with electrostatic field simulations. In the performed simulations, single electrons were homogeneously distributed inside the TPC and tracked until they reached the anode. The electrons were tracked with a resolution of 100 μm and the tracking of an electron was stopped when it touched the detector surface or the electrodes. The simulated azimuthal averaged event distribution inside the TPC was obtained with the following formula:

$$R_{\mathrm{observed}} = R_{\mathrm{start}} + R_{\mathrm{correction}}, \tag{4.11}$$

where R_{start} is the initial position of the electron and $R_{\mathrm{correction}}$ is the position difference between the start and the end of the tracked electron trace. In Figure 4.13 (right) the event distribution from

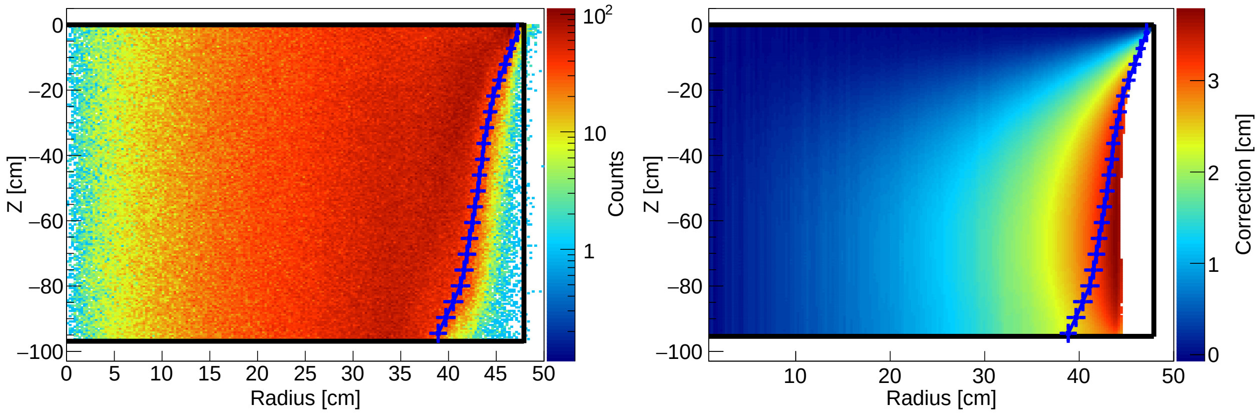

Figure 4.13: Left: $^{83\mathrm{m}}$Kr events inside the TPC in SR1. The black lines indicate the TPC boundaries. The blue points represent the observed event edge, which differs from the TPC radius Right: Simulated event distribution in the z-r plane in the nominal SR1 configuration. The colour code indicates the difference between the start and the end position of the tracked electron trace, which can be used to correct the data. The black lines indicate the TPC boundaries. The blue points represent the calculated event edge from $^{83\mathrm{m}}$Kr data, which differs significantly from the simulated event edge at the bottom of the TPC.

the simulation is shown and overlaid with the calculated detector event edge from $^{83\mathrm{m}}$Kr data. The colour code of the event distribution indicates the inwards bias of a certain position and can be used to correct the data (field distortion correction map). The event edge from the simulation matches the event edge from the $^{83\mathrm{m}}$Kr data at the top of the TPC and starts deviating with increasing interaction depth. That implies, that the inward bias of the observed event edge at high detector depth cannot be explained with a cathode voltage which is lower than designed and must have a different origin.

The appearance of an inwards bias of the events at high interaction depth could be related to a changed voltage configuration across the field shaping rings. A changed voltage configuration would generate a strong local field distortion, which forces the electrons to follow a more radial trajectory. A hypothesis is that the cathode is short-circuited with the first shaping ring, due to the largest inwards bias of events at high interaction depths. In order to verify the hypothesis, another simulation was performed where the first shaping ring was set on the same potential as the cathode, and electrons were tracked inside the TPC. In Figure 4.14 (left) the event distribution from the simulation is shown and overlaid with event edge from the $^{83\mathrm{m}}$Kr data. The results of the new simulation show that the event edge, in this case, agrees better with the event edge obtained from the data. Therefore, the $^{83\mathrm{m}}$Kr calibration data was radial position corrected with the simulated correction map. In Figure 4.14 (right) the position corrected $^{83\mathrm{m}}$Kr calibration data is shown in the z-r plane. After applying the correction from the simulation, the events at the bottom of the TPC are still further inwards than the TPC radius, which rules out the hypothesis of a short circuit between the first field shaping ring and the cathode, due to a too strong localised correction.

Another reason for the inwards bias of the observed event edge is related to a charge-up of the PTFE reflector panels, which was also observed inside the LUX TPC [173]. A charge-up of the PTFE reflector panels can happen due to trapped electrons or ions on the PTFE panels which cannot reach an electrode surface. The charged up PTFE panels disturb the local electric field and push the

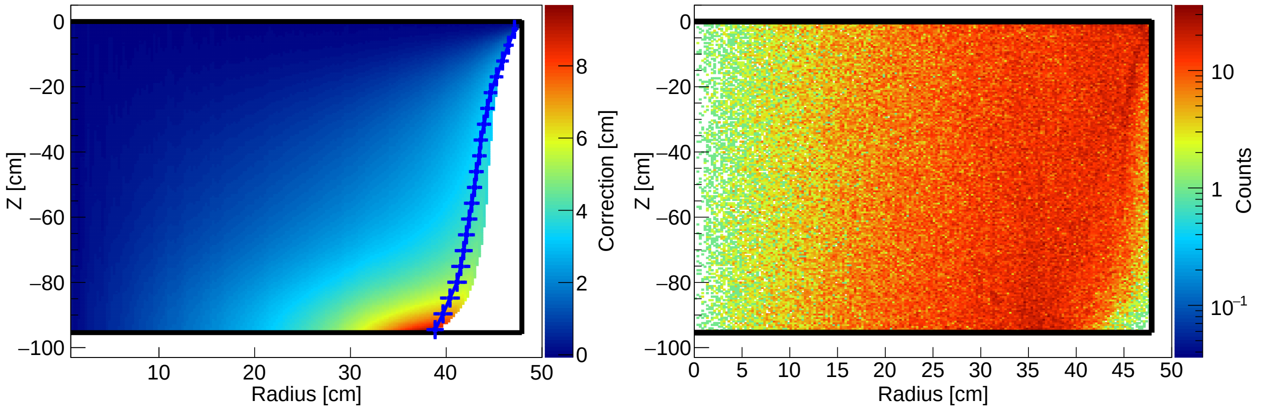

Figure 4.14: Left: The obtained event distribution from single electron simulations inside the TPC, with the assumption that the cathode is short-circuited with the first field shaping ring above it. The colour indicates the difference between the start and end position of the tracked electron trace, which corresponds to the correction factor of the data. The black lines indicate the TPC boundaries. The blue points represent the observed event edge from the $^{83\mathrm{m}}$Kr data, which differs from the observed event edge from the simulation. Right: The applied field correction map on the $^{83\mathrm{m}}$Kr calibration data for SR1. The black lines indicate the TPC boundaries. The events are more homogeneously distributed in the TPC, but some events are still absent, close to the cathode holder (bottom right). Events outside of the TPC are not shown.

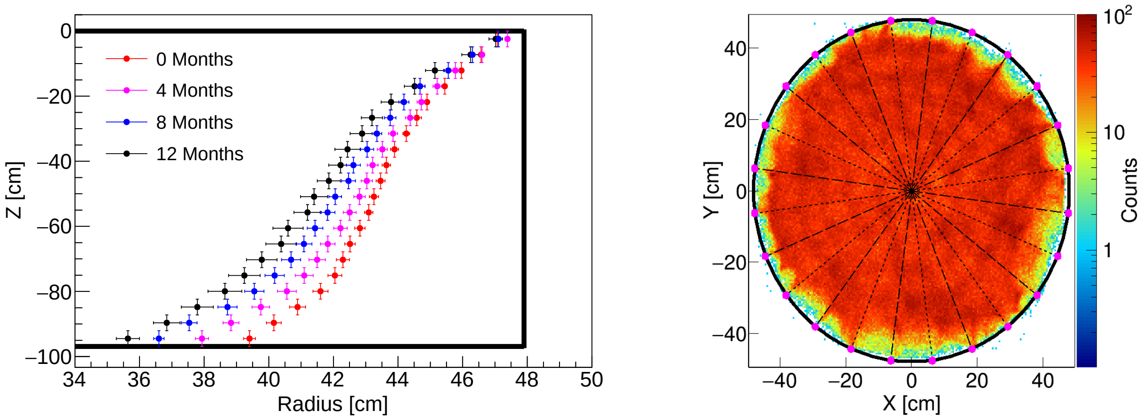

Figure 4.15: Left: The observed event edge for different $^{83\mathrm{m}}$Kr calibrations in SR1. It moves inwards, due to the further charge-up of the PTFE reflector panels. The black lines indicate the TPC boundaries. Right: x-y position event distribution of a $^{83\mathrm{m}}$Kr calibration in SR1. The black circle indicates the TPC radius. The events are inward biased, which can be correlated with the positions of the sliding reflectors. The fixed reflector positions are indicated as purple dots. On these positions, smaller inwards bias is observable.

electrons on a more radial trajectory. The effect of the charge-up of the PTFE reflector panels were investigated for the XENON1T TPC. The event edge from the $^{83\mathrm{m}}$Kr data was calculated for several months with the same procedure mentioned above. The calculated event edge over several months is shown in Figure 4.15 (left). The event edge moves further inwards due to the increased charge-up of the PTFE reflector panels, as a function of time. The x-y position distribution of the $^{83\mathrm{m}}$Kr events, shown in Figure 4.15 (right), reveals that the inwards bias of the event edge is strongest at the position of the sliding PTFE reflectors. The fixed reflectors hold the field shaping rings in place (described in section 3.2) and therefore, electrons or ions trapped on the PTFE reflector can escape via the contact to the field shaping rings. The sliding reflector, on the other hand, is not in contact with the field shaping ring and charges further up with time. The charge-up effect of the PTFE panels can be further investigated with the simulation framework, by placing different charge configurations on the PTFE panels. This investigation, however, is beyond the scope of this thesis. In this thesis, the fundamental steps were established to investigate the charge-up effect with the developed electrostatic simulation framework. The inwards bias of the event positions, due to the drift field distortions, was corrected by homogeneously distributing the $^{83\mathrm{m}}$Kr events inside the TPC, following the same procedure described in [174]. In the next section, the electrostatic simulation results were used to determine the electron drift velocity in liquid xenon and to establish a combined energy scale.

4.3.3 Combined Energy Scale and Electron Drift Velocity

The energy deposition from an interaction in the TPC generates both light and charge, which is measured as S1 and S2 signals, respectively. A strong anti-correlation between the S1 and S2 signals can be observed. The S1 and S2 signal size depends on the recombination probability, which depends on the number of ions (macroscopic anti-correlation) and of the applied electric field (microscopic anti-correlation), as shown in Figure 4.16. The recombination probability, and therefore the anti-correlation between S1 and S2 is well modelled by the Thomas-Imel model [175, 176]. Based on the anti-correlation between the S1 and S2 signals, a combined energy scale (CES) can be established.

The deposited energy in the TPC can be related to the number of produced quanta with the following formula:

$$E_{dep} = (N_{\text{photons}} + N_{\text{electrons}}) \times W, \tag{4.12}$$

where N_{photons} is number of produced photons, $N_{\text{electrons}}$ is the number of produced electrons, and $W = (13.7 \pm 0.2)\,\text{eV}$ [177] is the mean energy needed to produce a photon or an electron in xenon. N_{photons} and $N_{\text{electrons}}$ can be related using the detector response parameters g_1 and g_2 to the measured signals S1 and S2. g_1 and g_2 are defined by the following formulas:

$$g_1 = \frac{S1}{N_{\text{photons}}} \qquad g_2 = \frac{S2}{N_{\text{electrons}}}, \tag{4.13}$$

and they only detector dependent but independent of the source energy and the drift field. Different energies or electric fields have different charge and light yields, but the resulting charge (Q_y) and scintillation yield (L_y) will only move along a line as the total number of quanta is fixed. With g_1 and g_2, it is possible to combine the S1 and S2 signals into a combined energy scale, which is independent of the recombination. Therefore, the combined energy scale will result in a better energy resolution than for the S1 or S2 signals alone. The combined energy scale is then defined by the following expression:

$$E_{\text{CES}} = \left(\frac{S1}{g_1} + \frac{S2}{g_2}\right) \times W, \tag{4.14}$$

The detector response parameters g_1 and g_2 can be extracted by using multiple line sources with known energies or varying the drift field of one known energy by making a so-called *Doke plot* [180, 181]. In the work described in this thesis, the second approach was used, and the Doke plot was obtained by using the 41.5 keV energy line of the $^{83\text{m}}$Kr calibration at different drift fields. The $^{83\text{m}}$Kr population in the S1-S2 signal space at different cathode voltages was fitted with a two-dimensional elliptical Gaussian function in order to extract the scintillation (L_y) and charge yield (Q_y). The S2 signal collected in the bottom PMT array was used in order to avoid signal saturation in the PMTs, which are close to the interaction vertex. The two-dimensional rotated elliptical Gaussian function is defined by the following formula:

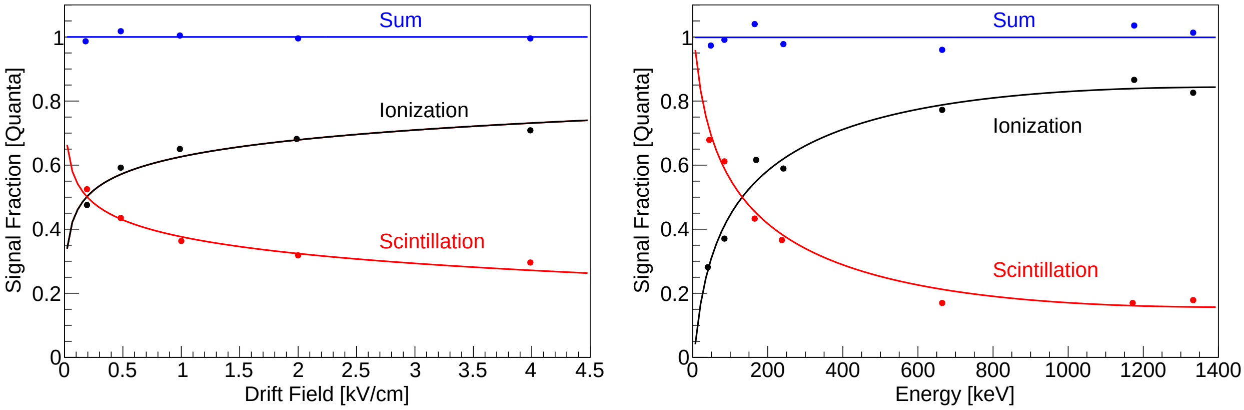

Figure 4.16: Left: Ionisation and scintillation yield as a function of the drift field excited by γ-rays with energy of 570 keV. The ionisation and scintillation yield have a strong anti-correlation depending on the drift field, which is called *macroscopic* anti-correlation. Data points taken from [178]. Right: Ionisation and scintillation yield as a function of γ-photon energy at a drift field of 0.53 kV/cm. The ionisation and scintillation yield have a strong anti-correlation depending on the γ-photon energy, which is called *microscopic* anti-correlation. Data points taken from [179].

Cathode Voltage [kV]	-15	-12	-8	-7	-6	-5	-4
Drift Field [V/cm]	146.7	119.08	80.52	72.4	62.9	53.7	44.4
rms [V/cm]	2.0	2.2	2.1	2.6	2.9	2.9	3.0

Table 4.5: Drift field for different applied cathode voltages inside the TPC inside a radius of 20 cm.

$$f(x,y) = A \times \exp\left(-\frac{((x-\mu_x)\cos\phi - (y-\mu_y)\sin\phi)^2}{2\sigma_x} - \frac{((x-\mu_x)\sin\phi + (y-\mu_y)\cos\phi)^2}{2\sigma_y}\right), \quad (4.15)$$

where A is the amplitude, σ_x and σ_y are the standard deviations of the S1 and S2 signals, respectively, ϕ is the rotation angle of the ellipse, μ_x is the mean of the S1 signal, and μ_y is the mean of the S2 signal. The $^{83\text{m}}$Kr data taken with an applied drift field of 80.5 V/cm in the (S1,S2) signal space is shown in Figure 4.17 (left) and fitted with equation 4.15. For this analysis $^{83\text{m}}$Kr events inside a reconstructed radius of 20 cm were considered, in order to avoid field distortion effects close to the PTFE panels. The scintillation and charge yields were extracted by normalising the mean S1 and S2 signals by the line energy. In Figure 4.17 (right) the Doke plot for different applied drift fields is shown. The data points were fitted with a function of the following form:

$$Q_y = \frac{W}{-g_1} \times L_y + \frac{g_2}{100W}, \quad (4.16)$$

where Q_y and L_y are the charge and light yields, respectively, at different applied drift fields of the 41.5 keV energy line. The drift fields for the different applied cathode voltages were simulated and extracted as described in the previous section in the same volume (Table 4.5). The detector response parameter g_1 was calculated to be (0.142 ± 0.009) PE/photon and g_2 was calculated to be (11.40 ± 0.44) PE/electron, which is in agreement with the published value [96] calculated from multiple line sources with known energies.

The drift velocity of electrons in liquid xenon can be measured with the delay time between the S1 and S2 signal. The maximum observable delay time corresponds to the cathode position and

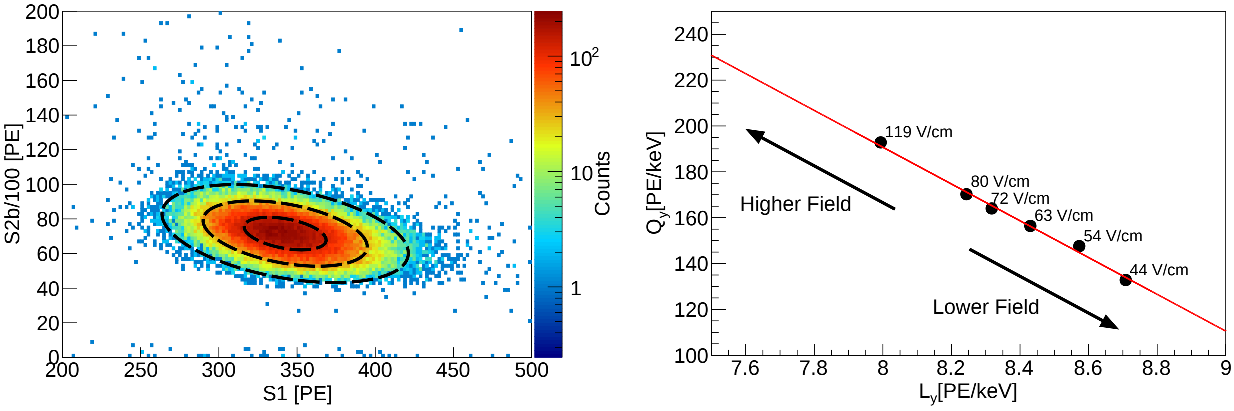

Figure 4.17: Left: Anti-correlation between S2 and S1 of a $^{83\text{m}}$Kr calibration at a drift field of 80.5 V/cm. The $^{83\text{m}}$Kr 41.5 keV energy line was fitted with a two-dimensional rotated elliptical Gaussian function, defined in equation 4.15. The black dotted lines indicated the 1,2 and 3σ ellipse. Right: Charge yield as a function of scintillation yield at different drift fields of the 41.5 keV energy line. The points were fitted with equation 4.16 (red line) in order to obtain the detector response parameter g_1 and g_2 from the slope and the interception with the y-axis.

the minimum delay time to the gate position. The distance between gate and cathode (L_{drift}) was measured in section 4.1 and the drift velocity is given by the following formula:

$$v_d = \frac{L_{\mathrm{drift}}}{t_{\mathrm{max}} - t_{\mathrm{min}}}, \tag{4.17}$$

where t_{max} and t_{min} are the maximum and minimum observable delay times, respectively. To measure t_{max} and t_{min}, a pure sample of $^{83\mathrm{m}}$Kr events at different cathode voltages were selected, in order to avoid a bias from delay times of non-physical events. The 41.5 keV energy line of $^{83\mathrm{m}}$Kr events were selected at different applied fields within the 3σ ellipse, as shown in Figure 4.17 (left). Events inside a reconstructed radius of 20 cm were considered in order to avoid field distortion effects close to the PTFE panels. The maximum and minimum delay times between the S1 and S2 signals were measured by fitting a Fermi Dirac function of the following form to the delay time distribution:

$$f(t) = \frac{A}{1 + e^{(t - t_{\mathrm{delay}})/b}}, \tag{4.18}$$

where t_{delay} is the maximum and minimum delay time between the S1, and S2 signals, A is the amplitude of the distribution, and b is a constant. In Figure 4.18 (left) the normalised maximum delay time distribution at an applied drift field of 80.5 V/cm is shown. The edge of the distribution was fitted with equation 4.18 in order to obtain the maximum delay time, and the drift velocity was calculated with equation 4.17. The obtained drift velocity for electrons in liquid xenon at a temperature of 177 K as a function of drift field is shown in Figure 4.18 (right) and compared to previous measurements. The drift velocity as a function of the electric field can be explained by the hot-electron theory of Shockley [189] and is described by the following equation:

$$v_d = \gamma^{-1/2} \times \mu_0 \times E, \tag{4.19}$$

where μ_0 is the electron mobility, and γ is the ratio between the lattice (T), and the hot-electrons (T_e) temperature. At low drift fields, the electron drift velocity becomes $v_d \simeq \mu_0 E$ with μ_0=2200 cm^2/(s×V)

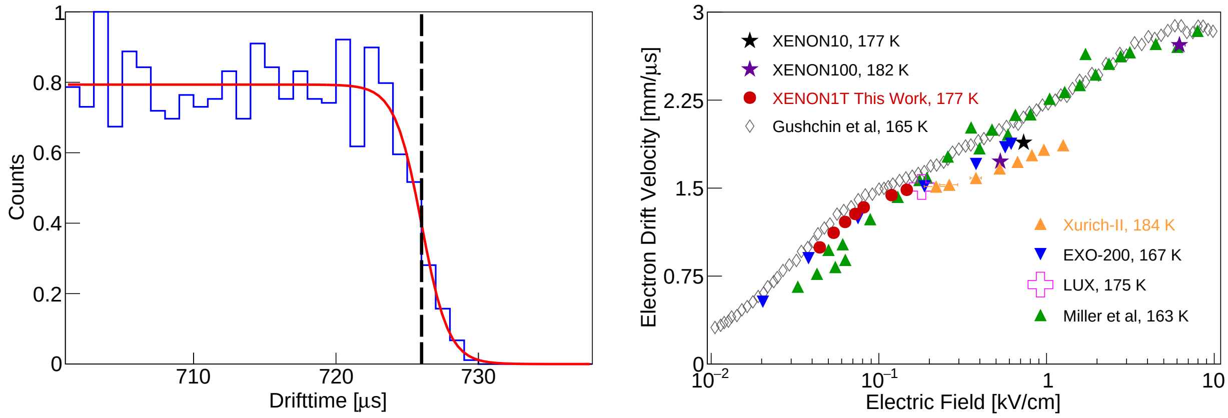

Figure 4.18: Left: Normalised delay time distribution at a drift field of 80.5 V/cm. The delay time distribution was fitted with a Fermi Dirac function (red line) in order to extract the maximal delay time (black line). Right: The measured drift velocity as function of drift field in the XENON1T TPC at 177 K (red points), along with several literature values: XENON10 [182] (black points at 177 K), XENON100 [183] (purple at 182 K), LUX [184] (pink at 175 K), EXO-200 [185] (blue points at 167 K), Xurich-II [124] (orange points at 184 K), Miller et al [186] (green points at 163 K) and Gushchin et al. [187] (grey points at 165 K). The liquid xenon temperatures of the measurements are included to account for possible variations as reported in [188].

[187]. At higher drift fields, there is a non-linear dependency of the drift velocity, and it becomes proportional to $E^{1/2}$. The measured drift velocity is in remarkable agreement with previous measurements. Small deviations to measurements at different temperatures can be found. This is due to a different electron mobility since the electron mobility in liquid xenon depends on: $\mu_0 \propto T^{-1/2}$ [190]. The purity of the xenon also may affect on the drift velocity in liquid xenon, as reported in [191, 192].

4.4 WIMP Search Result from a One Tonne×Year Exposure

The total acquired data of 278.8 days in a (1.30 ± 0.01) t fiducial volume needs to undergo different corrections, data quality checks and event selection criteria (cuts). Afterwards, a profile likelihood analysis parametrised in spatial (radius r and interaction depth z) and energy dimensions (cS1 and cS2) estimates the WIMP signal excess above the background.

The light (S1) and charge signals (S2) need to be corrected due to a non-homogeneous detector response. The drifting electrons can be captured by impurities, and therefore the S2 signals need to be corrected for the free electron lifetime. In addition, the S2 signals need to be corrected for a position dependent LCE and an inhomogeneous electron amplification in the gaseous xenon phase, due to the wrapping of the anode and the gate electrodes, which originates from the electrostatic force. The corrected S2 signals are denoted as cS2. The cS2 signals collected in the bottom PMT array (cS2b) were used for the energy reconstruction in order to avoid signal saturation in the PMTs, which are close to the interaction vertex. The S1 signals are corrected for the spatial variations of the LCE due to multiple reflections. The corrected S1 signals are denoted as cS1. The S1 and S2 signals are corrected from the internal monoenergetic calibration source $^{83\text{m}}$Kr by measuring the spatial variations of the detector response. The free electron lifetime increased from 380 μs at the beginning of the science run, to 680 μs at the end of the science run.

The ER events can be distinguished from the NR events by the ratio $\log_{10}$(cS2/cS1), as discussed in section 1.4. The ER band was regularly calibrated with the internal calibration source ^{220}Rn. The NR band was calibrated with the external neutron generator and an ^{241}AmBe calibration source.

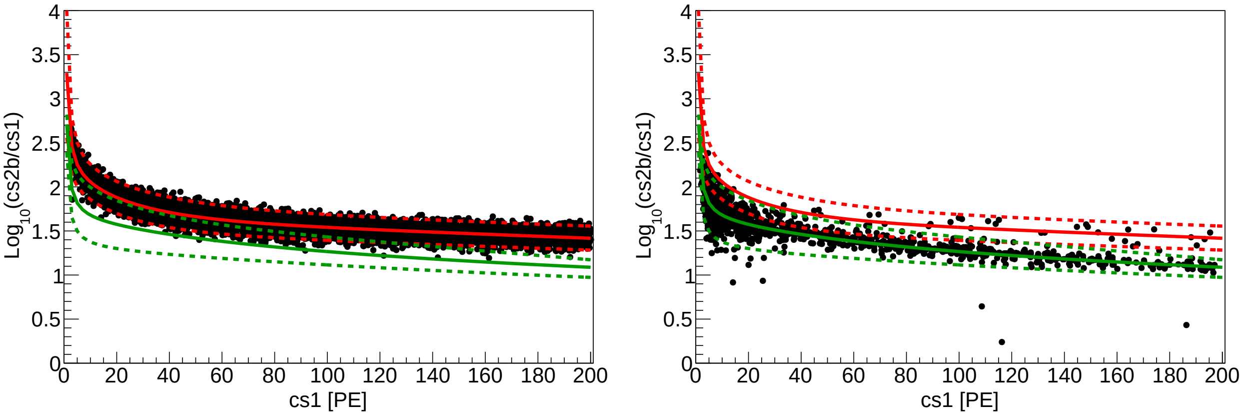

Figure 4.19: Left: ER events of all acquired ^{220}Rn calibrations during SR1 in the ($\log_{10}$(cS2b/cS1), cS1) space. The events populate a band, and the median (red line) with the $\pm 2\sigma$ quantiles (red dashed lines) are shown. For comparison, the NR band median (green solid line) with the $\pm 2\sigma$ (green dashed lines) quantiles are shown as well. Right: NR events of a ^{241}AmBe calibration during SR1 in the ($\log_{10}$(cS2b/cS1), cS1) space. The events populate a band, and the median (green solid line) with the $\pm 2\sigma$ quantiles (green dashed lines) are shown. For comparison, the ER band median (red solid line) with the $\pm 2\sigma$ (red dashed lines) quantiles are shown as well.

The NR signal reference region is defined between the NR median and the -2σ quantile, due to the overlap of the bands. In Figure 4.19, the ER and NR events are shown in the ($\log_{10}$(cS2b/cS1), cS1) space for ^{220}Rn and ^{241}AmBe calibrations runs. The NR calibration is contaminated with some ER background events, due to the ~3 weeks long time of ^{241}AmBe calibration. In addition, some events are visible below the NR band, which originate from double scatters in charge insensitive regions, such as the region below the cathode. A neutron event can scatter once below the cathode and once in the active target. In this case, the light signal will be correctly detected, but the charge signal will be reduced, because the charge below the cathode cannot reach the liquid/gaseous xenon boundary.

To ensure a proper event selection, a set of *data quality cuts*, which remove non-physical events due to bad detector performance, unusual photosensor responds, background events or other external circumstances, must be applied. A large fraction of the data quality cuts are obtained from the analysis of the regular detector calibrations with the $^{83\mathrm{m}}$Kr, ^{220}Rn and ^{241}AmBe calibration source, as well as with the neutron generator. In the next section, two data quality cuts for the dark matter search, developed during my PhD work, will be discussed. The description of the additional data quality cuts can be found in [96].

4.4.1 Data Quality Cuts

A ‘noise cut’ was developed in order to reject waveforms which cannot be analysed due to misidentified peaks, shifted baselines, or other conditions that can cause a very large amount of signal in the waveform, in addition to the main S1 and S2 signals. The main noise contribution comes from single electrons (SE), which produce S2 signals with a mean size of 29.70 PE [134] detected in both PMT arrays. The data processor can wrongly pair these single electron S2 signals with the main S2 and the ratio cS2/cS1 will have a compatible value with NR events. A large fraction of the single electrons are mainly produced in a short time (maximum drift time) after a large S1 or S2 signal, due to photoionisation of the metal components in the detector and impurities [126, 193]. In

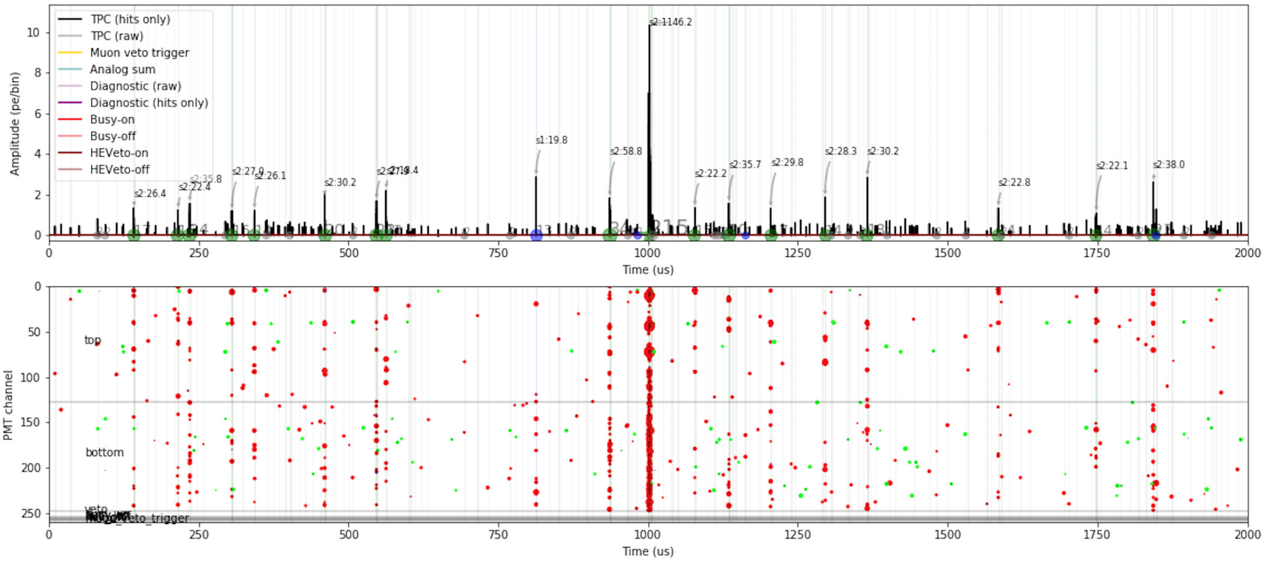

Figure 4.20: An event acquired during the ^{241}AmBe calibration in SR1. The top panel shows the summed waveform and the bottom panel the contributing PMTs (red circles). The waveform consists of an S2 signal centred at around 1 ms and several single electron S2s before and after the main S2 with a mean signal size of 22 PE. Due to the large amount of additional pulses in the waveform, the main S2 was miss paired. The event is rejected by the developed cut.

addition, some of the single electrons appear much later after the S2, due to a delayed extraction of the electrons from the liquid to the gaseous phase [194, 195]. In Figure 4.20 a waveform with a large number of single electrons S2 signals is shown. The data acquisition/event builder recorded the noisy event, and the data processor paired the S2 signal with a single electron signal. The goal of the developed 'noise cut' is to reject these class of events.

The length of a recorded waveform in XENON1T is 2 ms with the S2 signal centred at 1 ms. This allows for coverage of the whole drift length of the TPC. Therefore, the noise of the waveform was defined by the following formula:

$$\text{Noise} = \text{Pulses\_before\_S2} - \text{S1}. \tag{4.20}$$

The sum of all pulses before the main S2 signal (Pulses_before_S2) subtracted by the main S1 signal is an indicator of the amount of noise in a waveform. Therefore, this value is related to the probability of a misidentification of the S1 or S2 signals. In Figure 4.21 (left), the distribution of the noise parameter of the ^{241}AmBe calibration is shown. The cut on the noise parameter is defined on the 99 % quantile (300 PE) of this distribution, which is indicated as a magenta line in the Figure. The cut allows a couple of single electrons S2 signals, afterpulses and dark count events before an event is rejected. The signal acceptance was estimated to be flat >99 % as a function of cS1 on background data.

Furthermore, an 'S1 maximum PMT cut' was developed in order to reject events generated by light emission, afterpulses, below cathode events (Gamma or Neutron) or scintillation events in the photocathode. In such a case, some of the coincidence PMTs have an anomalously high contribution to the main S1 signal. The cut was loosely defined on the selected ER band obtained from ^{220}Rn calibration data, which is shown in Figure 4.21 (right). The cut boundary is a linear function of the following form:

$$S1_{\text{Max}} < 0.052 \times S1 + 4.15\,\text{PE}, \tag{4.21}$$

where $S1_{\text{Max}}$ is the number of photoelectrons of the highest contributing PMT to the S1 signal. The signal acceptance on NR events was obtained by selecting the NR band of the ^{241}AmBe calibration.

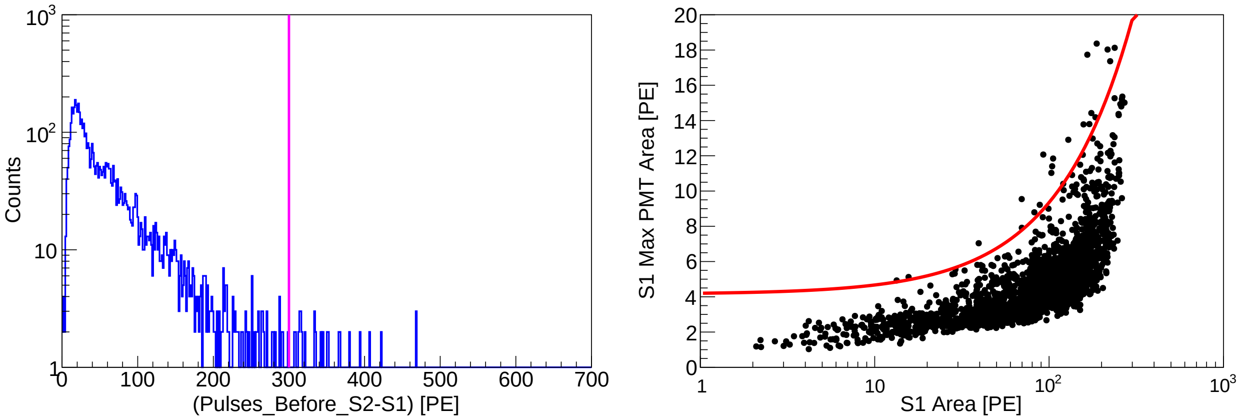

Figure 4.21: Left: The noise parameter distribution of the ^{241}AmBe calibration in SR1. The cut was defined on the 99 % quantile of this distribution (pink line). Events with a noise value higher than 300 PE are rejected. Right: The number of photoelectrons of the highest contributing PMT to the S1 signal as a function of the S1 signal (black points) in the ER band obtained from all ^{220}Rn calibrations during SR0. The S1 max PMT cut was defined as a linear function to this distribution (red line).

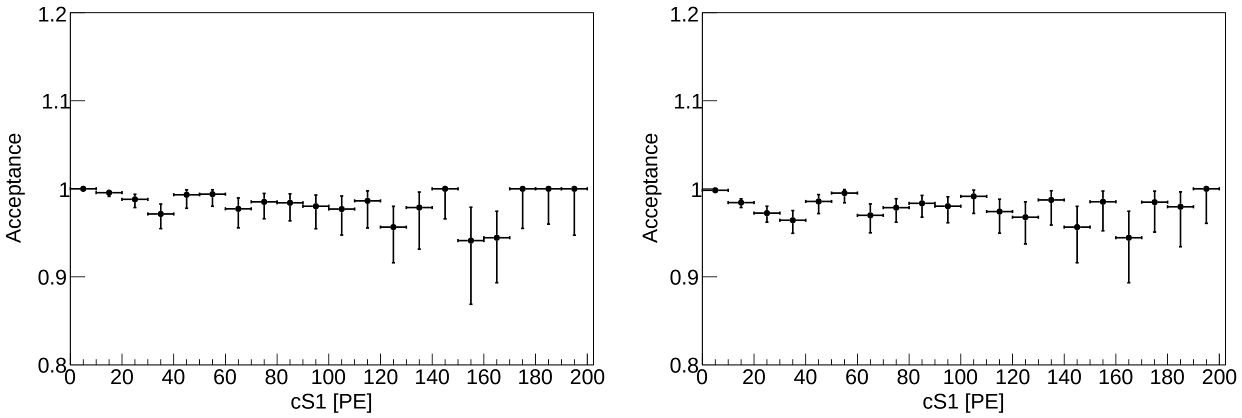

Figure 4.22: The S1 max PMT cut acceptance as a function of cS1 in SR0 (left) and SR1 (right).The acceptance was obtained with the $N-1$ method, by selecting the events inside the NR band from the ^{241}AmBe calibration. The signal acceptance drops slightly between $\sim$(20–50) PE, due to afterpulse events, which are rejected by the cut.

The ratio of the number of NR events after and before applying this cut defines the signal acceptance. In Figure 4.22 the NR signal acceptance of the 'S1 maximum PMT cut' in SR0 and SR1 are shown.

Besides the two developed data quality cuts, there are several additional cuts to ensure proper event selection which were not developed within the scope of this thesis. The description of the additional data quality cuts can be found in [96]. In the next section, the data analysis and the dark matter search results of the one tonne×year exposure will be discussed.

4.4.2 Spin-Independent WIMP-Nucleon Cross Section

The total amount of acquired science data with XENON1T corresponds to one tonne×year exposure in the fiducial volume. The science data was blinded in the NR region below the -2σ quantile of the ER band and above the S2 threshold of 200 PE. The signal and background models, as well as the data quality cuts and the signal corrections were established before unblinding. In addition, the science data was salted by injecting an unknown number of events into the data, in order to prevent fine-tuning of the models or the data selection criteria after unblinding. The WIMP search region was restricted by cS1 between 3 and 70 PE. This corresponds to an average of [1.4, 10.6] $\mathrm{keV_{ee}}$ (ER energy) or [4.9, 40.9] $\mathrm{keV_{nr}}$ (NR energy).

The XENON1T detector response to ER and NR was modelled with the best fit simulations between the ER and NR calibration data and the theoretical model (microphysics model and detection of the signals by the detector), similarly as described in [196, 96]. The simulated event distributions were simultaneously fitted to all acquired calibration data (^{220}Rn,^{241}AmBe and neutron generator data). The resulting fit posteriors were used to predict the NR and ER distributions in the analysis space of the science data, as well as the expected WIMP signal regions. With this modelling, a 99.7 % ER background rejection was achieved between the NR band median and the $-2\,\sigma$ quantile.

The ER background from materials is suppressed in the fiducial volume, due to the self-shielding power of the xenon. Therefore, the dominated ER background comes from the intrinsic radioactive sources, ^{85}Kr and ^{222}Rn. Due to the cryogenic distillation of $^{\mathrm{nat}}$Kr to a level of $^{\mathrm{nat}}\mathrm{Kr/Xe} = (0.66 \pm 0.11)$ ppt, the dominated ER background comes from the β-decays of ^{214}Pb, which originate from ^{222}Rn emanation. The total ER background in the fiducial volume below 25 keV_{ee} was measured to be $(82^{+5}_{-3}(\mathrm{sys}) \pm 3(\mathrm{stat}))$ events/(ton × year × keV_{ee}) after correcting for efficiency, which makes it the lowest ever achieved ER background in a direct dark matter detection experiment. It must be mentioned that the ER background was stable throughout both science runs and is in agreement with the ER background predictions of (75 ± 6) events/(ton × year × keV$_{ee}$).

The NR background from coherent-elastic neutrino-nucleus scattering [198, 199] (CEνNS) produced by solar neutrinos was modelled with the measured ^{8}B flux [200] and cross section measurements [201]. Cosmogenic neutrons from secondary particles produced by muons were rejected with the muon veto (described in section 3.1), and therefore, the contribution to the NR background is negligibly small. The main NR background originates from radiogenic neutrons from detector materials, and it is modelled through Geant4 Monte Carlo simulations [140].

The ^{210}Pb β-decays that occur directly on the PTFE reflector surface, due to the continuous plate out of ^{220}Rn, contaminate the fiducial volume with background events, which are called *surface events*. The surface events have a reduced S2 signal size, due to the partial absorption of the electrons by the PTFE surface. The ratio cS2/cS1 of the surface events has a compatible value with NR events and is considered in the background model. In addition, isolated S1 or S2 signals can be produced by PMT dark counts, energy deposits in light- or charge-insensitive regions or other circumstances which can fake a real interaction. This background component is called *accidental coincidence* and was also estimated before the unblinding.

The expected radiogenic neutron interactions in the 1.3 t fiducial volume will occur near the gate or the cathode, due to the neutron background from the PMT arrays. Therefore, the 1.3 t fiducial volume was segmented into a 0.65 t core volume, which is free of surface and radiogenic neutron events. The core volume was optimised in terms of signal/background in the (r, z) space. After unblinding, the segmentation was included in the statistical analysis of the data, in order to get an additional discrimination (interaction depth z) and thus a more precise interpretation of the data.

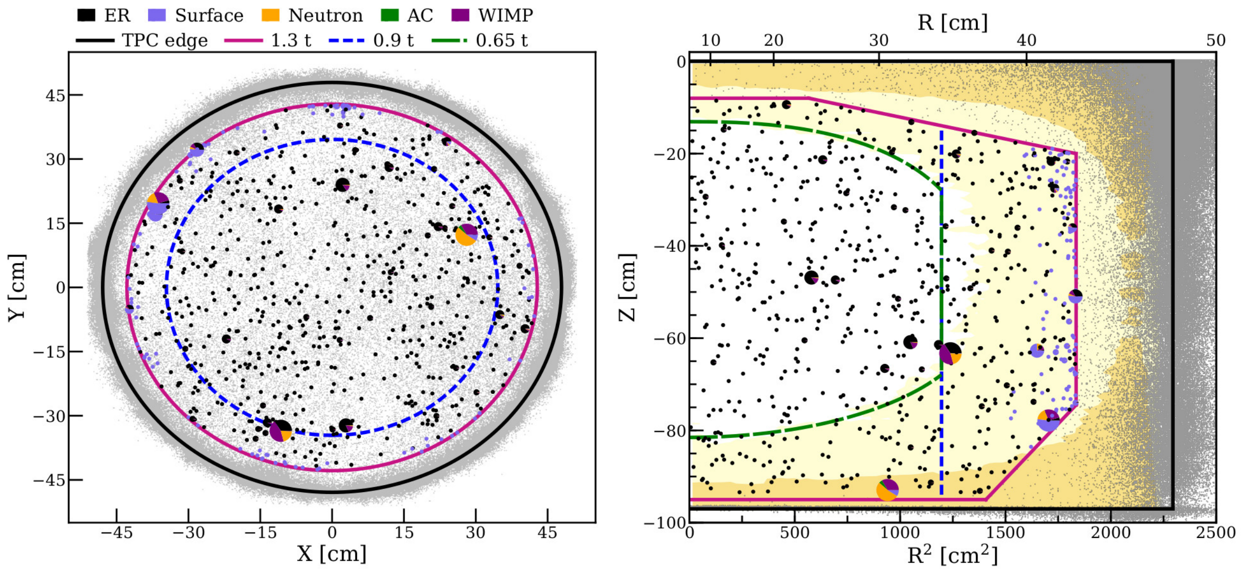

Figure 4.23: The x-y (left) and z-r^2 (right) event position distributions of the science data, which passed the selection criteria. The TPC boundary (black line), the 0.65 t core volume (dashed green line) and the 1.3 t fiducial volume (solid magenta line) are shown. The events within the 1.3 t fiducial volume are drawn as pie charts, which represent the best-fit PDF fraction of the background and signal components (assuming a 200 GeV WIMP and resulting best-fit $\sigma_{\mathrm{SI}} = 4.7 \times 10^{-47}\,\mathrm{cm}^2$). The yellow shaded area represents the 1σ (dark yellow) and 2σ (light yellow) probability density percentiles of the radiogenic neutron background component. Figure and caption published in [197].

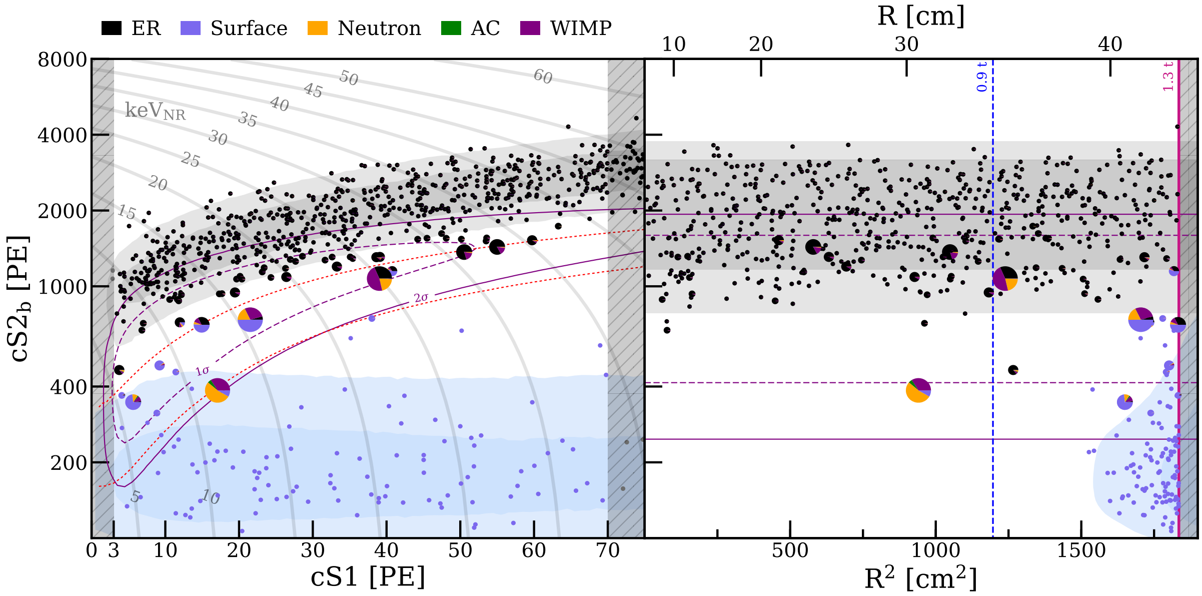

Figure 4.24: The science data in the (cS1, cS2b) (left) and in the (cS2b, r) (right) space. The events are drawn as pie charts, which represents the best-fit PDF fraction of the background and signal components (assuming a 200 GeV WIMP and resulting best-fit $\sigma_{\mathrm{SI}} = 4.7 \times 10^{-47}\,\mathrm{cm}^2$). The shaded regions show the highest-density contours for the surface (blue) and ER (grey) background components in SR1. The 1σ (purple dashed) and 2σ (purple solid) percentiles of a 200 GeV WIMP signal are overlaid for reference. The vertical shaded regions are outside of the region of interest. The NR median and the 2σ percentiles (left, red dotted lines) and the maximum radii (right) of the 0.9 t (blue dashed) and 1.3 t (magenta solid) masses are shown. The grey lines show iso-energy contours in NR energy. Figure and caption published in [197].

In Figure 4.25 (left) the background and a 200 GeV WIMP signal best-fit predictions inside the (1.30 ± 0.01) t fiducial volume and in the 0.9 t volume are shown.

The background predictions in the fiducial volume are shown in Table 4.6. The one tonne×year of science data contains a total of 739 events after unblinding inside the (1.30 ± 0.01) t fiducial volume in the region of interest, which pass the data quality cuts. The position distribution of the dark matter search data is shown in Figure 4.23. In Figure 4.24, the dark matter search data is presented

ER	Neutron	CEνNS	AC	Surface	Total BG	WIMPs$_{\text{best-fit}}$	Data
627 ± 18	1.43 ± 0.66	0.05 ± 0.01	$0.47^{+0.27}_{-0.00}$	106 ± 8	735 ± 20	3.56	739
1.62 ± 0.30	0.77 ± 0.35	0.03 ± 0.01	$0.10^{+0.06}_{-0.00}$	4.84 ± 0.40	7.36 ± 0.61	1.70	14

Table 4.6: Best-fit expected event counts with 278.8 days of science data in the 1.3 t fiducial volume for the full (cS1, cS2b) region of interest (first row) and, for illustration, in the NR signal reference region (second row). The table lists each background (BG) component separately and the total background, as well as the expectation for a 200 GeV WIMP prediction, assuming the best-fit $\sigma_{\mathrm{SI}} = 4.7 \times 10^{-47}\,\mathrm{cm}^2$. The observed events from data are also shown for comparison. Although the number of events in the reference region indicate an excess compared to the background expectation, the likelihood analysis, which considers both the full parameter space and the event distribution finds no significant WIMP-like contribution. Table and caption published in [197].

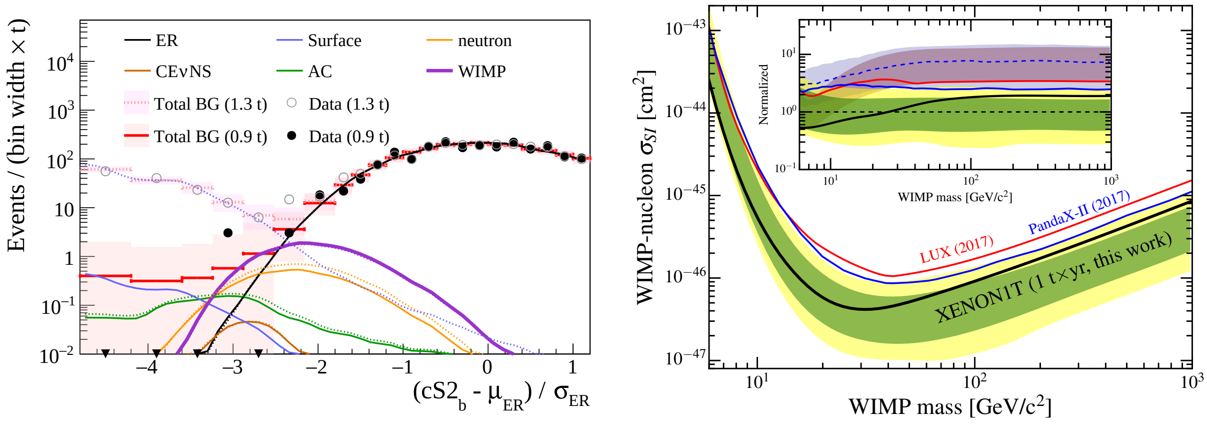

Figure 4.25: Left: Background and 200 GeV WIMP signal best-fit predictions, assuming best-fit $\sigma_{\mathrm{SI}} = 4.7 \times 10^{-47}$ cm^2, compared to DM search data in the 0.9 t (solid lines and markers) and 1.3 t (dotted lines and hollow markers) masses. The horizontal axis is the projection along the ER mean (μ_{ER}), shown in Figure 4.24, normalised to the ER 1σ quantile (σ_{ER}). Shaded bands indicate the 68 % Poisson probability region for the total background expectations. Right: 90 % confidence level upper limit on σ_{SI} from this work (thick black line) with the 1σ (green) and 2σ (yellow) sensitivity quantiles. Select previous results (LUX, PandaX-II) are overlaid. The inset shows these limits, their median sensitivities and corresponding $\pm 1\sigma$ quantiles, normalised to the median sensitivity calculated in this work. Figures and captions published in [197].

in the (cS1, cS2b) and in the (cS2b, r) space. The statistical interpretation of the data was performed by an extended unbinned likelihood with profiling over nuisance parameters in the (cS1, cS2b, r, z) space [202, 203]. Including r in the likelihood and modelling the surface background allowed us to extend the fiducial volume to 1.3 t. In addition, the core mass segmentation was used in the likelihood, which allowed us to categorise events based on the z position of the event, in order to get a more precise interpretation of the data. The most important model uncertainties were propagated to the likelihood and treated as nuisance parameters. A safeguard parameter [204] was added to the ER background in order to take into account a miss-modelling of the ER background.

The background only hypothesis is favoured by the likelihoods best-fit value to the science data with a p-value of 0.28, 0.41, and 0.22 at 6, 50, and 200 GeV, respectively. The confidence intervals (90 % C.L.) on the spin-independent cross section for different WIMP masses were calculated by using MC simulations [205, 206]. In Figure 4.25 the upper limit on the WIMP-nucleon spin-independent elastic scattering cross section at 90 % confidence level for WIMP masses above 6 GeV is shown. The upper limit with a minimum of 4.1×10^{-47}cm^2 at 30 GeV was the strongest upper limit at the time of writing this thesis.

After the analysis of the 278.8 days of science data, XENON1T continued to take data with a reduced radon background, due to the usage of a novel magnetically-coupled piston pump. In parallel the next phase of the XENON experiment is under design, which is XENONnT. The existing infrastructure of XENON1T will be reused for XENONnT, and the target mass of the TPC will be increased to $\sim$6 t. In the next chapter, the XENONnT experiment will be introduced, and the contributions of this PhD work to the experiment will be discussed in details.

"If one way be better than another, that you may be sure is Nature's way."

Aristoteles

CHAPTER 5

XENONnT Photosensor Evaluation Facility and Amplifier Development

In parallel to the XENON1T analysis which was discussed in chapter 4, the next phase of the XENON experiment was under design: XENONnT. The existing infrastructure of XENON1T will be reused for XENONnT, which ensures the rapid scalability of the TPC from $\sim 2\,\mathrm{t}$ to $\sim 6\,\mathrm{t}$ active target mass. A new TPC and a cryostat were designed, and in addition, an active neutron veto will surround the cryostat after the final installation. The light detectors of the XENONnT TPC will consist of ~ 500 3-inch Hamamatsu R11410-21 PMTs. The additional cabling will be realised by a second cable pipe through the water tank to the cryostat.

In section 5.1 we will give an introduction to the XENONnT experiment. This is followed by section 5.2, which gives a detailed description of the developed single-phase liquid xenon detector to evaluate a subsample of the XENONnT PMTs. In addition, the results of the XENONnT PMT characterisation from the commissioning run will be reported. Section 5.3 discusses the low-noise dual channel PMT signal amplifier developed for the XENONnT experiment, which will ensure a linear response of the detector from a few keV to the MeV energy-range, in order to improve the study of different physics channels at various energies. An example of such a study is the neutrinoless double beta decay search with the isotope ^{136}Xe at a Q-value of 2.458 MeV. The chapter will be concluded with an outline of the development of a cryogenic amplifier for future experiments.

5.1 The XENONnT Experiment

The XENONnT experiment will be located in Hall B of the underground research laboratory at LNGS in Italy. It will reuse the existing infrastructure of XENON1T, which was described in chapter 3. The XENONnT TPC is designed for a target mass of $\sim 6\,\mathrm{t}$ and it will be equipped with ~ 500 3-inch Hamamatsu R11410-21 PMTs for the light detection, arranged in bottom and top PMT arrays. The bottom PMT array will consist of 242 R11410-21 PMTs, arranged in a hexagonal structure, in order to cover the whole diameter of the TPC and thus to maximise the LCE. The top PMT array will be arranged in a hexagonal structure with 253 PMTs. Figure 5.1 (left) shows a preliminary design of the XENONnT TPC. The additional high voltage and signal cables for the PMTs will be routed through a new vacuum-insulated pipe from the cryogenic floor to the cryostat. The readout of the PMTs will be performed as in XENON1T. In addition, a low-gain amplified channel will be digitised in order to improve the detector response at high energies (described in section 5.3).

For the xenon gas purification, the existing gaseous xenon recirculation system of XENON1T through a hot metal getter will be reused and upgraded. A magnetically-coupled piston pump [207] was installed to replace the QDrives for the gaseous xenon recirculation, which will increase the total flow rate to ~ 100 standard litres per minute (SLPM). In addition to the xenon gas purification, a

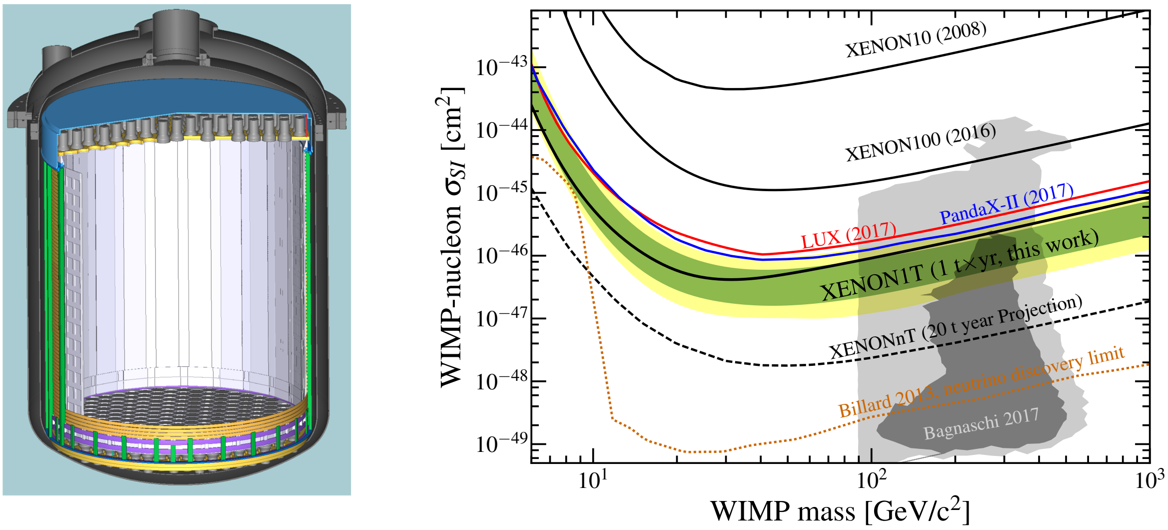

Figure 5.1: Left: A first design of the XENONnT TPC. Right: XENONnT sensitivity (90 % confidence level) to spin-independent WIMP-nucleon interaction. The black dashed line represents the median sensitivity. Figure published in [197].

liquid xenon purification system will be installed with a planned recirculation flow of ∼5 l/min. The liquid xenon will be pumped with commercially available (Barber-Nichols) pumps through two custom filters based on copper powder ($2\mathrm{Cu} + \mathrm{O}_2 \rightarrow 2\mathrm{CuO}$) for purification purposes. In order to store the total ∼8.2 t of xenon, a second xenon storage and recovery system (ReStoX-2) was developed. The system has a capacity of ∼10 t and can store the xenon in the gaseous, liquid or solid phase. ReStoX-2 will be located next to the infrastructure building, due to the additional space required.

The existing krypton distillation column of XENON1T with a height of ∼5 m will be reused for XENONnT. Therefore, the whole xenon gas inventory of XENONnT will be distilled down to a $^{\mathrm{nat}}$Kr concentration of 20 ppq[1] at the start of the science run. Furthermore, a dedicated distillation column to remove ^{222}Rn will be installed and integrated within the liquid and gaseous recirculation system. The online removal of ^{222}Rn with a distillation column was demonstrated with XENON100, where a reduction factor of >27 (at 95% confidence interval) was achieved [208].

The ER and NR background signals which originate from the detector materials will become negligible in XENONnT, due to the improved self-shielding and capability to detect multiple scatters in the larger detector. With a designed ^{222}Rn activity of 0.1 μBq/kg and a ^{85}Kr concentration of 20 ppq, the ER background induced by solar neutrinos becomes dominant.

The sensitivity of the XENONnT experiment to the spin-independent WIMP-nucleon cross section is calculated with the Profile Likelihood Ratio method [209] based on the background predictions and the conversion from deposited energy into S1 and S2 signals. The method is described in details in [140, 183, 210]. The test statistics of all considered cross sections for the signal (H_σ) and the background-only hypothesis (H_0) are obtained from Monte Carlo simulations. A p-value of 0.1 for the signal hypothesis is required to determine the upper limit (σ_{90}). The sensitivity of the XENONnT experiment is then given with the median of the upper limit from repeated simulations of the background-only hypothesis. In Figure 5.1 (right) the expected XENONnT median sensitivity is shown. The minimum spin-independent WIMP-nucleon cross section will be 1.6×10^{-48} cm^2 at a WIMP mass of 50 GeV [140].

---

[1] Parts per quadrillion, 1 ppq = 1×10^{-15} mol/mol.

5.2 XENONnT Light Sensors Evaluation Facility

The Hamamatsu R11410-21 PMT will be used as the light sensor for the XENONnT xenon-based dual-phase TPC. As described in section 3.4, the PMT offers a very low intrinsic radioactivity, a high quantum efficiency and a stable operation in liquid xenon. An evaluation of the PMTs in liquid xenon prior to the final installation in the XENONnT TPC is necessary, in order to avoid malfunctioning during data taking. In this section, the single-phase liquid xenon detector is described, which can house up to 10 R11410 PMTs and which was used to evaluate the XENONnT PMTs. The PMT characterisation from the commissioning run is presented, and furthermore, the developed software packages for the data acquisition are introduced.

5.2.1 Description of the Evaluation Facility

The XENONnT PMT evaluation facility (MarmotX) consists of a double-walled vacuum-insulated cryostat, which can house up to 10 R11410 PMTs. A CAD cross-sectional view of the setup is shown in Figure 5.2 (left). The 10 PMTs are inside the cryostat and organised in two arrays of five PMTs facing each other. Five PMTs covered with an insulation PTFE shell can be placed into an aluminium filler facing upwards, and they form the bottom PMT array. A 2 mm thick PTFE reflector with five cutouts for the PMTs is placed on top of the bottom PMT array. Other five PMTs with an insulation PTFE shell can be placed on top of the PTFE reflector facing downwards, and they form the top PMT array. The top PMT array is held in place with a metal plate with cutouts for the PMTs. The top and bottom arrays are connected to each other via stainless steel rods and connected to a support plate, which is screwed to the top of the cryostat. The cables from the bottom PMT array are routed to the support plate along grooves in the aluminium filler. The PMT bases of the top PMT array are covered with PTFE caps to prevent cables from touching the high voltages lines. A blue LED ($\lambda \sim 470\,\mathrm{nm}$) and a Pt-100 temperature sensor are placed in the middle of the setup. The LED is used for the PMT calibration. Furthermore, eight Pt-100 temperature sensors are installed onto a PEEK® rod at different heights covering the whole height of the cryostat. The PEEK® rod is connected to the support plate as well.

The cryostat can be filled with gaseous xenon with a dedicated gas system as shown in Figure 5.2

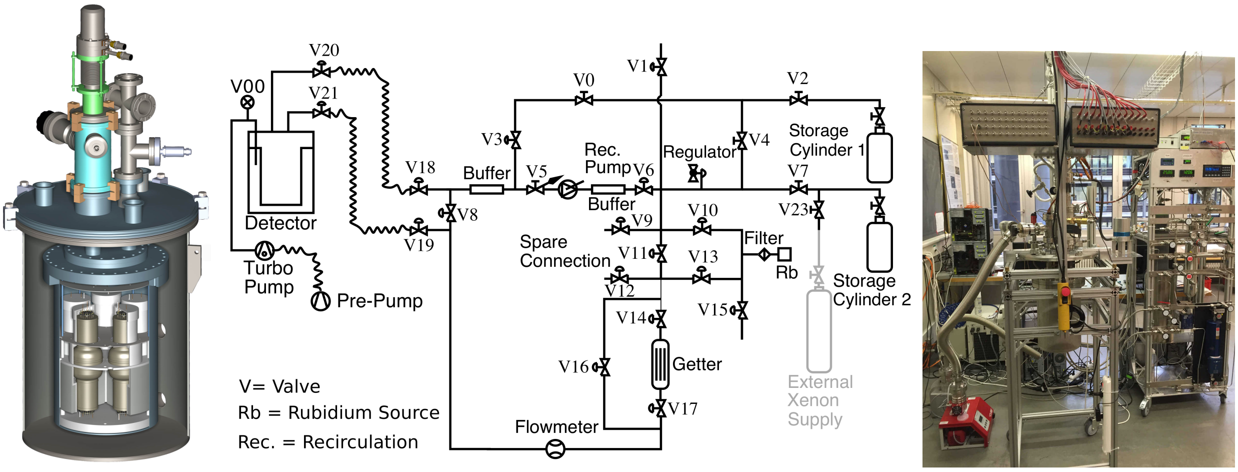

Figure 5.2: Left: A cross-sectional view of the XENONnT PMT liquid xenon evaluation facility. Centre: A schematic of the gas system, which is connected to the detector and to two storage cylinders. Right: A picture of the facility with the gas system and the two breakout boxes.

(centre). The gas system is connected to two xenon storage cylinders and to the cryostat. During operation, the xenon gas circulates with the help of a pump (KNF N022SN.9E) through a hot metal getter (SAES MonoTorr), in order to remove electronegative impurities. In addition, the gas system is equipped with a small chamber, which holds a ^{83}Rb source. This allows us to introduce the metastable $^{83\mathrm{m}}$Kr calibration source into the xenon gas flow, and thus into the facility. In order to submerge all of the PMTs in liquid xenon, $\sim$19 kg of xenon is needed. The warm xenon gas from the storage cylinders is liquefied at the cold head of a PTR (Iwatani PDC08) with a cooling power of 24 W at 164 K. The temperature in the chamber is controlled via a heating foil wrapped around the PTR cold head and regulated by a PID controller (Cryo-con 32). The inner cryostat is wrapped in a multi-layer insulation (MLI) foil, in order to reduce the thermal radiation losses. Furthermore, the volume between the inner and outer cryostat is continuously pumped out during operation with a turbo molecular pump (Pfeiffer HiCube 80) in order to achieve a vacuum insulation.

A CF40 potted feedthrough, consisting of 52 Kapton® insulated 30 AWG solid-core wires (Accuglass 100670), is installed to the setup for the high voltage supply of the PMTs. Inside the cryostat, female pins (D-Sub, Cu alloy, Au-plated) are crimped to the Kapton® wires. The crimped wires are held in place by two PTFE connectors, which were adapted from the connector design of the XENON1T experiment [152]. Outside the cryostat, the Kapton® wires are routed into a breakout box with 13 SHV and 13 banana socket connectors. Each SHV connector is connected to two Kapton® wires, in order to separate the grounds. A CF40 potted feedthrough which consists of 48 PTFE coaxial cables (RG 196) is installed in the setup for the PMT signal readout, biasing the LED and temperature sensors readouts. Inside the cryostat, male MMCX connectors are crimped to the PTFE coaxial cables. The crimped PTFE coaxial cables are held in place by two PTFE connectors [152], which were developed for the XENON1T experiment. Outside the cryostat, the PTFE coaxial cables are routed into a breakout box with 48 BNC connectors. Each BNC connector has an insulated ground and is connected to one PTFE coaxial cable. A picture of the breakout boxes is shown in Figure 5.2 (right).

The high-voltage cables are routed into a high voltage module (Wiener MPOD), which can supply up to −3 kV and is remotely controllable. The signals of the PMTs are routed into a ten-

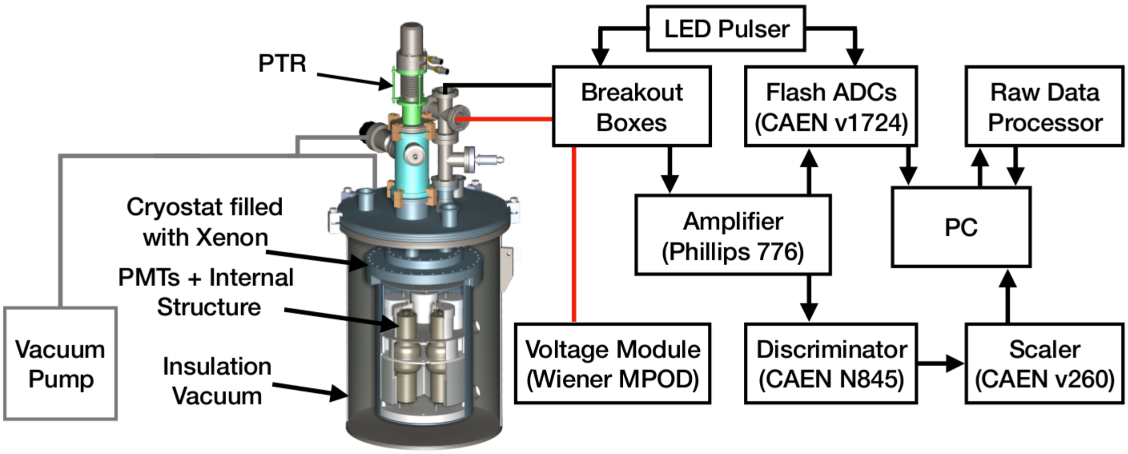

Figure 5.3: A sketch of the experimental apparatus and of the data acquisition system. The 10 PMTs are positioned in the centre of the cryostat facing each other and the cryostat is filled with xenon. The setup is cooled down with a PTR of 24 W at 164 K. The temperature in the chamber is controlled via a heating foil wrapped around the PTR cold head and regulated by a PID controller. The red lines indicate the high voltage cables and the black lines indicate the signal flow.

fold 776 Philips amplifier, duplicated, and the first copy of the signals digitised by two flash ADCs (CAEN v1724) for later analysis. The second copy is fed into a discriminator (CAEN N845) with a programmable threshold, and the resulting trigger output of the discriminator is propagated to a scaler (CAEN v260), allowing us to count the number of signals above the programmable threshold in a certain time window. The blue LED can be pulsed with a pulse generator (TTi TG5012A), which triggers the ADCs at the same time. A sketch of the experimental apparatus is shown in Figure 5.3.

In a commissioning run, 10 3-inch Hamamatsu R11410-21 PMTs for the XENONnT TPC were installed in the evaluation facility. The inner cryostat was pumped out with a turbo molecular pump down to a pressure of $\sim 10^{-5}$ mbar and filled with 1.8 bar of gaseous xenon. Afterwards, the cryostat was cooled down and filled with $\sim$ 11 kg of xenon. The pressure and temperature in the setup after the filling were (1.37 ± 0.01) bar and (176.7 ± 0.2) K, respectively. The evaluation facility offers a long-term monitoring of the gain, dark count and afterpulse rates evolution of the PMTs. Based on these parameters, the XENONnT PMTs are currently selected. The next section will describe the data acquisition system and the data processor. It is followed by a study of the micro-light emission and afterpulse evolution of the PMTs during the commissioning run.

5.2.2 Data Acquisition System and Data Processor

A data acquisition (DAQ) framework was developed in order to read out the CAEN v720, v724 and v730 VME flash ADC families, as well as the VME Scaler (CAEN V895) and discriminator (CAEN V830). The Application Programming Interface (API) of the software package and the source code can be found in [211].

The simplified Unified Modeling Language (UML) diagram of the flash ADCs is shown in Figure 5.4. The ADC modules are configured with a separate Extensible Markup Language (XML) file at the program start. Multiple ADC modules can be read out in the daisy chain mode, or independently. The baseline of the ADC can be set to a value between 0 and 2^{bits} depending on the signal polarity. The trigger to store an event from the ADC can be generated from an external trigger (NIM or TTL), a software trigger, a threshold dependent internal channel trigger or a coincidence trigger between two or more channels. All data of each event can be saved with the common trigger time stamp to a ROOT file of a predefined time period, including a configurable time span before the trigger. The

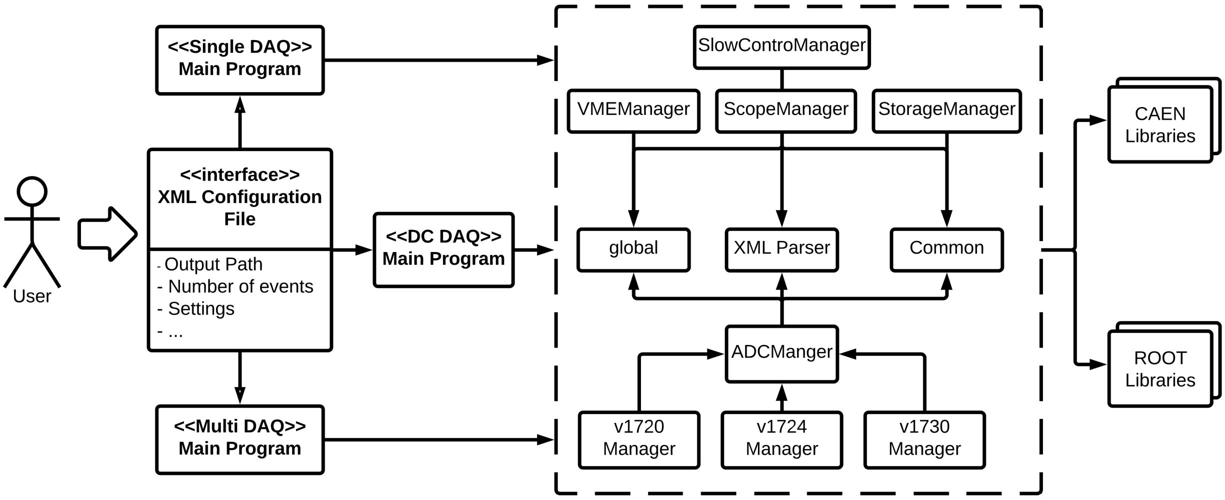

Figure 5.4: The simplified UML diagram of the developed flash ADC framework.

CAEN v1724 board offers the possibility to select the events according to a zero suppression criteria. The zero suppression allows the user to reduce the amount of data transferred from the board, by transferring only the useful information. All events are acquired with the common trigger and saved into the board memory. During the readout, the Field-Programmable Gate Array (FPGA) on the ADC board analyses the event and transfers it when the zero suppression condition is verified. The zero suppression condition can be set by a user-defined threshold on the signal. Another implemented feature of the DAQ framework is the oscilloscope mode, which displays the triggered events live on screen and can be analysed in real-time by pressing corresponding buttons on the keyboard.

A data processor was developed in order to calculate physical values from the acquired data of the flash ADCs. The API of the software package and the source code can be found in [212]. The data processor needs to be configured with the help of an XML file, which is parsed at the program start. In the first processing step, the baseline of the raw waveform is calculated using a user-defined number of samples from the left and right side of the acquired event window and subtracted from the waveform. The waveform is then inverted depending on the signal polarity. This results in a waveform, which baseline is centred around 0 mV. A peak finder algorithm starts to scan the waveform for excursions above a threshold (pulse). The threshold can be dynamically calculated from the standard deviation of the baseline or can be fixed to a static value. If a pulse exceeds the threshold, the integration of the pulse area starts. After the pulse reaches the calculated baseline, the integration is stopped. The integrated area is proportional to the signal charge, which needs to be multiplied by the following conversion factor:

$$Q = \frac{\frac{V}{2^{\text{bits}}} \times t}{e \times R}, \tag{5.1}$$

where V is the voltage range of the ADC, t is the sampling time of the ADC, e is the electron charge, bits is the resolution of the board in bits, and R is the input impedance of the ADC. In Table 5.1 the conversion factors for various ADCs are calculated. The integration window of the pulses can be customised by the user, which allows for a pulse shape analysis, as described in [213].

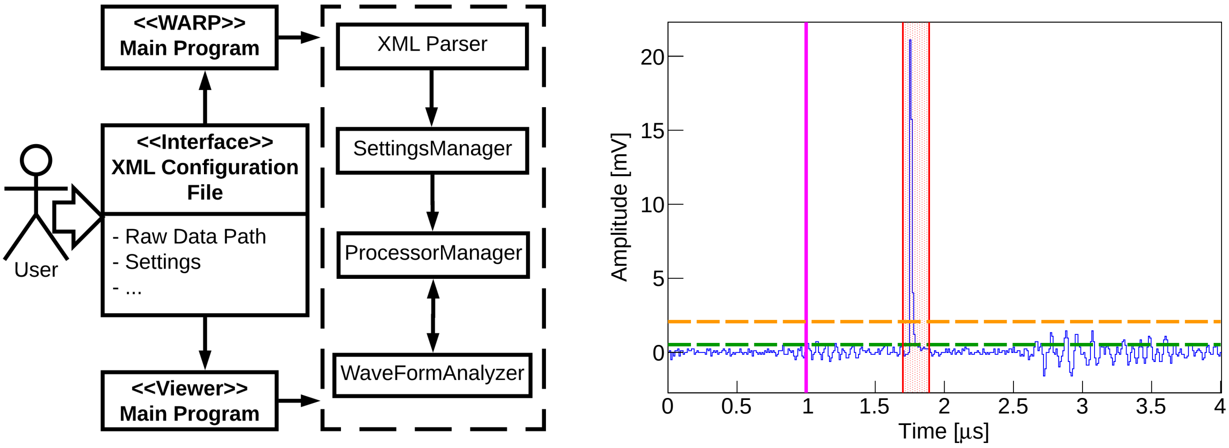

Figure 5.5: Left: The simplified UML diagram of the developed data processor. Right: A processed waveform of a R11410-21 PMT at a bias voltage of −1500 V. The event is processed with a high (orange dashed line) and a low threshold (green dashed line). The baseline is calculated within the first 1 μs (magenta solid line) and centred at around 0 mV. One pulse is integrated at $\sim$1.8 μs (red shaded area), and additional pulse properties are calculated. The electronic noise at $\sim$3 μs is rejected by the usage of a high and low threshold.

Module	Voltage Range [V]	Resolution [Bits]	Sampling Time [ns]	Conversion Factor
CAEN v1720	2	12	4	243808
CAEN v1724	2.25	14	10	171428
CAEN v1730	2	14	2	30476
PSI DRS4	1	16	0.2	381

Table 5.1: The conversion factor calculated by equation 5.1 for ADCs from different manufacturers.

In addition, it is possible to use a high and low threshold for the peak finder algorithm. The start of a possible signal is defined by an excursion above the user-defined low threshold. The possible signal is only recognised as a valid signal if the signal crosses the high threshold. Figure 5.5 (right) shows a processed event of an R11410-21 PMT with a low and high threshold configuration. The charge of the pulse, the height, width, position, rise time, decay time and other parameters such as baseline, rms and the total charge of the waveform are stored for later analysis in a ROOT tree. All the branches including their detailed description can be found in Appendix E.

5.2.3 Micro-Light Emission

The PMT arrangement in the evaluation setup in two arrays facing each other allows us to investigate the possible light emission of the PMTs before installation into the XENONnT TPC. As mentioned in section 3.4.2, high local electric fields inside the PMT can produce small discharges, and their corresponding emission of photons can reach the photocathode and generate a dark count event, which is called micro-light emission. This effect is strongly voltage dependent and can be measured at liquid xenon temperature, due to the absence of the thermionic emission. The behaviour of micro-light emission differs between the PMTs, because of the unique production process of each PMT. Therefore, all the potential XENONnT PMTs need to be evaluated with respect to their micro-light emission properties.

In the evaluation facility, each PMT from the top array faces a single PMT from the bottom

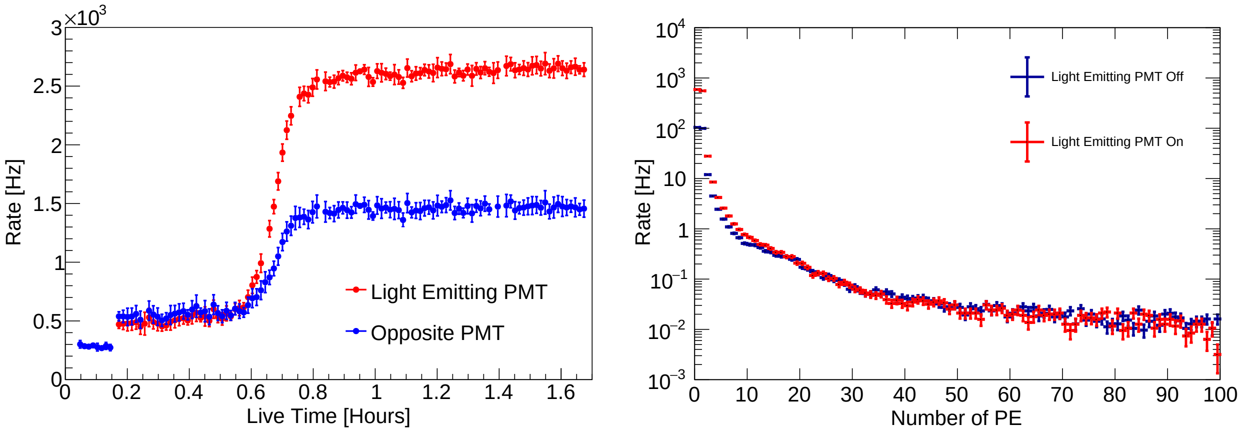

Figure 5.6: Left: The dark count rate of two facing PMTs over time. The light emitting PMT (red points) emits light as soon it is turned on, and the non light emitting PMT (blue points) receives the light. Right: The background spectrum of the non light emitting PMT (blue points) and the spectrum of the non light emitting PMT (red points) with the facing light emitting PMT at −1500V.

array at a gain of ∼ 5×10^6, which will be around the maximum operating gain in XENONnT. The dark count rate of both PMTs is monitored by counting the number of pulses per second with the scaler set at 0.3 PE threshold. Prior to the measurement, the 0.3 PE threshold was extracted from the height histogram of a gain calibration, and set with the discriminator. Figure 5.6 (left) shows the dark count rate of two facing PMTs in the commissioning run in liquid xenon (176.7 K) as a function of time. At the beginning of the measurement, the light emitting PMT is switched off, and the opposite PMT has a dark count rate of ∼ 250 Hz, which originates from thermionic emission and background events, which produce xenon scintillation light in the liquid xenon target. After the light emitting PMT is switched on, the dark count rate of both PMTs increases to a value of ∼ 500 Hz, due to the light emission. After a short period of time, the light emission of the light emitting PMT increases further, and a clear increase of the dark count rate in both PMTs can be observed.

The light emitting PMT was further investigated. To do this, the light emitting PMT was first switched off, and a background spectrum of the opposite PMT was acquired with the flash ADC at a ∼ 0.3 PE threshold. Afterwards, the PMT was turned on to −1500 V and −1600 V. At each voltage, a spectrum of the opposite PMT was acquired, which receives the light from the light emitting PMT. The background spectrum and the spectrum of the light emitting PMT at −1500 V are shown in Figure 5.6 (right). One can observe that the spectra differ significantly at the lower end from each other. The background spectrum was subtracted from the spectrum obtained when the light emitting PMT was switched on, and the resulting spectra for different operating voltages are shown in Figure 5.7. One can recognise that the primary micro-light emission is below 5 PE, mostly 1–2 PE and the rate increases with increasing voltage of the light emitting PMT, due to an increased probability of producing small discharges inside the PMT. By increasing the PMT voltage by 100 V the light emission rate increases by one order of magnitude.

The commissioning run showed that with this setup, light emitting PMTs can be efficiently detected and rejected prior the installation into the XENONnT detector. Furthermore, we verified that with decreasing bias voltage the effect of micro-light emission can be reduced by orders of magnitude. In addition, micro-light emission creates signals below 5 PE, which can be used to further reject accidental coincidences in the subsequent analysis.

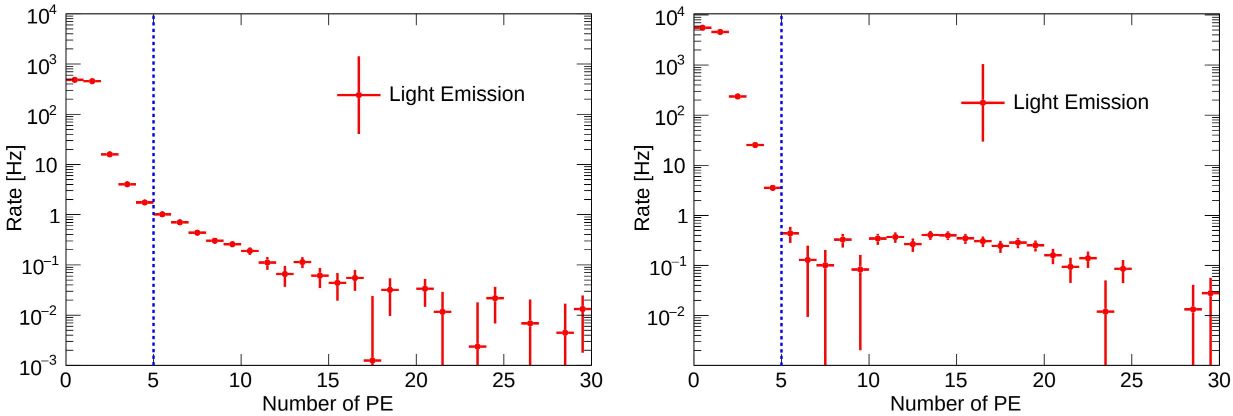

Figure 5.7: Left: Resulting micro-light emission spectrum at a PMT voltage of −1500 V (left) and −1600 V (right). The primary micro-light emission is below 5 PE (blue dashed line) and the rate increases with increasing PMT voltage (100 V) by one order of magnitude.

5.2.4 Afterpulse Evaluation

The liquid xenon setup offers an efficient way to evaluate PMTs in terms of vacuum quality. As shown in section 4.2, PMTs in XENON1T which have a vacuum leak and therefore a large amount of residual gases, behave unstably and become unusable with time in liquid xenon. In order to guarantee the stable performance of the PMTs in the XENONnT TPC, all PMTs procured for the experiment are evaluated in the liquid xenon facility. As described in section 3.4.2, there are delayed pulses (afterpulses) of the PMT with respect to the original pulse. The afterpulse of the PMT originates from the ionisation of the residual gas by photoelectrons produced by an incident photon, as well as from secondary electrons, which are back-scattered from the dynodes. The afterpulse delay time from the original signal depends on the ion mass, charge and bias voltage of the PMT. An appearance of an afterpulse at a time delay of the xenon ion (described by equation 3.4) indicates the presence of a vacuum leak and potential failure in future operation.

The PMTs inside the evaluation facility during the commissioning run were closely monitored for vacuum leak appearance. For these measurements, the PMTs were illuminated with an LED in liquid xenon. The photoelectrons generated by the LED inside the PMT ionise the residual gas, and a delay time spectrum can be measured. The LED is trigged by the data acquisition system and its intensity is set to $\sim$80 PE. A sample waveform is shown in Figure 5.8 (left). The LED illuminates the PMT $\sim 0.8\,\mu$s after the trigger. The pulse after the LED illumination can be correlated to an afterpulse generated by an ion inside the PMT. Figure 5.8 (right) shows a delay time spectrum after the LED illumination at a PMT voltage of -1500 V, acquired during the commissioning run. A 1 PE background is present after the LED illumination, which originates from dark count events and elastic back-scatters of the electrons from the dynodes. In addition, several populations can be identified at different delay times, which can be correlated to the residual molecules inside the PMT.

The delay time spectra of the PMTs were acquired at different voltages and each delay time distribution of the ions was fitted with a Gaussian function in order to extract the mean position (μ_{Ion}) and the spread (σ_{Ion}). The obtained delay times for different PMT voltages and ions can be found in Appendix F, where they are compared to the predicted delay times calculated by equation 3.4. The measured delay times show differences of up to 1–10 % from the predicted values. Therefore, the model for the delay times of the ions was determined experimentally. According to equation 3.4

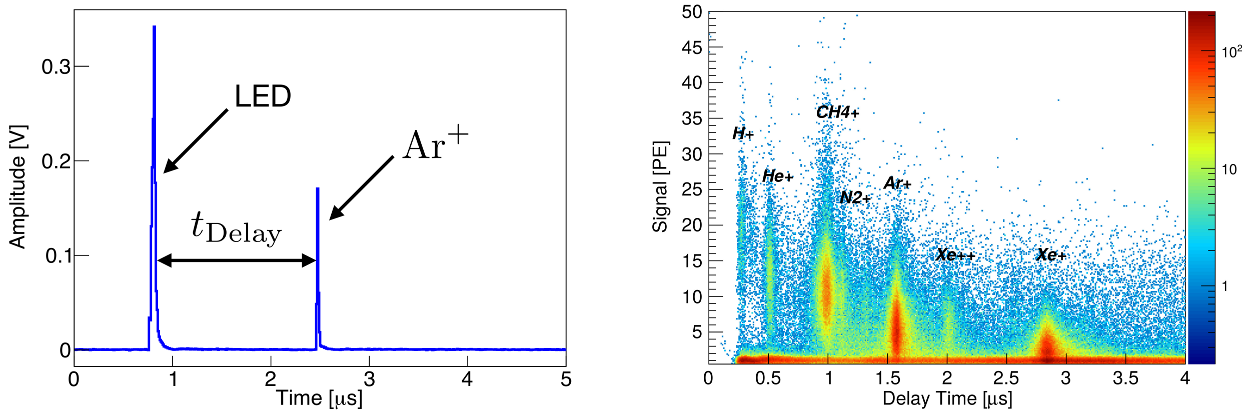

Figure 5.8: Left: Example of an afterpulse event of a R11410-21 PMT at -1500 V. The LED illuminates the PMT at $\sim 0.8\,\mu$s, and an afterpulse is observed at the delay time of argon. Right: An example of a delay time spectrum of a R11410-21 PMT at a bias voltage of -1500 V. The PMT has a vacuum leak, due to the appearance of afterpulse events with a delay time of $\sim 2.8\,\mu$s.

Ion	H^+	He^+	Ch_4^+	Ar^{++}	N_2^+	Ar^+	Xe^{++}	Xe^+
M/Q	1	4	16	20	28	40	65	131
Afterpulse Delay Time Spread [ns]	17	19	23	23	24	26	36	42
Afterpulse Delay Time at $-1500\,\mathrm{V}$ [μs]	0.26	0.51	1.0	1.11	1.31	1.58	2.02	2.85

Table 5.2: The measured afterpulse delay time and spread for different ions.

the delay times of the ions can be obtained by the following equation:

$$t_{\text{Delay}} = C(V)\sqrt{\frac{M}{Q}}\ [\mu\text{s}]\,, \tag{5.2}$$

where $C(V)$ is a constant depending on the PMT voltage, M is the number of nucleons in the ion, and Q is the ionisation number of the ion. The constant $C(V)$ was determined by fitting equation 5.2 to the experimentally measured ion delay time at different PMT voltages. In Figure 5.9 (left) a sample ion delay time as a function of Q/M at a PMT voltage of $-1500\,\mathrm{V}$ is shown. The delay times are fitted with equation 5.2 (red curve) in order to determine the constant C for different PMT voltages. In Figure 5.9 (right) the obtained constant C as a function of PMT voltage is shown. The data points were fitted with a polynomial (red curve) in order to have the constant C at different operating voltages. The constant C was measured for the 3-inch Hamamatsu R11410-21 PMT to be:

$$C(V) = 0.5\,V^2 - 2.4\times10^{-4}\,V + 5.1\times10^{-8}, \tag{5.3}$$

where V is the PMT voltage in standard units. In addition, the spread of the delay time of a specific ion is independent of the PMT voltage. In Table 5.2, the afterpulse delay times, calculated with equation 5.2, at a PMT voltage of $-1500\,\mathrm{V}$ are shown, along with the experimentally measured invariant afterpulse spread. The experimentally determined afterpulse delay times and spread for different PMT operating voltages are used for the calculation of the ion-specific afterpulse rates of the XENON1T and XENONnT PMTs.

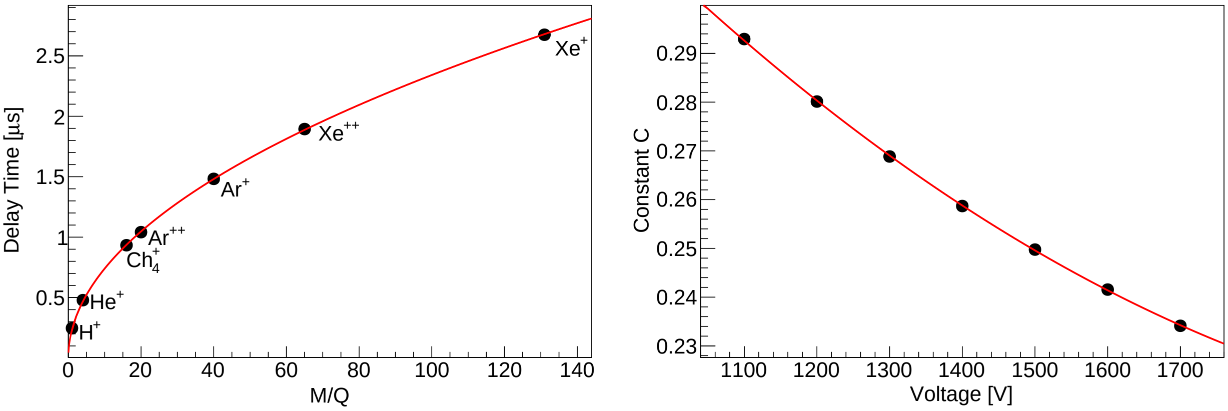

Figure 5.9: Left: The measured afterpulse delay time as a function of M/Q (black points) at a PMT voltage of $-1700\,\mathrm{V}$. The data points were fitted with equation 5.2 (red curve), in order to extract the constant C. Right: The measured constant C as a function of PMT voltage (black points). The data points were fitted with a polynomial (red curve), in order to extract the fit constant $C(V)$ for different operating voltages.

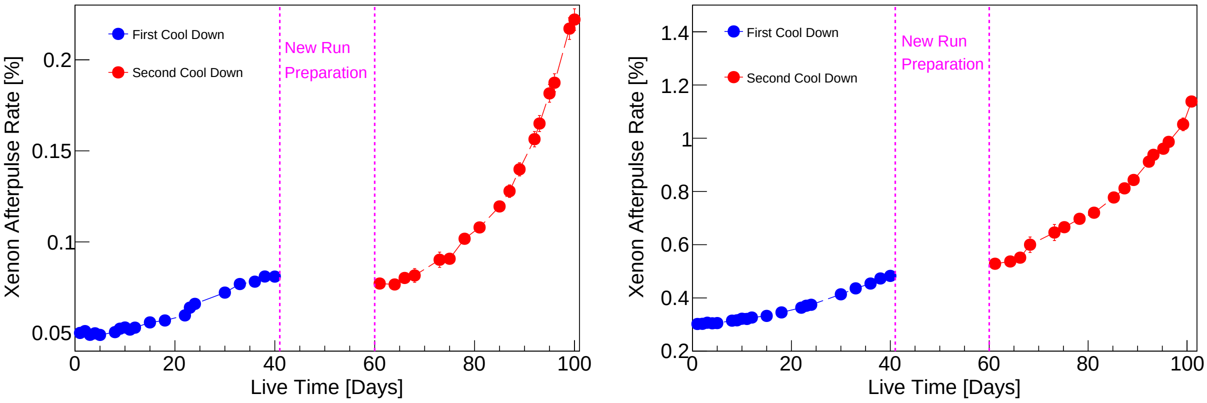

Figure 5.10: The xenon afterpulse rate of two PMTs (left and right) as a function of time in liquid xenon (176.7 K). The PMTs opened a leak during the first cooldown, which increases significantly after the second cooldown. The leak rate differs between the PMTs, due to the unique production process.

Furthermore, in order to evaluate the effect of cooling cycles on the PMT stability, the setup was warmed up, and the xenon recuperated. Afterwards, the setup was pumped out, cooled down and filled with 11 kg of xenon again. Two PMTs, which developed a leak in the first cooldown were continuously monitored in terms of their xenon afterpulse rate, which is proportional to the leak rate as discussed in section 4.2. The xenon afterpulse rate is defined by the following formula:

$$AP_{\mathrm{Xe}} = \frac{N_{\mathrm{xe}}}{\mu_{\mathrm{LED}} \times N_{\mathrm{events}}}, \tag{5.4}$$

where N_{xe} is the number of events in a $3\sigma_{\mathrm{xe}}$ time window around the xenon afterpulse delay time above 2.5 PE, μ_{LED} is the mean number of photoelectrons induced by the LED, and N_{events} is the number of LED pulses above 3 PE. The evolution of the xenon afterpulse rate in liquid xenon during two cooling cycles is shown in Figure 5.10. The time between the two cooldowns was used for pumping out the setup, pre-cooling and xenon filling. The xenon afterpulse rate increases significantly after the second cooldown. The slope of the data points changes from a nearly linear dependency in the first cooldown to an exponential dependency, which can be explained by an increased opening of the vacuum leak, due to the thermal stress on the PMT.

A large fraction of the XENON1T PMTs will be reused for XENONnT. As shown in section 4.2, some of these PMTs have a small leak rate. In order to avoid a further increase of the leak rate in XENONnT, even PMTs which have a xenon afterpulse rate larger than the detection sensitivity of 0.01 % will be replaced with new ones. All PMTs must be evaluated in terms of their gain, dark count rate, light emission and vacuum quality in the described evaluation facility.

5.3 Dual Channel Amplifier

The XENONnT experiment becomes compatible in rare event searches at higher energies than the WIMP recoil spectrum, due to the increased target mass. The xenon isotope ^{136}Xe is a potential neutrinoless double beta decay ($0\nu\beta\beta$) candidate, which has a $\sim$8.9 % abundance in natural xenon and is an example of a physics channel at high energies. The region of interest for the $0\nu\beta\beta$-decay channel of ^{136}Xe is at 2.458 MeV (Q-value), which is three orders of magnitude higher than the dark matter search region. The observation of the $0\nu\beta\beta$-decay would prove that neutrinos have a

Majorana mass component and the lepton number is not conserved. Therefore, a linear XENONnT detector response is required, in order to study different physics channels at various energies.

The Phillips 776 PMT signal amplifier, currently used in XENON1T (see section 3.1), is a good and extremely fast device. However, S1-S2 signals higher then the expected WIMP recoil spectrum $\sim$(3–40 keV) start to saturate the ADC and the amplifier, which makes additional signal corrections necessary. Considering this, a low-noise dual channel NIM amplifier module for the XENONnT experiment was developed, which will be discussed in the next sections. The amplifier is optimised for both, the keV energy-range for the WIMP search and the MeV energy-range for other physics channels like the $0\nu\beta\beta$-decay search.

5.3.1 Dual Channel Amplifier Design

The developed dual channel NIM module amplifier provides 16 independent, directly-coupled low-noise and low crosstalk amplifier boards. Each board has one input channel for the PMT signal, a high-gain output (HG) with a non-inverting voltage gain of 20 (gain 10 into 50 Ω load) and a low-gain output (LG) with a non-inverting voltage gain of 1 (gain 0.5 into 50 Ω load). The high-gain stage operates from direct current to 250 MHz, the low-gain stage from direct current to 200 MHz. Both stages have 50 Ω output impedance and are designed to drive 50 Ω loads. Therefore, the first output channel offers a ten-fold amplification of the signal for the dark matter search, and the second output a 0.5 attenuation of the signal for the MeV energy range. The specification of the developed amplifier module, including the electronic schematic can be found in Appendix G.

The experience from XENON10 [214], XENON100 [215] and XENON1T [144] showed that an amplification of the PMTs signals by a ten-fold amplifier is sufficient in order to achieve an excellent signal to noise ratio, and therefore to reach a very low detector threshold at the level of 0.3 PE per PMT. The operational amplifier OPA847 from Texas Instruments was chosen for the high gain output channel with a ten-fold amplification factor (into 50 Ω load). This operational amplifier offers an outstanding linearity over the whole ADC range, low noise, low power consumption, excellent recovery after saturation and a negligible drift over temperature.

As shown in section 3.4.3, the XENON1T PMTs response is linear over the ADC range (CAEN v1724) until the point of the ADC saturation. The saturation point of the ADC depends on the

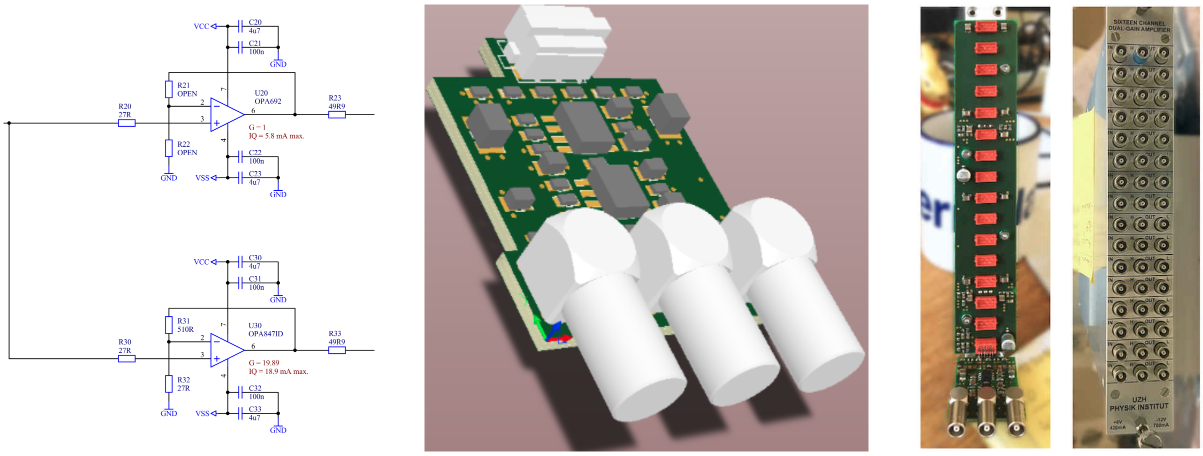

Figure 5.11: Left: The schematic of the XENONnT low and high gain amplifier channel. The high gain output channel corresponds to a ten-fold amplification and the low gain output channel corresponds to a 0.5 attenuation when driven with a 50 Ω load. Centre: CAD drawing of the PCB of a single amplifier channel. Right: The XENONnT amplifier without and with aluminium casing.

PMT Gain [10e6]	1	1.5	2	2.5	3	3.5	4	4.5
ADC Saturation [PE]	280868	187245	140433	112347	93622	80248	70217	62415

Table 5.3: ADC saturation point for different PMT gains without an amplifier for a typical S2 signal with a width of 1 μs, calculated by equation 3.5.

PMT gain and can be calculated with equation 3.5. In Table 5.3, the saturation points for different PMT gains are listed. The XENONnT PMTs will use the same base design as in XENON1T, and therefore the ADC voltage range is the limitation for physics at high energies (see section 3.4.3 for the discussion). The maximum expected S2 signal size for the XENONnT PMTs in the bottom PMT array at the Q-value of the $0\nu\beta\beta$-decay can be estimated with the following formula:

$$S2_{\text{Top}} = C_y \times \text{LCE} \times Q = 184350\,\text{PE}, \qquad (5.5)$$

where the LCE of the leading PMT is assumed to be $\sim 15\,\%$, the S2 charge yield C_y is assumed to be $\sim 500\,\text{PE/keV}$, and the Q-value is 2.458 MeV for the $0\nu\beta\beta$-decay of ^{136}Xe.

This conservative estimate is higher than the maximum recordable signal as listed in Table 5.3. Therefore, the low gain amplifier output channel was designed to have an impedance matched 0.5 attenuation of the signal. In this configuration, any high energy signal can be digitised without saturating the ADC. The operational amplifier OPA692 from Texas Instruments was chosen for the low gain channel and offers a good linearity over the whole PMT response, low noise, low power consumption, excellent recovery after saturation and a negligible drift over temperature.

The signal from each PMT will be passively split into the above mentioned different operational amplifiers on a PCB board. Each amplifier board is a print of the schematic as shown in Figure 5.11 (left). The amplifier board has a socket, which will be plugged into a separate PCB in order to supply the operational amplifiers with the necessary power. A single amplifier board with the electronics on top is shown in Figure 5.11 (centre). The whole amplifier module was designed to match the NIM standard, in order to use the already available infrastructure of the XENON1T experiment. Therefore, a maximum of 16 amplifier boards can be plugged into the same backplane of the NIM crate. The dual channel NIM amplifier module with and without aluminium housing is shown in Figure 5.11 (right). In the final amplifier version, the LEMO connectors were replaced with SMB connectors in order to achieve a better signal quality. The power consumption of the 16 channel

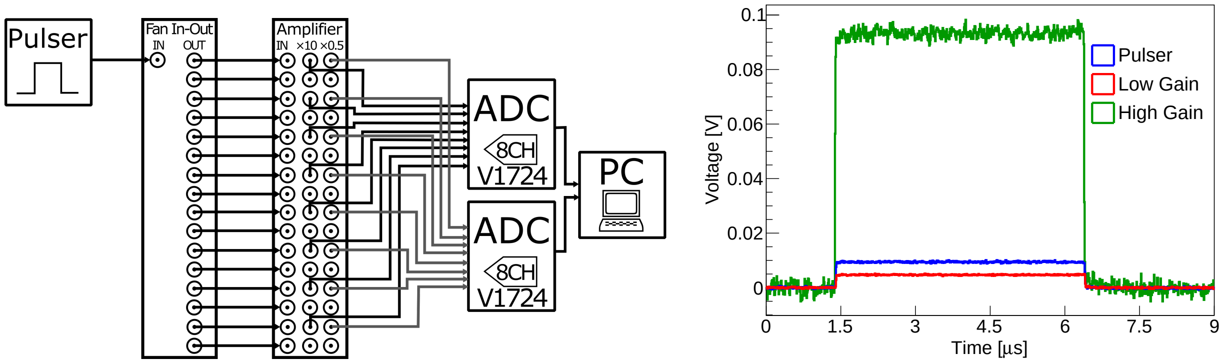

Figure 5.12: Left: Experimental setup of the amplifier linearity measurement. The explanation is given in the text. Right: The acquired raw waveforms from the pulser (blue), the high gain output channel (green) and the low gain output channel (red). The high gain output channel corresponds to a ten-fold amplification and the low gain output channel corresponds to a 0.5 attenuation.

dual channel amplifier module in the idle mode is ~400 mA on the −12 V line of the NIM crate. This value originates from the summation of the leakage current through all operational amplifiers. In total, 32 dual channel NIM amplifier modules were produced for the PMT signal amplification of the XENONnT experiment. The power consumption of all 32 amplifier modules in the idle mode is therefore ~54 W.

The next sections present the results of the dual channel NIM amplifier module evaluation in terms of signal quality.

5.3.2 Dynamic Range

The output linearity of the dual channel NIM module amplifier was verified in the experimental setup shown in Figure 5.12 (left). A pulse generator (TTI TG5012A) was used to generate square pulses. The pulse frequency was set to 1 kHz, the width to 5 μs and the pulse height was varied in 10 mV steps. This condition is far beyond the expected signal size and rate in XENONnT, in order to conservatively validate the amplifier module. The square pulse was duplicated 16 times by two FAN-IN FAN-OUT units (CAEN N625) and fed into each input channel of the amplifier module. The high and low gain channel of every second amplifier board and the original pulse were digitised by two CAEN v1724 flash ADCs. The ADCs were triggered with the TTL signal of the pulse generator. For each input pulse height, 20 000 events were acquired, stored and processed by the data processor described in section 5.2.2. The acquired waveforms of a specific pulse height are shown in Figure 5.12 (right).

The mean input and output pulse heights were calculated for each input pulse height by fitting the pulse height distributions with Gaussian functions. As long as the amplifiers have a linear response, the mean output pulse height is given as a product of the mean input pulse height and the amplification factor, which can be expressed by the following formula:

$$\mu_{\text{output}} = \mu_{\text{input}} \times A, \tag{5.6}$$

where μ_{output} is the mean output pulse height, μ_{input} is the mean input pulse height, and A is the amplification factor. The linearity result for one board is shown in Figure 5.13. The high and low gain output channels are linear over the whole range of the measurement. The amplification factor of the high gain output was measured to be ~10 and the amplification factor of the low gain output

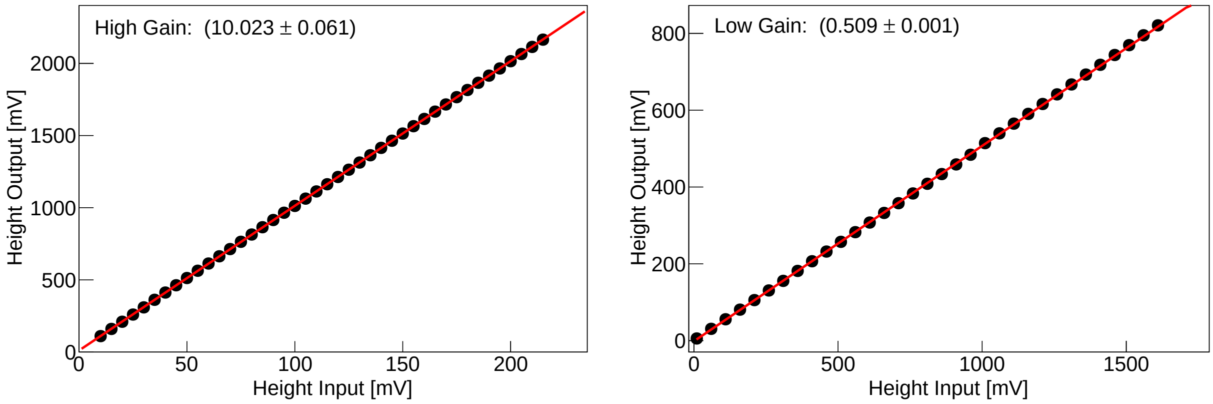

Figure 5.13: The mean output pulse height as a function of mean input pulse height for the high gain (left) and low gain (right) channels of one amplifier board. The amplification factor varies within ~1 % across all channels of the NIM module.

was measured to be ~0.5. The amplification factor between the 16 different boards of the dual channel NIM module amplifier varies within ~1 %, which is in agreement with the tolerances of the used electronic components. Given the high load during the measurement, there was no observable crosstalk between the different amplifier boards. Furthermore, no signal distortions were found in the low and high gain output channels.

In the next section, the dual channel NIM amplifier module will be verified with the fast PMT signals (~30 ns) in the low and high energy region.

5.3.3 PMT Performance

The performance of the dual channel NIM amplifier module was verified with a Hamamatsu R11410 - 21 PMT. The experimental setup is shown in Figure 5.14 (left). The PMT is centred in a light-tight box facing a blue LED ($\lambda \sim 470$ nm). The PMT signal is amplified, and both output channels are digitised with a CAEN v1724 flash ADC. The LED and ADC are triggered simultaneously by the external pulse generator (TTI TG5012A).

In the first step, the gain of the PMT was measured with the dual channel NIM amplifier module and with the Philipps 776 amplifier. For this purpose, 500 000 events with an LED intensity of around 1 PE per trigger were acquired. An example waveform is shown in Figure 5.14 (right). The measurement was repeated for different applied voltages, and the PMT gain was extracted with the fitting procedure as described in section 3.4.4.

The resulting gain as a function of voltage for the dual channel NIM amplifier module and the Philips 776 amplifier is shown in Figure 5.15 (left). The Philips 776 amplifier and the dual channel NIM amplifier module agree in the measured gain. The measured data points of each amplifier are fitted with equation 3.2. The parameter k was measured to be (0.66 ± 0.01), which is in agreement with the value obtained from XENON1T ($k_{\mathrm{XENON1T}} = (0.67 \pm 0.01)$). The fit is also consistent within the error bars for both amplifiers. Therefore, the same performance in the low energy region with the developed dual channel NIM amplifier module as with the Philips 776 amplifier is guaranteed.

In the second step, the PMT at a gain of $(4.81 \pm 0.03) \times 10^6$ was illuminated with different LED voltages, and the number of detected photoelectrons in the high and low gain output channel of the dual channel NIM amplifier module were recorded. The LED pulse width was fixed to 250 ns, and the pulse frequency was fixed to 100 Hz in order to get a linear response from the PMT (see section

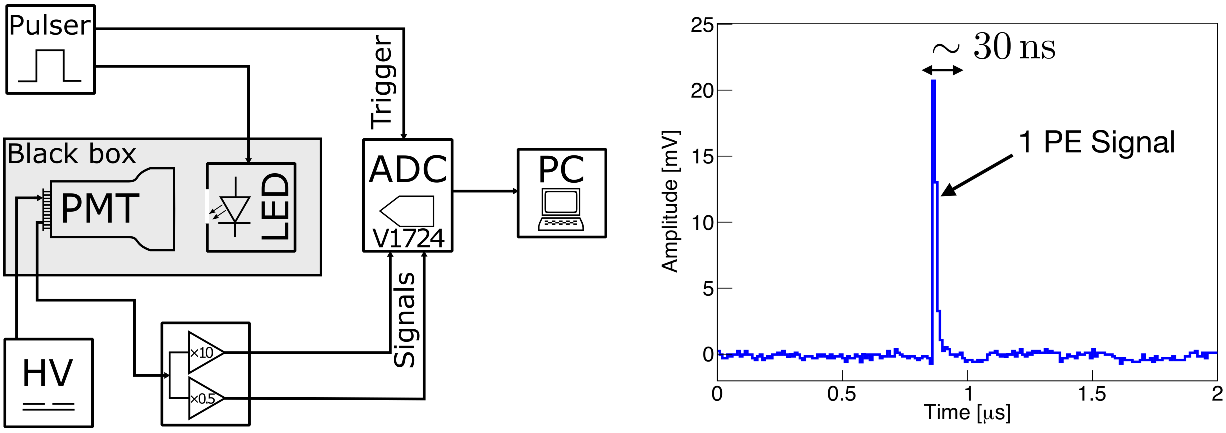

Figure 5.14: Left: The setup to evaluate the high and low gain amplifier output channels with a PMT. The explanation is given in the text. Right: The Hamamatsu R11410-21 PMT response to one photoelectron at the high gain output channel at −1500 V. The signal is around 30 ns long.

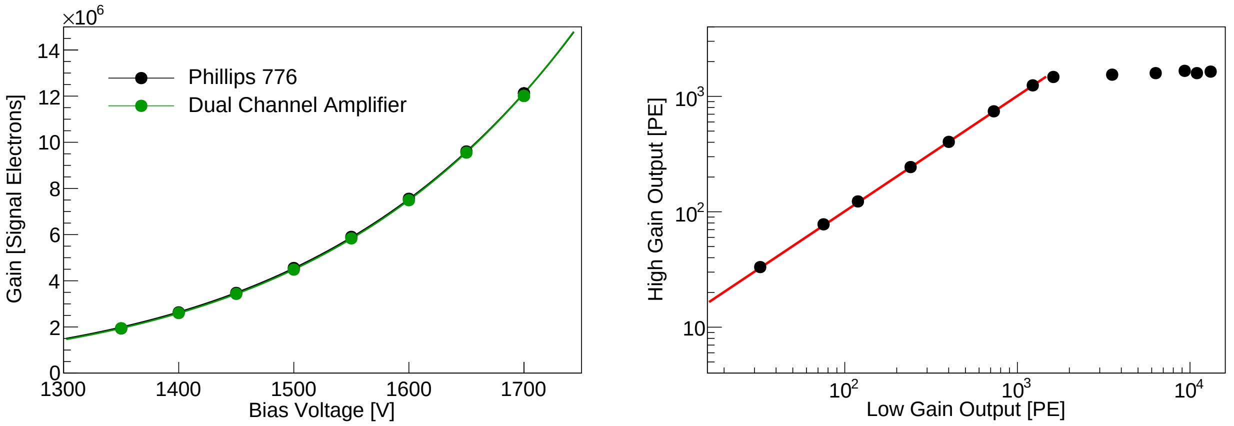

Figure 5.15: Left: The PMT gain as a function of bias voltage measured with the Philips 776 and dual channel NIM amplifier module. Right: The mean number of detected photoelectrons in the high gain channel as a function of detected photoelectrons in the low gain channel. The data points until the saturation of the high gain output channel were fitted with a linear function (red curve) in order to determine the proportionality between the channels.

3.4.3). In this configuration, the high gain and low gain output channels are expected to saturate at ∼ 1 400 PE and ∼ 29 000 PE, respectively, as calculated with equation 3.5.

The mean number of detected photoelectrons was extracted by fitting Gaussian function to the number of photoelectron distributions at every LED voltage setting. The mean number of detected photoelectrons in the high and low gain output channels were correlated as shown in Figure 5.15 (right). As long as the high gain output channel is not saturated, the mean number of detected photoelectrons in both channels is the same. As soon as the high gain output channel starts saturating the ADC, the mean number of detected photoelectrons in this channel stays constant. However, the mean number of detected photoelectrons in the low gain output channel continues to increase for increasing LED voltages. In this setup, the pulse generator was limited by the maximum output voltage driving the LED. Therefore, we reached a maximum mean number of ∼ 14 000 detected photoelectrons in the low gain channel, which is one magnitude higher than the mean number of detected photoelectrons in the high gain channel. The data points until 1 400 PE in the high gain output channel were fitted with a linear function, and the proportionality between the low and high gain output was measured from the slope to be (1.01 ± 0.04). That verifies that the low gain channel works reliable and can be used for the signal reconstruction at any energies.

This section concludes the verification of the developed dual channel module NIM amplifier. The amplifier module works as expected in the low and high energy region without any PMT signal distortion and saturation effects. After the successful verification phase, the amplifiers were mass produced (in total 32 modules) and will be integrated into the XENONnT experiment within the installation phase of the TPC.

5.4 Cryogenic Linear Amplifier

Signal damping and noise pickup in coaxial signal cables depend on the cable length, the cable material and the signal frequency. In current and future large-scale direct dark matter experiments, the coaxial signal cables from the light detector sensors will be several meters long and the noise pickup and signal damping will become significant before the amplification stage. Therefore, XENON1T uses specialised electronic noise filter boxes and a high operating voltage of the PMTs in order to achieve a sufficient SPE acceptance.

A way to solve this effect is to use an amplifier, which is cryogenically resistant and directly coupled to the PMT readout base. This has the advantage to lower the bias voltage of the PMT in a dark matter search experiment by increasing the gain of the amplifier without additional noise pickup from the cables, which results in an increase of the SPE acceptance. Furthermore, lowering the operational voltages has also the advantage that the particular effect of micro-light emission from the PMTs becomes negligible (described in section 5.2.3). In this section, a newly developed low noise cryogenic PMT amplifier, which can be stably operated in liquid xenon, will be discussed.

5.4.1 Cryogenic Amplifier Design

The output of the developed PMT readout base provides an independent, directly-coupled and low-noise amplifier. The amplifier is directly coupled to the output of the voltage divider network (described in section 3.4.1) and offers a high-gain output (HG) with a non-inverting voltage gain of 20 (gain 10 into 50 Ω load). The cryogenic amplifier operates from direct current to 250 MHz and has a 50 Ω output impedance in order to drive 50 Ω loads. Therefore, the signal amplification with a 50 Ω load is a ten-fold amplification, which is identical as the signal amplification in XENON10, XENON100 and XENON1T. The operational amplifier OPA847 was chosen as the cryogenic amplifier, due to its good signal linearity over the whole ADC range, low noise, power consumption, excellent recovery after saturation and negligible drift with temperature, as shown in section 5.3.

The schematic of the voltage divider network in connection to the cryogenic amplifier is shown in Figure 5.16 (left). The cryogenic amplifier is directly coupled to the output of the voltage divider network in order to reduce electromagnetic noise pickup. The amplifier needs to be externally biased with a 10 V voltage difference, depending on the PMT signal polarity. The schematic was printed on a standard PCB and is shown in Figure 5.16 (right). It is only slightly larger than the PCB which is used for the XENON1T PMT readout (Figure 3.6, right) and can be therefore easily placed on the existing PMTs. The signal is read out with a coaxial PTFE cable. The voltage for the PMT and the amplifier is provided with Kapton® insulated wires.

The performance of the developed cryogenic amplifier in liquid xenon will be discussed in the next section.

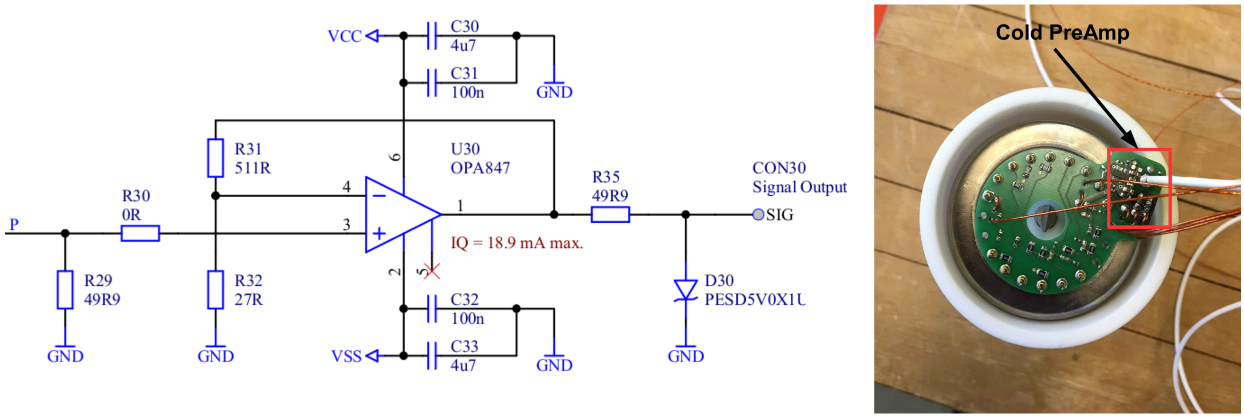

Figure 5.16: Left: The schematic of the cryogenic amplifier. Right: Picture of the PMT voltage divider network PCB with the connected cryogenic amplifier placed on a Hamamatsu R11410-21 PMT.

5.4.2 Performance in Liquid Xenon

The evaluation of the cryogenic amplifier was performed in the single-phase liquid xenon detector described in section 5.2.2. The Hamamatsu R11410-21 PMT with the cryogenic amplifier readout base was positioned at the bottom of an aluminium filler, and the setup was filled with 11 kg of xenon. That ensured that the PMT and the cryogenic amplifier were completely submerged in the liquid. The xenon was constantly purified by circulating it through a hot metal getter, in order to remove electronegative impurities such as oxygen, and therefore to increase the overall light yield of the setup. The amplified signal from the cryogenic amplifier was digitised by a CAEN v1724 flash ADC and the data was processed by the data processor described in section 5.2.

As a first step, we measured the gain of the PMT with the cryogenic amplifier in liquid xenon. The ADC was operated in the self-trigger mode with a constant threshold of ∼ 0.3 PE. The recorded events originate from PMT dark counts and xenon scintillation light produced by particle interactions inside the liquid xenon. From the regularly acquired spectrum, the gain was extracted using the fitting procedure to the spectrum, as described in section 3.4.4. The cryogenic amplifier worked stably in liquid xenon at a temperature of 185.5 K, as shown in Figure 5.17 (left). The mean measured gain was 4.99×10^6 with an rms of 0.03×10^6. The gain did not drift during the period of measurement. We also measured the pulse rate of the PMT as a function of time, as shown in Figure 5.17 (right). The pulse rate increases with time, due to the continuous purification of the xenon, and hence the increase in light yield. The developed cryogenic amplifier performed in a stable mode at any time of the measurement.

In order to evaluate the cryogenic amplifier performance with larger signals, we injected the metastable ^{83m}Kr calibration source into the liquid xenon by recirculating the xenon gas through a mixing chamber, which houses a ^{83}Rb source. The metastable ^{83m}Kr is 41.5 keV above the ground state and decays through emission of 32.1 keV and 9.4 keV conversion electrons with a half-life of 1.83 h to the ground state. In this measurement, the ADC was operated in the self-trigger mode with a constant threshold of ∼ 2.5 PE in order to reject background events and therefore to save drive storage space. Figure 5.18 (left) shows the two signals (32.1 keV and 9.4 keV) from the ^{83m}Kr decay using the cryogenic amplifier.

The acquired events were processed, and the ^{83m}Kr events were selected via a set of basic data

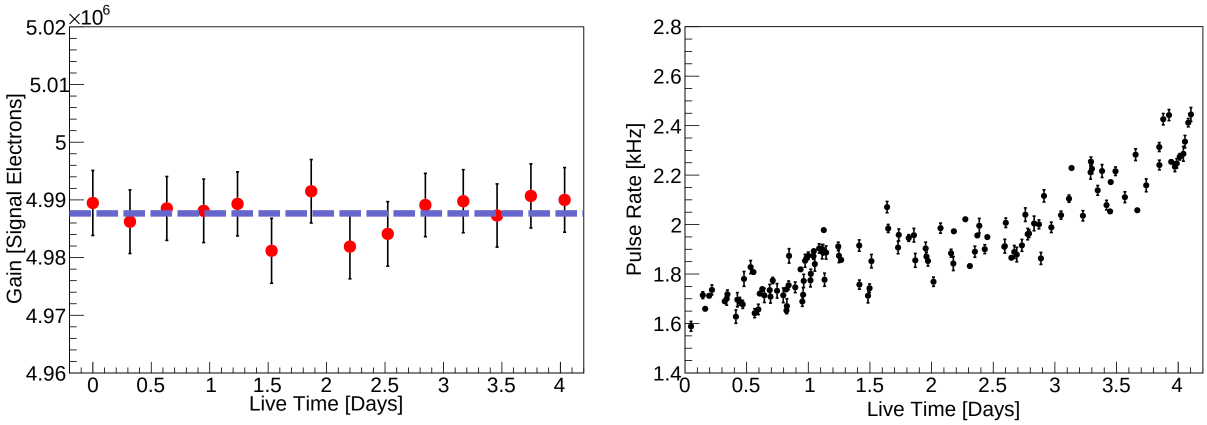

Figure 5.17: Left: Measured PMT gain as a function of time with a cryogenic amplifier in liquid xenon. The blue dashed line indicates the mean gain value. Right: The pulse rate of the PMT as a function of time. The pulse rate increases due to the continuous purification of the xenon, and hence the light yield.

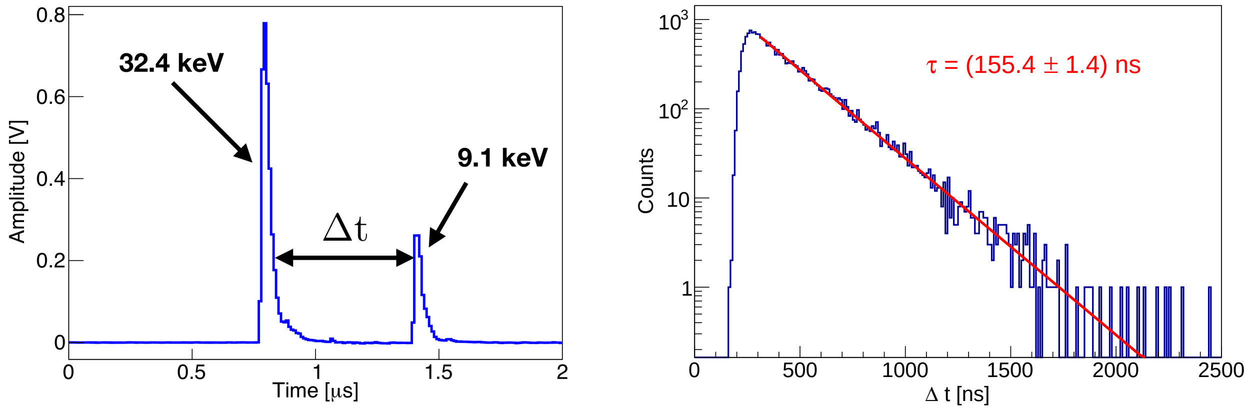

Figure 5.18: Left: A sample waveform of $^{83\mathrm{m}}$Kr decay through 32.1 keV and 9.4 keV conversion electrons. Right: Delay time distribution between the 32.1 keV and 9.4 keV conversion electrons. The distribution was fitted with an exponential function (red curve), in order to obtain the half-life of the 9.4 keV ^{83}Kr excited state.

quality cuts. Figure 5.18 (right) shows the distribution of the delay time between the 32.1 keV and 9.4 keV signal. An exponential fit to the distribution led to a half-life of the 9.4 keV ^{83}Kr excited state of (155.4 ± 1.4) ns, which is in agreement with previous measurements [216].

The development of the cryogenic amplifier is of general interest for future xenon-based detectors. The DARWIN [217] (DARk matter WImp search with liquid xenoN) experiment will be the ultimate dark matter detector, which will probe the entire parameter region for all WIMP masses until the neutrino interactions with the target become an irreducible background [218]. DARWIN will house an active target mass of ~ 40 t liquid xenon and will be able to probe the WIMP-nucleon cross sections down to $\sim 10^{-49}\,\mathrm{cm}^2$ for a WIMP mass of ~ 50 GeV. The developed cryogenic amplifier can be used for the photosensor readout of the DARWIN experiment, which has the advantage to overcome the issue of signal damping and noise pickup. In addition, an external amplifier would not be needed, because the cryogenic amplifier (OPA847) performs in the same way as the external linear amplifier of XENON1T, which was verified in section 5.3. The power consumption of one cryogenic amplifier is ~ 0.2 W, which needs to be considered in the design of the cryogenic system. Furthermore, the low radioactivity of the cryogenic amplifier needs to be proven in the future.

As shown in section 4.2, PMTs show some disadvantages as photosensors in noble liquid TPCs and contribute a significant fraction to the radiogenic background [140]. A potential solid-state alternative for the PMTs will be the silicon photomultipliers (SiPMs), which are under consideration for DARWIN. They allow for an increase of the photosensitive area coverage of the TPC, due to their compact geometry. In the next chapter, the R&D work to identify a suitable VUV-sensitive SiPM will be discussed. Furthermore, the design for a liquid xenon-based dual-phase TPC employing SiPMs for the light detection will be presented.

"If I have seen further it is by standing on the shoulders of giants."

Isaac Newton

CHAPTER 6

Silicon Photomultipliers for Future Xenon Experiments

The DARWIN detector will be the ultimate dark matter xenon-based dual-phase TPC, which will probe the entire parameter region for WIMPs, until the neutrino interactions with the target become an irreducible background [218]. The DARWIN TPC will house an active target mass of $\sim 40\,\mathrm{t}$ liquid xenon and will be able to probe the WIMP-nucleon cross sections down to $\sim 10^{-49}\,\mathrm{cm}^2$ for a WIMP mass of $\sim 50\,\mathrm{GeV}$. The DARWIN collaboration is currently in the process of performing the necessary R&D towards a multi-ton liquid xenon dark matter detector. In order to reduce the radiogenic background and increase the overall LCE of the TPC, a potential solid-state alternative for PMTs are the silicon photomultipliers (SiPMs), due to their compact geometry.

In section 6.1 we will give an introduction to the DARWIN experiment. It is followed by section 6.2, which will introduce the different SiPM characteristics and present a suitable VUV-sensitive SiPM for the DARWIN experiment together with the results of the detection probability and dynamic range measurements at 300 K. In section 6.3 we will introduce the developed cryogenic experimental setup and present the performed temperature dependent measurements of the VUV-sensitive SiPM in a gaseous nitrogen atmosphere. The chapter will be concluded with the development and characterisation of a SiPM array for the Xurich xenon-based dual-phase TPC, in order to verify the suitability of SiPMs for the DARWIN experiment.

6.1 The DARWIN Experiment

The DARWIN experiment will be designed to address different science channels with a xenon-based dual-phase TPC, using 50 t liquid xenon as a total mass. The primary goal of DARWIN will be to serve as the ultimate dark matter detector with a low energy threshold and an ultra-low background level [217]. The sensitivity for the spin-independent WIMP-nucleon cross section interactions will be improved in the DARWIN experiment by ten-fold, in comparison to XENONnT. The detector will be sensitive to WIMPs masses above 5 GeV and will probe the WIMP-nucleon cross sections down to $\sim 10^{-49}\,\mathrm{cm}^2$ for a WIMP mass of $\sim 50\,\mathrm{GeV}$. Overall, DARWIN will be limited in sensitivity by the neutrino background, which will start dominating the recoil spectrum at low cross sections [219]. In Figure 6.1 (right) the predicted DARWIN median sensitivity for an exposure of 200 $(\mathrm{t}\times\mathrm{y})$ is shown.

Another goal with DARWIN will be to measure the low-energy solar neutrino flux (*pp* and ^{7}Be-neutrinos) with a statistical precision below 1 %. This flux can be measured by observing the elastic neutrino-electron scattering in liquid xenon, which is given by the following process [220]:

$$\nu + e^- \rightarrow \nu + e^- \tag{6.1}$$

Furthermore, the standard model process of coherent neutrino-nucleus scattering (CEνNS) will also be observable with DARWIN, which was for the first time measured by the COHRENT collaboration [201]. The largest fraction of the CEνNS rate will come from the ^{8}B solar neutrinos, which will introduce a low energy nuclear recoil signal:

$$\nu + N \rightarrow \nu + N \tag{6.2}$$

In addition, the DARWIN TPC will contain more than 3.5 t of ^{136}Xe, which can be used for the search of the neutrinoless double beta decay. Other rare event searches with DARWIN will include the observation of supernova neutrinos, axions and axion-like-particles [217].

The DARWIN collaboration is currently in the process of performing several R&D projects in order to study different detector designs and address open questions. The DARWIN detector will be based on the technique of the dual-phase TPC, as described in section 1.4. The TPC will have a diameter of $\sim$2.6 m with a drift length of $\sim$2.6 m. The baseline design foresees usage of the same existing state-of-the-art components as in XENONnT. A first detector design is shown in Figure 6.1 (left). The light readout is based on two photosensor arrays equipped with 3-inch diameter PMTs above and below the liquid xenon target, which would require $\sim$1800 sensors to cover the entire diameter surface. In order to reach a low energy threshold, a two or three fold coincidence among the PMTs is needed, and the light and charge yields need to be maximised.

PMTs show disadvantages (vacuum leaks, light emission and limited detector granularity) in noble liquid TPCs, and contribute significantly to the radiogenic background [140], due to (α,n)-reactions inside the ceramic of the PMT stem. A potential solid-state alternative for the PMTs are the SiPMs, which are under consideration for DARWIN. Their advantages are in their compact geometry, low operating voltage, simplicity of readout and excellent single photoelectron resolution. Additional considerations are low radioactivity levels, decreasing costs and scalable mass production. They would allow an increase of the light yield by equipping the TPC with a 4π coverage, due to their compact geometry. In addition, they offer a high detector granularity in the top array for the x-y position reconstruction and help to further reject surface events from the detector walls.

VUV-sensitive SiPMs are available from different vendors and have a comparable gain to currently used PMTs. Additional SiPM requirements are low dark count rates, required to minimise the rate of accidental coincidences at low energy thresholds, and good signal-to-noise ratio, for a high SPE

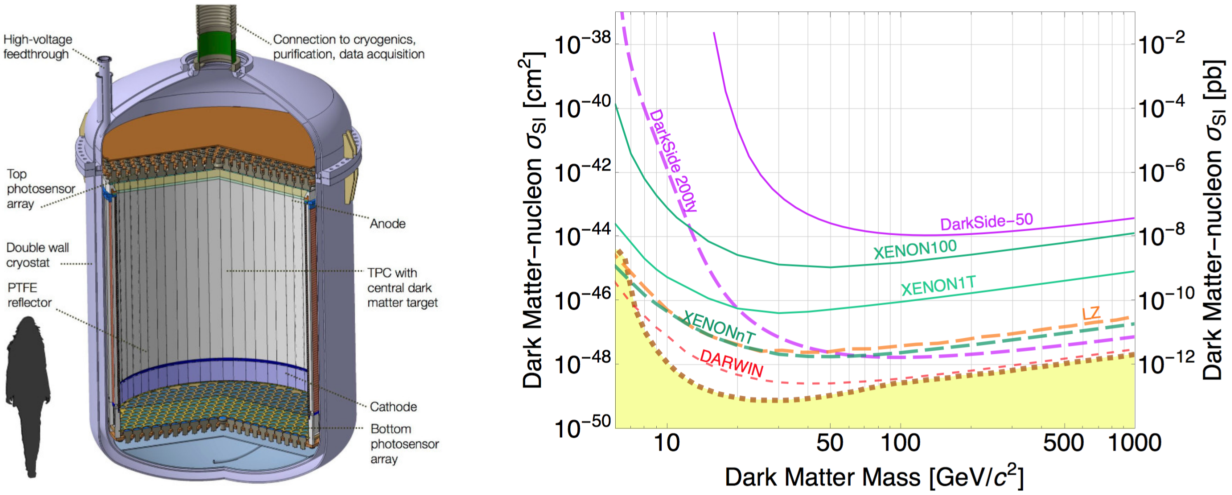

Figure 6.1: Left: The baseline design of the DARWIN xenon-based dual-phase TPC. Right: DARWIN sensitivity (90 % confidence level) to spin-independent WIMP-nucleon interaction. The red solid line represents the median sensitivity. Shown are upper limits from current experiment (solid lines), as well as the sensitivity projections for future experiments (dashed lines). The neutrino background is indicated as dashed brown line [218]. Figure produced with [99].

detection efficiency. The stability of the SiPM performance characteristics like dark counts, crosstalk and afterpulses at liquid xenon temperature needs to be further studied, and the effect of these parameters on the low energy detector threshold must be investigated. In the next section, the SiPM performance characteristics will be further discussed, and a potential SiPM for the usage in a xenon-based dual-phase TPC will be presented.

6.2 Basic SiPM Characteristics

SiPMs are arrays of reverse-biased avalanche photodiodes (APDs) operated in Geiger mode with a quenching resistor in series and connected in parallel to form a single output. Each APD has the same geometrical size and is an independently operating unit. The APD is based on the principle of a PIN photodiode, which was invented by Jun-ichi Nishizawa and his colleague in 1950 [221].

The depletion zone of an APD is designed to support higher electric fields and to be operated at a reverse bias voltage. In Figure 6.2 (left) an APD cross-section view built on a p-type silicon substrate and the resulting electric field across the APD are shown. An incoming photon with an energy larger than the band gap of silicon ($E_\gamma > 1.12\,\mathrm{eV}$ [223]) is absorbed in the intrinsic region (i) and creates a primary electron-hole pair (photoelectron). Due to the electric field across the APD, the electron and hole drift toward the n^+ and p^+ side, respectively. The saturation drift velocity of electrons in silicon at 300 K is $\sim 1.05 \times 10^7\,\mathrm{cm/s}$ [224]. The photoelectron may reach the high electric field p-n^+ junction (multiplication region), where the electron is strongly accelerated. The electron can obtain a sufficiently high energy to create a secondary electron-hole pair via collisions with the crystal lattice (impact ionisation). The primary and secondary electrons are accelerated and further create secondary electron-hole pairs via impact ionisation. This process results in an exponentially increasing avalanche of secondary electron-hole pair production (avalanche process). The avalanche is self-sustaining if the number of created secondary electron-hole pairs per time (ionisation rate) is larger than the extraction rate from the multiplication region. This condition is true if the applied reverse-bias voltage is above the so-called *breakdown voltage* (V_{break}). The

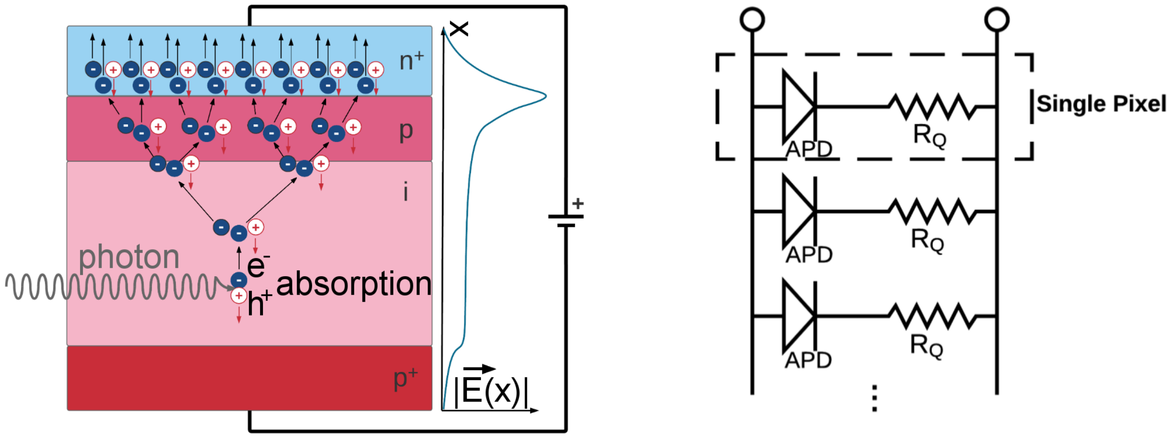

Figure 6.2: Left: An APD cross-section view built on a p-type silicon substrate and the resulting electric field (blue curve) across the diode. A photon is absorbed in the intrinsic region (i) and creates a primary electron-hole pair (photoelectron). The photoelectron drifts towards the high field p-n^+ junction (multiplication region), where it starts an avalanche process via impact ionisation. Figure adapted from [222]. Right: The equivalent circuit diagram of a SiPM. The SiPM is an array of reverse-biased APDs operated in Geiger mode with a quenching resistor (R_q) in series and connected in parallel to form a single output. Figure taken from [222].

breakdown voltage depends on the temperature and doping profile of the p-n junction, which will be further discussed in section 6.3.

After several nanoseconds, the avalanche needs to be shut off (quenched), in order to detect further photons and prevent the diode from overheating, due to the exponentially increasing avalanche current. Therefore, the APD is in series with a so-called *quenching resistor* with a large resistance ($R_\mathrm{q} = 100\,\Omega - 1\,\mathrm{M}\Omega$). The avalanche current produces a voltage drop on the quenching resistor, and therefore reduces the voltage across the avalanche multiplication region below the breakdown voltage. The avalanche will be extinguished, and the breakdown across the avalanche multiplication will come back (recharge), due to the decreasing voltage on the quenching resistor. During the recharge time, the APD is not sensitive to further photons. In Figure 6.2 (right) the equivalent circuit of a SiPM is shown.

In the next section, the readout and the pulse shape of a potential $6{\times}6\,\mathrm{mm}^2$ VUV-sensitive SiPM for the DARWIN experiment will be discussed. It is followed by the developed measurement procedure in order to calculate the dynamic range and the voltage-dependent detection probability of this device. In addition, the results of the measurements will be presented.

6.2.1 VUV-Sensitive SiPM, Readout Electronics and Signal Pulse Shape

A SiPM which is under consideration for the DARWIN experiment is the S13371 $12{\times}12\,\mathrm{mm}^2$ VUV-sensitive SiPM from Hamamatsu. This SiPM was optimised for operation in experiments using liquid xenon as a target and was first developed for the MEG experiment at PSI [225]. The SiPM consists of four independent $6{\times}6\,\mathrm{mm}^2$ VUV-sensitive segments. Each $6{\times}6\,\mathrm{mm}^2$ segment can be read out independently or in various combinations as described in [222]. A picture of the device is shown in Figure 6.3 (left). The single APD size (cell) of the SiPM is $50\,\mu\mathrm{m} \times 50\,\mu\mathrm{m}$ and sensitive to xenon scintillation light at 178 nm with a photodetection efficiency of $\sim 24\,\%$ [226].

The produced avalanche current pulse of the SiPM segment is read out with a dedicated electronic readout board. In Figure 6.3 (right) the electronic schematic for the readout of one SiPM segment is shown. The SiPM is connected on the cathode side to the bias voltage in series with a $10\,\mathrm{k}\Omega$ resistor to limit the current, in order not to damage the device. The anode side is grounded with a $50\,\Omega$ resistor and capacitively coupled to an external voltage amplifier [222, 227].

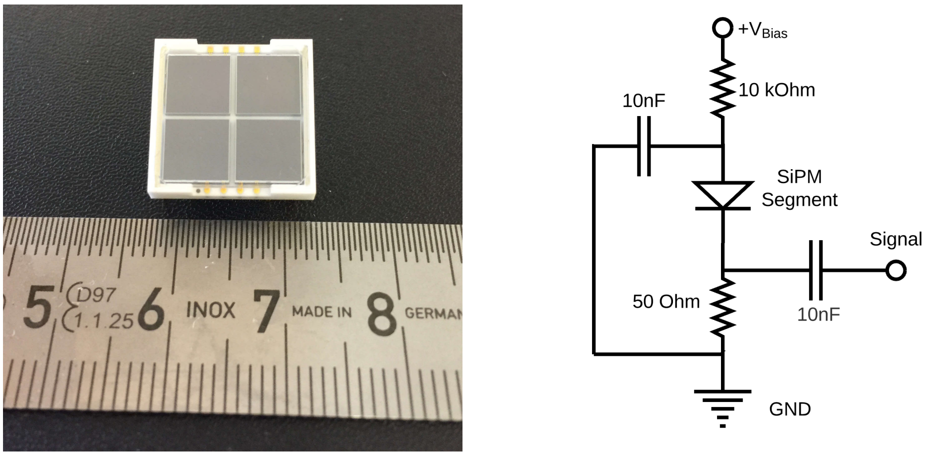

Figure 6.3: Left: A picture of a S13371 $12{\times}12\,\mathrm{mm}^2$ VUV-sensitive SiPM from Hamamatsu. The SiPM consists of four independent $6{\times}6\,\mathrm{mm}^2$ VUV-sensitive segments. Right: The readout schematic of one $6{\times}6\,\mathrm{mm}^2$ segment. The segment is positively biased, and the current pulse of the SiPM is read out with a capacitor. Figure published in [227].

The response of the SiPM cell to an absorbed photon can be electrically modelled, as described in [228]. The electrical model of a SiPM cell is shown in Figure 6.4 (left) and it consists of the capacitance (C_J) of the avalanche multiplication region, the total resistance (R_S) of the APD, a voltage source (V_BR), a switch (S), the quenching resistor (R_Q) and the bias voltage source (V_Bias). The SiPM is non-conducting in the absence of any photons and C_J is completely charged via the applied bias voltage V_Bias. If a photon is absorbed in the SiPM cell and the produced photoelectron triggers an avalanche, the switch S closes at $t = 0$. Due to the voltage drop across the resistor R_Q, the capacitor C_J discharges to a maximum current as a function of time, which is described by the following equation:

$$I(t) = I_0 \times \left[1 - \exp\left(\frac{-t \times (R_\mathrm{Q} + R_\mathrm{S})}{C_\mathrm{J} R_Q R_\mathrm{S}}\right)\right] \qquad \text{with} \qquad I_0 = \frac{V_\mathrm{Bias} - V_\mathrm{Break}}{R_Q + R_\mathrm{S}}, \tag{6.3}$$

where the term $\Delta V = V_\mathrm{Bias} - V_\mathrm{Break}$ is called *over-voltage*, which is independent of temperature and SiPM device. The avalanche is typically quenched after a time period of $\sim 10^{-11}$ s and when the maximum current is reached, the switch S opens again. The capacitor C_J charges through the resistor R_Q again to the applied bias voltage V_Bias. The recharge process is given by:

$$I(t) = I_0 \times e^{-t/\left(R_Q \times C_\mathrm{J}\right)}, \tag{6.4}$$

where $\tau = R_Q \times C_\mathrm{J}$ is the time constant of the recharging process. After the capacitor C_J is completely recharged, the SiPM cell is sensitive again to another photon. The resistance of the APD (R_S) depends on the applied bias voltage, due to the varying length of the depletion region of the p-n junction. The value of R_S varies between $\mathcal{O}\,(10\,\Omega)$ and $\mathcal{O}\,(100\,\Omega)$. Therefore, R_S is much smaller than the quenching resistor R_Q and will be neglected in the further calculations.

In Figure 6.4 (right), a digitised photon response of the $6{\times}6\,\mathrm{mm}^2$ VUV-sensitive SiPM at 300 K with an applied over-voltage of 5 V is shown. The output current rises in a time interval of $\sim 10^{-11}$ s to the maximum current, which is described by equation 6.3. After the avalanche is quenched, the cell capacitance recharges with the time constant which is described by equation 6.4. The recovering

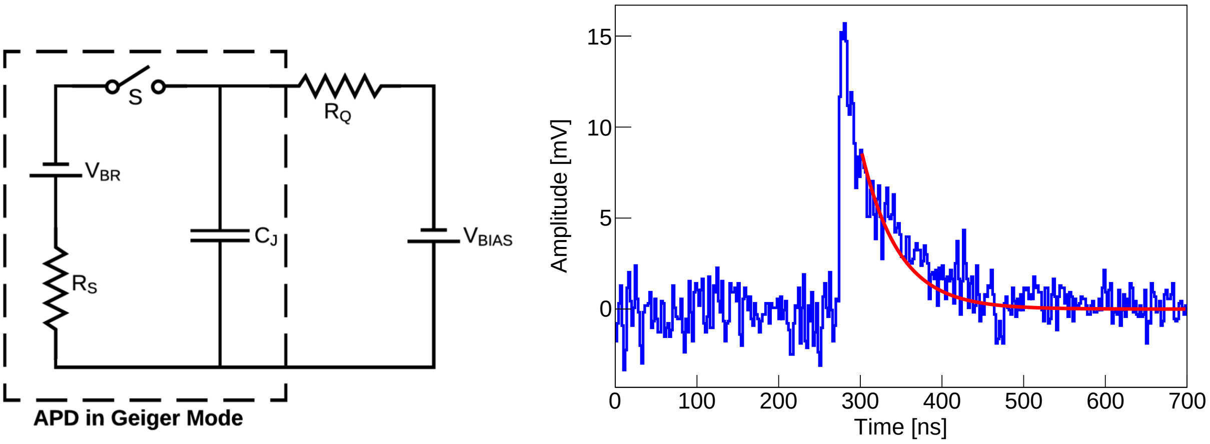

Figure 6.4: Left: The electrical model of a SiPM cell. It consists of the capacitance C_J of the avalanche multiplication region, the total resistance R_S of the APD, a voltage source V_BR, a switch S, the quenching resistor R_Q and the bias voltage source V_Bias. Right: A digitised photon response of the $6{\times}6\,\mathrm{mm}^2$ VUV sensitive SiPM at 300 K with an applied over-voltage of 5 V. The SiPM cell recovery time was fitted with an exponential function (red line) and measured to be (48 ± 3) ns.

time was measured to be (48 ± 3) ns by fitting an exponential function to the tail of the recharging process. The cell capacitance depends on the pixel size and therefore, a smaller cell size results in a shorter recovery time. The time integral of the pulse yields the total charge Q produced in the avalanche process and is given by the following expression:

$$Q = \int_{t=0}^{t} I(t) \times \mathrm{dt} = C_{\mathrm{J}} \times (V_{\mathrm{Bias}} - V_{\mathrm{Break}}). \tag{6.5}$$

The output charge Q of one cell is fixed, even if a second photon is absorbed in the cell simultaneously. The SiPM response becomes non-linear if the photon flux is high and multiple photons enter the same cell. The dynamic range of the SiPM will be discussed and measured in the next section.

6.2.2 Dynamic Range and Detection Probability

The dynamic range of the SiPM is limited by the number of APD cells, due to the dead time during the avalanche process of the cells. If the number of incident photons increases, two or more photons start entering the same APD cell and the signal output starts degrading because each cell can only detect one photon at the same time. The linearity of the SiPM is given by the empirically found equation [229]:

$$N_{\mathrm{Detected}} = N_{\mathrm{Total}} \times \left[1 - \exp\left(-\frac{N_{\mathrm{Photon}} \times \mathrm{PDE}}{N_{\mathrm{Total}}}\right)\right], \tag{6.6}$$

where N_{Detected} is the number of detected photoelectrons, N_{Total} is the total number of cells, PDE is the photon detection efficiency, and N_{Photon} is the number of incident photons. The output signal is linear to the number of incident photons as long as the number of incident photons is smaller than half the number of available cells. This assumption is valid for pulses much shorter than the recovery time and if the photons are uniformly distributed across the SiPM surface.

The PDE depends on several intrinsic properties of the SiPM and is given by the following product:

$$\mathrm{PDE}(\lambda, \Delta\mathrm{V}) = \mathrm{QE}(\lambda) \times \epsilon \times \mathrm{DP}(\Delta\mathrm{V}), \tag{6.7}$$

where QE(λ) is the wavelength-dependent quantum efficiency (equivalent to the probability to absorb the incident photon in the intrinsic region), ϵ is the geometrical fill factor (equivalent to the

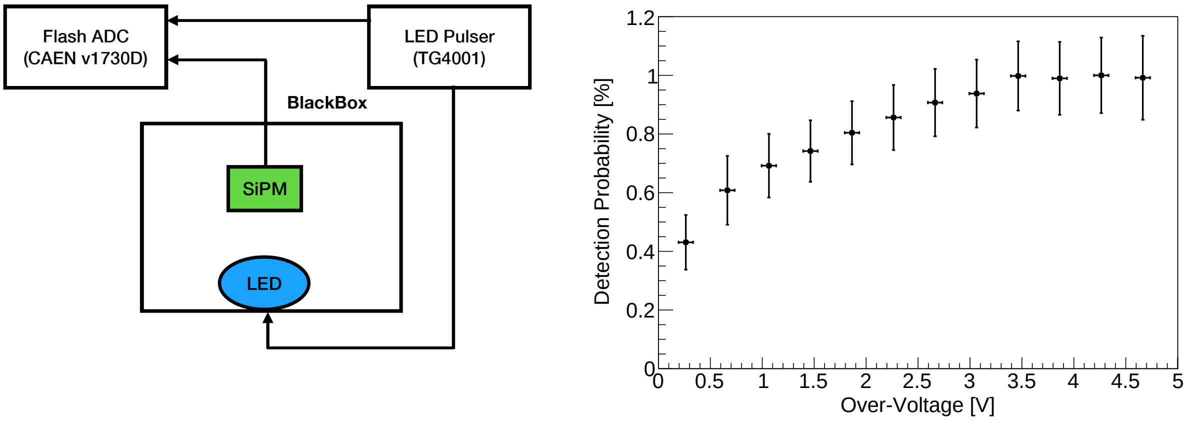

Figure 6.5: Left: The experimental setup of the detection probability measurement. The SiPM is placed in a light-tight box above an LED. The signal of the SiPM is amplified, digitised and stored for later analysis. Right: The measured detection probability as a function of over-voltage of the SiPM at 300 K. The detection probability reached 100 % at an over-voltage of ~3.5 V.

percentage of active area of the SiPM), and DP(ΔV) is the over-voltage dependent detection probability, which is the probability that the produced photoelectron will initiate an avalanche. The over-voltage dependent detection probability DP(ΔV) can be measured by illuminating the SiPM with a fixed light source intensity and varying the bias voltage. The mean number of detected photoelectrons at every bias voltage is expected to be the same but may vary, due to different detection probabilities. The normalised mean number of produced photoelectrons at every bias voltage defines the detection probability.

The voltage-dependent detection probability of the 6×6 mm^2 VUV sensitive SiPM was measured at 300 K in the setup shown in Figure 6.5 (left). The SiPM was placed in the centre of a light-tight box above a blue LED (λ = 405 nm). The LED intensity was fixed to ∼100 PE, and the bias voltage of the SiPM was varied in steps of 0.4 V. The signals of the SiPM were amplified by a 100-fold amplifier, digitised and stored on a PC. The data was processed with the developed data processor described in section 5.2. The detection probability at every bias voltage is then given by the following expression:

$$\mathrm{DP}(\Delta\mathrm{V}) = \frac{N_{\mathrm{Detected}}(\Delta V)}{N_{\mathrm{max}}}, \tag{6.8}$$

where $N_{\mathrm{Detected}}(\Delta V)$ is the number of detected photoelectrons at a given bias voltage, and N_{Max} is the number of detected photoelectrons at the maximal bias voltage (assuming $\mathrm{DP}(\Delta\mathrm{V}_{\mathrm{max}}) = 1$). In Figure 6.5 (right) the measured detection probability as a function of over-voltage is shown. The detection probability increases with over-voltage until it reaches a plateau of 100 %. The plateau is reached for over-voltages larger than 3.5 V. The result is in agreement with previous measurements, for which a similar over-voltage dependent detection probability has been observed [230, 231].

The dynamic range of the 6×6 mm^2 VUV sensitive SiPM was measured at 300 K in a similar setup, which is shown in Figure 6.6 (left). The SiPM is placed above an LED (λ = 405 nm) inside a light-tight box. A part of the generated LED light is taken by an optical fibre and guided to an 1-inch PMT (Hamamatsu R8520), which is placed next to the SiPM. The output signals of both photosensors are amplified, digitised and stored for later analysis. The response of the 1-inch

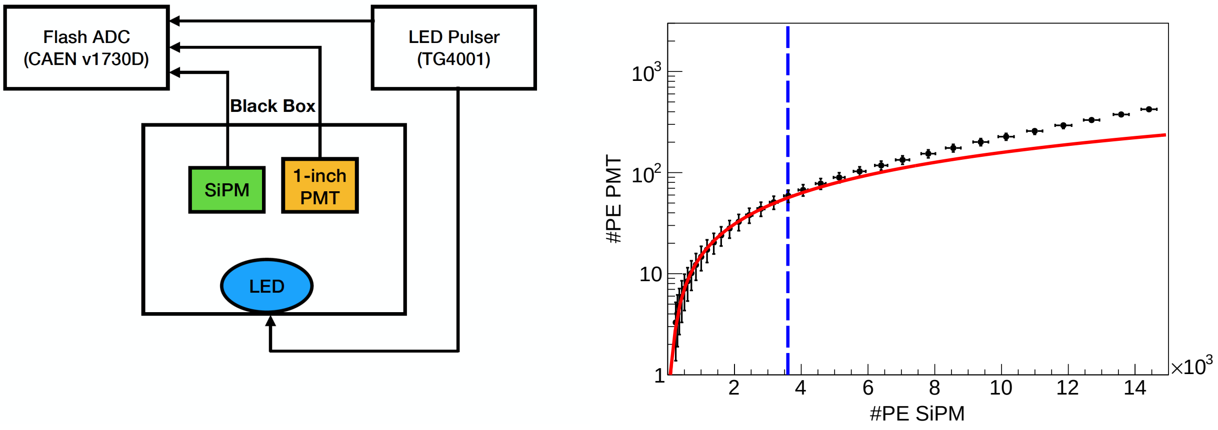

Figure 6.6: Left: The experimental setup of the dynamic range measurement. The SiPM and an 1-inch PMT are placed inside a light-tight box above an LED. The signal of the SiPM and PMT are amplified, digitised and stored for later analysis for different LED settings. Right: The number of detected photoelectrons in the PMT as a function of the number of detected photoelectrons in the SiPM (black points). The SiPM output increases linear with the PMT output for increasing LED intensities and is fitted with a linear function (red line). At around detected 3 600 PE with the SiPM, a ∼4 % deviation from the linear response can be observed (blue dashed line).

PMT is linear over the whole ADC range, which was verified in the experiment described in section 3.4. The SiPM was set to an over-voltage of 4 V, and the LED was pulsed with a square pulse of a width of 200 ns and at a rate of 100 Hz. The LED intensity was varied and the number of photoelectrons in the SiPM and PMT was monitored. As long as the SiPM output is linear, the SiPM output signal grows linearly with the PMT signal. The data points will not follow exactly equation 6.6, because the pulse width was much longer than the recovery time. The acquired signal distribution for different LED light intensities was fitted with a Gaussian function for the SiPM and PMT. The mean of the Gaussian determines the number of measured photoelectrons. The number of measured photoelectrons of the PMT and SiPM were plotted against each other and fitted with a linear function, in order to determine the linearity. The data points until 2 000 PE were included in the fit. The result is shown in Figure 6.6 (right). The output of the $6{\times}6\,\mathrm{mm}^2$ VUV sensitive SiPM response is linear until ∼3 600 PE (4 % deviation from the fit). For higher LED illumination, the SiPM response starts to deviate from the linear behaviour. This value needs to be considered in the design of a xenon-based dual-phase TPC like DARWIN, which considers employing SiPMs photosensors.

In the next section, the SiPM was characterised at various temperatures in a gaseous nitrogen environment, and its performance was long-term monitored, which is partially published in [227].

6.3 Temperature dependent SiPM Characterisation

In the last section we discussed the basic principle of the VUV-sensitive $6{\times}6\,\mathrm{mm}^2$ SiPMs and measured the dynamic range and the voltage-dependent detection probability at 300 K. In this section we present the temperature dependent measurements of the VUV-sensitive $6{\times}6\,\mathrm{mm}^2$ SiPM of various performance parameters, along with a detailed description of the developed low-temperature evaluation setup, and the long-term performance of the device. A evaluation of the SiPM in a low-temperature setup is necessary since the data sheet provided by the manufactures does not cover the temperature regime of interest. The measured SiPM properties are also of general interest for a variety of potential applications besides DARWIN. The section is partially published in [227].

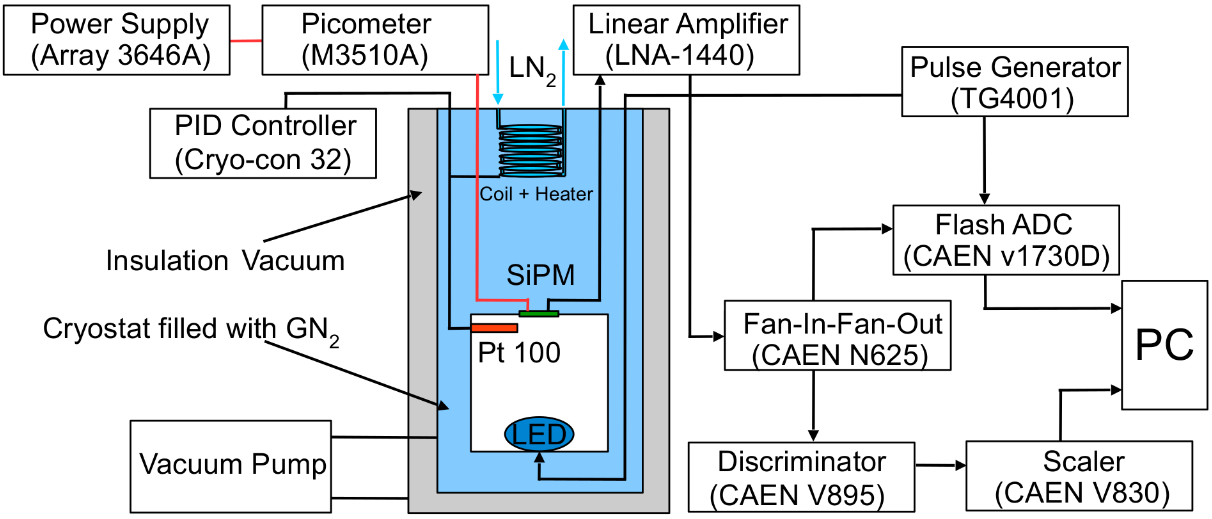

Figure 6.7: A sketch of the experimental apparatus and of the data acquisition system. The SiPM is positioned near the centre of the cryostat on a PTFE holder, and the cryostat is filled with gaseous nitrogen. Liquid nitrogen is flushed through the cooper coil and the temperature is controlled via a heating foil wrapped around the coil and regulated by a PID controller. Published in [227].

6.3.1 Low-Temperature SiPM Evaluation Setup

A sketch of the experimental setup used in all temperature dependent measurements is shown in Figure 6.7. The inner chamber contains a PTFE holder, which can support either a PMT or several SiPMs at the same time. The temperature is measured by two Pt-100 resistant thermometers placed at 2 mm distance to the SiPM inside the holder. The inner volume is first evacuated using a turbo molecular pump to a pressure below 10^{-4} mBar and filled with gaseous nitrogen with a purity level of 99.9999 % (6.0) to avoid condensation of water or other gases. The nitrogen pressure within the chamber is maintained at $\sim$1.8 bar. Liquid nitrogen is flushed through a copper cooling coil to cool down the chamber, with the cooling power maintained by a constant flow rate which can be set at the outlet of the copper coil. A heating foil wrapped around the cooling coil and regulated by a PID controller (Cryo-con 32) allows us to control the temperature. Prior to every measurement, we waited for 30 mins until the temperature was stable within ± 0.02 K. Paragaph published in [227].

The VUV-sensitive 6×6 mm^2 SiPM is positioned near the centre of the cryostat on a PTFE holder, facing a blue LED ($\lambda = 405$ nm). A pulse generator (TTi TG5012A) is used to bias the LED with a square pulse and to simultaneously trigger the data acquisition system. An external power supply (Array 3646A) provides the bias voltage for the SiPM, and a picoampere meter (M3510A) is used to measure the corresponding current. The signal from the SiPM is amplified by a 100-fold commercial low noise amplifier (RF Bay LNA-1440). The amplified signal is duplicated over a Quad Linear FAN-IN FAN-OUT (CAEN N625). The first signal copy is digitised by a flash ADC (CAEN V1730D) with a sampling frequency of 500 MHz, an input range of 0–2 V, a bandwidth of 250 MHz and a resolution of 14 bits, for later analysis. The second copy is fed into a discriminator (CAEN V895) with a programmable threshold, and the resulting trigger signal of the discriminator is propagated to a scaler (CAEN V830), allowing to count the number of SiPM pulses above a programmable threshold in a certain time window. Paragaph published in [227].

6.3.2 Single Photon Response, Breakdown Voltage and I-V Characteristics

To measure the gain, resolution and breakdown voltage, a single photoelectron spectrum is first acquired by illuminating the SiPM with light from the blue LED. The LED is triggered by an

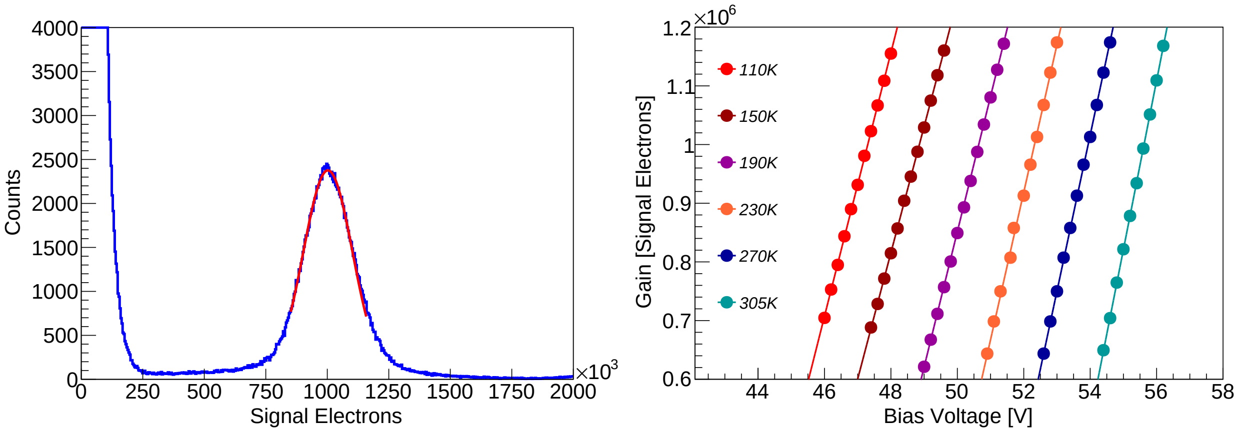

Figure 6.8: Left: Example of one single photoelectron spectrum (blue curve) at a bias voltage of 54.0 V and an operating temperature of 270 K. The photoelectron peak is fitted with a Gaussian function (red curve) to obtain the gain. Right: The gain as a function of bias voltage at different temperatures in gaseous nitrogen. The gain data points at every temperature are fitted with a linear function in order to obtain the breakdown voltage at the intersection of the fit with the x-axis. Published in [227].

external pulse generator with a frequency of 1 kHz and provides an illumination rate of ~ 1 photon for every trigger. For each bias voltage, 500 000 events have been acquired. Each digitised event captured a window of 1 μs, and the raw signal traces were stored on a computer. The gain was obtained from the charge spectrum by fitting the first photoelectron peak with a Gaussian function, as shown in Figure 6.8 (left). The charge of the SiPM pulses was calculated with the data processor described in section 5.2.2. The mean (μ_{SPE}) of the Gaussian corresponds to the gain and the ratio between the mean μ_{SPE} and the standard deviation (σ_{SPE}) to the resolution. Paragaph in [227].

In Figure 6.8 (right) we show the obtained gains between 110 K – 300 K as a function of bias voltage. The gain depends linearly on the bias voltage, which is described by equation 6.5. The collected data points at each temperature setting were fitted with a linear function to obtain the breakdown voltage, which is at the intersection of the linear functions with the x-axis, and the cell capacitance is obtained from the slope. The breakdown voltage decreases linearly towards lower temperatures, as shown in Figure 6.9 (left). We obtained a decrease in the breakdown voltage of (48.6 ± 0.4) mV/K. This is expected due to the increase of the ionisation rates with decreasing temperature. The ionisation rate depends on the impact ionisation threshold energy, the optical-phonon energy and the free mean path of phonon generation [232]. The secondary electrons in the avalanche multiplication region can scatter with the crystal lattice and emit phonons or create other electron-hole pairs by impact ionisation. With a higher temperature, the secondary electrons lose more energy to the crystal lattice. Therefore, a higher electric field is needed to obtain sufficiently high energy for the impact ionisation. The breakdown voltage as a function of temperature shows a quasi-exponential shape in [233] but can be very well approximated with a linear function in a small temperature regime, which is consistent with our measurements. The resolution decreases with over-voltage ($\Delta V = V_{\mathrm{bias}} - V_{\mathrm{break}}$) for all temperatures to the lowest measured resolution of $\sim 9\,\%$ at $\Delta V = 5.6$ V. This value is superior to cryogenic PMTs, which show a resolution of around 25–30% [150]. Paragaph published in [227].

The produced charge during the avalanche process is equivalent to the product of the capacitance and the applied over-voltage ($Q = C \times \Delta V$), the SiPM cell capacitance is obtained from the slope of the fitted linear function. We measured a SiPM cell capacitance of (356.4 ± 0.2) fF at 170 K. With the obtained recovery time from the previous section ($\tau = 48$ ns) we can calculate the quenching resistor R_Q with equation 6.4. The quenching resistor varies from $\sim 1\,\mathrm{M\Omega}$ at 300 K up to $\sim 1.3\,\mathrm{M\Omega}$ at 110 K. The slight increase of the quenching resistance has, therefore, no effect on the pulse shape

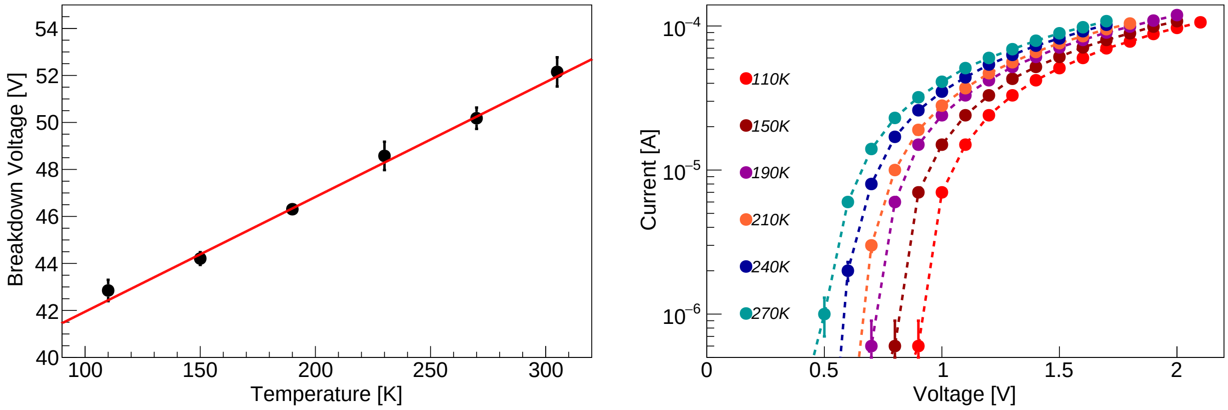

Figure 6.9: Left: The breakdown voltage as a function of temperature (black data points) along with a linear fit (red curve). The explanation is given in the text. Right: The forward biased I-V curve at different temperatures. The resistance of the APD is obtained by fitting the curves with a linear function at high voltages, which increases with decreasing temperature. Published in [227].

of the SiPM at different temperatures. Paragaph published in [227].

We forward biased the SiPM at different temperatures to determine the resistance of the SiPM from the linear dependency between voltage and current at high bias voltages, as shown in Figure 6.8 (right). The resistance of the SiPM varies from $\sim 10.7\,\mathrm{k\Omega}$ at 300 K up to $\sim 11\,\mathrm{k\Omega}$ at 110 K. The number of single cells of the SiPM can be calculated via the ratio between the resistance of the quenching resistor and the SiPM resistance. The ratio corresponds to a minimum number of ~ 11 k individual cells. It has to be mentioned that this value is a lower limit, due to the neglected resistance of the p-n junction. Paragaph published in [227].

6.3.3 Dark Count Rate and Optical Crosstalk

The SiPM features several noise characteristics, which can be grouped into uncorrelated noise, such as thermally generated dark counts, and pixel discharging correlated noise, such as crosstalk. In this section, we will discuss the dark count rates and the optical crosstalk. Paragaph published in [227].

The major contribution to the dark counts at 300 K are the thermally generated electrons in the avalanche region of the cell, which can initiate an avalanche. Silicon has an indirect band gap, which suppresses the direct transitions of the electrons from the valence band to the conduction band. The crystal impurities introduce trap levels inside the band gap, which assist the thermally generated electrons to reach the valence band. The Shockley-Read-Hall (SRH) carrier generation model [234] describes this process, and the dark count rate (DCR) at a specific temperature is given by the following expression:

$$\mathrm{DC}_{\mathrm{SRH}} \propto T^2 \times e^{-\frac{E_a}{k_B T}}, \tag{6.9}$$

where T is the crystal temperature, E_a is the defect ionisation energy or activation energy, and k_B is the Boltzmann's constant. The DCR is therefore exponentially temperature dependent. In addition, the electrons have a finite probability to tunnel through the band gap from the valence band to the conduction band in the high electric field region of the avalanche region. The tunnelled electron can trigger an avalanche and contributes to the DCR. The probability of tunnelling increases with a higher applied over-voltage, due to the stronger electric field. The electrons can tunnel directly through the band gap from the valence band to the conduction band, or the tunnelling can be

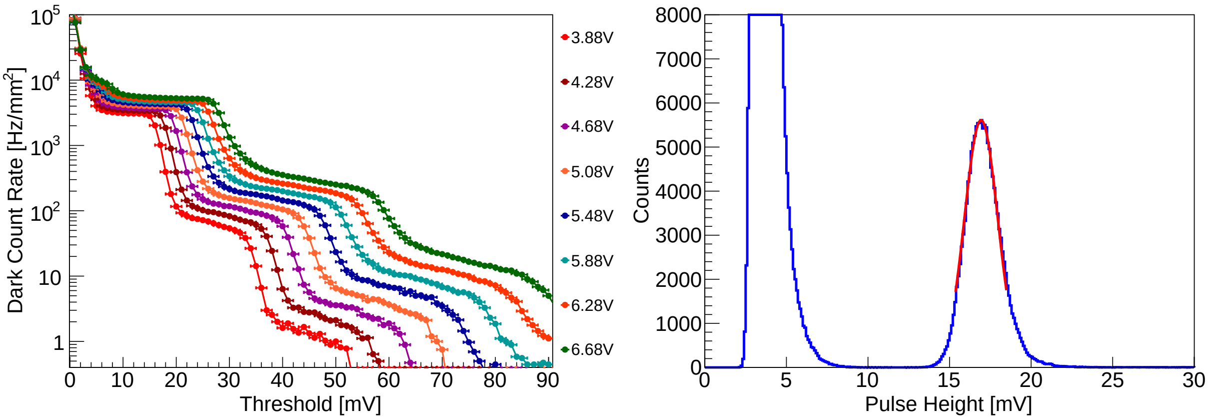

Figure 6.10: Left: Dark count rate as a function of the signal threshold for different over-voltages at 260 K. The behaviour is characterised by a series of 'plateaus', which correspond to 0.5 PE, 1.5 PE and 2.5 PE pulse heights. Right: Example of an obtained pulse height histogram (blue curve) of the gain calibration where the single photoelectron peak is fitted with a Gaussian function (red curve). The mean value is used to calculate the 0.5 PE and 1.5 PE thresholds. Published in [227].

assisted by trap levels introduced by impurities. Therefore, the DCR is expected to depend on the bias voltage as well, in addition to its temperature dependence.

The DCR was measured by counting thermally generated single SiPM pulses at different bias voltages as a function of temperature above a 0.5 PE threshold ($\mathrm{DCR}_{0.5\,\mathrm{PE}}$). These measurements were performed at temperatures above 230 K, for lower fluctuations in the dark count rate [227].

At each temperature setting, the SiPM dark count rate was measured by sweeping through different signal thresholds. Figure 6.10 (left), shows the results of the dark count rate for different over-voltages and thresholds at a temperature of 260 K. At each measured over-voltage, the curve was evaluated at the 0.5 PE threshold. The 0.5 PE threshold was measured for the different over-voltages by fitting the pulse height histogram from the gain calibration with a Gaussian function, as shown in Figure 6.10 (right). The obtained dark count rate as a function of over-voltage at each temperature setting was fitted with a linear function, as shown in Figure 6.11 (left). Figure 6.11 (right) shows the dark count rate as a function of temperature for various over-voltages. The dark count rate decreased three orders of magnitude when going from room temperature to 230 K and was fitted with an exponential function. We measured an activation energy of (0.52 ± 0.2) eV, which is close to half of the band gap energy of silicon ($E_g^{\mathrm{Si}} = 1.12$ eV [233]). This implies that trap levels are present in the centre of the silicon band gap, which acts as a dominant SRH carrier generation centre. This effect was also observed in [235]. The fitted exponential function can be used to extrapolate the DCR at a lower temperature for various over-voltages. Paragaph published in [227].

Optical crosstalk is also a correlated noise contribution to the original pulse from the cell. During the avalanche process, triggered by an initial photoelectron, a photon can be emitted via recombination of an electron-hole pair. The photon can reach the active area of a neighbouring cell directly or indirectly via reflections on the substrate, and can triggers another avalanche there. The additional pulse is called *crosstalk pulse* and is not separated in time from the original pulse [236]. The probability that an electron in the avalanche region emits a photon of an energy larger than 1.14 eV is $\sim 2.9 \times 10^{-5}$ [237] and independent of temperature. Therefore, the SiPM with an average gain of 10^6 can emit 29 photons, which can reach a neighbouring cell. The optical crosstalk is expected to depend on the SiPM gain and thus the bias voltage, as well as on the internal SiPM structure, which stops the propagation of the photons inside the cell.

The crosstalk rate was measured by counting thermally generated single pulses at different bias

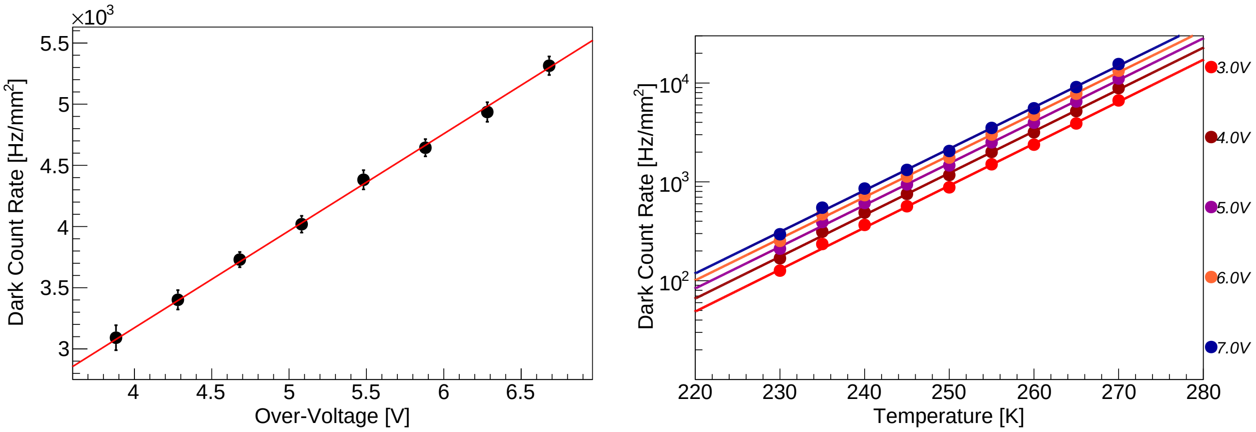

Figure 6.11: Left: Dark count rate as a function of over-voltage at 260 K. The points are fitted with a linear function (red line). Right: The dark count rate as a function of temperature for different over-voltages from 3 to 7 V. The rates follow an exponential decrease over three orders of magnitude and are fitted with an exponential function, see text. Published in [227].

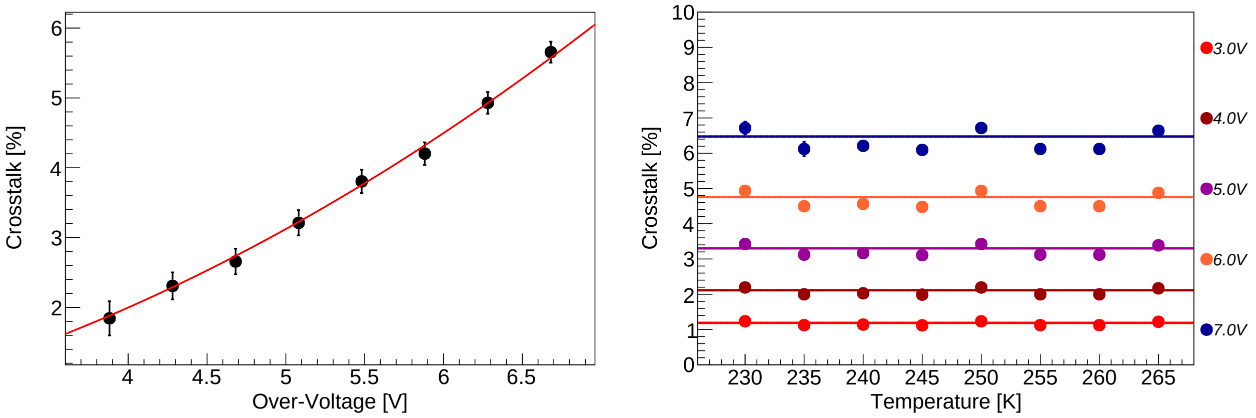

Figure 6.12: Left: Crosstalk rate as a function of over-voltage at 260 K. The points are fitted with a function in the form $a \times \Delta V^2$ (red curve). Right: The crosstalk rate as a function of temperature for different over-voltages, from 3 to 7 V. The crosstalk rate remains constant with temperature and the data points are fitted with a constant function (solid lines). Published in [227].

voltages as a function of temperature at 0.5 PE and 1.5 PE thresholds. Crosstalk events will appear as pulses larger than 1 PE, which corresponds to a simultaneous avalanche of two cells. Dark count events are considered to generate 1 PE pulses. The accidental coincidence rate that two cells have a dark count avalanche is $\sim 10^{-5}$ Hz at 300 K, and therefore not needed to be considered in the analysis. The crosstalk is then defined by the following ratio:

$$\text{Crosstalk} = \frac{\text{DCR}_{1.5\,\text{PE}}}{\text{DCR}_{0.5\,\text{PE}}}, \tag{6.10}$$

where $\text{DCR}_{0.5\,\text{PE}}$ and $\text{DCR}_{1.5\,\text{PE}}$ are the DCRs at 0.5 PE and 1.5 PE threshold, respectively. The $\text{DCR}_{0.5\,\text{PE}}$ and $\text{DCR}_{1.5\,\text{PE}}$ for different over-voltages were obtained by interpolating the dark count rate as a function of signal threshold at the corresponding pulse thresholds. The obtained crosstalk rate as a function of over-voltage at each temperature setting was fitted with a function $a \times \Delta V^2$, where a is a free parameter, as shown in Figure 6.12 (left). The fit function at every temperature was evaluated at the same over-voltage. Figure 6.12 (right), shows the crosstalk rates as a function of temperature for a set of over-voltages. We observe that the crosstalk rate stays constant with temperature, as seen also in [238]. This allows us to evaluate this parameter for different temperatures by fitting the obtained data points with a constant function. Paragaph published in [227].

6.3.4 Afterpulse Rates and Long-Term Stability at 172 K

Additional correlated noise sources are called *afterpulses*. Afterpulses in the SiPM have a different origin than afterpulses in the PMT. During the avalanche process, secondary electrons can be trapped in energy levels inside the band gap, which are created by impurities inside the crystal lattice [239]. The trapped electron can be released after a time delay, which causes an additional avalanche process, indistinguishable from a pulse of one absorbed photon. If the trapped electron is released during the recharge process, it can initiate another avalanche process with less charge output than the gain of the pixel, which is visible as a smaller pulse in the tail of the initial pulse. The time delay between the two pulses is of the order of nanoseconds, and the peak finding algorithm is not able to distinguish these two peaks and integrates both of them. The amount of output charge depends on the recharge state of the cell and will, therefore, smear the output spectrum. The afterpulse probability is over-voltage dependent because the probability that an electron is captured in an energy level is over-voltage and gain dependent.

A lower limit on the afterpulse rate at 172 K as a function of over-voltage was measured. Therefore, the 1 PE population from the gain calibration was selected as a clean sample, which is assumed not to contain afterpulses. Pulses with a larger output charge are counted as afterpulses and the afterpulse rate is given by the following expression:

$$P_{\mathrm{AP}} = \frac{N_{>1\mathrm{PE}}}{N_{1\mathrm{PE}}}, \tag{6.11}$$

where $N_{>1\mathrm{PE}}$ is the number of pulses with an output charge larger than the 1 PE, and $N_{1\mathrm{PE}}$ is the number of pulses with a charge of 1 PE. This method underestimates the real afterpulse rate because afterpulses with a large delay time from the initial pulse will fall inside the 1 PE population and are not distinguishable with this method. Afterpulse events caused by a 1 PE event are supposed to have a slightly larger charge, but a similar height than an afterpulse-free 1 PE pulse. Therefore, the afterpulse-free 1 PE population was extracted in a discrimination space, where we plot the pulse charge as a function of pulse height, as shown in Figure 6.13 (left). The charge of the afterpulses increases from 1 PE to a maximum charge of 2 PE depending on the recharge state of the cell. The number of afterpulse-free 1 PE events were selected within 3σ contour of the two-dimensional elliptical Gaussian fit to the distribution (black dashed line on Figure 6.13, left). Pulses outside of the 3σ contour are considered as afterpulses. The 2D Gaussian function, which was used for fitting the data points, is expressed by equation 4.15.

The afterpulse rate was calculated for different over-voltages as shown in Figure 6.13 (right). The afterpulse increases with the over-voltage, due to the increased probability of capturing an electron inside the trap level. The data points were fitted with an exponential function in order to extract the afterpulse rate of a specific over-voltage.

In addition, we measured the dark count rate and gain of the SiPM at a mean temperature of 172 K in gaseous nitrogen for 27 days. For this measurement, we controlled the temperature

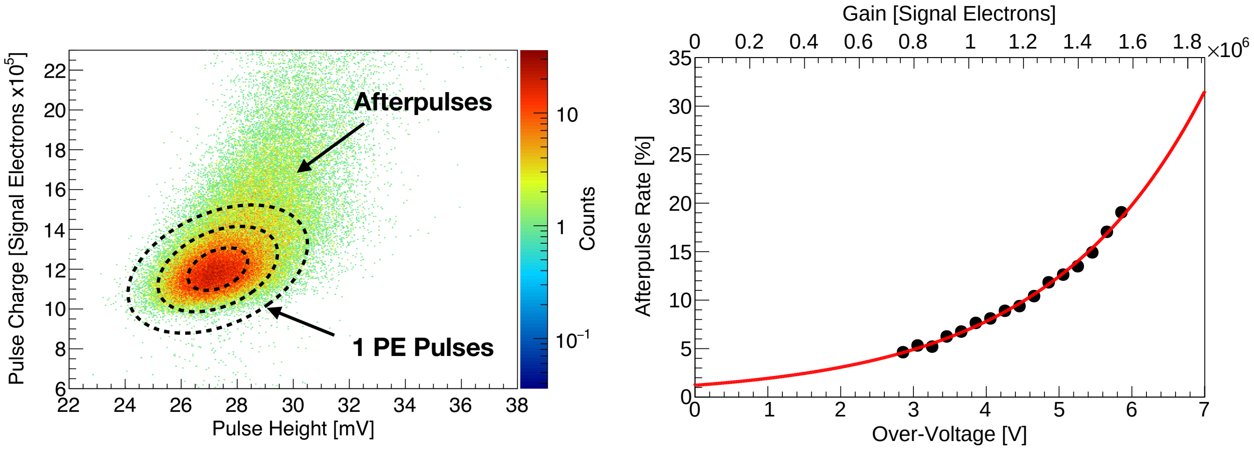

Figure 6.13: Left: The pulse charge as a function of pulse height at a temperature of 172 K and an over-voltage of 6 V. The 1 PE population is fitted with a 2D Gaussian function and selected within the 3σ contour for the afterpulse calculation. The 1σ, 2σ and 3σ contour are indicated with black dashed lines. Events outside the 3σ contour are considered to be afterpulses. Right: Afterpulse rate as a function of over-voltage and gain (black points). The data points are fitted with an empirically found exponential function (red curve), which describes the afterpulse rate accurately in the measured over-voltage regime.

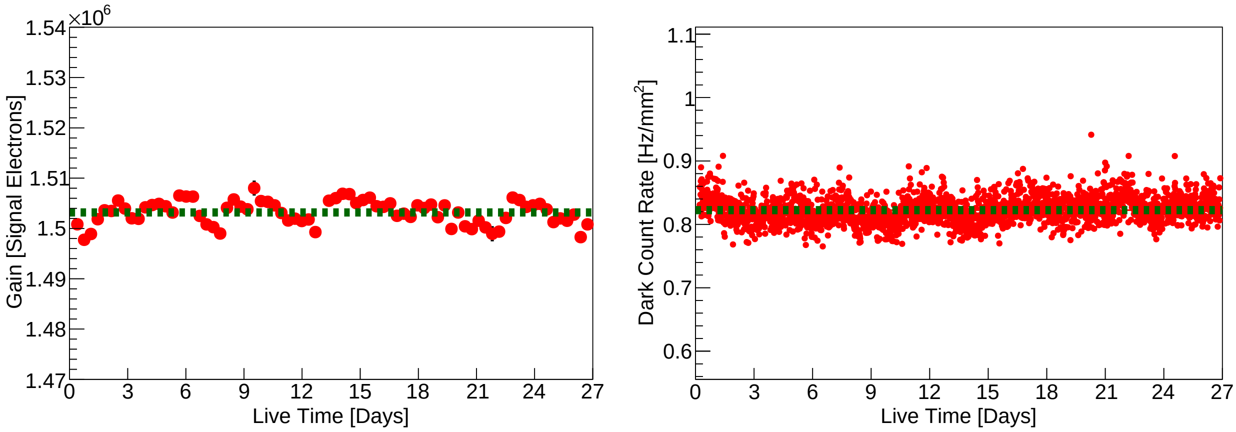

Figure 6.14: (Left): Gain stability at a temperature of 172 K as a function of time. The data (red points) was collected over a period of 27 days. The green dotted line indicates the mean gain value, which is 1.50×10^6 with an rms of 0.01×10^6. (Right): Dark count rate (red data points) at a 0.5 PE threshold and a temperature of 172 K. The green dotted line indicates the mean rate, which is $0.82\,\mathrm{Hz/mm^2}$ with an rms of $0.03\,\mathrm{Hz/mm^2}$. Published in [227].

via the nitrogen flow through the copper coil, which resulted in a less nitrogen consumption and a temperature rms of ∼ 0.14 K. The SiPM was operated at an over-voltage of 5.6 V, which corresponds to a gain of 1.50×10^6, for an excellent signal-to-noise ratio and thus less susceptibility to changes in the noise conditions in the laboratory. Paragaph published in [227].

We continuously monitored the dark count rate, and we regularly performed a gain calibration with LED light. The gain evolution is shown in Figure 6.14 (left). The measured mean value is 1.50×10^6 with an rms of 0.01×10^6. The gain fluctuations can be correlated with the temperature fluctuations due to the nitrogen dewar exchange, and are below 1 %. The SiPM shows a good long-term stability without any visible gain drift. The dark count rate at a 0.5 PE threshold is shown in Figure 6.14 (right). It remains stable over the entire measurement period with a mean normalised rate per area of $0.82\,\mathrm{Hz/mm^2}$ and an rms of $0.03\,\mathrm{Hz/mm^2}$. At a similar temperature, PMTs show an average dark count rate of $0.01\,\mathrm{Hz/mm^2}$ [150]. Therefore, further developments by the manufacturer are necessary in order to achieve compatible dark count rates. Paragaph published in [227].

The implications of the results of the performed measurements on the DARWIN experiment will be discussed in the next section.

6.3.5 Summary and Implications for the DARWIN Detector

In the previous section, we discussed the temperature dependent behaviour of the VUV-sensitive $6{\times}6\,\mathrm{mm^2}$ SiPM. In this section, we will discuss the implication of the performed measurements on the DARWIN experiment. The SiPMs in DARWIN will be fully immersed in liquid or gaseous xenon, and therefore, the expected operating temperature will be ∼ 170 K. In Table 6.1, the SiPM characteristics extrapolated to 170 K are summarised. The DCR is pixel size dependent, due to the increased absolute number of impurities and the implied trap-assisted DCR. Therefore, the DCR was normalised to the total active area in order to allow comparison with SiPMs from different producers. In Appendix H, the dark count rate, the crosstalk, the afterpulse rate and the gain as a function of over-voltage at 170 K are shown.

The DARWIN baseline design foresees a TPC with a diameter of ∼ 2.6 m. The surface coverage of this diameter with SiPMs above and below the liquid xenon target would result in ∼ 228 000

Over-Voltage [V]	Gain [10^6]	Dark Count [Hz/mm^2]	Crosstalk [%]	Afterpulse [%]	DP [%]
1.9	0.5	$\sim$0.25	$\sim$0.5	$\sim$2.9	$\sim$80
3.8	1	$\sim$0.51	$\sim$1.9	$\sim$7.1	$\sim$100
5.6	1.5	$\sim$0.75	$\sim$4.1	$\sim$16.4	$\sim$100
7.6	2	$\sim$1.0	$\sim$7.6	$\sim$41.7	$\sim$100

Table 6.1: Extrapolated gain, dark count rate, crosstalk, afterpulse rate and photoelectron detection probability (DP) for differently applied over-voltages at 170 K.

VUV-sensitive 6×6 mm^2 SiPMs. The cell recovery time of these SiPMs is $\sim$48 ns, which is fast enough to recover between an S1 and S2 signal. The dynamic range of a single SiPM is limited to around 3 600 PE, as shown in the previous section. Monte Carlo simulations must be performed for the DARWIN experiment in order to determine the optimal array configuration without SiPM saturation. Furthermore, the SiPMs have an excellent single photon count compatibility, and their gain is compatible with 3-inch PMTs from Hamamatsu (R11410-21) [150].

A major disadvantage of the SiPMs for a potential use in large-scale detectors is the high dark count rate. Dark count pulses from two or more SiPM channels may generate an accidental coincidence, which contributes to the background signal. In order to achieve low energy threshold and background level in a large-scale detector equipped with $\sim$228 000 SiPMs, the accidental coincidences must be reduced to a level of the order of $\mathcal{O}(10^{-3})$ Hz. A three-fold coincidence with SiPMs across all channels would result in an accidental rate of $\sim$3 kHz at an over-voltage of 5.6 V and operating temperature of 170 K. However, in liquid xenon 3-inch PMTs (R11410-21) show an average dark count rate of 0.01 Hz/mm^2 [150]. Equipping the DARWIN experiment with $\sim$1 800 of those PMTs below and above the liquid xenon target would result in an accidental coincidence rate of $\sim$6 mHz using a three-fold coincidence across the channels. Therefore, the dark count rate of the SiPMs needs to be further reduced by the manufacturer by avoiding impurities inside the silicon, in order to achieve a compatible accidental coincidence rate. One could use a six-fold coincidence with SiPMs in order to achieve a compatible accidental coincidence rate as with PMTs, but this may shift the detector energy threshold to higher values.

The crosstalk and afterpulse rate of SiPMs have an impact on the energy scale and the energy resolution of a dual-phase TPC, which is not understood yet. Therefore, it is necessary to equip a xenon-based dual-phase TPC with SiPMs in order to study the effects on the detector performance. In the next section, a design will be presented, which equips the Xurich R&D detector with an array of SiPMs for the xenon light detection. Further SiPM requirements for large-scale dark matter detectors are discussed in [240].

6.4 SiPM Upgrade for the Xurich Detector

In the last section, we discussed the measurement results of one segment (6×6 mm^2) of the S13371 12×12 mm^2 VUV-sensitive SiPM from Hamamatsu. The implication of some of the evaluated parameters (gain, bias voltage, recovery time and DCR) on a dual-phase TPC can be estimated as shown in the last section. The crosstalk and afterpulse rate will have an impact on the energy scale, which needs to be further investigated with a dual-phase TPC. Therefore, the top PMT of the Xurich [124] xenon-based dual-phase TPC will be replaced with an array of S13371 12×12 mm^2 VUV-sensitive SiPMs. The upgrade will allow testing of the behaviour of the SiPMs in a TPC environment and hence their suitability for larger liquid xenon experiments.

In Figure 6.15, a CAD drawing and a picture of the Xurich detector are shown. The liquid xenon target of the Xurich TPC consists of a cylindrical chamber enclosed by a PTFE reflector with a diameter of 31 mm and a drift length of 30.5 mm. Seven field shaping rings are placed around the target volume to ensure a homogeneous drift field. The cathode, gate and anode consist of hexagonal meshes with an optical transparency of 93 % and a thickness of 100 μm. The gate and the anode are separated by a distance of 4 mm and the liquid/gaseous xenon boundary is set in between both electrodes. Two cylindrical 2-inch Hamamatsu-R9869 PMTs are placed in PTFE holders above and below the target for the detection of the photons produced by an incident particle. The detector is designed to study ionisation and scintillation yields of low-energy electronic and nuclear recoils. The current design does not allow for any x-y position reconstruction of the interaction vertex, due to the absence of a hit pattern in the PMTs produced by the S2 signal. Further information on the detector design can be found in [125].

The upgrade of the Xurich detector foresees the replacement of the PMT above the liquid xenon target with an array of SiPMs, in order to detect a hit pattern of the S2 signal and to evaluate the SiPM behaviour in a TPC. The detection of the S2 hit pattern in the SiPM array allows for the reconstruction of the interaction vertex with the help of a pattern recognition algorithm. In the next section, the SiPM array design, the necessary LCE simulations and the pattern recognition algorithm will be discussed. The section will be concluded with first results on the performance of the SiPM array in liquid xenon.

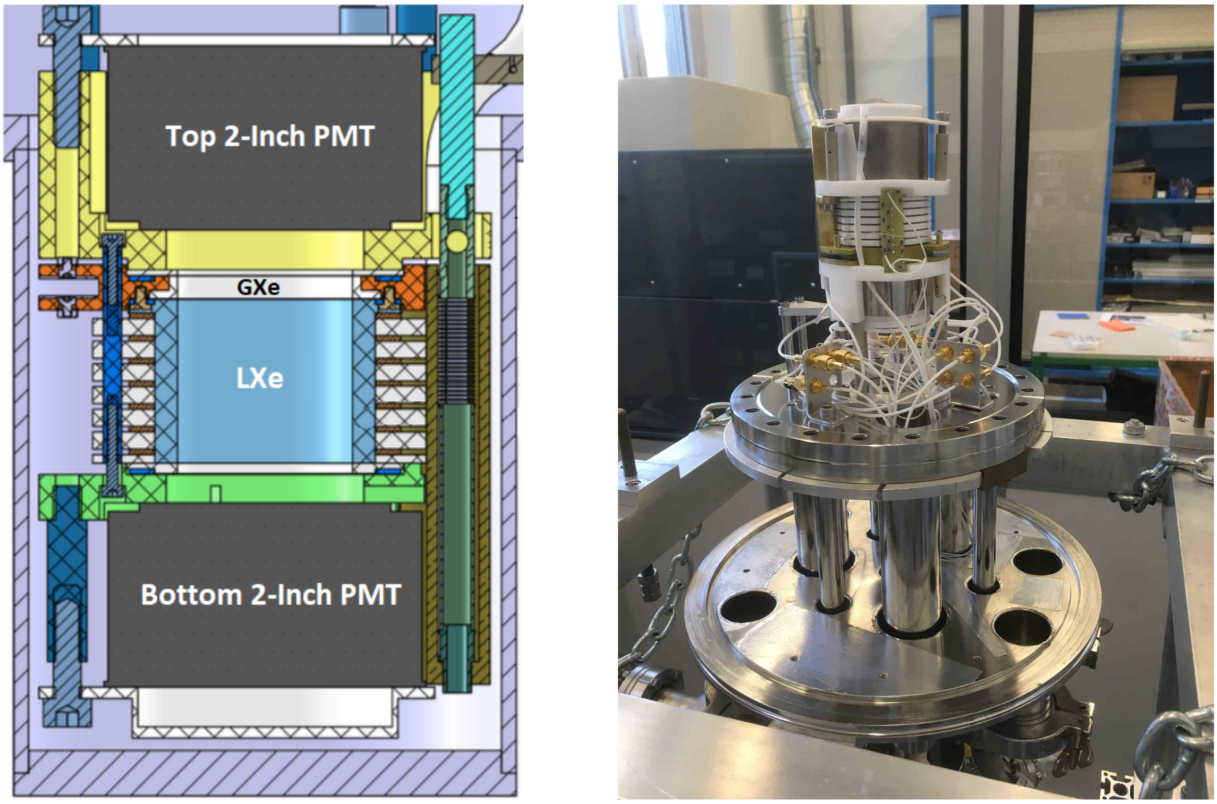

Figure 6.15: Left: The CAD drawing of the Xurich xenon TPC. The liquid xenon target is enclosed by a PTFE reflector. Above and below the target a 2-inch PMTs are installed for the light detection. Figure adapted from [125]. Right: A picture of the opened Xurich detector during a maintenance period. The detector is turned upside down for easier accessibility of the core components.

6.4.1 SiPM Array Design and Readout

The SiPM of choice for the Xurich TPC upgrade is the S13371 $12\times12\,\mathrm{mm}^2$ VUV-sensitive SiPM from Hamamatsu, introduced in the previous section, which offers a compact geometry with four independent $6\times6\,\mathrm{mm}^2$ channels, thus a high detector granularity. In Figure 6.16 (left) the detailed array design with the holder and the readout PCB board are shown. The SiPM array will house four $12\times12\,\mathrm{mm}^2$ S13371 SiPMs (16 $6\times6\,\mathrm{mm}^2$ channels) and will exactly replace the space occupied by the currently installed 2-inch PMT without doing any modifications to the TPC, as shown in Figure 6.16 (centre). The SiPM arrangement was designed to cover the entire TPC diameter and to achieve a maximum light collection efficiency (LCE).

The readout board houses the same readout electronics for 16 channels, as described in section 6.2.1. In addition, the readout board houses for every channel a cryogenic amplifier with a non-inverting gain of 20, which will reduce the electronic pick-up noise to a negligible level. The electronic schematic of the cryogenic amplifier for one channel is presented in Figure 6.16 (right). The main component is the operational amplifier OPA697, which was verified in section 5.4 as stably operable in liquid xenon. The additional heat dissipation of the whole PCB board including the operational amplifier is around 3 W. The increased heat load can be handled by the cooling system of the Xurich detector, which has on average 18 W extra cooling power. The detailed electronics schematic can be found in Appendix J.

The distance from the surface of the SiPM array to the anode was designed to be 5 mm in order to achieve the best position resolution. As a rule of thumb, the distance of the photosensor to the anode is required to be the same as the maximum width of the photosensor. This rule was verified in previous xenon-based dual-phase TPCs [179], and it was taken into account for the design of the SiPM array for the Xurich TPC. The developed SiPM array design was verified with VUV photon simulation using the GEANT4 toolkit, as described in the next section. The simulations were used to predict the x-y position reconstruction via an S2 pattern recognition algorithm.

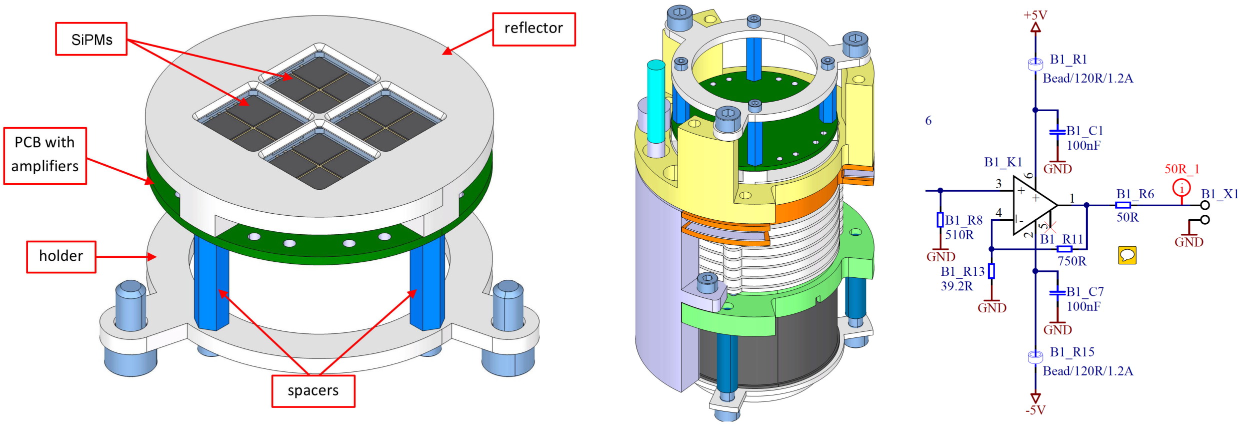

Figure 6.16: Left: The CAD drawing of the developed SiPM array. It consists of 16x $6\times6\,\mathrm{mm}^2$ SiPM channels, which are read out independently via a PCB board attached to the back. The cryogenic signal amplifier is close to the SiPM on the PCB board. Centre: The CAD drawing of the installed SiPM array inside the Xurich detector. The SiPM array replaces the currently used top 2-inch PMT. Right: The electronic schematic of one channel of the cryogenic amplifier, which is printed on the readout PCB board. Every channel uses the same readout schematic.

6.4.2 S1 and S2 LCE Simulation

In order to achieve a low energy threshold, the light and charge yields of an interaction inside the liquid xenon target need to be maximised. Therefore, the current Xurich detector implementation has a high light and charge yield of 7.9 PE/keV and 31 PE/keV at 32.1 keV, respectively, at a drift field of ∼ 1 kV/cm, with a free electron lifetime of 200 μs [124]. The light and charge yield correspond to a low energy threshold of (2–3) keV in the NR equivalent energy scale depending on the applied drift field [124].

To verify that a similar LCE with the upgraded Xurich detector can be achieved, various VUV photon simulations were performed. In order to do this, the new Xurich detector geometry consisting of 16 SiPMs ($6\times6\,\mathrm{mm}^2$) and one 2-inch PMT were implemented into the GEANT4 [241] toolkit. The toolkit takes into account the various physical processes while interacting with different materials of the detector, as well as the different reflection indices of the used materials. The same relevant optical parameters were used as in [125]. The LCE parameter of the VUV photon simulation is needed to be optimized and it is defined by the following expression:

$$\mathrm{LCE} = \frac{N_{\mathrm{Observed}}}{N_{\mathrm{Emitted}}}, \tag{6.12}$$

where N_{Observed} is the number of detected photons in the top SiPM array and in the bottom PMT, and N_{Emitted} is the number of emitted photons in the simulation.

The S1 scintillation light of interest is generated within the liquid xenon volume enclosed by the PTFE reflector, cathode and gate. The VUV photons were uniformly initiated in the active liquid xenon volume with an alpha source, which produced 5 000 photons per event. Figure 6.17 (left) shows the event distribution for different interaction depths (z) as a function of radius squared (r^2). The black lines indicate the PTFE reflector surface, cathode and gate. The simulated photons are counted for the LCE measurements if they hit the sensitive surface of the top SiPM array or the bottom PMT. The spatial LCE map is shown in Figure 6.17 (right). The LCE map shows a spatial variation of the LCE, due to a different amount of reflections depending on the initial position of the photons. After the detector upgrade, the acquired S1 signals need to be corrected for the spatial variations of the LCE. This can be done with the LCE map obtained from Monte Carlo simulations

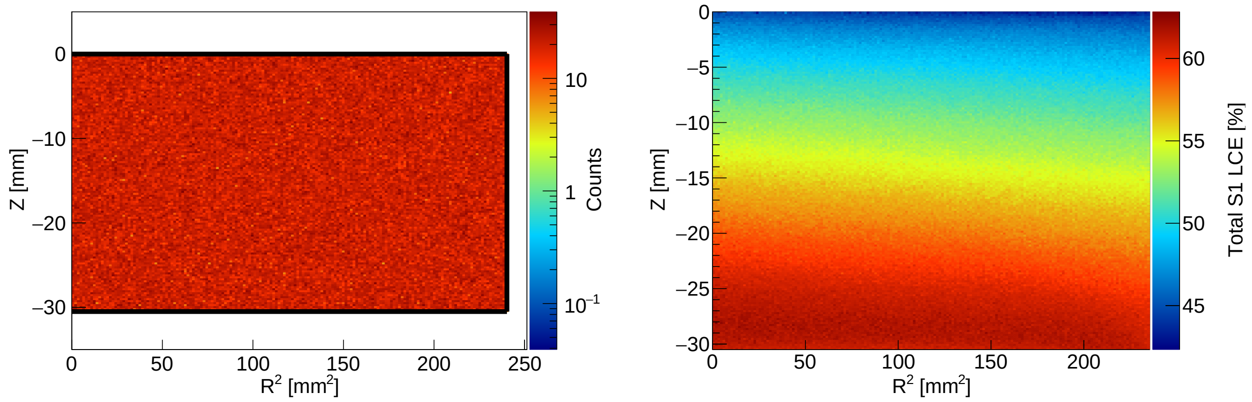

Figure 6.17: Left: The simulated event distribution for different interaction depths (z) as a function of the radius squared (r^2). The black lines indicate the PTFE reflector surface, cathode and gate. Right: The spatial LCE map, which shows variation depending on the initial position of the photons. The variations of the LCE map can be explained by multiple reflections of the photons and variate with radius at the level of ∼ 1.5 %.

Configuration	S1 LCE [%]	S1 RMS [%]	S2 LCE [%]	S2 RMS [%]
Top: SiPM Array Bottom: 2-inch PMT	55.28	3.25	59.20	1.96
Top: 2-inch PMT Bottom: 2-inch PMT	59.41	3.76	-	-

Table 6.2: The total average LCE for the S1 and S2 signals for the upgraded Xurich detector and the current implementation. The numbers of the current implementation are taken from [242]

or from the LCE map obtained from measurement of a monoenergetic calibration source.

The secondary photons (S2 signal) of the drifted electrons are mainly produced in a small layer below the anode in the presence of high electric field [243]. Therefore, in the simulation, the VUV photons were uniformly initiated in a range of 0.5 mm below the anode with an alpha source, which produced 10 000 photons per event. Figure 6.18 (left) shows the implemented Xurich geometry inside the GEANT4 framework with the initiated VUV photons visualised, which represent the S2 signal. The photon travel path is indicated with green lines. If a photon hits the active array of the top SiPM surfaces or the bottom PMT, the photon is absorbed and counted for the LCE measurement, and the hit pattern on the SiPM array is stored. The total S2 LCE as a function of radius is shown in Figure 6.18 (right). No dependence on the z coordinate is expected, due to the small S2 signal generation layer. The S2 LCE shows a slight variation with radius, due to incomplete surface coverage of the inner TPC diameter. The variation of the S2 LCE with radius can be also obtained from measurement of a monoenergetic calibration source after the final array installation. In addition, the dependency can be used to match the Monte Carlo simulation to the data.

In Table 6.2 the total average LCE for the upgraded Xurich detector and the current implementation are listed. With the upgraded Xurich detector, the S1 LCE will decrease by ∼3 % in comparison to the current implementation. The active area of the SiPM array covers ∼79 % of the TPC diameter, whereas the current implementation with the 2-inch PMT covers 100 % of the

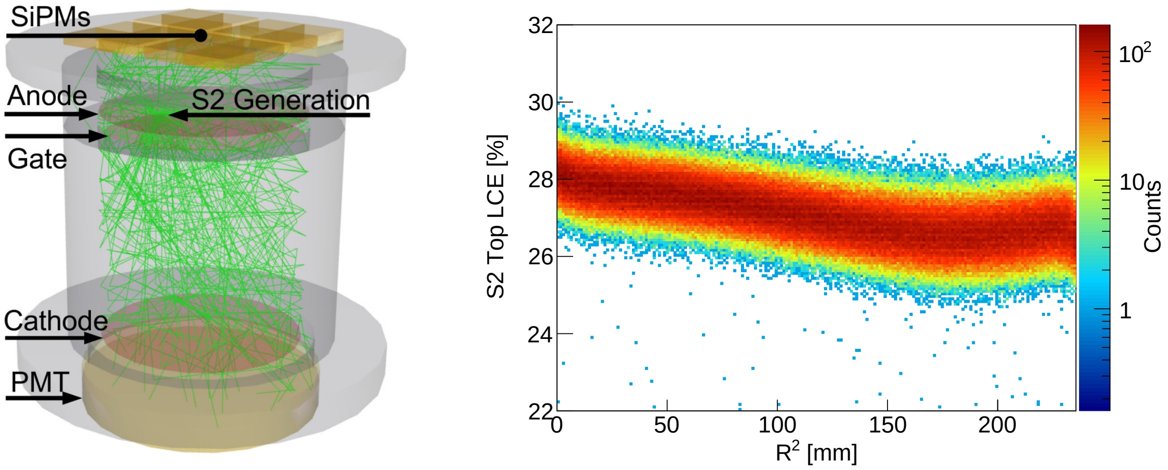

Figure 6.18: Left: The Xurich geometry implemented in the GEANT4 framework in which the initiated VUV photons (green lines) are visualised. The individual components are labelled, and the PTFE reflectors are indicated with grey. The electrodes are implemented as disks with a certain transparency and photon absorption probability. Right: The S2 top LCE as a function of squared radius. The LCE shows a ∼2 % variation with radius, due to incomplete surface coverage of the inner TPC diameter.

TPC diameter. The main advantage of this upgrade lies in the possibility of the x-y position reconstruction of the interaction vertex with a hit pattern recognition algorithm, which can tolerate the disadvantage of a reduced LCE, due to the high photon intensity of the S2 signal. The pattern recognition algorithm will be discussed in the next section.

6.4.3 Neural Network for x-y Event Vertex Reconstruction

Artificial neural networks (NN) are commonly used for pattern recognition purpose [244]. A NN consists of several layers of neurons, which are connected with weighted links ω_{ij} to each other. The individual neurons in a layer receive the weighted output of all neurons from the previous layer. The output of the individual neurons in the layer are then computed by taking into account an external activation function f. After the entire network has been executed, the output of the last layer corresponds to the answer of the entire network. A NN algorithm was developed for the x-y position reconstruction of the interaction vertex for the upgraded Xurich detector, using the Tensorflow [245] framework. As shown in Figure 6.19 (left), the NN consists of 16 input layers, which represent the top SiPM array, three hidden layers with 10, 30 and 10 neurons, and an output layer with two neurons providing the x and y coordinates of an event. The type of the NN is feed-forward because every neuron in each layer depends only on neurons in the previous layer. The number of hidden layers and their configuration were optimised empirically.

The NN was trained on a Monte Carlo dataset, for which the output is known for the configuration of the input parameters. The NN was trained on the S2 signal Monte Carlo data, which was described in the previous section. 500 000 events were uniformly distributed in the x-y plane in a range of 0.5 mm below the anode. Each event consisted of 10 000 photons, which were isotropically emitted and the NN was trained based on these events with a back-propagation learning algorithm. In Figure 6.19 (right) an example of the simulated S2 hit pattern in the SiPM array is shown. The individual light distributions in the SiPMs were normalised by the total number of photons detected in the

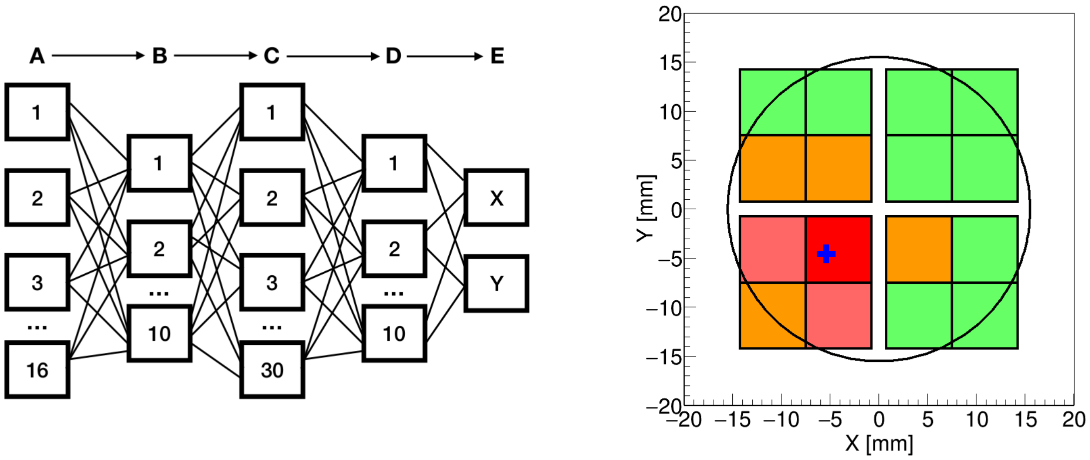

Figure 6.19: Left: The neural network architecture used for the position reconstruction in the Xurich detector. The neural network consists of 16 input layers (A) which represent the top SiPM array, three hidden layers with 10, 30 and 10 neurons (B, C, D), and an output layer (E) with two neurons providing the x and y coordinates of an event. Right: A simulated S2 light pattern for the top SiPM array. The blue cross indicates the simulated event location. The SiPM directly above the event detects most of the light (red). SiPMs further away from the interaction see less light (light red, orange, green). The black circle indicates the TPC boundary, and the black squares the individual SiPM segments.

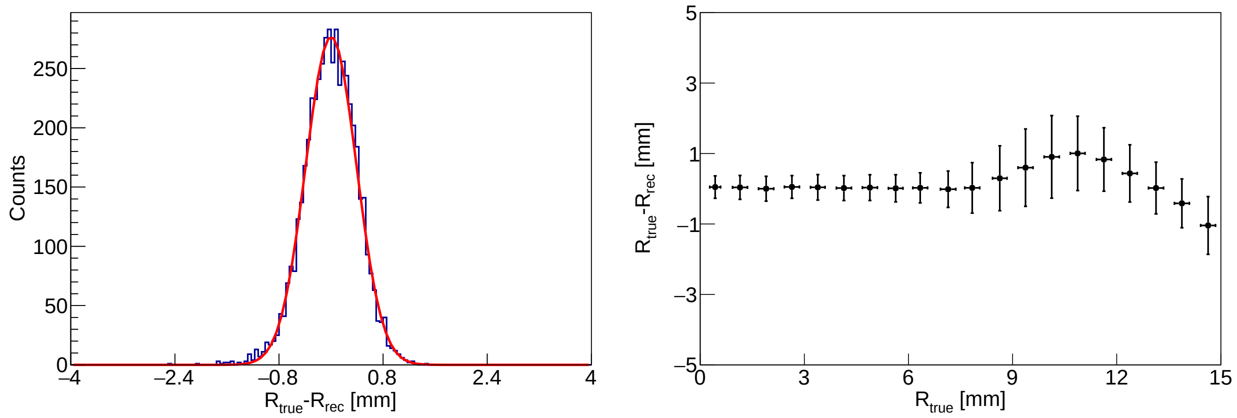

Figure 6.20: Left: Difference between the simulated ($R_{\rm true}$) and reconstructed ($R_{\rm rec}$) radii for the central part of the TPC ($R < 9$ mm). The distribution is fitted with a Gaussian function (red line). The standard deviation σ of the Gaussian refers to the reconstruction resolution and was measured to be 0.4 mm. Right: The absolute reconstruction error as a function of radius. The reconstruction uncertainty increases towards the edge of the detector, due to the lower SiPM coverage in this region.

top array. The blue cross indicates the initial S2 event location. The LCE maps used for the NN training are presented in Appendix I.

The NN position reconstruction algorithm was verified on a Monte Carlo dataset, which was not used for the training process. The Monte Carlo test dataset consisted of 10 000 events, and the parameter of interest was the radial coordinate r, due to the cylindrical symmetry of the Xurich detector. In Figure 6.20 (left), the difference between the simulated and reconstructed radial positions of the events is shown. The distribution is centred at around zero and fitted with a Gaussian function. The standard deviation (σ) of the Gaussian refers to the reconstruction resolution and was measured to be 0.4 mm. The difference between the simulated and reconstructed radial positions as a function of the radius is shown in Figure 6.20 (right). The reconstruction uncertainty increases towards the edge of the detector, due to the lower SiPM coverage in this region. The reconstruction resolution is sufficient to fiducialise the Xurich detector and to further reject events at the edge of the target volume.

The developed SiPM array was constructed and an initial performance evaluation in liquid xenon was performed, in order to guarantee the proper functioning of the amplifier readout base and the SiPMs, which will be described in the next section.

6.4.4 SiPM Array Performance in Liquid Xenon

The developed SiPM array was evaluated in the single-phase liquid xenon detector described in section 5.2, in order to validate the design and the readout electronics. The section is partially published in [227]. The SiPM was positioned near the centre of the inner detector facing a small PTFE chamber containing an ^{241}Am calibration source (described in [246]) with an α energy of 5.486 MeV and a half-life of 432 years. The ^{241}Am calibration source was placed in the centre of the PTFE chamber, located $\sim$5 cm below the SiPM array. The readout chain was the same as in section 6.3.1, but the external amplifier (LNA-1440) was removed, due to the usage of the cryogenic amplifier. The setup was filled with $\sim$11 kg of xenon and the SiPM was completely submerged in the liquid at a pressure of $\sim$1.54 bar. The xenon was constantly purified by circulating it through a hot metal getter ($\sim$4 SLPM) and the gas system was equipped with a mixing chamber that allowed us to introduce the metastable $^{83\mathrm{m}}$Kr calibration source (described in [216]) into the liquid. [227].

We measured the event rate and the gain of the SiPM array in liquid xenon for 15 days. The temperature of the setup increased linearly during this time by $\sim$1 K, resulting in a pressure increase of 0.05 bar. For this measurement, we operated the flash ADC in a self-trigger mode with a constant threshold of 0.5 PE. We regularly acquired the single photoelectron spectrum and extracted the gain using the same procedure as described in section 6.3.2. In Figure 6.21 (right) the mean gain of the individual SiPMs in liquid xenon at a temperature of $\sim$185 K and an over-voltage of 5.7 V is shown. The gain variations between the different segments are less than 1 % and within the error bars of the gain estimation. The mean combined gain (cryogenic amplifier + SiPM gain) of the array is 3.11×10^7 with an rms of 0.06×10^7. The mean resolution of the array is 5.62 % with an rms of 0.11 %. The long-term stability of the gain of the SiPM segment 0 (the SiPM indexing is shown in Figure 6.21) and the pressure inside the setup is shown in Figure 6.23 (left). The combined gain of all segments show a slight decrease over time, due to the slight temperature and pressure increase in the detector. Paragaph published in [227].

The event rate was measured at a threshold of 0.5 PE, and the behaviour of SiPM segment zero as a function of time is shown in Figure 6.23 (right). This rate consists of thermally generated pulses in the SiPM and pulses due to the detected xenon scintillation light. The observed event rate increases over the measurement period due to the continuous purification of the xenon, and thus an increase in the light yield. We injected a $^{83\mathrm{m}}$Kr calibration source at three different time points into the gas system and hence into the liquid, visible in the three peaks above the smooth distribution. The event rate differs among these peaks, due to the different $^{83\mathrm{m}}$Kr injection times. During the last $^{83\mathrm{m}}$Kr injection we waited until the event rate of the SiPM stabilised at a constant level, to achieve a homogeneous event distribution inside the detector. We extracted the $^{83\mathrm{m}}$Kr decay time by fitting the event rate after the third $^{83\mathrm{m}}$Kr injection with an exponential function combined with a linear function, which models the increase of the background event rate due to the xenon purification. The fit resulted in an average decay time of (1.86 ± 0.03) h. This value is in agreement with previous measurements [247] and consistent with the published value of 1.83 h [248]. Paragaph in [227].

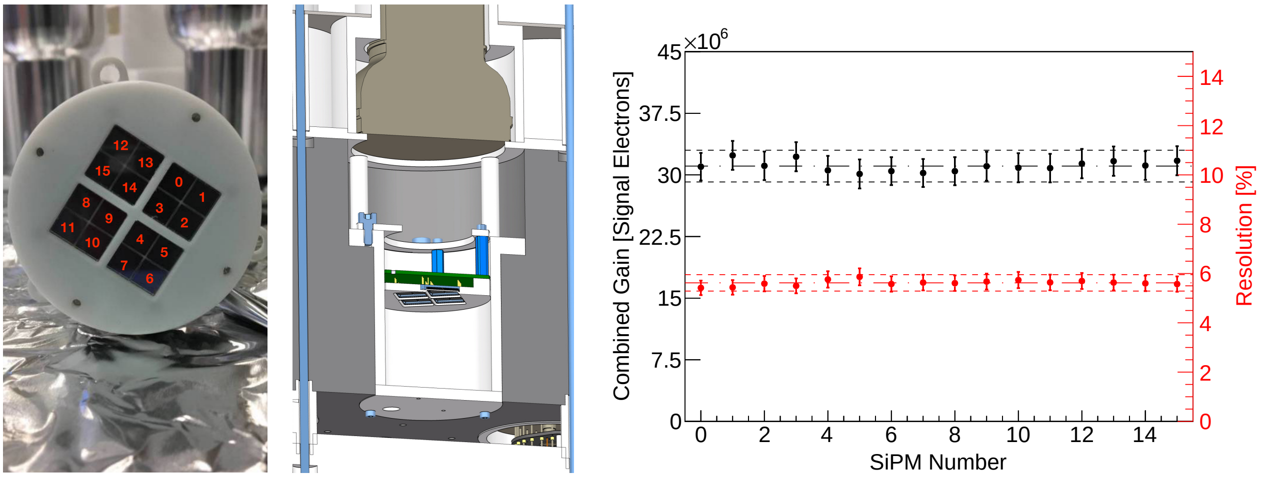

Figure 6.21: Left: The produced top SiPM array of the Xurich detector. It consists of four S13371 $12\times12\,\mathrm{mm}^2$ VUV sensitive SiPM from Hamamatsu. Centre: A CAD drawing of the installed SiPM array inside the single-phase liquid xenon detector described in section 5.2. The stable operation in liquid xenon of the SiPM array will be verified in this setup. Right: The combined gain and resolution of the SiPM array in liquid xenon at a temperature of $\sim$185 K and over-voltage of 5.7 V. The mean combined gain and resolution of the array is 3.11×10^7 and 5.62 %, respectively.

We measured the light yield evolution in the liquid xenon setup for 15 days. For this purpose, we continuously monitored the xenon scintillation light produced by α-decays of an ^{241}Am α-source. We regularly acquired a charge spectrum for every segment with the ADC, as shown in Figure 6.22

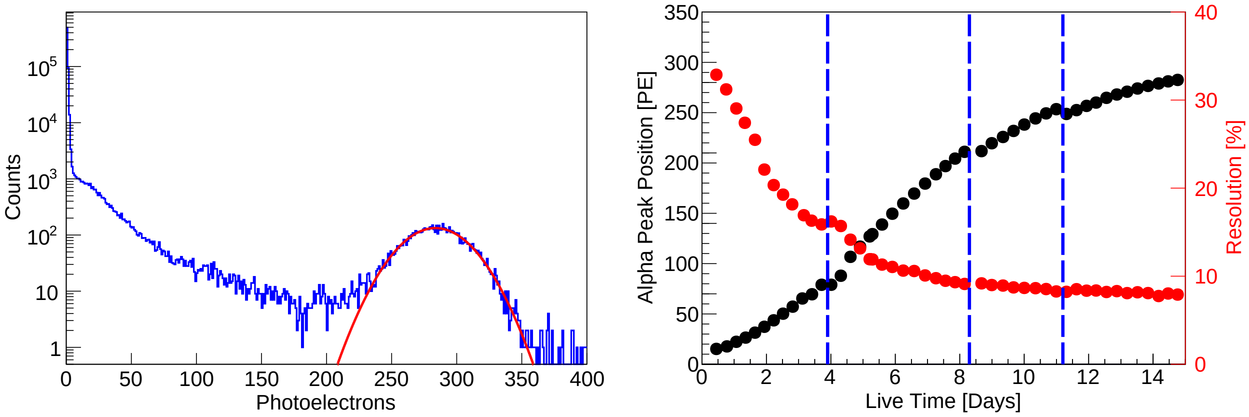

Figure 6.22: Left: The measured S1 SiPM spectrum of segment 0 with the ^{241}Am source in liquid xenon. At high energies, the α-peak is visible and fitted with a Gaussian function (red curve) to obtain the mean α-peak position. Right: The mean α-peak position (black points) and resolution (red points) over time for 15 days of segment 0. The measured position increases due to the continuous purification of the xenon gas, and hence this leads to an increase in the light yield. The observed dips can be correlated with times when we stopped the xenon gas recirculation (blue dashed lines). Published in [227].

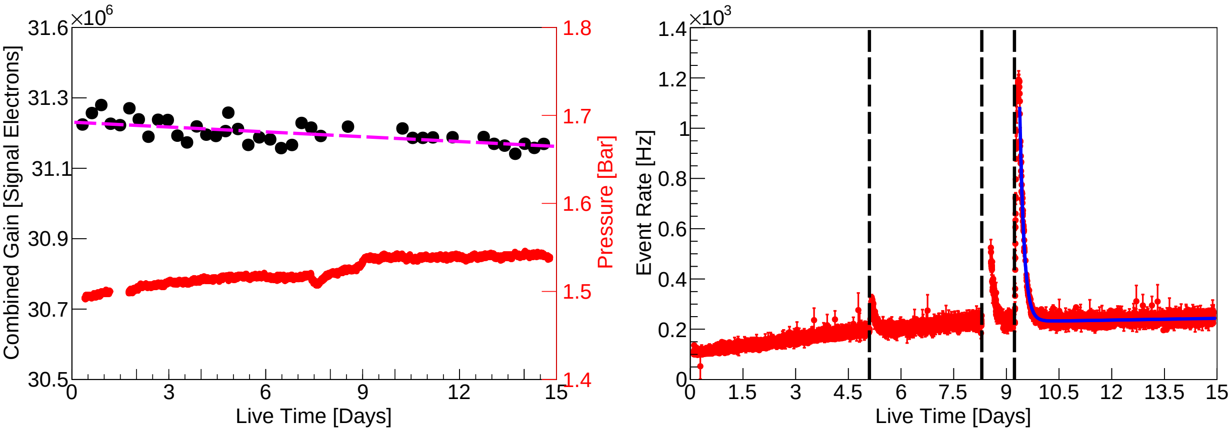

Figure 6.23: Left: The gain of the SiPM segment 0 in liquid xenon (black points) and pressure inside the setup (red points) as a function of time for 15 days. The gain, fitted with a linear function (magenta dashed line) shows a slight decrease, which is correlated to a pressure and temperature increase in the detector with time. Right: The event rate measured by the SiPM segment 0 at a 0.5 PE threshold. It increases with time, due to the continuous purification of the xenon gas, and hence increase in light yield. We injected $^{83\mathrm{m}}$Kr three times into the setup (black dashed lines), visible by the three peaks above the smooth distribution. By fitting the event rate after the third $^{83\mathrm{m}}$Kr injection with an exponential combined with a linear function (blue curve), to model the background events, we obtain the expected $^{83\mathrm{m}}$K-decay time of (1.86 ± 0.03) h. Published in [227].

(left) for one particular measurement. We converted the number of signal electrons to photoelectrons by using the measured gain, shown in Figure 6.23 (left). The α-peaks were fitted with Gaussian functions to obtain their mean position. Figure 6.22 (right) shows the evolution of the α-peak position in time, which continuously shifts to higher values due to xenon gas purification and thus the increase in the overall light yield. We stopped the recirculation through the getter three times, due to the $^{83\mathrm{m}}$Kr injections, which is visible as a decrease in the α-peak position. After 15 days of measurement, we reached a light yield of (45.29 ±0.16) PE/MeV. The energy resolution computed on the α-peak improved from 32% at the start to 8% at the end of the measurement. Paragaph published in [227].

The performed measurements verified that the SiPM array works as expected in a liquid xenon environment and the installation inside the Xurich detector can be performed. At the time of writing this thesis, the developed SiPM array was successfully installed inside Xurich detector, and the commissioning phase of the detector started. The necessary studies were performed in order to guarantee a stable operation inside the detector, and the necessary Monte Carol simulations were made to allow for the x-y position reconstruction of the interaction vertex, which will be used in the processing stage of the acquired data.

“Nothing in life is to be feared, it is only to be understood. Now is the time to understand more, so that we may fear less.”

Marie Curie

CHAPTER 7

Summary and Conclusions

Observations at cosmological and astronomical scales indicate that the majority of matter in our Universe is in the form of non-relativistic and long-lived dark matter particles. The nature of dark matter remains a missing puzzle piece for physicists. The XENON1T detector, a dual-phase time projection chamber (TPC) using 2 t liquid xenon as a target mass, is the world’s most sensitive direct dark matter detection experiment at the time of writing this thesis. It sets the best limit on the spin-independent WIMP-nucleon scattering cross section above 6 GeV with a minimum of $4.1 \times 10^{-47}\,\mathrm{cm}^2$ at 30 GeV of 90 % confidence level. The race to discover dark matter will continue with multi-ton liquid xenon TPCs, such as XENONnT and DARWIN. During my PhD work, I was involved in every aspect of the development, operation and characterisation of the XENON1T TPC, including the analysis of the 278.8 days of science data. In addition, detector R&D was performed as a first step towards ultra-low-background multi-ton liquid xenon TPCs.

The XENON1T photomultiplier tubes (PMTs) and voltage divider network response were studied and verified, in order to guarantee a linear response to interactions of different energies. The dynamic range is guaranteed from 0 PE to $\sim 140\,000$ PE light intensities (depending on the PMT gain), which is limited by the dynamic range of the used digitisers. In addition, the XENON1T TPC design was trial assembled and verified in a specially developed evaluation setup at $-100\,^{\circ}\mathrm{C}$. The results of the trial assembly guided the design and the final assembly and commissioning of the TPC at LNGS. Furthermore, the thermal expansion coefficient of PTFE was measured, and the total target mass and drift length of the TPC were calculated. Due to the gained experience with the trial TPC assembly, I was co-responsible for the cleaning and assembly of the XENON1T TPC at the University of Münster and LNGS, which after the successful commissioning phase led to the world best direct dark matter detector.

During the TPC commissioning phase, a procedure was developed to measure and monitor the PMT afterpulse rate based on multiple photoelectron emission from an external light source. The measurement results assisted in diagnosing the behaviour of the TPC during data. The PMT calibration including the afterpulse, gain and single photoelectron acceptance was performed regularly, typically twice a week. The results of the calibrations were stored in a dynamic database, which was also developed within my PhD work. The database can be accessed with a web-based visualisation tool, which allows for monitoring of the evolution of various quantities of interest and visualising their correlation. This tool was crucial to characterise the detector stability.

The electrostatic boundary element field solver of KEMField was successfully adapted into a newly developed framework, which is dedicated to electrostatic field simulations of noble gas dual-phase TPCs, including electron particle tracking. The framework was verified with a detailed simulation of a small xenon-based dual-phase TPC (Xurich) and various electrostatic problems. The capacitance of the unit cube was simulated with high precision, and the simulation results are compatible with the current best limit obtained from Monte Carlo simulation. In addition, a model of the XENON1T detector was precisely implemented based on the CAD drawings into the framework.

The simulated electron trajectory inside the detector revealed a charge-up of the PTFE panels over the detector runtime. The detector specific drift and extraction field were extracted from the simulations and were used to determine the drift velocity of electrons in liquid xenon at different drift fields, and the results are in agreement with previous measurements. Furthermore, the detector response was studied at different drift fields, and a combined energy scale was determined based on the results.

In order to guarantee a proper event selection of the science data, two data quality cuts were developed, which reject non-physical events at high NR signal acceptance level (97 %–99 %). The cuts were verified on calibration data and were used to ensure that in the acquired 278.8 days of science data there are no non-physical events in the region of interest. A profile likelihood analysis parametrised in spatial and energy dimensions indicates no significant access above 3σ of the background-only hypothesis at all WIMP masses. XENON1T has set the best limit on the spin-independent WIMP-nucleon scattering cross section above 6 GeV, which excludes a large fraction of previously unexplored WIMP parameter space at the time of writing this thesis.

Another important topic of this thesis was the R&D work for the future multi-ton experiment XENONnT. The XENONnT dark matter detector will become, due to $\sim 6\,\mathrm{t}$ of liquid xenon target mass, very competitive in the neutrinoless double beta-decay search ($0\nu\beta\beta$) at a Q-Value of 2.458 MeV. To address the challenge of a linear response of the TPC from a few keV to the MeV energy range an amplifier was developed. The amplifier offers two channels: one high gain output for the keV energy WIMP dark matter search, and a low gain output for the MeV energy-range. The amplifier will be integrated into the XENONnT experiment for the readout of the top and bottom array PMTs with the start of the detector construction.

In order to guarantee the functionality of all PMTs in the XENONnT detector and to avoid a possible failure during the detector runtime, all procured PMTs must be tested in liquid xenon beforehand. To do this, an evaluation setup, which can house up to ten 3-inch PMTs, was built, including the measurement procedure to determine PMT characteristics and the software to read out, process and analyse the data. The entire measurement procedure is established and fully automatized throughout this work. In order to test the functionality of the setup, one commissioning run was performed. At the time of writing this thesis, the setup is still in use to evaluate the last PMT batches for the XENONnT experiment. After the completed measurement campaign, the setup will be used for the further R&D work with silicon photomultipliers (SiPMs).

SiPMs are a promising replacement candidate for PMTs and have been studied during my PhD for a future application in the ultimate dark matter detector DARWIN. The VUV sensitive S13371 $12\times12\,\mathrm{mm}^2$ SiPM from Hamamatsu was characterised, and procedures were developed to measure the pixel capacitance, quenching resistance, dynamic range and voltage-dependent detection probability of a photoelectron. We discovered that the detection probability of a photoelectron reaches 100 % at an over-voltage of $\sim 3.5\,\mathrm{V}$, and the dynamic range is limited by the number of incident photons. The SiPM response was measured to be linear within 4 % until 3 600 PE.

The SiPM gain, breakdown voltage, dark count rate and correlated noise pulses were measured as a function of temperature. In order to do that, a low-temperature SiPM setup was developed by upgrading an existing facility, including the measurement procedure to measure the SiPM characteristics. We measured a gain in the order of 10^6, corresponding to the typical gain of PMTs. The breakdown voltage decreases as a function of temperature, which reduces the operation voltage while maintaining the same gain. We measured that the dark count rate decreases over several orders of magnitude when going from room temperature to 172 K, to $\sim 0.8\,\mathrm{Hz/mm}^2$ at a gain of 1.5×10^6 and an over-voltage of 5.6 V. The main dark count contribution is trap-assisted thermally generated electrons. The dark count rate is still an order of magnitude too high for the DARWIN experiment in order to achieve a compatible accidental coincidence rate as with PMTs. The crosstalk rate was measured to be invariant of the temperature, and a measurement procedure for the afterpulse rate was established. In addition, the SiPM were successfully operated at a temperature of 172 K for almost one month without showing any degradation of gain or instabilities in the dark count rate.

Furthermore, a SiPM array for the Xurich detector was developed, including the precise modelling of the scintillation light collection with Monte Carlo simulations. The SiPM array will replace the PMT above the liquid xenon target and will allow an event reconstruction with sub-millimetre precision by using a neural network pattern recognition algorithm. The neural network algorithm was designed with the machine learning framework TensorFlow. The neural network was trained and verified with Monte Carlo data. For the readout of the SiPMs, a cryogenic readout base with an integrated pre-amplifier was designed, which is directly coupled to the SiPM output and therefore operative in liquid xenon. The SiPM array was successfully commissioned in liquid xenon and calibrated with a ^{241}Am calibration source. In addition, the SiPM array was calibrated with xenon scintillation light using an internal $^{83\mathrm{m}}$Kr source mixed with the xenon, where the measured half-life agrees with previous measurements. The final installation in the Xurich detector will start with the next maintenance phase. We expect an improvement in the data quality, due to the x-y event reconstruction with a 0.4 mm precision measured from Monte Carlo data.

The nature of dark matter remains an unanswered question to date. The scalability of the target mass of a xenon-based dual-phase TPC and the continuous improvement of used technologies show the potential to explore the entire experimentally accessible WIMP parameter space in the future, with a multi-ton detector. The journey to detect dark matter with a multi-ton xenon dual-phase TPC will be filled with unexpected challenges and discoveries, which will help to further understand the Universe. I hope that the information and developments provided by my work will bring research one step closer of the realisation of the ultimate direct dark matter experiment.

Appendices

APPENDIX A

Xurich - Simulation Implementation and Results

This appendix gives the details of the implemented parts of the Xurich TPC into the simulation framework (see chapter 2). In Table A.1 the implemented parts with their corresponding voltages are listed. The cathode, gate and anode meshes, as well as the cryostat, level-control and PMTs were created with CATIA [249] and meshed with triangles by Salome [115]. The remaining parts were programmed by using C++ into the framework. The PTFE parts were not implemented, due to the similar dielectric constant as liquid xenon. The liquid/gaseous xenon boundary was implemented with a charged dielectric surface, which follows equation 2.4.

In addition, this appendix gives the simulation results of the XURICH TPC at different cathode voltages. In Table A.2 the drift and extraction field at different applied cathode voltages are listed. The simulation for the charge distributions took ∼8.8 hours and 670 000 iterations with the Robin Hood solver until an accuracy below 10^{-8} for the equipotential surfaces was reached. The drift field is calculated by fiducialising the target, by removing 3 mm from the top and bottom in order to reduce the field non-uniformity. The extraction field is calculated as the averaged electric field in the gaseous xenon between the gate and anode electrodes. The root mean square (rms) of the drift and extraction field was used as the uncertainty. The extraction field decreases with decreasing cathode voltage, due to an increased field leakage through the gate mesh. Overall, for all tested cathode voltages the extraction field is sufficient to achieve a 100 % electron extraction efficiency.

Part	Voltage [V]	Dielectric ϵ_r	# Sub-Elements
Cryostat	0	-	4 224
Level-control	0	-	15 880
Top PMT	−940	-	11 424
Bottom PMT	−870	-	11 424
Field Shaping Rings $i \in [0;6]$	$-78 - i{\times}395$	-	154 000
Anode + Holder	4 000	-	61 200
Gate + Holder	0	-	59 730
Cathode + Holder	−3 000	-	59 730
Liquid/Gaseous Xenon Boundary	-	2/1	94 800
Total Number of Sub-Elements:			472 412

Table A.1: Implemented Xurich geometry into the simulation framework.

Cathode Voltage [kV]	Drift Field [kV/cm]	Extraction Field [kV/cm]
−4	1.26 ± 0.03	10.34 ± 0.14
−3.5	1.11 ± 0.03	10.33 ± 0.14
−3	0.96 ± 0.03	10.32 ± 0.14
−2.5	0.81 ± 0.03	10.30 ± 0.14
−2	0.67 ± 0.03	10.28 ± 0.14
−1.5	0.53 ± 0.03	10.27 ± 0.14
−1	0.38 ± 0.03	10.25 ± 0.14
−0.6	0.26 ± 0.03	10.23 ± 0.14
−0.45	0.22 ± 0.03	10.23 ± 0.14

Table A.2: The drift and extraction field at different applied cathode voltages.

APPENDIX B

R8520 PMT - Dynamic Range Measurement

This appendix gives the dynamic range measurement results of the 1-inch Hamamatsu R8520 PMT. A front picture of the PMT is shown in Figure B.1 (left). A detailed description of the readout base for this type of PMT can be found in [147, 179, 250]. The total readout base resistance was 12.5 MΩ. The dynamic range was measured at a combined gain of 2×10^7 (PMT gain + amplifier gain) and following the procedure given in section 3.4.3. Therefore, the PMT voltage was set to −730 V, which resulted in a base current of $\sim 58\,\mu$A.

The dynamic range measurement results of this configuration are shown in Figure B.1 (right). The PMT response is linear within 4 % for small and large signals in a frequency range of 0–250 Hz until the saturation point of the ADC, at around 14 000 PE, which is in agreement with the predicted value using equation 3.5. For an increased signal frequency (above ∼ 250 Hz) the PMT starts to deviate from the linear response and an over-linearity is observed. Saturation effects due to insufficiently available charge on the dynode stages are visible for a frequency of 2 000 Hz, which results in a decrease of the linearity before the saturation point of the ADC. The measured over-linearity for the R8520 PMT is less than the one for the R11410 PMT, due to the higher base current of the readout base. However, the readout base of the R8520 PMT has fewer capacitors at the last dynode stages than the R11410 PMT readout base, which results in an earlier saturation.

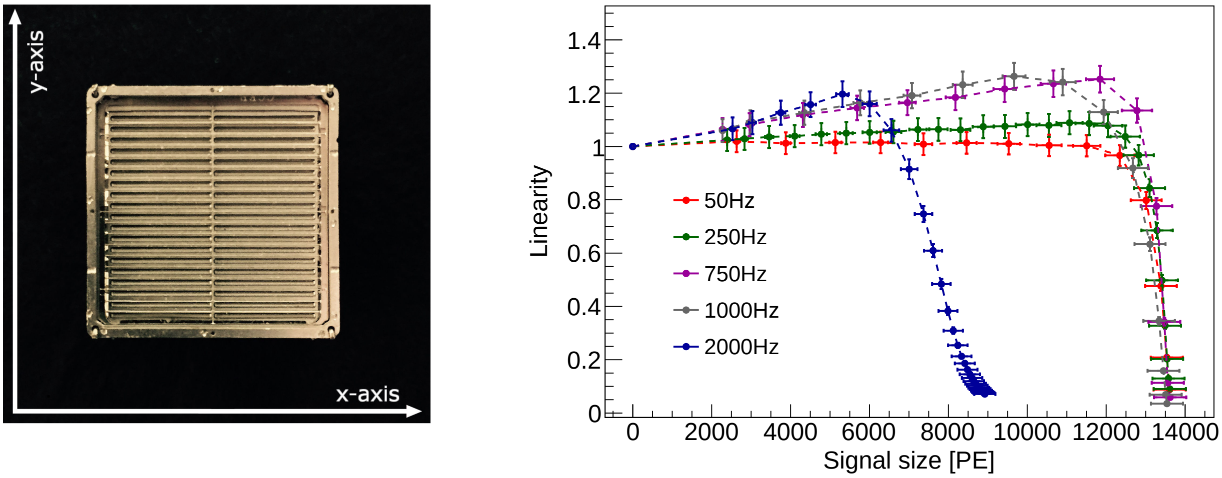

Figure B.1: Left: Front view of the Hamamatsu R8520 PMT. The R8520 PMT consists of 10 dynode stages, and it is nominally operated at −800 V. Right: The Dynamic range of the Hamamatsu R8520 PMT with a combined gain of 2×10^7. The explanation is given in the main text.

APPENDIX C

XENON1T - PMT Leak and Afterpulse Rates

This appendix gives the maps of the excluded PMTs at the end of SR1, as well as the leak and afterpulse rates of the individual PMTs. In Figure C.1 the XENON1T top and bottom PMT array are shown. PMTs which are excluded from the SR1 analysis are filled with red colour (in total 36 PMTs). In SR0, PMT 190 was turned on and included in the analysis.

In addition, the averaged leak rate of each PMT was extracted by fitting a linear function to the total afterpulse rate as a function of time. The slope of the linear fit defines the leak rate. In Figure C.2 (left) the leak rate of each PMT is shown. PMTs with a vacuum leak are marked with red and show a large leak rate. PMTs without a vacuum leak show a negligibly small leak rate, which originates from outgassing of the inner PMT surfaces. In addition, some of the PMTs show a stronger outgassing than others, due to the different production processes.

Furthermore, the afterpulse rate of the specific ions was measured for each PMT as described in section 4.2.1. In Figures C.2, C.3, C.4 and C.5 the afterpulse rates of the ions at the end of SR1 are shown. The detection sensitivity of the ion-specific afterpulse rate is $\sim 0.001\,\%$. Helium is present in all of the PMTs installed in XENON1T. PMTs with a vacuum leak show a xenon afterpulse rate, which is larger than $0.01\,\%$. It needs to be mentioned that only PMTs with a visible argon afterpulse rate developed a vacuum leak, which indicates an irregularity during the production process.

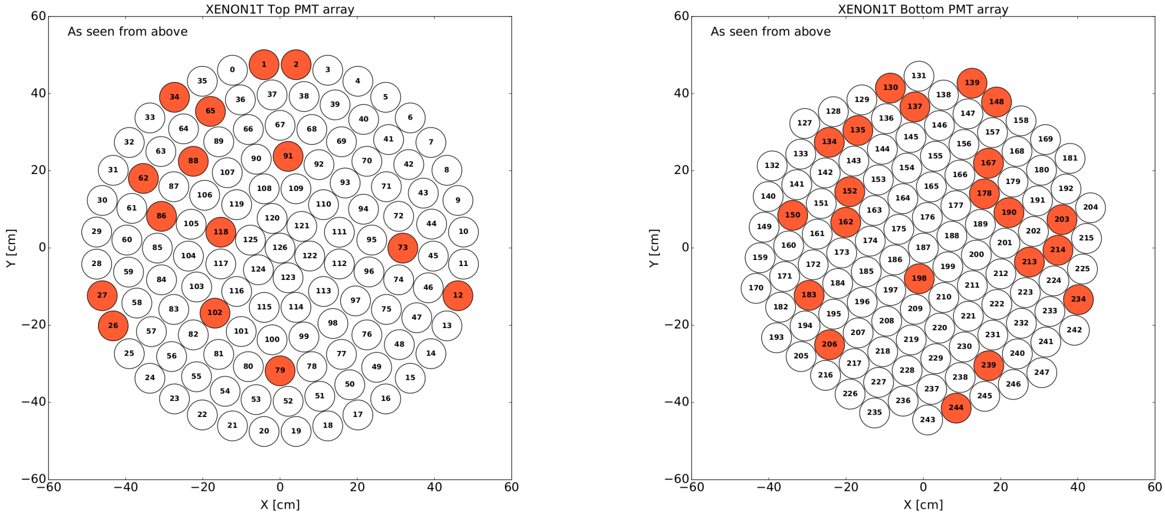

Figure C.1: The XENON1T top (left) and bottom (right) PMT array. PMTs which are turned off or excluded from the SR1 analysis are indicated in red. In total 36 PMTs have been excluded from the analysis. In addition, PMT 190 was turned on in SR0.

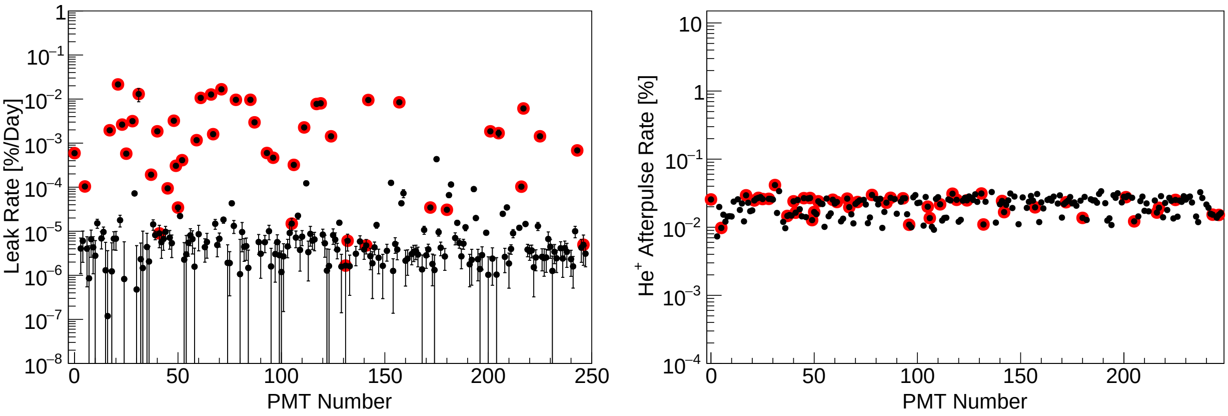

Figure C.2: The leak rate (left) and the He^{+} afterpulse rate (right) of each PMT. The red points indicate PMTs with a xenon afterpulse rate larger than 0.01 %.

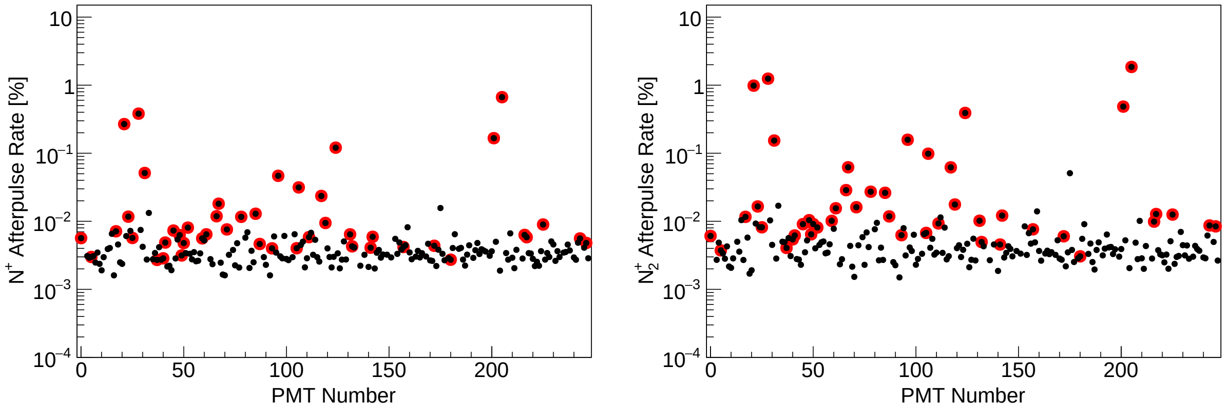

Figure C.3: The N^{+} afterpulse rate (left) and the N$_2^{+}$ afterpulse rate (right) of each PMT. The red points indicate PMT with a xenon afterpulse rate larger than 0.01 %.

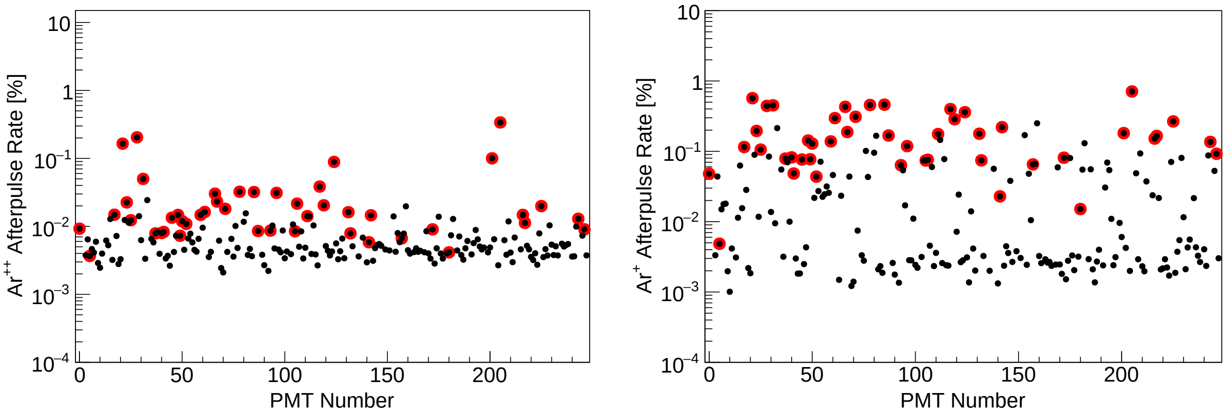

Figure C.4: The Ar^{++} afterpulse rate (left) and the Ar^{+} afterpulse rate (right) of each PMT. The red points indicate PMT with a xenon afterpulse rate larger than 0.01 %.

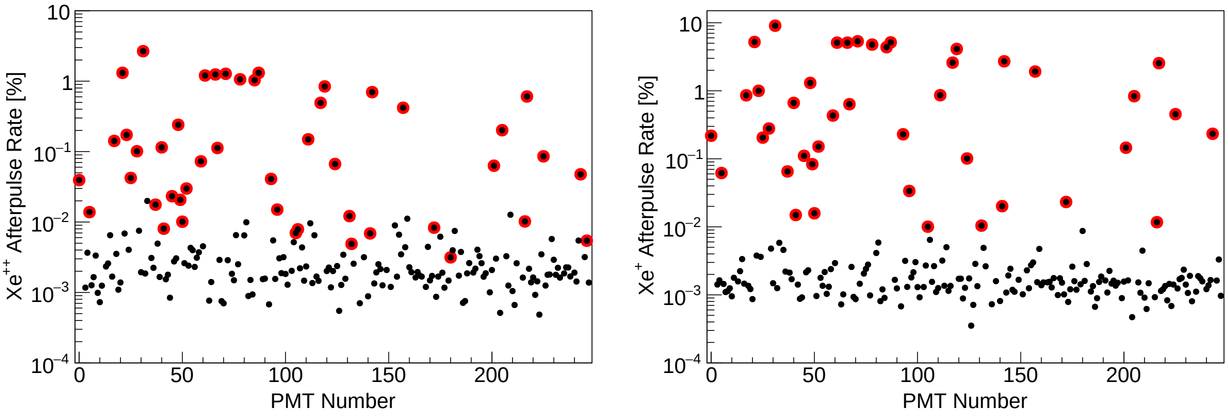

Figure C.5: The Xe^{++} afterpulse rate (left) and the Xe$_2^+$ afterpulse rate (right) of each PMT. The red points indicate PMT with a xenon afterpulse rate larger than 0.01 %.

APPENDIX D

XENON1T - Simulation Implementation and SR0 Results

This appendix gives the details of the implemented parts of the XENON1T TPC into the simulation framework (see chapter 2). In Table D.1 the implemented parts with their corresponding voltages are listed. The gate, anode and top screening meshes, as well as the PMTs were generated with CATIA [249] and meshed with triangles by Salome [115]. The remaining parts were programmed by using C++ into the framework. The PTFE parts were not implemented, due to the similar dielectric constant as liquid xenon. The liquid/gaseous xenon boundary was implemented with a charged dielectric surface, which follows equation 2.4.

In addition, this appendix gives the electrostatic field simulation results of SR0 with the developed electrostatic simulation framework. The analysis is the same as for SR1 and was described in section 4.3. A first electrostatic field simulation was performed at the nominal configuration for a cathode voltage of −12 kV. In Figure D.1, the azimuthal averaged drift and extraction field are shown. The drift field and extraction field were calculated within the magenta line. In Figure D.2 (left), $^{83\mathrm{m}}$Kr data of a calibration run during SR0 is shown inside the TPC. The event edge (blue points) was calculated by slicing the event distribution in different z-slices and fitting the slices with a Fermi-Dirac function (described by equation 4.10). An inward bias of the event edge is observable for

Part	Voltage [V]	Dielectric ϵ_r	# Sub-Elements
Cryostat	0	-	134 800
Bell	0	-	21 900
Top PMT Array $i \in [0;128]$	$[0;-1700]$	-	502 272
Top Screening Mesh + Holder	−1 550	-	126 072
Anode + Holder	4 000	-	591 079
Liquid/Gaseous Xenon Boundary	-	2/1	149 700
Gate + Holder	0	-	560 780
Field Shaping Rings $i \in [0;74]$	$(-V_c/197.5)\times(185 - i\times2.5)$	-	592 000
Cathode + Holder	SR0: −12 000 SR1: −8 000	-	141 920
Bottom Screening Mesh + Holder	SR0: −1 550 SR1: −2 500	-	129 920
Bottom PMT Array $i \in [0;120]$	$[0;-1700]$	-	478 728
Total Number of Sub-Elements:			3 299 251

Table D.1: Implemented XENON1T geometry into the simulation framework.

interactions deep inside the TPC (high z coordinate) and close to the TPC boundary (high radii R). In Figure D.2 (right), the simulated field correction map is shown and overlaid with the event edge from the data. The field correction map was obtained by tracking single electrons uniformly distributed inside the TPC until the anode. A mismatch between the data and the simulation is observed.

In a second electrostatic field simulation, the first field shaping ring and the cathode was set on the same potential, in order to study the hypotheses of a short circuit. In Figure D.3 (left) the azimuthal averaged field correction map for the tuned configuration is shown, and the event edge (red points) obtained from the $^{83\mathrm{m}}$Kr data is overlaid, leading to a better match between the simulation and the data. The $^{83\mathrm{m}}$Kr calibration data was corrected for the radial position with the simulated correction map. In Figure D.3 (right), the position corrected $^{83\mathrm{m}}$Kr calibration data is

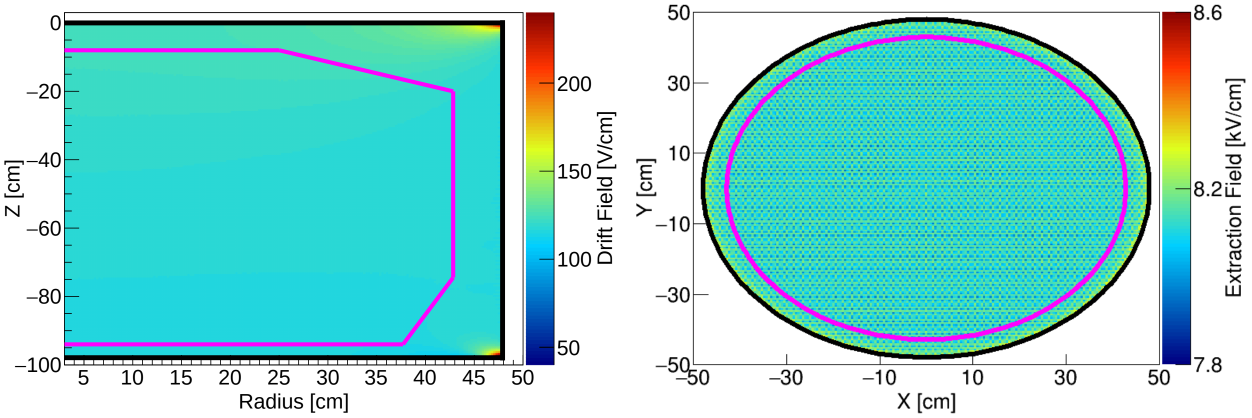

Figure D.1: The azimuthal averaged drift field inside the TPC (left) and the extraction field in the x-y plane (right). The magenta lines indicate the 1.3 t fiducial volume, and the black lines represent the TPC boundary. The drift and extraction field was calculated within the magenta lines.

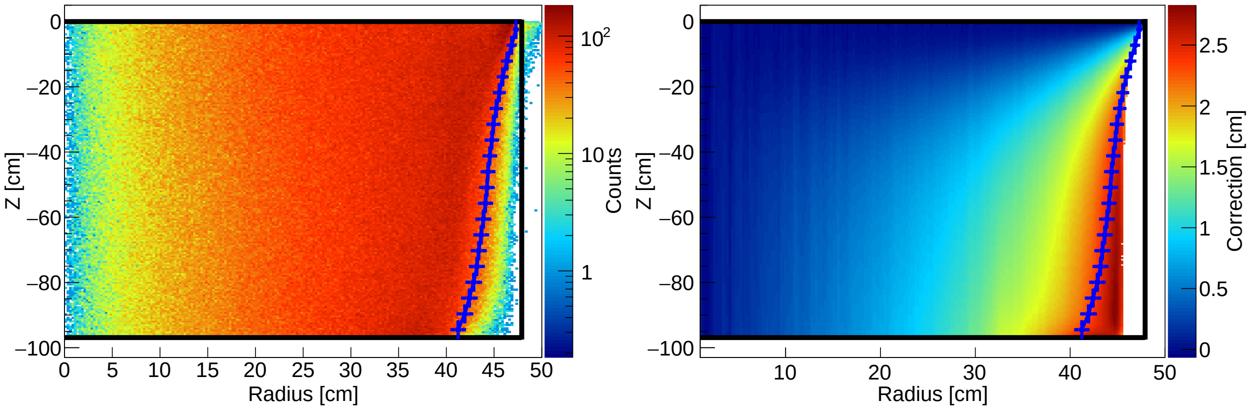

Figure D.2: Left: The $^{83\mathrm{m}}$Kr event distribution inside the TPC. The blue points represent the calculated event edge and the black lines represent the TPC boundary. Right: The field correction map inside the TPC, overlaid with the calculated event edge from the $^{83\mathrm{m}}$Kr data (blue points). The black lines represent the TPC boundary. A mismatch between the data and simulation is observed at high values of radius R and interaction depth z.

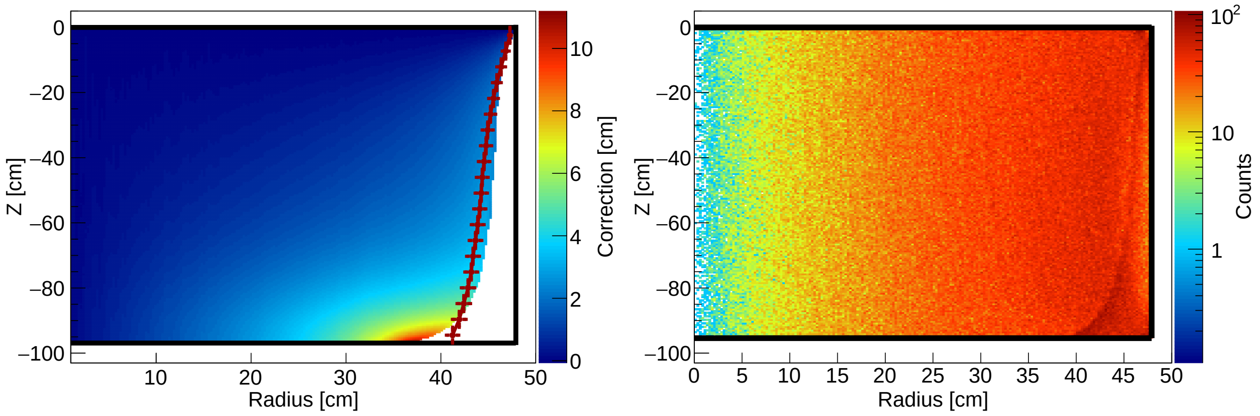

Figure D.3: Left: The field correction map inside the TPC overlaid with the calculated event edge from the $^{83\text{m}}$Kr data (red points). The black lines represent the TPC boundary. The simulation and data match better in this simulation. Right: The applied field correction map on the $^{83\text{m}}$Kr calibration data. The black lines indicate the TPC boundaries. The events are more homogeneously distributed in the TPC, but some of the events are too localised corrected, which is visible at high radii R.

shown inside the TPC. After applying the correction from the simulation, the events at the bottom of the TPC are still further inwards inside the TPC, which rules out the hypothesis of a short circuit between the first field shaping ring and the cathode, due to a too strong localised correction. The origin of the inwards bias for interactions deep inside the TPC originates from the charge up of the PTFE panels.

APPENDIX E

Data Processor - Output Format

This appendix gives the ROOT data output format of the developed data processor. All branches with descriptions are listed in Table E.1. The grey marked branches need to be activated via the XML-file and are not stored by the default in order to save computation time.

Branch	Data type	Description
event	Integer	Event number
time	Double	Timestamp in seconds
baselinesavg	Double	Baseline average in fractions of 2^{bits}
baselineright	Integer	Number of samples from the right
baselineleft	Integer	Number of samples from the left
rms	Double	Baseline rms in fractions of 2^{bits}
threshold	Double	Used threshold to identify pulses
nbpulses	Integer	Number of identified pulses
trace	array	Data of the raw waveform
area	vector<double>	Integrated pulse area in fractions of $2^{\text{bits}} \times$ Samples
height	vector<double>	The maximum height in fractions of 2^{bits}
position	vector<double>	Position of the maximum height in samples
width	vector<double>	The full integration width of the pulses
width10	vector<double>	The width of the pulses at 10 % height
width50	vector<double>	The width of the pulses at 50 % height
leftedge	vector<double>	Position of the left edge of the pulses in samples
rightedge	vector<double>	Position of the right edge of the pulses in samples
entropy	vector<double>	Entropy of the pulses
peakdistance	vector<double>	Closest Distance to the next pulse in samples
risecomponent	vector<double>	Area of the pulses until the maximum height
decaycomponent	vector<double>	Area of the pulses until the right edge
decaytime	vector<double>	Recovery time (τ) of the pulses
decaytimeerror	vector<double>	Fit error on the recovery time of the pulses

Table E.1: The data processor output format with description.

APPENDIX F

R11410 PMT - Afterpulse Ion Delay Time

This appendix gives for the 3-inch Hamamatsu R11410 PMTs the afterpulse delay time of several ions as a function of voltage. The afterpulses have been initiated by a blue LED ($\lambda = 405\,\text{nm}$) with an intensity of $\sim 80\,\text{PE}$. The delay times have been extracted by fitting Gaussian functions to the delay time distributions of the ions. In Figures F.1, F.2, F.3 and F.4 the delay time for different ions

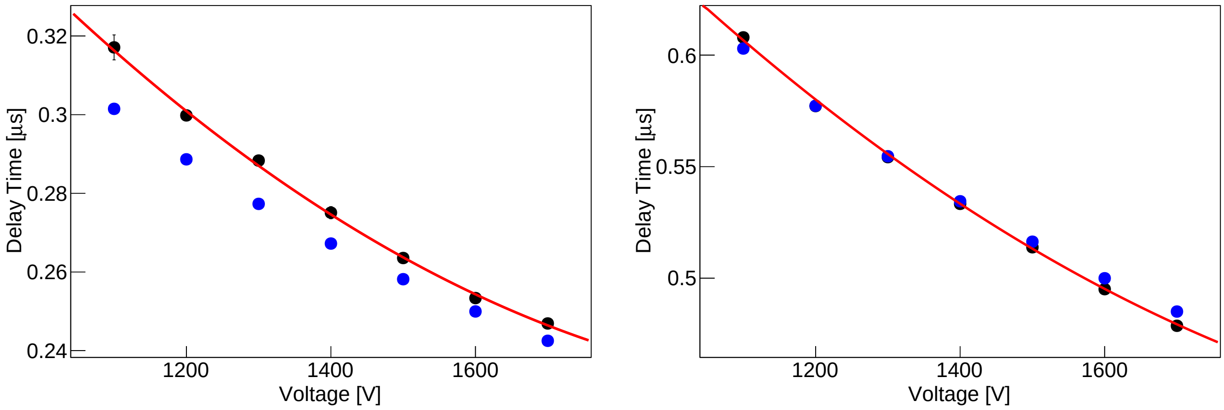

Figure F.1: H^{++} (left) and He^{+} (right) afterpulse delay time as a function of PMT voltage.

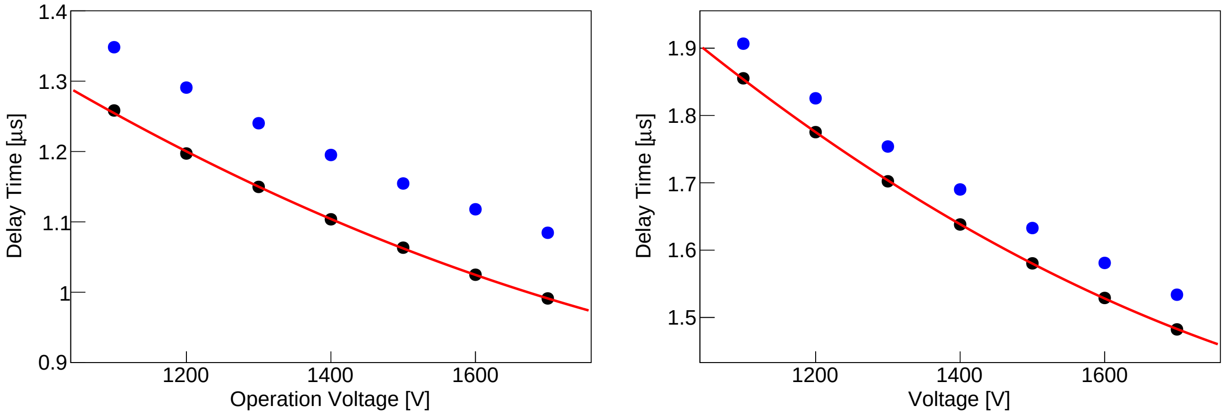

Figure F.2: Ar^{++} (left) and Ar^{+} (right) afterpulse delay time as a function of PMT voltage.

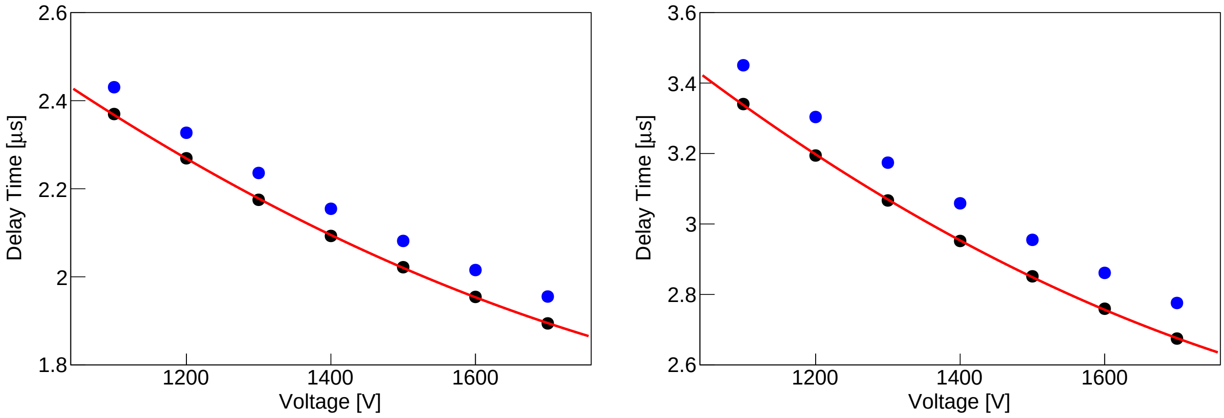

Figure F.3: Xe^{++} (left) and Xe^{+} (right) afterpulse delay time as a function of PMT voltage.

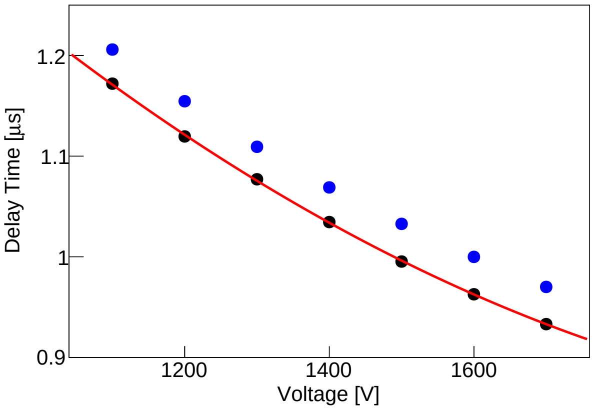

Figure F.4: Ch_4^{+} afterpulse delay time as a function of PMT voltage.

as a function of PMT voltage are shown (black data points) and compared to the theoretical values calculated by equation 3.4 (blue points). The data points were fitted with polynomial functions for visualisation purpose (red curves). The theoretical values show a difference to the experimentally obtained delay times at the level of ∼0–10 %.

APPENDIX G

XENONnT - Dual Channel Amplifier Specifications

This appendix reports the datasheet of the developed low noise dual channel NIM module amplifier for the XENONnT experiment. The low noise dual channel NIM module amplifier provides 16

Parameter	Specification
Number of Input Channels	16 independent input channels
Crosstalk	>90 dB isolation between channels, DC to 50 MHz
Outputs per Input Channel	1x high-gain output channel (HG) 1x low-gain output channel (LG)
Power Supply (Idle mode)	+6 V, 400 mA –12 V, 400 mA
Input/Output Connector	Sub Miniature version B (SMB) female
Input/Output Impedance	50 Ω
Used Operational Amplifier	HG: OPA847ID(TI) LG: OPA692ID (TI)
Voltage Gain	HG: 20 (10 into 50 Ω load) LG: 1 (0.5 into 50 Ω load)
Bandwidth	HG: DC to 250 MHz LG: DC to 200 MHz
Rise- and Fall time (10 % to 90 %)	HG: 3 ns with VOUT = 1 V step LG: 3 ns with VOUT = 1 V step
Input Voltage Noise Density	HG: 1.6 $\mathrm{nV}/\sqrt{\mathrm{Hz}}$ LG: 7.75 $\mathrm{nV}/\sqrt{\mathrm{Hz}}$
Input Offset Voltage	HG: 1 mV LG: 6 mV
Input Offset Voltage Drift	HG: 3 μV/K LG: 20 μV/K

Table G.1: Datasheet of the developed low noise dual channel NIM module amplifier.

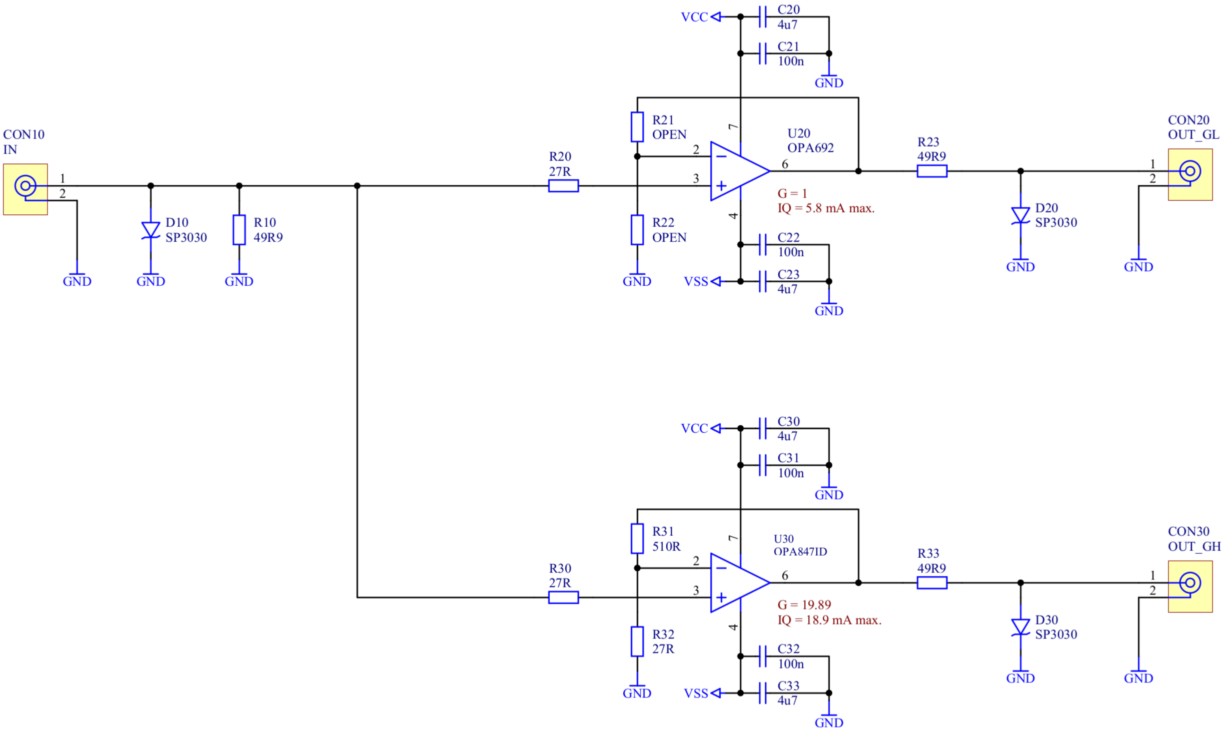

Figure G.1: The electronic schematic of the XENONnT dual channel amplifier. The input signal from the PMT is passively split into two operation amplifiers (OPA847 and OPA692). The amplifiers are designed to drive 50 Ω and have a bandwidth above the XENONnT flash ADCs (40 MHz).

independent, directly-coupled amplifiers. Each channel has two outputs: the high-gain stage (HG) with a non-inverting voltage gain of 20 (gain 10 into 50 Ω load) and the low-gain stage (LG) with a non-inverting voltage gain of 1 (gain 0.5 into 50 Ω load). The high-gain stage operates from DC to 250 MHz, the low-gain stage from DC to 200 MHz. Both stages have 50 Ω output impedance and are designed to drive 50 Ω loads. All specifications are listed in Table G.1. The electronic schematic of one amplifier board is shown in Figure G.1. The operational amplifier OPA847 from Texas Instruments was chosen for the high gain output channel with a ten-fold amplification factor (into 50 Ω load), and the operational amplifier OPA692 from Texas Instruments was chosen for the low gain channel. The amplifiers are designed to drive 50 Ω loads. The XENONnT dual channel amplifier NIM module will house 16 amplifier boards.

APPENDIX H

SiPM - Measurement Summary at 170 K

This appendix gives the summary of the measurement results at 170 K of the S13371 12×12 mm^2 VUV-sensitive SiPM from Hamamatsu. This SiPM is from general interest in experiments using xenon as a target. In Figure H.1, the gain, the single photoelectron peak (SPE) resolution, the dark count rate and the crosstalk rate as a function of over-voltage are shown. The parameters were measured as described in section 6.3.

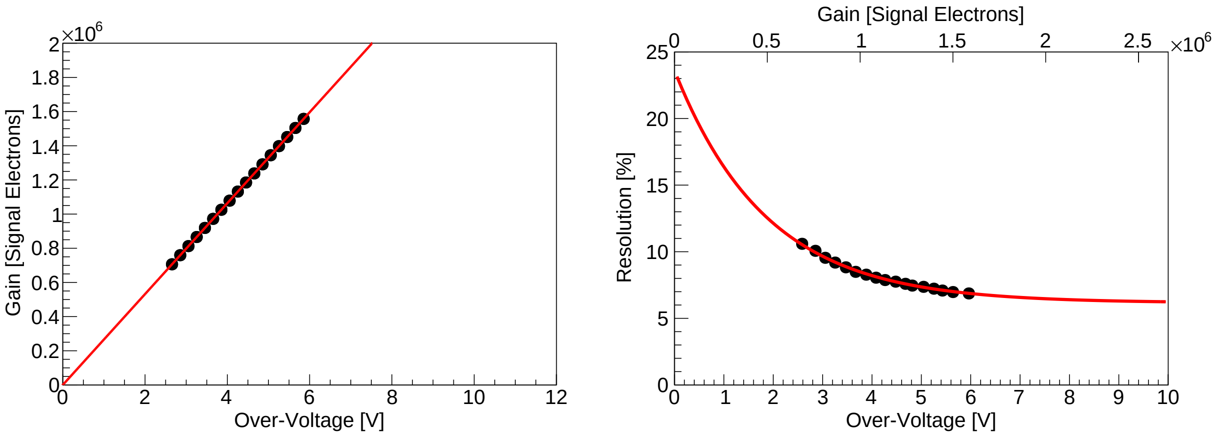

(a) Gain as a function of over-voltage

(b) SPE resolution as a function of over-voltage

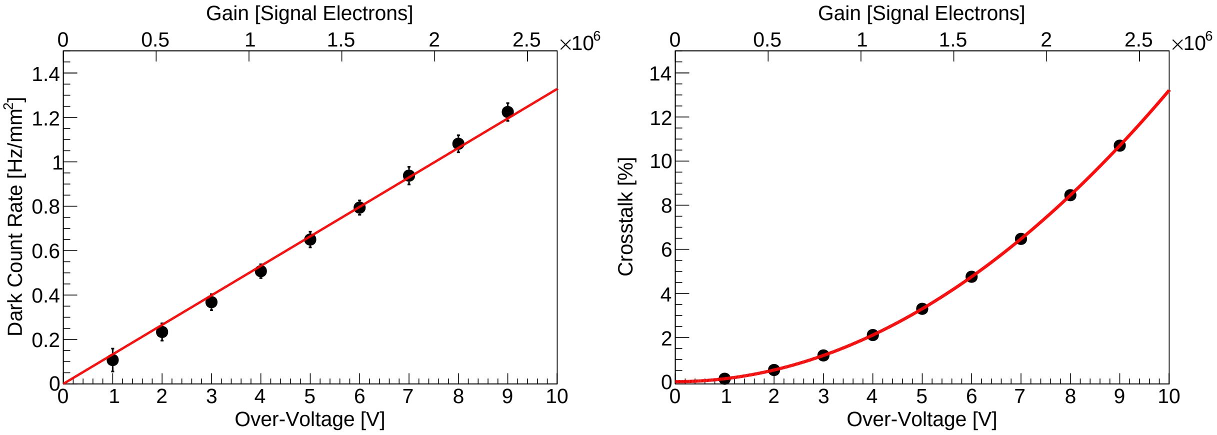

(c) Dark count rate as a function of over-voltage

(d) Crosstalk as a function of over-voltage

Figure H.1: Measured SiPM characteristics at 170 K.

APPENDIX I

Xurich - Per SiPM S2 Detection Maps

This appendix gives the simulated per SiPM S2 signal detection maps. In Figure I.1 the simulated S2 signal detection maps for each SiPM in the x-y plane are shown. The simulated S2 signals in the x-y plane were used to train the Neural Network (NN) algorithm based on the S2 signal detection maps of each SiPM. The NN algorithm was used for the x-y position reconstruction and was verified with 10 000 simulated S2 signals, which differ from the training dataset. The SiPM array does not cover the whole TPC diameter. Therefore, the NN x-y position reconstruction at the edge is worse than in the centre of the TPC. The fraction of detected photons is maximum for S2 signals close to the SiPMs. The maximum fraction of detected photons per SiPM is around 5 %.

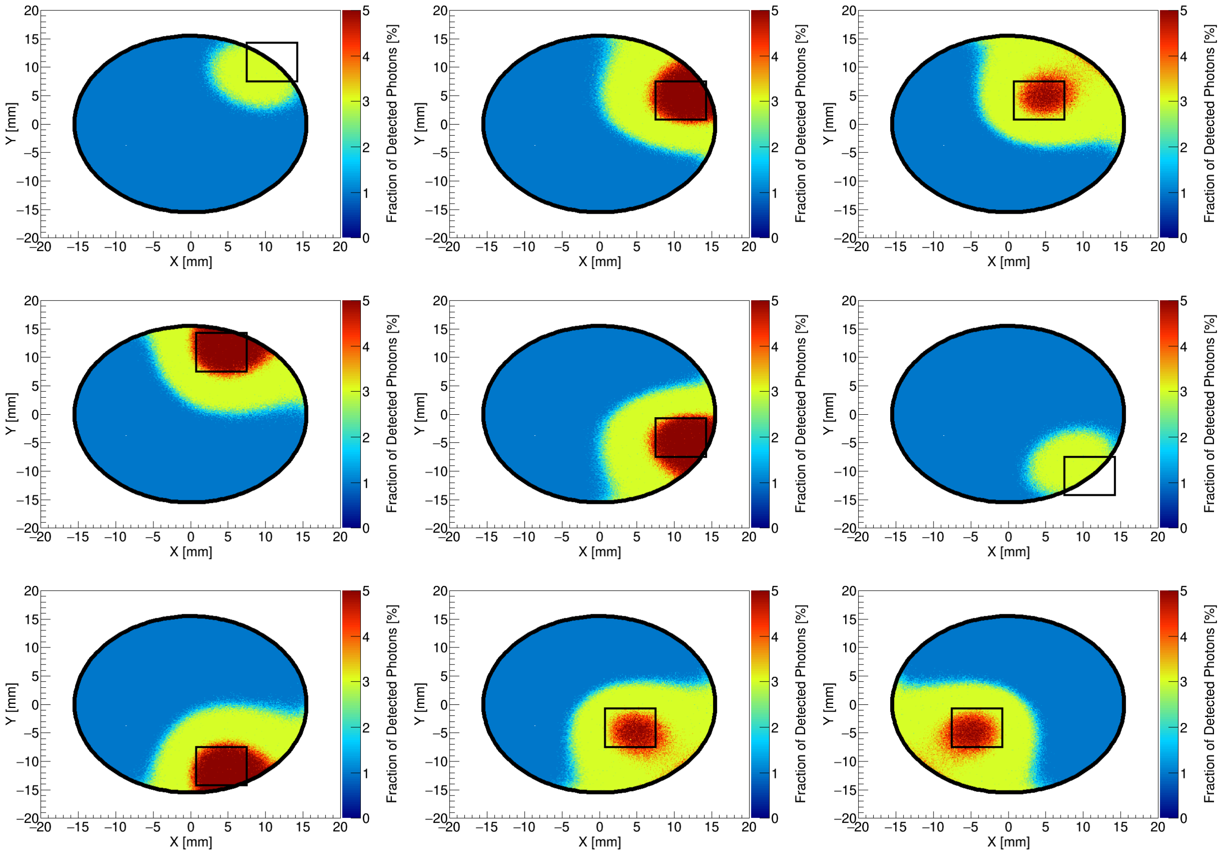

Figure I.1

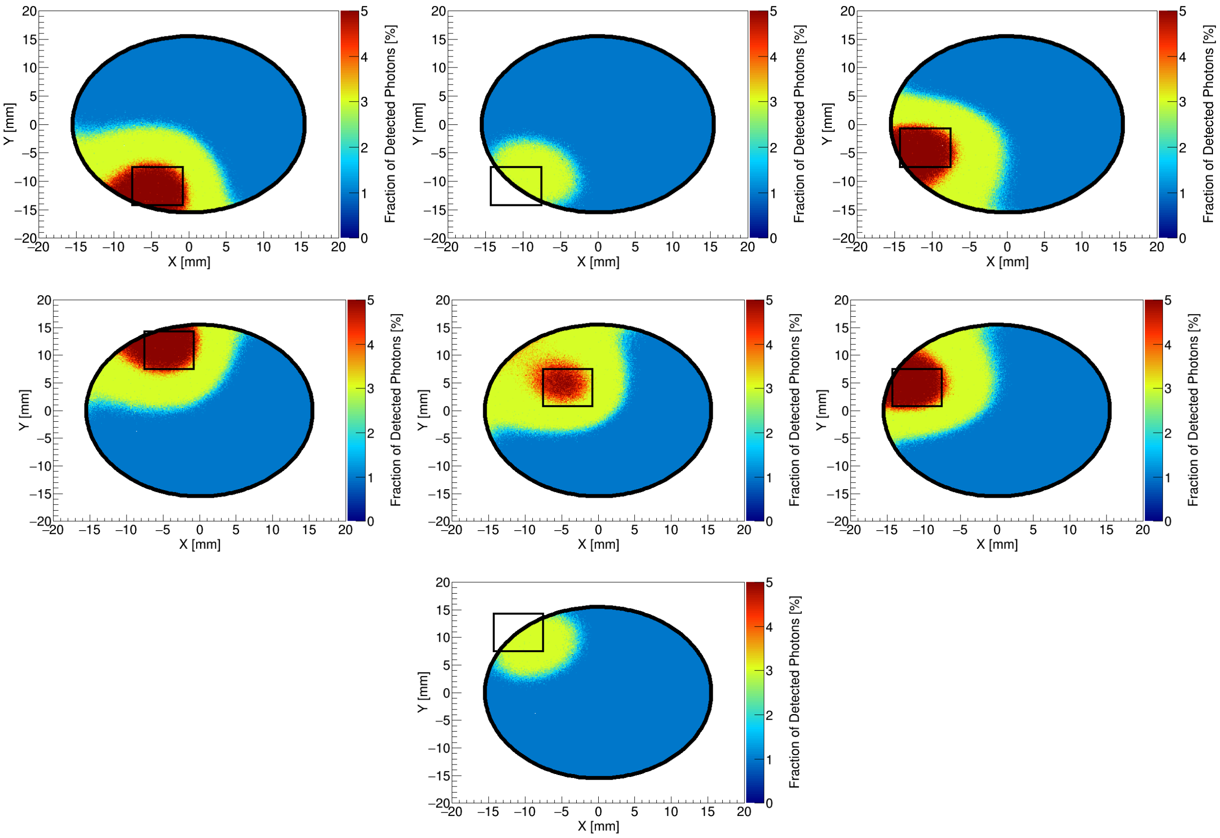

Figure I.1: The detected photons of each SiPM from the S2 signal in the x-y plane. The black circle indicates the TPC radius and the black square indicates the corresponding SiPM.

APPENDIX J

Xurich - SiPM Array Specifications

This appendix gives the specifications of the developed cryogenic SiPM array readout board. The readout board consists of 16 independent, directly-coupled amplifiers. Each amplifier channel is designed to read out one segment of the S13371 12×12 mm^2 VUV-sensitive SiPM from Hamamatsu. Each amplifier channel offers a high-gain stage (HG) with a non-inverting voltage gain of 20 and is cryogenic resistant. The high-gain stage operates from DC to 250 MHz. The channels have a 50 Ω

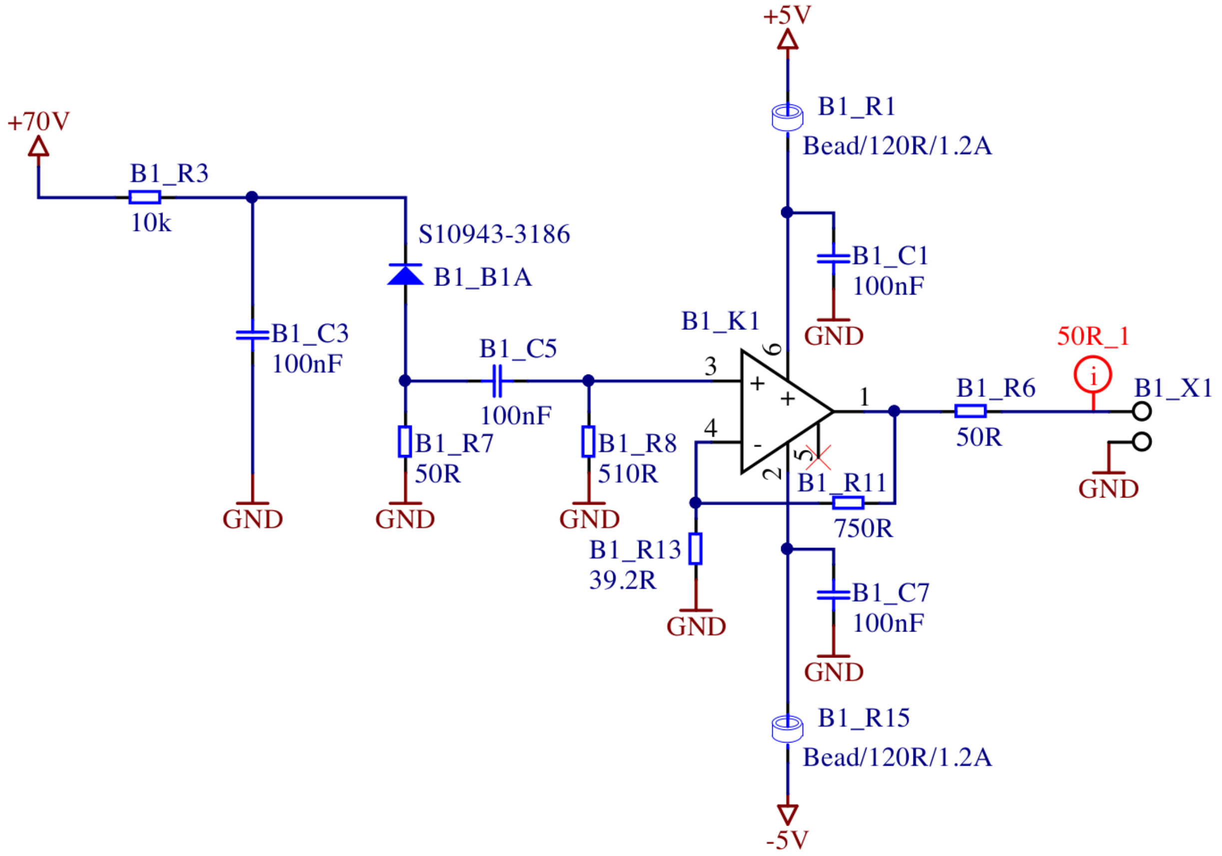

Figure J.1: The electronic schematic of a single channel of the cryogenic SiPM array amplifier. The amplifier is cryogenically resistant and directly coupled to the SiPM, which reduces the pickup noise to a negligible level. The amplifier needs to be biased in a range of ±10 V, depending on the signal polarity. The power consumption of the amplifier is $\sim$0.2 W.

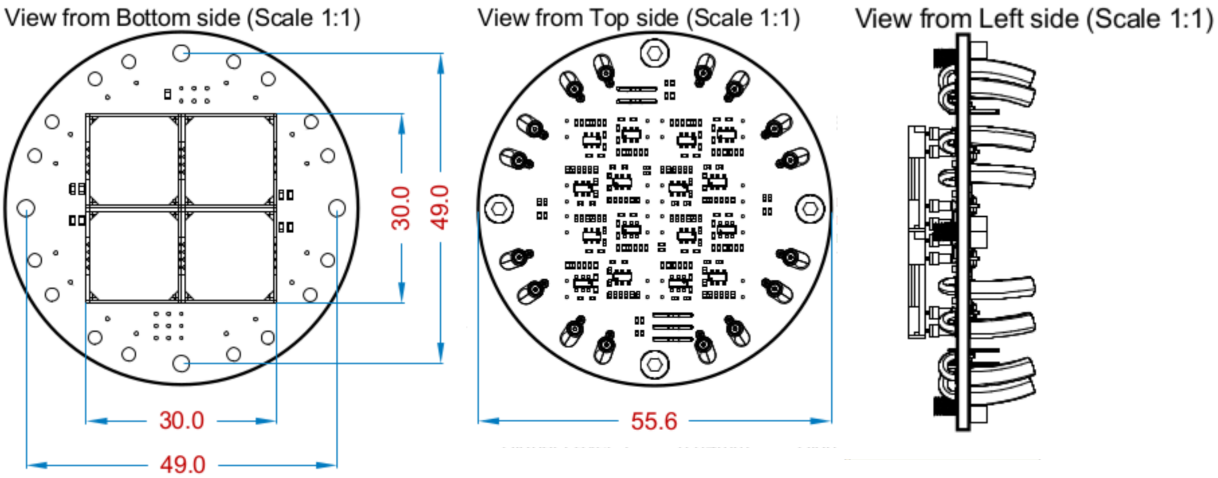

Figure J.2: The technical drawings of the Xurich SiPM readout board. All 16 SiPM segments are read out independently via PTFE cables (RG 196). A common bias voltage for the SiPMs and the amplifiers is applied via Kapton® cables.

output impedance and are designed to drive 50 Ω loads. The operational amplifier OPA847 from Texas Instruments was chosen for the high gain output channel. The electronic schematic of one readout channel is shown in Figure J.1. The amplifier is cryogenically resistant and directly coupled to the SiPM, which reduces the pickup noise to a negligible level. Furthermore, the amplifier needs to be biased in a range of ±10 V. The bias voltage polarity depends on the SiPM signal polarity.

The readout PCB of the SiPM array has an independent amplifier for each SiPM (16 in total). The technical drawing of the PCB board with the electronic components is shown in Figure J.2. The bias voltage of the SiPMs and of the amplifier is applied to the board via Kapton® cables and is the same for each channel. The signal of each channel is read out independently via coaxial PTFE cables (RG 196).

List of Figures

List of Tables

Bibliography

[1] Leszek Roszkowski, Enrico Maria Sessolo, and Sebastian Trojanowski. WIMP dark matter candidates and searches—current status and future prospects. *Rept. Prog. Phys.*, 81(6):066201, 2018.

[2] Gianfranco Bertone, Dan Hooper, and Joseph Silk. Particle dark matter: Evidence, candidates and constraints. *Phys. Rept.*, 405:279–390, 2005.

[3] Adam G. Riess et al. Observational evidence from supernovae for an accelerating universe and a cosmological constant. *Astron. J.*, 116:1009–1038, 1998.

[4] Laura Baudis. Dark matter detection. *J. Phys.*, G43(4):044001, 2016.

[5] Teresa Marrodán Undagoitia and Ludwig Rauch. Dark matter direct-detection experiments. *J. Phys.*, G43(1):013001, 2016.

[6] Fritz Zwicky. Die rotverschiebung von extragalaktischen nebeln. *Helvetica Physica Acta*, 6:110–127, 1933.

[7] Fritz Zwicky. On the masses of nebulae and of clusters of nebulae. *The Astrophysical Journal*, 86:217, 1937.

[8] M. Girardi, S. Borgani, G. Giuricin, F. Mardirossian, and M. Mezzetti. Optical luminosities and mass-to-light ratios of nearby galaxy clusters. *Astrophys. J.*, 530:62, 2000.

[9] Vera C. Rubin and W. Kent Ford Jr. Rotation of the andromeda nebula from a spectroscopic survey of emission regions. *The Astrophysical Journal*, 159:379, 1970.

[10] Isaac Newton. *Philosophiae naturalis principia mathematica*, volume 1. G. Brookman, 1833.

[11] Yoshiaki Sofue and Vera Rubin. Rotation curves of spiral galaxies. *Ann. Rev. Astron. Astrophys.*, 39:137–174, 2001.

[12] Fabio Iocco, Miguel Pato, and Gianfranco Bertone. Evidence for dark matter in the inner Milky Way. *Nature Phys.*, 11:245–248, 2015.

[13] K. G. Begeman, A. H. Broeils, and R. H. Sanders. Extended rotation curves of spiral galaxies: Dark haloes and modified dynamics. *Mon. Not. Roy. Astron. Soc.*, 249:523, 1991.

[14] Martin C. Weisskopf, Harvey D. Tananbaum, Leon P. Van Speybroeck, and Stephen L. O'Dell. Chandra x-ray observatory (cxo): overview. In *X-Ray Optics, Instruments, and Missions III*, volume 4012, pages 2–17. International Society for Optics and Photonics, 2000.

[15] David Harvey, Richard Massey, Thomas Kitching, Andy Taylor, and Eric Tittley. The non-gravitational interactions of dark matter in colliding galaxy clusters. *Science*, 347:1462–1465, 2015.

[16] Charles L. Bennett et al. Four-year cobe dmr cosmic microwave background observations: maps and basic results. *The Astrophysical Journal Letters*, 464(1):L1, 1996.

[17] N. Jarosik et al. Seven-year wilkinson microwave anisotropy probe (wmap) observations: sky maps, systematic errors, and basic results. *The Astrophysical Journal Supplement Series*, 192(2):14, 2011.

[18] R. Adam et al. Planck 2015 results. I. Overview of products and scientific results. *Astron. Astrophys.*, 594:A1, 2016.

[19] P. A. R. Ade et al. Planck 2015 results. XIII. Cosmological parameters. *Astron. Astrophys.*, 594:A13, 2016.

[20] M. Milgrom. A modification of the Newtonian dynamics: implications for galaxy systems. *Astrophys. J.*, 270:384–389, 1983.

[21] Jacob D. Bekenstein. Relativistic gravitation theory for the MOND paradigm. *Phys. Rev.*, D70:083509, 2004. [Erratum: Phys. Rev.D71,069901(2005)].

[22] J.E. Felten. Milgrom's revision of newton's laws-dynamical and cosmological consequences. *The Astrophysical Journal*, 286:3–6, 1984.

[23] Davi C. Rodrigues, Valerio Marra, Antonino del Popolo, and Zahra Davari. Absence of a fundamental acceleration scale in galaxies. *Nature Astronomy*, 2018.

[24] Nick E. Mavromatos, Mairi Sakellariadou, and Muhammad Furqaan Yusaf. Can the relativistic field theory version of modified Newtonian dynamics avoid dark matter on galactic scales? *Phys. Rev.*, D79:081301, 2009.

[25] C. Alcock et al. The MACHO project: Microlensing results from 5.7 years of LMC observations. *Astrophys. J.*, 542:281–307, 2000.

[26] Simon D.M. White, C.S. Frenk, and Marc Davis. Clustering in a neutrino-dominated universe. *The Astrophysical Journal*, 274:L1–L5, 1983.

[27] Steven Weinberg. A new light boson? *Phys. Rev. Lett.*, 40:223–226, Jan 1978.

[28] R. D. Peccei and Helen R. Quinn. CP conservation in the presence of pseudoparticles. *Phys. Rev. Lett.*, 38:1440–1443, Jun 1977.

[29] Luca Visinelli and Paolo Gondolo. Dark matter axions revisited. *Physical Review D*, 80(3):035024, 2009.

[30] Daniel J. H. Chung, Edward W. Kolb, and Antonio Riotto. Superheavy dark matter. *Phys. Rev.*, D59:023501, 1999.

[31] Kenneth Greisen. End to the cosmic-ray spectrum? *Physical Review Letters*, 16(17):748, 1966.

[32] Vadim Kuzmin and Igor Tkachev. Ultrahigh-energy cosmic rays, superheavy long living particles, and matter creation after inflation. *JETP Lett.*, 68:271–275, 1998.

[33] Alexey Boyarsky, Oleg Ruchayskiy, and Mikhail Shaposhnikov. The role of sterile neutrinos in cosmology and astrophysics. *Annual Review of Nuclear and Particle Science*, 59:191–214, 2009.

[34] Alexander Kusenko. Sterile neutrinos: The Dark side of the light fermions. *Phys. Rept.*, 481:1–28, 2009.

[35] C. Hasterok. *Gas Purity Analytics, Calibration Studies, and Background Predictions, towards the First Results of XENON1T*. PhD thesis, Ruprecht-Karls-Universität, Heidelberg, 2017.

[36] Gerard Jungman, Marc Kamionkowski, and Kim Griest. Supersymmetric dark matter. *Phys. Rept.*, 267:195–373, 1996.

[37] Theodor Kaluza. Zum Unitätsproblem der Physik. *Sitzungsber. Preuss. Akad. Wiss. Berlin (Math. Phys.)*, 1921:966–972, 1921.

[38] Oskar Klein. Quantentheorie und fünfdimensionale relativitätstheorie. *Zeitschrift für Physik*, 37(12):895–906, 1926.

[39] Howard E. Haber and Gordon L. Kane. The search for supersymmetry: probing physics beyond the standard model. *Physics Reports*, 117(2-4):75–263, 1985.

[40] Stephen P. Martin. A supersymmetry primer. In *Perspectives on supersymmetry II*, pages 1–153. World Scientific, 2010.

[41] Lyndon Evans and Philip Bryant. LHC Machine. *JINST*, 3:S08001, 2008.

[42] Andreas Birkedal, Konstantin Matchev, and Maxim Perelstein. Dark matter at colliders: A Model independent approach. *Phys. Rev.*, D70:077701, 2004.

[43] Oliver Buchmueller, Caterina Doglioni, and Lian-Tao Wang. Search for dark matter at colliders. *Nature Physics*, 13(3):217, 2017.

[44] Morad Aaboud et al. Search for dark matter at $\sqrt{s} = 13$ TeV in final states containing an energetic photon and large missing transverse momentum with the ATLAS detector. *Eur. Phys. J.*, C77(6):393, 2017.

[45] Albert M. Sirunyan et al. Search for dark matter and unparticles in events with a Z boson and missing transverse momentum in proton-proton collisions at $\sqrt{s} = 13$ TeV. *JHEP*, 03:061, 2017. [Erratum: JHEP09,106(2017)].

[46] Louis E. Strigari. Galactic Searches for Dark Matter. *Phys. Rept.*, 531:1–88, 2013.

[47] M. Ackermann et al. Search for Gamma-ray Spectral Lines with the Fermi Large Area Telescope and Dark Matter Implications. *Phys. Rev.*, D88:082002, 2013.

[48] M. L. Ahnen et al. Indirect dark matter searches in the dwarf satellite galaxy Ursa Major II with the MAGIC Telescopes. *JCAP*, 1803(03):009, 2018.

[49] A. Abramowski et al. Search for a dark matter annihilation signal from the galactic center halo with hess. *Physical Review Letters*, 106(16):161301, 2011.

[50] Thomas Schweizer, G. Hermann, W. Hofmann, and Masahiro Teshima. Cherenkov Telescope Array: The next-generation ground-based gamma-ray observatory. In *Proceedings, 30th International Cosmic Ray Conference (ICRC 2007): Merida, Yucatan, Mexico, July 3-11, 2007*, volume 3, pages 1313–1316, 2007. [3,1313(2007)].

[51] M. G. Aartsen et al. Search for annihilating dark matter in the Sun with 3 years of IceCube data. *Eur. Phys. J.*, C77(3):146, 2017.

[52] S. Adrian-Martinez et al. Limits on Dark Matter Annihilation in the Sun using the ANTARES Neutrino Telescope. *Phys. Lett.*, B759:69–74, 2016.

[53] Lars Bergstrom, Torsten Bringmann, Ilias Cholis, Dan Hooper, and Christoph Weniger. New limits on dark matter annihilation from AMS cosmic ray positron data. *Phys. Rev. Lett.*, 111:171101, 2013.

[54] Jan Conrad. Indirect Detection of WIMP Dark Matter: a compact review. In *Interplay between Particle and Astroparticle physics (IPA2014) London, United Kingdom, August 18-22, 2014*, 2014.

[55] Mark W. Goodman and Edward Witten. Detectability of Certain Dark Matter Candidates. *Phys. Rev.*, D31:3059, 1985.

[56] Andrzej K. Drukier, Katherine Freese, and David N. Spergel. Detecting cold dark-matter candidates. *Phys. Rev. D*, 33:3495–3508, Jun 1986.

[57] R. Bernabei et al. The DAMA/LIBRA apparatus. *Nucl. Instrum. Meth.*, A592:297–315, 2008.

[58] Francis Froborg. SABRE: WIMP modulation detection in the northern and southern hemisphere. *J. Phys. Conf. Ser.*, 718(4):042021, 2016.

[59] R. Bernabei et al. Searching for wimps by the annual modulation signature. *Physics Letters B*, 424(1-2):195–201, 1998.

[60] Godehard Angloher et al. Results from 730 kg days of the cresst-ii dark matter search. *The European Physical Journal C*, 72(4):1971, 2012.

[61] R. Agnese et al. Projected Sensitivity of the SuperCDMS SNOLAB experiment. *Phys. Rev.*, D95(8):082002, 2017.

[62] E. Armengaud et al. Performance of the EDELWEISS-III experiment for direct dark matter searches. *JINST*, 12(08):P08010, 2017.

[63] A. Aguilar-Arevalo et al. Search for low-mass WIMPs in a 0.6 kg day exposure of the DAMIC experiment at SNOLAB. *Phys. Rev.*, D94(8):082006, 2016.

[64] C. Amole et al. Dark Matter Search Results from the PICO-60 C_3F_8 Bubble Chamber. *Phys. Rev. Lett.*, 118(25):251301, 2017.

[65] K. Abe et al. Light WIMP search in XMASS. *Phys. Lett.*, B719:78–82, 2013.

[66] P. A. Amaudruz et al. Design and Construction of the DEAP-3600 Dark Matter Detector. *Submitted to: Astropart. Phys.*, 2017.

[67] P. Agnes et al. First Results from the DarkSide-50 Dark Matter Experiment at Laboratori Nazionali del Gran Sasso. *Phys. Lett.*, B743:456–466, 2015.

[68] J. Calvo et al. Commissioning of the ArDM experiment at the Canfranc underground laboratory: first steps towards a tonne-scale liquid argon time projection chamber for Dark Matter searches. *JCAP*, 1703(03):003, 2017.

[69] Frank J. Kerr and Donald Lynden-Bell. Review of galactic constants. *Monthly Notices of the Royal Astronomical Society*, 221(4):1023–1038, 1986.

[70] J. Silk, B. Moore, J. Diemand, J. Bullock, M. Kaplinghat, L. Strigari, et al. Particle dark matter: observations, models and searches. *Bertone ed*, 2010.

[71] Martin C. Smith et al. The rave survey: constraining the local galactic escape speed. *Monthly Notices of the Royal Astronomical Society*, 379(2):755–772, 2007.

[72] J.D. Lewin and P.F. Smith. Review of mathematics, numerical factors, and corrections for dark matter experiments based on elastic nuclear recoil. *Astroparticle Physics*, 6(1):87–112, 1996.

[73] Gianfranco Bertone, Dan Hooper, and Joseph Silk. Particle dark matter: Evidence, candidates and constraints. *Physics Reports*, 405(5-6):279–390, 2005.

[74] Gianfranco Bertone. *Particle dark matter: observations, models and searches.* Cambridge University Press, 2010.

[75] P Toivanen, M Kortelainen, J Suhonen, and J Toivanen. Large-scale shell-model calculations of elastic and inelastic scattering rates of lightest supersymmetric particles (lsp) on i 127, xe 129, xe 131, and cs 133 nuclei. *Physical Review C*, 79(4):044302, 2009.

[76] A. Liam Fitzpatrick, Wick Haxton, Emanuel Katz, Nicholas Lubbers, and Yiming Xu. Model Independent Direct Detection Analyses. 2012.

[77] A. Liam Fitzpatrick, Wick Haxton, Emanuel Katz, Nicholas Lubbers, and Yiming Xu. The Effective Field Theory of Dark Matter Direct Detection. *JCAP*, 1302:004, 2013.

[78] Nikhil Anand, A. Liam Fitzpatrick, and W. C. Haxton. Weakly interacting massive particle-nucleus elastic scattering response. *Phys. Rev.*, C89(6):065501, 2014.

[79] E. Aprile et al. Effective field theory search for high-energy nuclear recoils using the XENON100 dark matter detector. *Phys. Rev.*, D96(4):042004, 2017.

[80] J. B. Albert et al. Improved measurement of the $2\nu\beta\beta$ half-life of ^{136}xe with the exo-200 detector. *Phys. Rev. C*, 89:015502, Jan 2014.

[81] P. J. Linstrom and W. G. Mallard, editors. *NIST Chemistry WebBook, NIST Standard Reference Database Number 69.* National Institute of Standards and Technology, Gaithersburg MD, 20899, June 2005.

[82] Curt Suplee. Nist xcom: Photon cross sections database. https://www.nist.gov/pml/xcom-photon-cross-sections-database, Visited on 05/29/2018.

[83] Dave Brown. Evaluated nuclear data file (endf) retrieval and plotting. http://www.nndc.bnl.gov/sigma/index.jsp?as=132&lib=endfb7.1&nsub=10, Visited on 05/29/2018.

[84] R.E. Shamu. High-pressure gas scintillation counters. *Nuclear Instruments and Methods*, 14:297–301, 1961.

[85] T. Doke. Fundamental properties of liquid argon, krypton and xenon as radiation detector media. *Portugal. Phys.*, 12:9–48, 1981.

[86] T. Doke, H. J. Crawford, A. Hitachi, J. Kikuchi, P. J. Lindstrom, K. Masuda, E. Shibamura, and T. Takahashi. Let Dependence of Scintillation Yields in Liquid Argon. *Nucl. Instrum. Meth.*, A269:291–296, 1988.

[87] S. Kubota, M. Hishida, and J. Raun. Evidence for a triplet state of the self-trapped exciton states in liquid argon, krypton and xenon. *Journal of Physics C: Solid State Physics*, 11(12):2645, 1978.

[88] Joshua Jortner, Lothar Meyer, Stuart A. Rice, and E.G. Wilson. Localized excitations in condensed ne, ar, kr, and xe. *The Journal of chemical physics*, 42(12):4250–4253, 1965.

[89] Akira Hitachi, Tan Takahashi, Nobutaka Funayama, Kimiaki Masuda, Jun Kikuchi, and Tadayoshi Doke. Effect of ionization density on the time dependence of luminescence from liquid argon and xenon. *Phys. Rev.*, B27:5279–5285, 1983.

[90] I.T. Steinberger and U. Asaf. Band-structure parameters of solid and liquid xenon. *Physical Review B*, 8(2):914, 1973.

[91] Elena Aprile et al. Simultaneous measurement of ionization and scintillation from nuclear recoils in liquid xenon for a dark matter experiment. *Physical review letters*, 97(8):081302, 2006.

[92] Lutz Althüse. Xenon1t blessed plots. XENON1T Internal Note, 2018.

[93] Elena Aprile, Karl L Giboni, Pawel Majewski, Kaixuan Ni, and Masaki Yamashita. Proportional light in a dual-phase xenon chamber. *IEEE Transactions on nuclear science*, 51(5):1986–1990, 2004.

[94] B.A. Dolgoshein, V.N. Lebedenko, and B.U. Rodionov. New method of registration of ionizing-particle tracks in condensed matter. *ZhETF Pisma Redaktsiiu*, 11:513, 1970.

[95] E. Aprile et al. XENON100 Dark Matter Results from a Combination of 477 Live Days. *Phys. Rev.*, D94(12):122001, 2016.

[96] E. Aprile et al. First Dark Matter Search Results from the XENON1T Experiment. *Phys. Rev. Lett.*, 119(18):181301, 2017.

[97] Xiangyi Cui et al. Dark Matter Results From 54-Ton-Day Exposure of PandaX-II Experiment. *Phys. Rev. Lett.*, 119(18):181302, 2017.

[98] D. S. Akerib et al. Results from a search for dark matter in the complete LUX exposure. *Phys. Rev. Lett.*, 118(2):021303, 2017.

[99] Saab Tarek and Figueroa Enectali. Wimp limit plotter. `http://cdms.berkeley.edu/limitplots/mm/WIMP_limit_plotter.html`, Visited on 08/2/2018.

[100] William B.J. Zimmerman. *Multiphysics modeling with finite element methods*, volume 18. World Scientific Publishing Company, 2006.

[101] Susanne C. Brenner and L.R. Scott. The mathematical theory of finite element methods. 1994.

[102] Daniel Furse et al. Kassiopeia: A Modern, Extensible C++ Particle Tracking Package. *New J. Phys.*, 19(5):053012, 2017.

[103] A. Osipowicz et al. KATRIN: A Next generation tritium beta decay experiment with sub-eV sensitivity for the electron neutrino mass. Letter of intent. 2001.

[104] D. Cubric, B. Lencova, F.H. Read, and J. Zlamal. Comparison of fdm, fem and bem for electrostatic charged particle optics. *Nuclear Instruments and Methods in Physics Research Section A: Accelerators, Spectrometers, Detectors and Associated Equipment*, 427(1-2):357–362, 1999.

[105] Thomas Corona. *Methodology and Application of High Performance Electrostatic Field Simulation in the KATRIN Experimentr.* PhD thesis, University of North Carolina at Chapel Hill Graduate School, 2015.

[106] David J. Griffiths. *Introduction to electrodynamics.* Prentice Hall, 1962.

[107] Predrag Lazić, Hrvoje Štefančić, and Hrvoje Abraham. The robin hood method–a novel numerical method for electrostatic problems based on a non-local charge transfer. *Journal of Computational Physics*, 213(1):117–140, 2006.

[108] Predrag Lazić, Hrvoje Štefančić, and Hrvoje Abraham. The robin hood method—a new view on differential equations. *Engineering analysis with boundary elements*, 32(1):76–89, 2008.

[109] Joseph A. Formaggio, Predrag Lazic, Thomas Joseph Corona, Hrvoje Stefancic, Hrvoje Abraham, and Ferenc Gluck. Solving for micro-and macro-scale electrostatic configurations using the robin hood algorithm. *Progress In Electromagnetics Research*, 39:1–37, 2012.

[110] Julien Wulf. Electrostatic Field Simulations and Low-Temperature Measurements for a Xenon-based Dual-Phase Noble Gas Dark Matter Detector. Master's thesis, Karlsruhe Institute of Technolgy, 2014.

[111] Julien Wulf. Xslap - xenon simulation and analysis package. `https://github.com/Physik-Institut-UZH/XSLAP`, 2018.

[112] Bjarne Stroustrup. *The C++ programming language*. Pearson Education India, 2000.

[113] Daniel Franz Rudolf Hilk. *Electric field simulations and electric dipole investigations at the KATRIN main spectrometer*. PhD thesis, Karlsruhe Institute of Technology, 2017.

[114] Christophe Geuzaine and Jean-François Remacle. Gmsh: A 3-d finite element mesh generator with built-in pre-and post-processing facilities. *International journal for numerical methods in engineering*, 79(11):1309–1331, 2009.

[115] Andre Ribes and Christian Caremoli. Salome platform component model for numerical simulation. In *Computer Software and Applications Conference, 2007. COMPSAC 2007. 31st Annual International*, volume 2, pages 553–564. IEEE, 2007.

[116] Will J. Schroeder, Bill Lorensen, and Ken Martin. *The visualization toolkit: an object-oriented approach to 3D graphics*. Kitware, 2004.

[117] James Ahrens, Berk Geveci, Charles Law, C Hansen, and C Johnson. 36-paraview: An end-user tool for large-data visualization. *The visualization handbook*, 717, 2005.

[118] William Gropp, Ewing Lusk, Nathan Doss, and Anthony Skjellum. A high-performance, portable implementation of the mpi message passing interface standard. *Parallel computing*, 22(6):789–828, 1996.

[119] Rene Brun and Fons Rademakers. Root—an object oriented data analysis framework. *Nuclear Instruments and Methods in Physics Research Section A: Accelerators, Spectrometers, Detectors and Associated Equipment*, 389(1-2):81–86, 1997.

[120] Chi-Ok Hwang, Michael Mascagni, and Taeyoung Won. Monte carlo methods for computing the capacitance of the unit cube. *Mathematics and Computers in Simulation*, 80(6):1089–1095, 2010.

[121] Chi-Ok Hwang and Michael Mascagni. Electrical capacitance of the unit cube. *Journal of applied physics*, 95(7):3798–3802, 2004.

[122] Carolo Friderico Gauss. Theoria attractionis corporum sphaeroidicorum ellipticorum homogeneorum. In *Werke*, pages 3–22. Springer, 1877.

[123] Ralph L Amey and Robert H Cole. Dielectric constants of liquefied noble gases and methane. *The Journal of Chemical Physics*, 40(1):146–148, 1964.

[124] L. Baudis et al. A Dual-phase Xenon TPC for Scintillation and Ionisation Yield Measurements in Liquid Xenon. *Eur. Phys. J.*, C78(5):351, 2018.

[125] Francesco Piastra. *Materials Radioassay for the XENON1T Dark Matter Experiment, and Development of a Time Projection Chamber for the Study of Low-energy Nuclear Recoils in Liquid Xenon.* PhD thesis, University of Zurich, 2017.

[126] E. Aprile et al. Observation and applications of single-electron charge signals in the XENON100 experiment. *J. Phys.*, G41:035201, 2014.

[127] L. Jacques, W. Bruynooghe, R. Boucique, and W. Wieme. Experimental determination of the primary and secondary ionisation coefficients in krypton and xenon. *Journal of Physics D: Applied Physics*, 19(9):1731, 1986.

[128] F.I.G.M. Borges et al. Operation of gas proportional scintillation counters in a low charge multiplication regime. *Nuclear Instruments and Methods in Physics Research Section A: Accelerators, Spectrometers, Detectors and Associated Equipment*, 422(1-3):321–325, 1999.

[129] G. Bellini et al. Cosmic-muon flux and annual modulation in Borexino at 3800 m water-equivalent depth. *JCAP*, 1205:015, 2012.

[130] E. Aprile et al. Conceptual design and simulation of a water Cherenkov muon veto for the XENON1T experiment. *JINST*, 9:P11006, 2014.

[131] Berkeley nucleonics corporation. `https://www.berkeleynucleonics.com/`, Visited on 05/05/2018.

[132] Caen. `http://www.caen.it/`, Visited on 05/05/2018.

[133] Philips. `http://www.phillipsscientific.com`, Visited on 05/05/2018.

[134] Jelle Aalbers. *Dark matter search with XENON1T.* PhD thesis, Universiteit van Amsterdam, 2018.

[135] Skutek. `http://www.skutek.com`, Visited on 05/05/2018.

[136] J. Aalbers and C. Tunnell. The pax data processor v6.4.2, February 2017.

[137] E. Aprile et al. Removing krypton from xenon by cryogenic distillation to the ppq level. *Eur. Phys. J.*, C77(5):275, 2017.

[138] Elena Aprile et al. Facility and method for supplying liquid xenon, 2013.

[139] C.Y. Chen, Y.M. Li, K. Bailey, T.P. O'connor, L. Young, and Z.-T. Lu. Ultrasensitive isotope trace analyses with a magneto-optical trap. *Science*, 286(5442):1139–1141, 1999.

[140] E. Aprile et al. Physics reach of the XENON1T dark matter experiment. *JCAP*, 1604(04):027, 2016.

[141] Sebastian Lindemann and Hardy Simgen. Krypton assay in xenon at the ppq level using a gas chromatographic system and mass spectrometer. *Eur. Phys. J.*, C74:2746, 2014.

[142] M. Yamashita, T. Doke, K. Kawasaki, J. Kikuchi, and S. Suzuki. Scintillation response of liquid xe surrounded by ptfe reflector for gamma rays. *Nuclear Instruments and Methods in Physics Research Section A: Accelerators, Spectrometers, Detectors and Associated Equipment*, 535(3):692 – 698, 2004.

[143] Basho Kaminsky. Final xe1t reflector - optical measurements. XENON1T Internal Note, 2015.

[144] E. Aprile et al. The XENON1T Dark Matter Experiment. *Eur. Phys. J.*, C77(12):881, 2017.

[145] E. Aprile et al. Material radioassay and selection for the XENON1T dark matter experiment. *Eur. Phys. J.*, C77(12):890, 2017.

[146] A. Einstein. Über einen die erzeugung und verwandlung des lichtes betreffenden heuristischen gesichtspunkt. *Annalen der Physik*, 322(6):132–148, 1905.

[147] Annika Behrens. *Light Detectors for the XENON100 and XENON1T Dark Matter Search Experiments*. PhD thesis, University of Zurich, 2014.

[148] E. Aprile et al. Lowering the radioactivity of the photomultiplier tubes for the XENON1T dark matter experiment. *Eur. Phys. J.*, C75(11):546, 2015.

[149] L. Baudis et al. Gator: a low-background counting facility at the gran sasso underground laboratory. *Journal of Instrumentation*, 6(08):P08010, 2011.

[150] P. Barrow et al. Qualification Tests of the R11410-21 Photomultiplier Tubes for the XENON1T Detector. *JINST*, 12(01):P01024, 2017.

[151] Fralock cirlex® applications. `http://www.fralock.com/aerospace/composite-materials/cirlex/cirlex-applications/`, Visited on 05/06/2018.

[152] Gaudenz Kessler. *Inelastic WIMP-Nucleus Interactions in XENON100 and Cables and Connectors for XENON1T*. PhD thesis, University of Zurich, 2016.

[153] Owen Willans Richardson. *On the Negative Radiation from Hot Platinum*. University Press, 1901.

[154] Daniel Mayani. *Photomultiplier Tubes for the XENON1T Dark Matter Experiment and Studies on the XENON100 Electromagnetic Background*. PhD thesis, University of Zurich, 2017.

[155] Hamamatsu Handbook. *Photomultiplier Tubes: Basics and Applications*. Hamamatsu Photonics, 3 edition, 2007.

[156] S.-O. Flyckt. *Photomultiplier tubes: principles and applications*. Photonis, 2002.

[157] D.R. Carter. Photomultiplier handbook: Theory, design, application. *Lancaster,(PA): Burle Industries, Inc*, 1980.

[158] A.G. Wright. Method for the determination of photomultiplier collection efficiency. *Applied optics*, 49(11):2059–2065, 2010.

[159] Florian Kaether and Conradin Langbrandtner. Transit time and charge correlations of single photoelectron events in r7081 photomultiplier tubes. *Journal of Instrumentation*, 7(09):P09002, 2012.

[160] L. Baudis, S. D'Amato, G. Kessler, A. Kish, and J. Wulf. Measurements of the position-dependent photo-detection sensitivity of the Hamamatsu R11410 and R8520 photomultiplier tubes. 2015.

[161] Sandro D'Amato. SandBox: A facility for XENON photosensors characterization and measurements of photocathode uniformity, 2014.

[162] R. Saldanha, L. Grandi, Y. Guardincerri, and T. Wester. Model Independent Approach to the Single Photoelectron Calibration of Photomultiplier Tubes. *Nucl. Instrum. Meth.*, A863:35–46, 2017.

[163] F.C. Nix and D. MacNair. The thermal expansion of pure metals: copper, gold, aluminum, nickel, and iron. *Physical Review*, 60(8):597, 1941.

[164] Susumu Hirakawa and Tetuo Takemura. Transitions and phases of polytetrafluoroethylene. *Japanese Journal of Applied Physics*, 8(6):635, 1969.

[165] Richard K. Kirby. Thermal expansion of polytetrafluoroethylene (teflon) from- 190° to+ 300° c. *Journal of Research of the National Bureau of Standards*, 57(2):91–94, 1956.

[166] P.J. Rae and D.M. Dattelbaum. The properties of poly(tetrafluoroethylene) (ptfe) in compression. *Polymer*, 45(22):7615 – 7625, 2004.

[167] Payam Pakarha. *Calibration System of the Photosensors for the XENON1T Dark Matter Search Experiment, and Response of Liquid Xenon to Low-energy Neutron Interactions.* PhD thesis, University of Zurich, 2017.

[168] R. F Lang et al. Characterization of a deuterium–deuterium plasma fusion neutron generator. *Nucl. Instrum. Meth.*, A879:31–38, 2018.

[169] Friedrich Paschen. Über die zum funkenübergang in luft, wasserstoff und kohlensäure bei verschiedenen drucken erforderliche potentialdifferenz. *Annalen der physik*, 273(5):69–96, 1889.

[170] Luke Welling and Laura Thomson. *PHP and MySQL Web development.* Sams Publishing, 2003.

[171] B. N. V. Edwards et al. Extraction efficiency of drifting electrons in a two-phase xenon time projection chamber. *JINST*, 13(01):P01005, 2018.

[172] S. Nissen. Implementation of a fast artificial neural network library (fann). Technical report, Department of Computer Science University of Copenhagen (DIKU), 2003. http://fann.sf.net.

[173] D. S. Akerib et al. 3D Modeling of Electric Fields in the LUX Detector. *JINST*, 12(11):P11022, 2017.

[174] D. S. Akerib et al. $^{83\mathrm{m}}$Kr calibration of the 2013 LUX dark matter search. *Phys. Rev.*, D96(11):112009, 2017.

[175] J. Thomas and D. A. Imel. Recombination of electron-ion pairs in liquid argon and liquid xenon. *Phys. Rev. A*, 36:614–616, Jul 1987.

[176] M. Szydagis et al. Nest: a comprehensive model for scintillation yield in liquid xenon. *Journal of Instrumentation*, 6(10):P10002, 2011.

[177] Carl Eric Dahl. *The physics of background discrimination in liquid xenon, and first results from Xenon10 in the hunt for WIMP dark matter.* PhD thesis, Princeton U., 2009.

[178] E. Conti et al. Correlated fluctuations between luminescence and ionization in liquid xenon. *Phys. Rev. B*, 68:054201, Aug 2003.

[179] Alexander Kish. *Dark Matter Search with the XENON100 Experiment.* PhD thesis, University of Zurich, 2011.

[180] Tadayoshi Doke, Akira Hitachi, Jun Kikuchi, Kimiaki Masuda, Hiroyuki Okada, and Eido Shibamura. Absolute scintillation yields in liquid argon and xenon for various particles. *Japanese Journal of Applied Physics*, 41(3R):1538, 2002.

[181] M. Miyajima, T. Takahashi, S. Konno, T. Hamada, S. Kubota, H. Shibamura, and T. Doke. Average energy expended per ion pair in liquid argon. *Phys. Rev. A*, 9:1438–1443, Mar 1974.

[182] Peter F. Sorensen. *A Position-Sensitive Liquid Xenon Time-Projection Chamber for Direct Detection of Dark Matter.* PhD thesis, Brown University, 2008.

[183] E. Aprile et al. Analysis of the XENON100 Dark Matter Search Data. *Astropart. Phys.*, 54:11–24, 2014.

[184] D. S. Akerib et al. First results from the LUX dark matter experiment at the Sanford Underground Research Facility. *Phys. Rev. Lett.*, 112:091303, 2014.

[185] J. B. Albert et al. Measurement of the Drift Velocity and Transverse Diffusion of Electrons in Liquid Xenon with the EXO-200 Detector. *Phys. Rev.*, C95(2):025502, 2017.

[186] L. S. Miller, S. Howe, and W. E. Spear. Charge transport in solid and liquid ar, kr, and xe. *Phys. Rev.*, 166:871–878, Feb 1968.

[187] E.M. Gushchin, A.A. Kruglov, and I.M. Obodovskii. Electron dynamics in condensed argon and xenon. *Zh, Eksp. Teor. Fiz*, 82:1114–1125, 1982.

[188] P. Benetti et al. A simple and effective purifier for liquid xenon. *Nuclear Instruments and Methods in Physics Research Section A: Accelerators, Spectrometers, Detectors and Associated Equipment*, 329(1):361 – 364, 1993.

[189] W. Shockley. Hot electrons in germanium and ohm's law. *Bell Labs Technical Journal*, 30(4):990–1034, 1951.

[190] Finn M. Jacobsen, Norman Gee, and Gordon R. Freeman. Electron mobility in liquid krypton as function of density, temperature, and electric field strength. *Phys. Rev. A*, 34:2329–2335, Sep 1986.

[191] K. Yoshino, U. Sowada, and W. F. Schmidt. Effect of molecular solutes on the electron drift velocity in liquid ar, kr, and xe. *Phys. Rev. A*, 14:438–444, Jul 1976.

[192] W. E. SPEAR and P. G. LE COMBER. A possible explanation of the observed electron drift velocity saturation in solid ar, kr, and xe. *Phys. Rev.*, 178:1454–1456, Feb 1969.

[193] E. Santos et al. Single electron emission in two-phase xenon with application to the detection of coherent neutrino-nucleus scattering. *JHEP*, 12:115, 2011.

[194] D. Akimov et al. Observation of delayed electron emission in a two-phase liquid xenon detector. *Journal of Instrumentation*, 11(03):C03007, 2016.

[195] Peter Sorensen. Electron train backgrounds in liquid xenon dark matter search detectors are indeed due to thermalization and trapping. 2017.

[196] E. Aprile et al. Signal Yields of keV Electronic Recoils and Their Discrimination from Nuclear Recoils in Liquid Xenon. *Phys. Rev.*, D97:092007, 2018.

[197] E. Aprile et al. Dark Matter Search Results from a One Tonne×Year Exposure of XENON1T. *Phys. Rev. Lett.*, 121(11):111302, 2018.

[198] Daniel Z. Freedman, David N. Schramm, and David L. Tubbs. The weak neutral current and its effects in stellar collapse. *Annual Review of Nuclear Science*, 27(1):167–207, 1977.

[199] A. Drukier and L. Stodolsky. Principles and applications of a neutral-current detector for neutrino physics and astronomy. *Phys. Rev. D*, 30:2295–2309, Dec 1984.

[200] Aldo M. Serenelli, W. C. Haxton, and Carlos Pena-Garay. Solar models with accretion. I. Application to the solar abundance problem. *Astrophys. J.*, 743:24, 2011.

[201] D. Akimov et al. Observation of Coherent Elastic Neutrino-Nucleus Scattering. *Science*, 357(6356):1123–1126, 2017.

[202] F. James. Interpretation of the shape of the likelihood function around its minimum. *Computer Physics Communications*, 20(1):29–35, 1980.

[203] Maurice S. Bartlett. Approximate confidence intervals. ii. more than one unknown parameter. *Biometrika*, 40(3/4):306–317, 1953.

[204] Nadav Priel, Ludwig Rauch, Hagar Landsman, Alessandro Manfredini, and Ranny Budnik. A model independent safeguard against background mismodeling for statistical inference. *JCAP*, 1705(05):013, 2017.

[205] Gary J. Feldman and Robert D. Cousins. Unified approach to the classical statistical analysis of small signals. *Physical Review D*, 57(7):3873, 1998.

[206] C. Patrignani, Particle Data Group, et al. Review of particle physics. *Chinese physics C*, 40(10):100001, 2016.

[207] Ethan Brown et al. Magnetically-coupled piston pump for high-purity gas applications. 2018.

[208] E. Aprile et al. Online^{222} Rn removal by cryogenic distillation in the XENON100 experiment. *Eur. Phys. J.*, C77(6):358, 2017.

[209] Glen Cowan, Kyle Cranmer, Eilam Gross, and Ofer Vitells. Asymptotic formulae for likelihood-based tests of new physics. *Eur. Phys. J.*, C71:1554, 2011. [Erratum: Eur. Phys. J.C73,2501(2013)].

[210] E. Aprile et al. Likelihood Approach to the First Dark Matter Results from XENON100. *Phys. Rev.*, D84:052003, 2011.

[211] Julien Wulf. Daq - data acquistion system. `https://github.com/Physik-Institut-UZH/DAQ`, 2018.

[212] Julien Wulf. Warp - raw data processor. `https://github.com/Physik-Institut-UZH/WARP`, 2018.

[213] Manuel Walter. *Background Reduction Techniques for the Gerda Experiment.* PhD thesis, University of Zurich, 2015.

[214] E. Aprile et al. Design and Performance of the XENON10 Dark Matter Experiment. *Astropart. Phys.*, 34:679–698, 2011.

[215] E. Aprile et al. The XENON100 Dark Matter Experiment. *Astropart. Phys.*, 35:573–590, 2012.

[216] A. Manalaysay et al. Spatially uniform calibration of a liquid xenon detector at low energies using 83m-Kr. *Rev. Sci. Instrum.*, 81:073303, 2010.

[217] J. Aalbers et al. DARWIN: towards the ultimate dark matter detector. *JCAP*, 1611:017, 2016.

[218] J. Billard, L. Strigari, and E. Figueroa-Feliciano. Implication of neutrino backgrounds on the reach of next generation dark matter direct detection experiments. *Phys. Rev.*, D89(2):023524, 2014.

[219] Marc Schumann, Laura Baudis, Lukas Bütikofer, Alexander Kish, and Marco Selvi. Dark matter sensitivity of multi-ton liquid xenon detectors. *JCAP*, 1510(10):016, 2015.

[220] L. Baudis, A. Ferella, A. Kish, A. Manalaysay, T. Marrodan Undagoitia, and M. Schumann. Neutrino physics with multi-ton scale liquid xenon detectors. *JCAP*, 1401:044, 2014.

[221] Earl Gates. *Introduction to electronics.* Cengage Learning, 2011.

[222] D'Amato Sandro. Characterization of silicon photomultiplier arrays in liquid xenon and development of dedicated read-out electronics. Master's thesis, University of Zurich, 2016.

[223] K.P. O'Donnell and X. Chen. Temperature dependence of semiconductor band gaps. *Applied physics letters*, 58(25):2924–2926, 1991.

[224] C. Canali, G. Majni, R. Minder, and G. Ottaviani. Electron and hole drift velocity measurements in silicon and their empirical relation to electric field and temperature. *IEEE Transactions on Electron Devices*, 22(11):1045–1047, 1975.

[225] Shinji Ogawa. Liquid xenon calorimeter for MEG II experiment with VUV-sensitive MPPCs. *Nucl. Instrum. Meth.*, A845:528–532, 2017.

[226] Hamamatsu. S13371 datasheet, 2018.

[227] L. Baudis, M. Galloway, A. Kish, C. Marentini, and J. Wulf. Characterisation of silicon photomultipliers for liquid xenon detectors. *Journal of Instrumentation*, 13(10):P10022, 2018.

[228] Roland H. Haitz. Model for the electrical behavior of a microplasma. *Journal of Applied Physics*, 35(5):1370–1376, 1964.

[229] D. Renker and E. Lorenz. Advances in solid state photon detectors. *Journal of Instrumentation*, 4(04):P04004, 2009.

[230] B.F. Aull, A.H. Loomis, D.J. Young, R.M. Heinrichs, B.J. Felton, and P.J. Daniels. Geiger-mode avalanche photodiodes for three-dimensional imaging. 13:335–349, 01 2002.

[231] S. Catalanotti, A. G. Cocco, G. Covone, M. D'Incecco, G. Fiorillo, G. Korga, B. Rossi, and S. Walker. Performance of a SensL-30035-16P Silicon Photomultiplier array at liquid argon temperature. *JINST*, 10(08):P08013, 2015.

[232] Y. Okuto and C. R. Crowell. Energy-conservation considerations in the characterization of impact ionization in semiconductors. *Phys. Rev. B*, 6:3076–3081, Oct 1972.

[233] C. R. Crowell and S. M. Sze. Temperature dependence of avalanche multiplication in semiconductors. *Applied Physics Letters*, 9(6):242–244, 1966.

[234] W. Shockley and W. T. Read. Statistics of the recombinations of holes and electrons. *Phys. Rev.*, 87:835–842, Sep 1952.

[235] Pagano et al. Dark current in silicon photomultiplier pixels: Data and model. *IEEE Transactions on Electron Devices*, 59:2410–2416, 09 2012.

[236] Ivan Rech, Antonino Ingargiola, Roberto Spinelli, Ivan Labanca, Stefano Marangoni, Massimo Ghioni, and Sergio Cova. Optical crosstalk in single photon avalanche diode arrays: a new complete model. *Opt. Express*, 16(12):8381–8394, Jun 2008.

[237] Roger Newman. Visible light from a silicon $p-n$ junction. *Phys. Rev.*, 100:700–703, Oct 1955.

[238] M. Biroth, P. Achenbach, E. Downie, and A. Thomas. Silicon photomultiplier properties at cryogenic temperatures. *Nucl. Instrum. Meth.*, A787:68–71, 2015.

[239] Chen Xu. *Study of the Silicon Photomultipliers and Their Applications in Positron Emission Tomography.* PhD thesis, University of Hamburg, 2014.

[240] Chris Marentini. Characterization of Novel VUV-Silicon Photomultipliers and their Application in Xenon-Based Dual-Phase TPCs. Master's thesis, University of Zurich, 2018.

[241] S. Agostinelli et al. GEANT4: A Simulation toolkit. *Nucl. Instrum. Meth.*, A506:250–303, 2003.

[242] Michelle Galloway. Xurich optical photon simulations. Internal Working Group Note, 2016.

[243] Elena Aprile, Alexander I. Bolozdynya, Aleksey E. Bolotnikov, and T. Doke. *Noble gas detectors.* John Wiley & Sons, 2006.

[244] Nasser M Nasrabadi. Pattern recognition and machine learning. *Journal of electronic imaging*, 16(4):049901, 2007.

[245] Martín Abadi et al. TensorFlow: Large-scale machine learning on heterogeneous systems, 2015. Software available from tensorflow.org.

[246] Laura Baudis, Giovanni Benato, Rugard Dressler, Francesco Piastra, Ilya Usoltsev, and Manuel Walter. Enhancement of Light Yield and Stability of Radio-Pure Tetraphenyl-Butadiene Based Coatings for VUV Light Detection in Cryogenic Environments. *JINST*, 10(09):P09009, 2015.

[247] L. W. Kastens, S. B. Cahn, A. Manzur, and D. N. McKinsey. Calibration of a Liquid Xenon Detector with Kr-83m. *Phys. Rev.*, C80:045809, 2009.

[248] Edgardo Browne, Richard B Firestone, and Virginia S Shirley. *Table of radioactive isotopes.* Wiley, New York, NY, 1986. Based on the 7th ed. of C.M. Lederer. Table of isotopes. New York, Wiley, 1978.

[249] Michael Hoffmann. *CAD, CAM mit CATIA V5: NC-Programmierung, Postprocessing, Simulation*, volume 5. Hanser Verlag, 2005.

[250] Guillaume Plante. *The XENON100 Dark Matter Experiment: Design, Construction, Calibration and 2010 Search Results with Improved Measurement of the Scintillation Response of Liquid Xenon to Low-Energy Nuclear Recoils.* PhD thesis, Columbia University, 2012.